Modeling, characterization and trajectory planning of a planar micro-conveyance device based on a digital actuator array

Simon Duque Tisnes

UNIVERSITÉ DE TECHNOLOGIE DE COMPIÈGNE

CNRS Roberval Laboratory

Department of Mechanical Engineering

Mechatronics, Energy, Electricity & Integration Research Unit

PhD dissertation

Modeling, characterization & trajectory planning of a planar micro-conveyance device based on a digital actuator array

---

by SIMÓN DUQUE TISNÉS

2020

Reviewer:	Prof. Dr. YASSINE HADDAB
Reviewer:	Dr. CÉDRIC CLEVY
Jury member:	Prof. Dr. ELIE LEFEUVRE
Jury member:	Prof. Dr. BETTY LEMAIRE – SEMAIL
Jury member:	Prof. Dr. STÉPHANE RÉGNIER
Jury member:	Prof. Dr. VINCENT LANFRANCHI
Advisor:	Dr. LAURENT PETIT
Advisor:	Prof. Dr. CHRISTINE PRELLE
Invited:	Dr. ÉMILE MARTINCIC

Para Pipa, Nana y Yoya.
Para mis padres, quienes son mi ejemplo de vida.

Acknowledgments

First, I'd like to thank Laurent Petit and Christine Prelle, my advisors, for their support, evaluation and the working conditions they always thrived to provide to their students. I always felt welcomed and pertinent within the research team. My special gratitude to Laurent for his guidance and discussions on these years as his PhD student. I really appreciated the independence and responsibility that he conferred me, and the trust that those attributes represent. At the same time, he kept a detailed and valuable follow of the progress and problems of my work. All of this coupled with Laurent's very busy schedule. I could not have a better advisor for my PhD.

I'd also like to thank Frédéric Lamarque for his productive and interesting discussions. The kinematic experimental results were possible thanks to his connections with other research groups on the university and the trust he conferred me to use such an expensive material as the Photron FastCam.

I'd like to thank Sergio Rodriguez Cadavid for his clever idea of bringing the system to mechanical equilibrium to optimize its operation. This idea formed the basis of Section 5.2 and, over all, for his friendship. Also, I thank Atif Tasneem for his internship work as part of our research project. His contributions were important for Chapter 6, specially, the virtual interface Section 6.5. I thank Douglas Brown for his very useful open-source software "Tracker". His software allowed the image processing method used to measure all experimental results of Chapter 4 and Chapter 7.

I thank my fellow labmates and friends on the university for the enjoyable atmosphere and memories: board games, cultural exchange (food!), snow fights, sports (specially tennis and ultimate), bike tours... I had a wonderful time during these years.

Lastly, and most important, I heartily thank Miriam for her support and patience during my whole PhD and also her valuable comments on this manuscript.

Abstract

The increased demand for compact, intelligent and multi-functional products is met by miniaturizing components like sensors, actuators and processors. Therefore, the manufacturing systems must adapt, which draws attention to the subject of microfactories. This research investigates a modular array of digital electromagnetic actuators based on the Lorentz force principle as a microconveyor device for the microfactory. A dynamic model of the array is developed and used in a feed-forward, open-loop scheme inside a trajectory controller. The dynamic model is derived from analytical studies of the electromagnetic, magnetic, friction and contact mechanics forces present on the array. The trajectory controller uses adapted A* and Theta* (Θ*) pathfinding algorithms. The resulting controller computes the optimal path to transport the object on the array between the target positions, minimizing energy consumption, displacement time and trajectory error, whilst avoiding collisions. Experimental tests on a microfabricated array prototype with a 5×5 matrix of microactuators are held to validate the dynamic model and evaluate this array's performance. The tests use two cameras and image processing software to measure the displacement of loads from 0.2 to 9 g at speeds up to $2\,\mathrm{mm\,s^{-1}}$. The dynamic model predicts the array's behavior with low root-mean-square and mean-absolute errors. The results show that the array is a viable alternative to the microconveyors for the microfactory.

Keywords: microelectromechanical systems (MEMS), micro engineering, microsystem technologies (MTS), actuator array, conveyance system, digital actuator, collaborative actuation, electromagnetic actuator, planar motion, smart surface, microfactory.

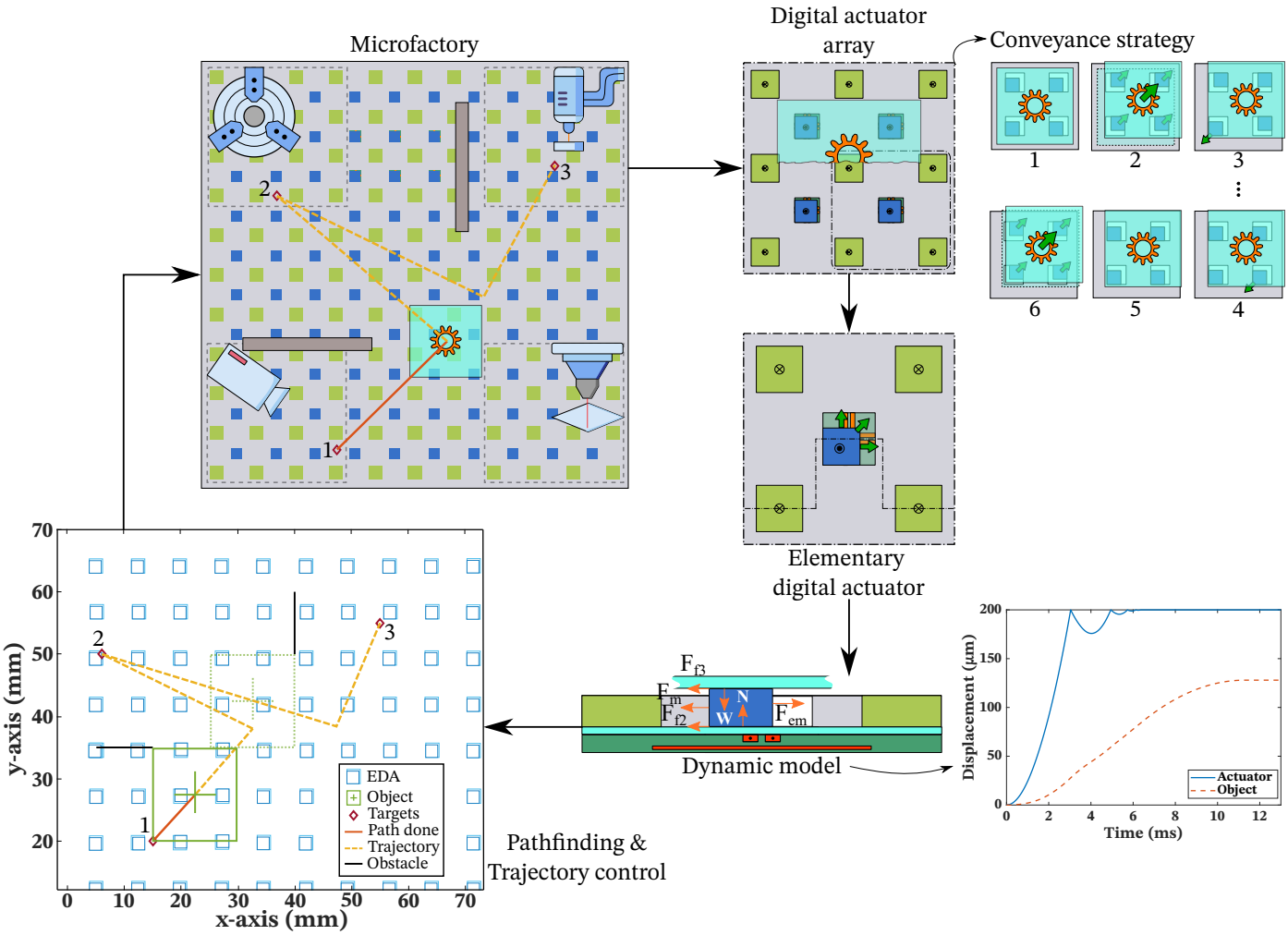

Graphical abstract

Contents

Acronyms

DAA digital actuator array

DoF degree of freedom

EDA elementary digital actuator

FPM fixed permanent magnet

MAE mean-absolute error

MAPF multi-agent pathfinding

MPM mobile permanent magnet

RMSE root-mean-square error

Introduction

This dissertation is a contribution to the miniaturization of manufacturing systems. More precisely, the control of a conveyance system directed towards the microfactory. The microfactory is a proposed solution to the need of miniaturization of manufacturing systems. Why is there a need to miniaturize the manufacturing systems, how does the microfactory contribute to this need and how does this dissertation contribute to the microfactory?

The increased demand for compact, intelligent and multi-functional products like smartphones, smartwatches, personal computers, wearable technology, headphones, cameras, remote access keys, or energy harvesters can only be met by packaging more and more sensors, actuators and processors into the products. Miniaturization has been the industries' answer to this new paradigm of market demand [Hsu02]. Miniaturization is the idea to downscale a system or component in size to satisfy, principally, space and functionally requirements. A larger number of functional components such as sensors, actuators and processors can be integrated after being miniaturized. Miniaturization produced an unexpected range of applications and performance improvements to numerous industries.

To produce miniature components for small scale and compact products, the miniaturization of the manufacturing systems (the microfactory) is proposed as a solution [Mis+02; OMA04; Jär+15; Zha+17]. The idea of implementing manufacturing machines proportional to the size of the goods produced was born in Japan in 1991 and was called *microfactory* in 1999 [Mis+02; OMA04]. Thus, the microfactory is defined as "a small-size production system suitable for the manufacture of small products with micro and/or macro-sized features. It is the philosophy of downscaling the production equipment closer to the size of the produced goods" [Jär+15].

Microfactories are often characterized by modularity, reconfigurability and mobility. As the machines are smaller, they usually consume less energy and raw materials, and generate less waste. They require less factory floor space, reducing the energy used for illumination, air-conditioning and heating. They also produce less waste heat [Jär+15]. The transfer distances of pieces are shorter, reducing transportation and logistics [OMA04].

Current microfactories produce components for multiple products from different industries (see Section 1.5.4 for microfactory examples). These products need to be properly sorted, conveyed and aligned in each step of its manufacture and assembly process. This is the task of the conveyor of such microfactory. Current conveyance solutions are based on miniature belt conveyors and serial processes with grippers, which are not efficient nor flexible to the increasing demand on those manufacturing systems [LA12]. Conveyors actuating on multiple degrees of freedom, able to execute parallel procedures and easy reconfigurable, add flexibility and further compact the microfactory.

This dissertation proposes a modular array of digital electromagnetic actuators based on the Lorentz force principle as a microconveyor device. The modular design ensures the flexibility, reconfigurability and mobility needed for the microfactory. The digital actuation provides repeatable positions, low energy consumption and ease of integration thanks to the open-loop control. The Lorentz electromagnetic principle generates large strokes with medium forces and response times compared with other actuation principles.

This dissertation **research question** is then: How to exploit an *array* of *digital electromagnetic actuators* as a *conveyance system* to transport objects between different machining/quality stations of a *microfactory*, efficiently in terms of consumed energy, displacement time, final position and trajectory error, and avoiding collisions with obstacles or other transported objects?

To answer the research question, this thesis develops a dynamic model of the basic structure of the array (the elementary digital electromagnetic actuator). This dynamic model is then generalized for the array. The dynamic model is deduced from the physical principles behind the actuator's operation. The dynamic model is then used as a feed-forward control of the array to define the control variables needed to obtain a given displacement. An experimental campaign is then executed to validate the dynamic model and its ability to predict the array's behavior. This experimental tests study all the input/output relations of the array. To know which displacement is optimal for the given task, pathfinding algorithms are adapted to the array to convey the objects minimizing the consumed energy, displacement time, final position and trajectory error, and avoiding collisions with obstacles or other transported objects.

Figure 1 presents this manuscript's body structure. The thesis is developed on the first three parts: Background; Dynamic model; and Conveyance. Part four presents the conclusions and perspectives of this work. Part five, Appendix, defines multiple terms used along the text and presents additional results. The content covered on parts one to three is described next.

Chapter 1 defines the emphasized words of the research question. The con-

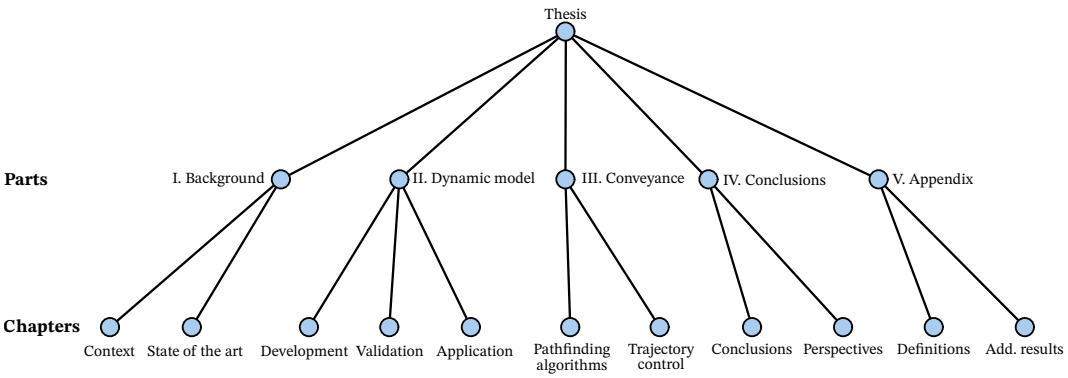

Figure 1: Dissertation tree.

cept of *digital actuator*, and the functions needed to obtain such a device, are treated. The advantages/drawbacks of digital actuation against analog actuation is discussed. Examples of digital actuators exploiting material properties, electromagnetic circuits and locking systems are presented. A classification of digital actuators by the number and nature of its discrete positions is proposed with examples for each type. Then, a *conveyor* is defined within its family of systems: planar motion systems. The difference of the conveyors to its related systems is explained by their requirements. Examples of planar motion systems are presented. Afterwards, the idea of arranging multiple actuators in an *array* to obtain a system able to accomplish complex tasks is explained. Examples of array loudspeakers, adaptive optic mirrors, displays, and tactile interfaces are presented. Then, this dissertation's application context, the *microfactory*, is explained in detail. This section goes from the need of miniaturize the manufacturing systems to the place of microfactories in this challenge, along with microfactory examples from the research and industrial fields. Chapter 1 finishes with the scope and context of this dissertation as part of the "Tridimensional micro-conveyance systems for the micro-factory" (ALVEO) research project, funded by the national research agency of France: Agence Nationale de la Recherche (ANR). ALVEO's objective is to develop tridimensional micro-conveyance systems satisfying the needs of the microfactory environment.

Chapter 2 presents the state of the art related to: micro planar motion systems (divided by physical principles of their actuators); contact mechanics modeling; and pathfinding. The first section, micro planar motion systems, explains and exemplifies electrostatic, electrothermal, electrowetting, piezoelectric, pneumatic and electromagnetic systems. The section discusses the advantages and drawbacks of each physical principle. The second section, contact mechanics, presents the theories and modeling of two crucial phenomena of this dissertation's system: collisions of the mobile part against the limiting cavity and friction phenomena, as a stick-slip friction conveyance principle is used. The final section, pathfinding,

presents the vast approaches developed in the literature to solve the conveyance problem: efficiently move one or multiple objects between desired positions avoiding obstacles and collisions.

Chapter 3 explains the principles and characteristics of the elementary digital actuator (EDA) and the digital actuator array (DAA). The array conveyance strategy is explained and its use on the microfactory context discussed. Then a 5×5 DAA prototype is presented. This chapter develops the dynamic model, starting from the force analysis of the digital actuator and its kinematic phenomena such as collisions and rebounds. The electromagnetic driving forces, magnetic holding forces, friction forces, collision and rebound events are studied. This basic model is then generalized to the array under certain assumptions. The assumptions are evaluated and the model uncertainties discussed.

Chapter 4 presents the array characterization and experimental model validation. The experimental conditions, materials and experimental setups of the tests are explained. The experimental tests aim to study the influence of all inputs of the DAA on the uni-dimensional and bi-dimensional motion of the actuator and conveyed object. The model correlation with the outputs is measured and discussed for each input-output relation.

Chapter 5 explores three dynamic model applications. First, the scaling and miniaturization potential of the actuator is treated. Second, the current profile optimizing the energy consumption on the EDA is deduced. This principle can be used to find wished displacement, speed, acceleration profiles of the EDA and conveyed object on the DAA. Lastly, the dynamic model is extended to any actuator and array geometry. The dynamic model is adapted to a different shape of actuator and array to validate the modular modeling idea.

Chapter 6 explains the pathfinding and trajectory control of the DAA. How to represent the DAA environment, how to find the correct path on the environment and how to optimize the DAA performance are the questions answered in this chapter. A virtual interface of the DAA is developed to predict the behavior of the real system.

Chapter 7 presents the experimental tests of the DAA as a conveyance device. Conveyance speed, distance, energetic efficiency, pathfinding and trajectory control are evaluated. The total active area of the DAA is demonstrated to be exploitable, with the influence of the transition between columns studied. These criteria help to find an optimum working point of the DAA. The final tests are the computation and execution of bi-dimensional trajectories on the DAA.

Finally, Chapter 8 and Chapter 9 present the conclusions and perspectives of this thesis, respectively.

Publication list

Partial results of the presented thesis have been published in:

- S. Duque Tisnes *et al.*, "Long-range Planar Conveyance Device Based On A Digital Electromagnetic Actuator Array," in 2020 Symposium on Design, Test, Integration & Packaging of MEMS and MOEMS (DTIP), Jun. 2020, pp. 1–5.
- S. Duque Tisnes, L. Petit, C. Prelle, and F. Lamarque, "Modeling and experimental validation of a planar micro conveyor based on a 2 x 2 array of digital electromagnetic actuators," IEEE/ASME Trans. Mechatronics, vol. 4435, no. c, 2020.
- S. Duque Tisnes, Z. Shi, L. Petit, C. Prelle, and F. Lamarque, "Characterization of a micro-fabricated digital actuator array as a micro-factory conveyor device," in 2019 IEEE/ASME International Conference on Advanced Intelligent Mechatronics (AIM), Jul. 2019, pp. 382–387.
- S. Duque Tisnes, L. Petit, and C. Prelle, "Control strategies for a micro-conveyance system based on an electromagnetic digital actuator array," in 2018 12th France-Japan and 10th Europe-Asia Congress on Mechatronics, Sep. 2018, pp. 137–142.

Part I

Background & state of the art

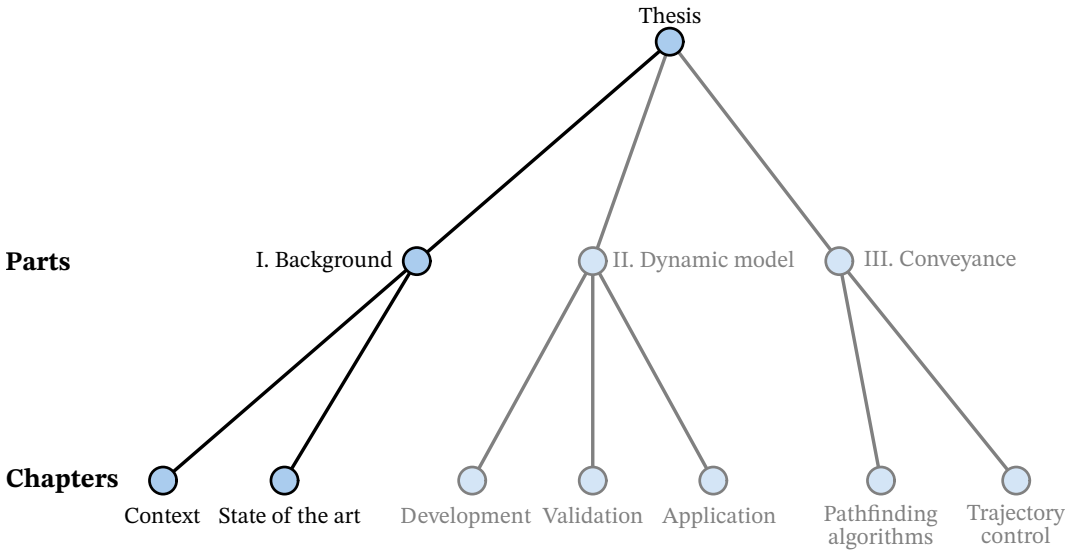

Chapter 1

Background & definitions

This chapter defines the mechatronics concepts discussed in this dissertation. These concepts will place this dissertation's context and subject, give the criteria to evaluate the solutions presented in the state of the art against the solution developed in this work, and set the five central topics of this dissertation's research project: 1. Digital actuation. 2. Planar motion actuation systems. 3. Actuator arrays for complex applications. 4. Electromagnetic-mechanic modeling. 5. Trajectory generation (pathfinding).

This chapter explains the first three topics of this dissertation. It starts by defining what is an actuator from an energy point of view, which needs the general definition of an energy transformer device (transducer). This is important because this dissertation's work is applied to an actuator system. Then, the notion of stroke is defined, which will divide the actuators in analog and digital actuators. This actuator division by its stroke states is then studied. This division presents the concept of digital actuation and its advantages/drawbacks over traditional analog actuators (topic 1). Afterwards, two applications of actuators to planar motion are described and differentiated: positioning and conveyance systems (topic 2). This is followed by a section presenting the concept of actuator arrays. These arrays perform complex tasks by combining and coordinating multiple actions of individual actuators (topic 3). Finally, the context of this dissertation is treated with the introduction of the microfactory environment, the current need and challenges of such a system and the scope of this dissertation's work.

1.1 Transducer

A transducer is a device which transforms energy from one type to another, even if both energy types are in the same energy domain [Pon05] [1]. For example, a device

[1] This dissertation uses the "alphabetic-numeric" reference style, see [Gar07; Leh+19]

transforming thermal energy (from the thermal domain) into mechanical energy (to mechanical domain) and another transforming translational energy (a type of mechanical energy domain) to rotational energy (another type of mechanical energy domain) are both transducers. A transducer can be used to monitor a state of a system, which corresponds to the concept of sensor. A sensor is thus a transducer able to monitor the status of a system (ideally) without influencing it [Pon05]. Normally the definition of sensor is refined to a transducer that transforms energy from any domain or type into electrical energy, so it can be implemented in a wider system with compatibility ease. A transducer can also be used to change a state of a system, which corresponds to the concept of actuator.

1.1.1 Actuator

In this dissertation two definitions are combined to form the concept of actuator. In one hand, the energy based and state control definition. On the other hand, the controllable work definition. An actuator can be defined as a transducer able to impose a system state (ideally) without being influenced by the load imposed on it [Pon05]. This definition is normally refined to a transducer that transforms electrical energy to mechanical energy. Another complementary definition of actuator can be added: an actuator is a controllable work-producing machine [HFA97]. Normally, the work produced by the actuator is injected into the studied system as mechanical work. So, an actuator is a controllable energy transformer device whose output is used in the form of work to change, in a desired way, a state of a system (Figure 1.1).

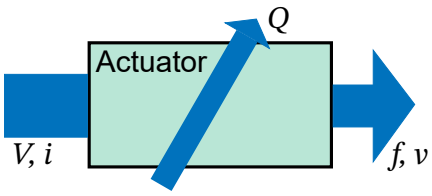

Figure 1.1: Actuator concept. Electric energy input (V, i) gets transformed to useful mechanical energy (f, v) as output. Some energy is lost in the transformation (Q) (adapted from [Pon05]).

1.2 Actuation division by stroke states : Analog & Digital actuation

To compare the wide variety of actuators, some evaluating criteria (metrics) are necessary. The mechanical requirements of an actuator application can be

expressed in terms of force, stroke, stiffness, volume, mass, response time (or operating frequency), power, efficiency and resolution [HFA97]. The performance metrics used in this dissertation are classified, defined and explained in Appendix A. Among them, the stroke characteristic is crucial for this dissertation as it will define the digital/analog actuation principle.

1.2.1 Stroke

The distance range in which an actuator can operate is called stroke. It is the maximum available displacement that the actuator can deliver [Pon05]. When the actuator is based in shape-changing phenomena such as piezoelectrics, or shape memory alloys, the stroke is also called maximum strain [HFA97].

Actuators can be classified based on the attainable states inside their stroke. The number and nature of the attainable states inside the stroke defines the analog (or continuous) actuation principle and the digital (or discrete) actuation principle. Let us first treat the nature of the states in terms of their mechanical equilibrium stability.

1.2.2 Equilibrium points and their stability

An object is said to be in mechanical equilibrium if the net forces acting on that object is zero ($\sum \vec{F} = 0$), i.e., the object has no change in momentum. The points in space where such a condition is valid are called equilibrium points. These equilibrium points are the candidates to be stable points of the system.

1.2.2.1 Potential energy-based stability

If the object is exclusively under conservative forces, such as under the gravitational field of the earth (Figure 1.2), then the equilibrium can be expressed in terms of its potential energy, U, as $\vec{F} = -\nabla U$ [Tay05]. This yields the expression of the equilibrium points $\nabla U = 0$. To evaluate the stability, the Laplacian of the potential energy is evaluated on the equilibrium points, i.e., $\nabla^2 U\big|_{(\nabla U=0)}$:

- When $\nabla^2 U\big|_{(\nabla U=0)} > 0$: the potential energy is at a local minimum. This is a stable equilibrium point. The response to a small perturbation is a force directed towards the equilibrium point, thus trying to conserve this state (Stable in Figure 1.2).
- When $\nabla^2 U\big|_{(\nabla U=0)} < 0$: the potential energy is at a local maximum. This is an unstable equilibrium point. The response to the slightest perturbation is

a force directed away from the equilibrium point, thus changing the system state (Unstable in Figure 1.2).

- When $\nabla^2 U\big|_{(\nabla U=0)} = 0$ or if When $\nabla^2 U\big|_{(\nabla U=0)}$ is undefined and higher order derivatives are also undefined: the equilibrium point is neutral stable and a small perturbation or displacement will not change the system's potential energy, thus remaining in the same neutral stable state (Neutral stable in Figure 1.2).

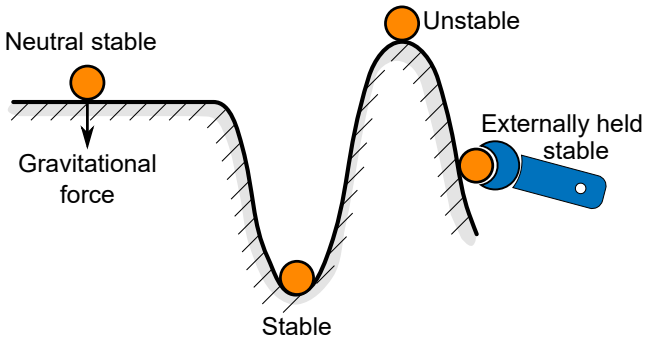

Figure 1.2: Equilibrium stability by potential energy (adapted from [Hus15]).

The externally held position in Figure 1.2 is a stable state, as the external force, called "holding force", will compensate the diverging force of the system to keep the object in place ($\sum \vec{F} = 0$). The holding force will support a certain degree of perturbation to the maintained state, thus acting as a local potential energy minimum (stable state).

1.2.2.2 Lyapunov based stability

A more general definition of a stable state is the Lyapunov definition, which is not restricted to conservative forces:

A state x^e is a Lyapunov stable equilibrium if: for every neighborhood of states of x^e there is another neighborhood of x^e such that every temporal evolution of the state, starting in the second neighborhood, remains in the first neighborhood at every given time. This can be expressed mathematically as: A state x^e is a stable equilibrium if for every neighborhood of states of x^e (a set of states denoted as U with $x^e \in U$) there is another neighborhood V of x^e (thus $x^e \in V$) which is contained in U ($V \subseteq U$) such that every solution $x(t)$ starting in V, this is $x(0) \in V$, remains in U for $t \geq 0$ [HS06]. Notice that $x(t)$ does not need to approach or be equal to x^e. If x^e is not stable, then it is unstable.

An equilibrium state x^e is asymptotically stable if, under the same mentioned conditions, x^e is Lyapunov stable and $x(t)$ tends to x^e when t tends to ∞ [HS06].

An equilibrium that is Lyapunov stable but not asymptotically stable is neutral stable. Both stabilities are represented in Figure 1.3.

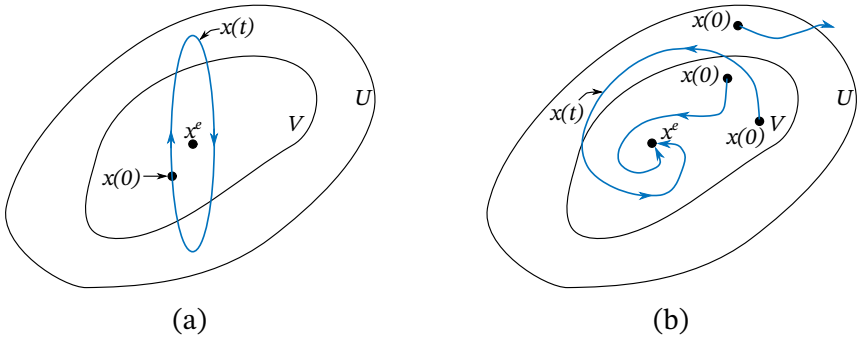

(a) (b)

Figure 1.3: Equilibrium stability by Lyapunov definition. (a) Lyapunov stable. (b) Lyapunov asymptotically stable (adapted from [HS06]).

1.2.3 Analog or continuous actuators

Multiple definitions of analog (or continuous) actuation principle can be found in the literature, e.g.:

- If an actuator is continuously position-controllable and accepts a continuous range of input command values, it is denoted as a "Continuous-Range-of-Motion Actuator", or "Continuous Actuator" [MC06].
- If the actuator's mobile part can attain, theoretically, all positions between the two limits defining the actuator's stroke, the actuator is analog [Pet09].

In this dissertation, the analog (or continuous) actuation principle is defined as follows. If every possible position inside the actuator stroke is an attainable neutral stable state of the mobile part of the actuator, then this actuator is an analog (or continuous actuator). The actuator presented in Figure 1.4a shows an analog actuator. Inside the actuator stroke there are an infinity of neutral stable positions, all of them attainable by the continuous motion of the lead screw. Figure 1.4b represents the analog actuator with the circular part as its mobile part and the dotted positions as some of the infinite neutral stable positions attainable in the stroke. Normally, the output of the actuator is wished to be stable (not neutral stable as in this case), thus, analog actuators need a constant input of energy to transform the attained neutral stable positions into maintained stable positions (in the example, a blocking force to the lead screw). For high precision, the analog actuator needs a sensing system to measure the attained position and evaluate the error compared to the wished position. This must be coupled with a closed loop control system that ensures the correct positioning of the actuator. Then, an analog actuator for high precision needs two supplementary systems

(sensing and control) and these added components can create further restrictions and requirements to the system's operation environment. Because of this, integrating an analog actuator to a system could be complex. Given this closed loop control operation, analog actuators can compensate manufacturing errors in their structure to a certain degree, easing the exigence in their manufacturing process and lowering their costs.

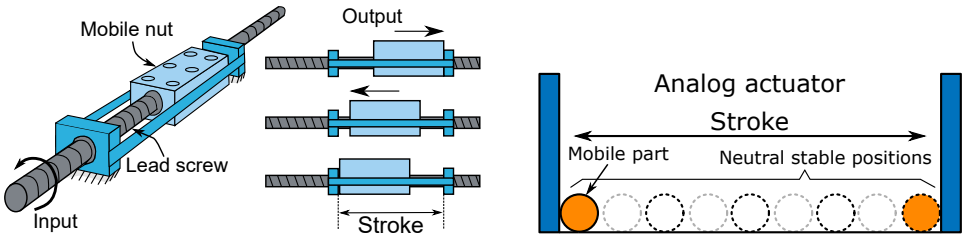

(a) (b)

Figure 1.4: Analog actuator example. (a) lead screw and nut linear actuator. (b) some of the infinite actuator's states inside its stroke.

1.2.3.1 Functions in an analog actuator

Analog actuator requires just one function to operate: a function to actuate, displace, or switch the mobile part of the actuator inside its stroke, called "driving function". The driving function of any actuator is a force that displaces its mobile part. This force can be achieved with a plethora of physical phenomena such as electromagnetic, electrostatic, electrothermal, ion-based, optic, piezoelectric, pneumatic or hydraulic. As the driving function is needed in both analog and digital actuators, it will be covered in Chapter 2, Section 2.1, for both digital and analog actuators.

1.2.4 Digital or discrete actuators

Multiple definitions of digital (or discrete) actuation principle can be found in the literature, e.g.:

- The digital actuator's mobile part can only reach several well-known and repeatable positions defined in the actuator's fabrication. When the mobile part is switched between these positions, it passes through different transient intermediate positions and are not reached permanently in a normal operation of the digital actuator [Pet09].
- If an actuator is able to exert only a null force or its maximum exertable force and/or if it is able to generate only a null motion or the total stroke motion, then the resulting actuator is a digitalized force or a digitalized stroke actuator [Bor08].

- Discrete actuation is a design paradigm that exploits the advantage of changing the system state in discrete steps. Each state of the system is designed to be stable and does not require power to be maintained [PDD07].
- If an actuator has only a finite number of discrete stable positions, and its input command range is discrete, as well, we denote this type of actuator as a "Discrete-Range-of-Motion Actuator", or "Discrete Actuator" [MC06].

From these definitions, it is noticeable that they are not completely equivalent, but they use common concepts: the division of the stroke in a finite number of states (positions); the nature of these states (stable, neutral stable or unstable) and the input/output shape (digital or stepped shape). [Pet09] gives the most general definition without treating the stability of the reachable positions. [Bor08] gives a very narrow definition by only considering on-off or null-full actuators as digital actuators. [PDD07] gives the notion of discrete variation of states in the actuator but considers only stable states as valid. [MC06] is similar to [PDD07] but links also the input command of the actuator.

In this dissertation, the digital (or discrete) actuation principle is defined as follows: if there are a finite and precise number of attainable states of the mobile part of the actuator inside its stroke, and only those states are considered as valid states for its working operation, then the actuator is said to be digital. These states of interest are called discrete states and can be stable, neutral stable or unstable states. The use of only certain states of the stroke causes the output of these actuators to show a "step" or "digital" shape (Figure 1.5a). The input of these actuators could be any kind of signal, although, normally, pulsed signals are used as input commands. Figure 1.5 illustrates the difference between analog and digital actuators (the number of states exploited) and the difference it makes to their outputs.

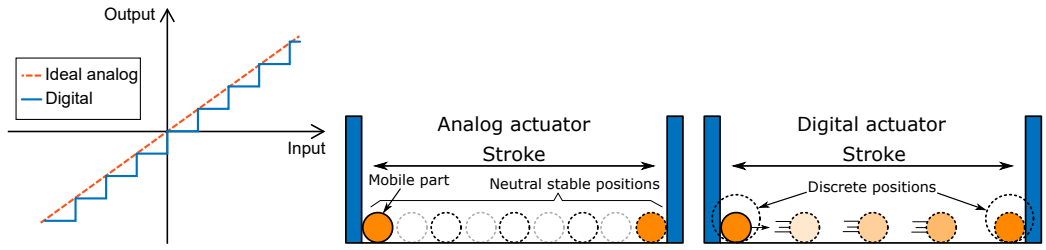

Figure 1.5: Analog and digital actuator difference. (a) output difference. (b) some of the infinite analog actuator's neutral stable states inside its stroke. (c) only two discrete neutral stable states allowed for the digital actuator.

Lets define the functions that a digital actuator needs to operate, the way to generate these functions and, finally, present a classification of digital actuators.

1.2.4.1 Functions in a digital actuator

A digital actuator requires two functions to operate: a function to actuate, displace, or switch the mobile part of the actuator between its discrete positions, called "driving function" (as with analog actuators) and a function to differentiate the neutral stable states from the discrete states to be exploited by the digital actuator, a "discretization function".

1.2.4.1.1 Driving function As already stated, the driving function of any actuator is a force that displaces its mobile part. This force can be achieved with a plethora of physical phenomena such as electromagnetic, electrostatic, electrothermal, ion-based, optic, piezoelectric, pneumatic or hydraulic. As the driving function is needed in both analog and digital actuators, it will be covered in Chapter 2, Section 2.1, for both digital and analog actuators.

1.2.4.1.2 Discretization function The discretization function can be accomplished by the same driving force with a proper control, or by an additional system. The use of the driving force as discretization function is exemplified in Figure 1.6. The mobile part is switched only between the ends of the analog actuator stroke with the driving force (discrete digital). An optional blocking force at each end can be added to make the discrete positions stable (stable digital). Normally, this solution is referred as an analog actuator driven in a digital way (or on-off), because the discretization function is a product of the same actuation principle than the driving force and it consumes energy to work.

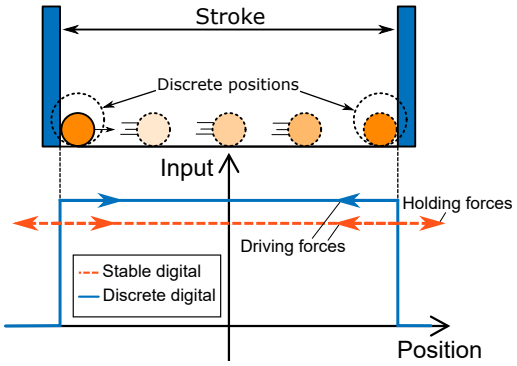

Figure 1.6: Use of the driving force as discretization function.

When the discretization function is accomplished by an additional system, the additional system is called the "holding function".

1.2.4.1.3 Holding function When the discretization function is achieved by an additional system that creates stable positions for the mobile part and keep

these states under external disturbances, the additional system is called “holding function”. The holding function acts as a force to the actuator’s mobile part, thus called “holding force”. The holding force modifies the potential energy (U) topography of the actuator to create the stable positions (Figure 1.7). The driving and holding functions are represented in Figure 1.7b: the driving force opposes the potential energy, thus it requires energy to displace the mobile part of the actuator. The holding force is designed to consume zero energy when attracting the system to the stable states by using passive forces. Different ways to generate the holding function in an actuator are discussed in the next section.

The simplest digital actuator example is a bistable or switch actuator, as illustrated in Figure 1.7a (other type of digital actuators will be discussed later). Inside the actuator stroke there are only two discrete and stable positions that are considered valid to the actuator’s operation, typically at both ends of the stroke. Any other position of the actuator will be directed towards one of the two stable states. There is an unstable state at the center of the actuator, which is not valid to its operation and, in practice, it is never attained.

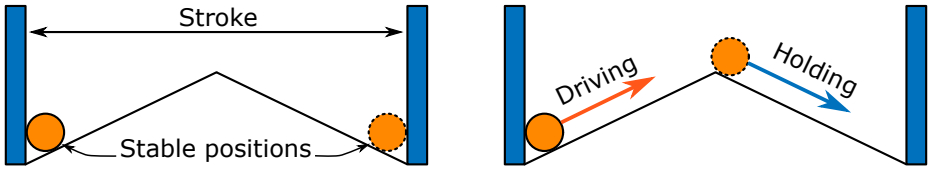

(a) (b)

Figure 1.7: Digital actuator example. (a) bistable actuator stable positions. (b) driving and holding functions in a bistable actuator.

1.2.4.2 Holding function generation

Different ways to achieve the holding function in an actuator are presented and discussed in the following sections.

1.2.4.2.1 Material elastic restitution forces The most common solution to generate the holding force is the elastic restitution forces of elastic materials such as springs, buckled beams or membranes. This is because they do not require external energy supply, they are well modeled by analytical mechanical models [MGK18] or finite element models and they can be fabricated with microfabrication techniques. The downsides are their fatigue limit, some observed nonlinear mechanics [RSM06] and the importance of the frequency analysis of the structure to their behavior.

Figure 1.8 presents some examples of digital actuators using this solution. [Suz+16] (Figure 1.8a) used the electrostatic force as driving force for their

actuator and a double buckled beam as holding force function. The buckled beam was stable when buckled in one direction (left or right). When the driving force pressed the buckled beam towards the other side, the buckled beam resisted this force by deformation and, after a critical deformation value, it “snapped through” to the other stable position. The same principle, but in a membrane shape, was used by [MGK18] (Figure 1.8b). [CP12] generated the holding force function using leaf springs to define two stable positions (Figure 1.8c), and also developed the concept with linear springs (Figure 1.8d). Finally, [MKD17] presented a linear spring to ensure one stable position of a valve for hydraulic control, coupled with an active locking system to create a second stable position (Figure 1.8e). This system would be a hybrid holding force system.

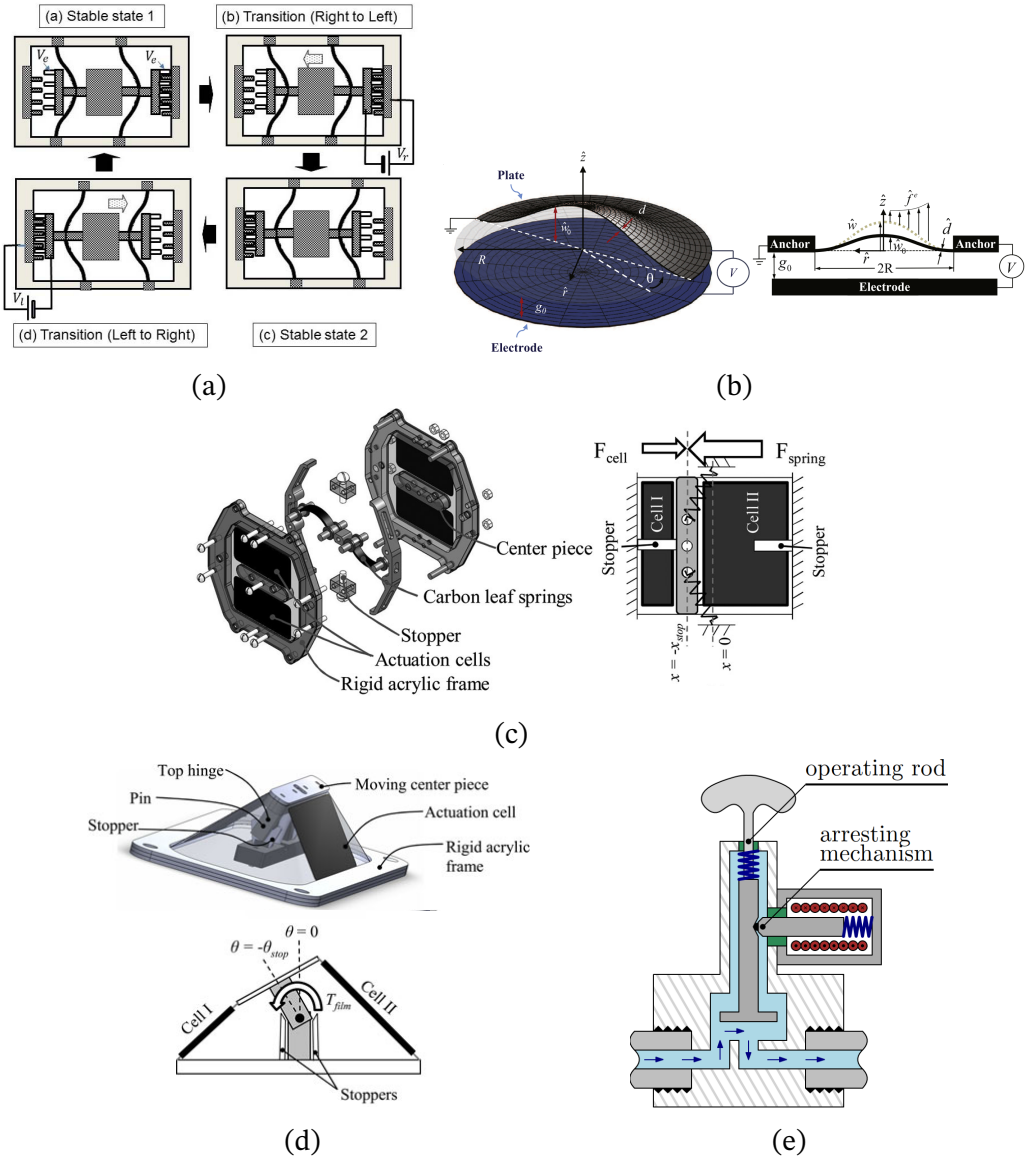

Figure 1.8: Elastic restitution holding forces. (a) Buckled beam [Suz+16]. (b) Buckled plate or membrane [MGK18]. (c) Leaf springs [CP12]. (d) Linear springs [CP12]. (e) Linear spring and active lock (hybrid holding function) [MKD17].

1.2.4.2.2 Electromagnetic forces The attraction or repulsion force between two permanent magnets can be exploited to create stable positions for the digital actuator. Their magnetization, distance and size will determine the intensity of the magnetic force. This principle is exploited in this dissertation and will be studied in more detail in Chapter 3. The advantages are:

- Zero energy consumption.
- Non-contact nature, avoiding friction forces, fatigue and other mechanical problems.
- The scalability of the permanent magnet on permanent magnet forces.
- The known analytical magnetic force models for basic geometries.

Their disadvantages are:

- Their fabrication process is not completely adapted to the microfabrication methods (but there is progress in this area [AW09]).
- Thermal sensibility and loss of magnetization with temperature.
- The undesirable attraction to other ferromagnetic elements out of the actuation system.
- No analytical magnetic force models for complex shapes, but numerical approximations.

In the work of [MKD17], they proposed a digital valve using the permanent magnet force as holding function. The plunger allowed the flow to pass and was kept in that position by the right permanent magnet (Figure 1.9a). If the electromagnetic force was activated, the plunge moved to the left, closing the flow and the plunger arrived to the left permanent magnet influence. In [SS11] (Figure 1.9b), the authors used a permanent magnet and a magnetic circuit to generate the holding force of their digital relay. The electrothermal actuators moved the contact between both output ports and the steady magnetic field across the ports created an attracting force to the contact at each stable position.

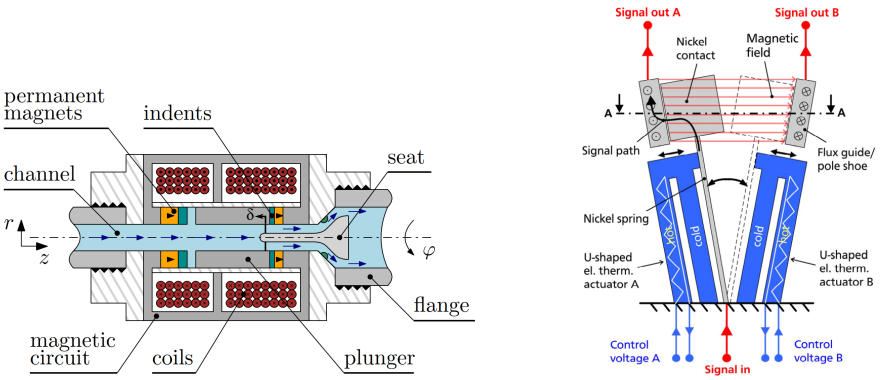

(a) (b)

Figure 1.9: Electromagnetic holding forces. (a) Permanent magnet holding the plunger [MKD17]. (b) Permanent magnet field holding the contact [SS11].

1.2.4.2.3 Locking systems A supplementary actuator that locks the mobile part in the stable positions is another alternative. Locking systems have the advantages of ensuring very precise stable position and minimizing the energy consumption of the main actuator's power source. Locking systems generate higher holding forces than the passive methods, but, they consume power to generate the holding force. More signals are needed to control the actuation system, producing a more complex solution. The hybrid solution presented in [MKD17] is a clear example of this category: once the valve was open by any pulling mean in the actuation rod of Figure 1.10a, the electromagnet solenoid was activated, blocking the valve in the open position. To switch to the closed position, the solenoid had to be switched off so that the spring could push the rod downwards and close the flow. [Cho+13] designed a passive-activated lock using a magnet (sub-magnet in Figure 1.10b). This magnet was repelled from the principal electromagnetic circuit if an unwanted return of the system occurs, deploying a lock and blocking the system in a safe stable state. [Gao+19] used a passive locking system, a latch-lock, which engaged to the mobile part, locking and stabilizing it. To disengage, the actuator used the same movement to reset the first state.

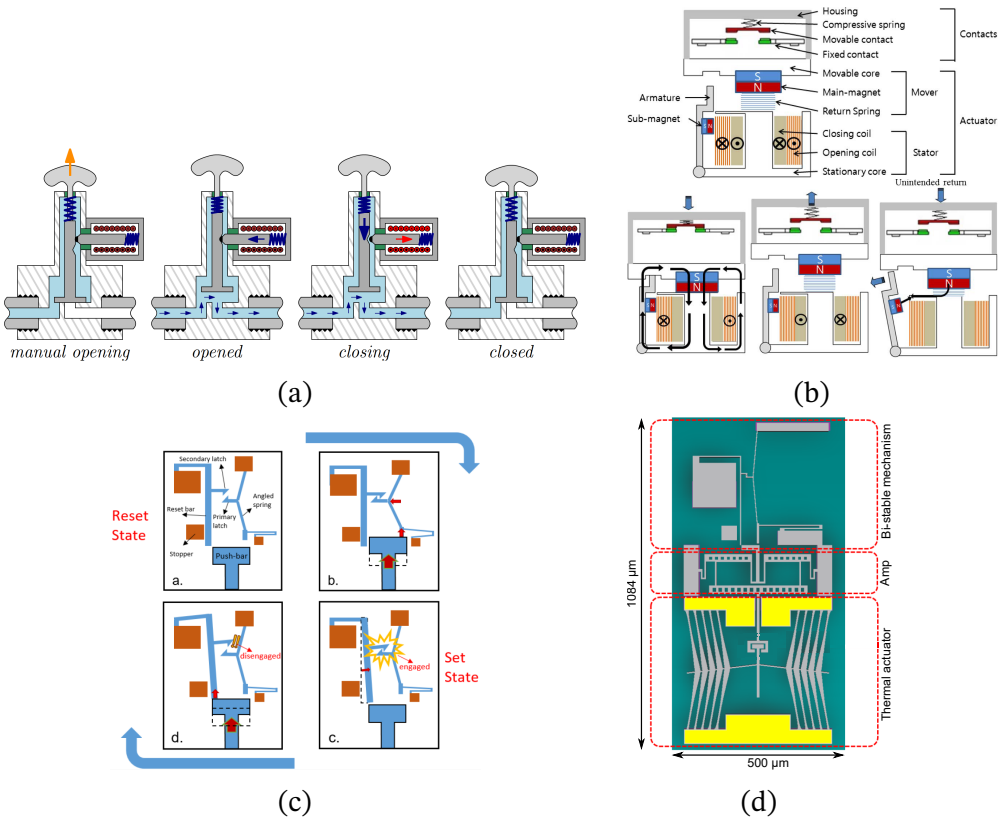

Figure 1.10: Locking holding function. (a) Electromagnetic solenoid lock [MKD17]. (b) Magnetic lock [Cho+13]. (c) Two state latch-lock stable mechanisms by [Gao+19]. (d) Experimental prototype of [Gao+19].

1.2.4.3 Digital actuators classification

In this section, a classification of the digital actuator systems is proposed. The classification is based on the stability nature and interaction of the discrete positions of the digital actuator [Pet18].

1.2.4.3.1 Type 1: Exclusively stable positions If all the discrete positions of the digital actuator are stable states, then this digital actuator is of type 1. They are often called by the number of stable positions: bistable (already explained in Figure 1.7a), tristable, quadristable, and so on. Other denomination is simply bistable for two stable states and "multistable" for more stable states. Multistable mechanisms are usually built by connecting multiple bistable mechanisms using the elastic restitution force of materials (Figure 1.11).

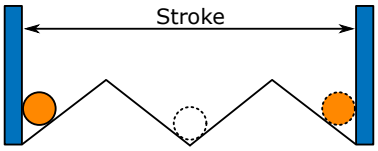

Figure 1.11: Type 1 exclusively stable discrete positions. A tristable (or multistable) digital actuator schema.

The already presented electrostatic digital actuator by [Suz+16] belongs to this type (Figure 1.8a). The double buckled allowed a stroke of 28 µm with a switch energy requirement of 4.14×10^{-10} J.

Figure 1.12 presents some examples of type 1 digital actuators. [WCP14] presented a tristable mechanism using two serially connected bistable buckling beams. The tristability of the mechanism originated from the different actuation loads of the two bistable mechanisms. The mechanism stable states and force diagram are presented in Figure 1.12a. The mechanism stroke was 260 µm with a maximum blocking force (F_{2max}) of 800 µN. The already presented work of [CP12] (Figure 1.8d) also belongs to this type of digital actuators. The linear springs in their actuator created two stable positions showed in the force diagram of Figure 1.12c.

1.2.4.3.2 Type 2: Stable and neutral stable positions If there are both stable and neutral stable positions inside the digital actuator stroke, then the actuator is of type 2. Generally, the discrete positions of the actuator are the stable positions, and the neutral stable positions are avoided, as illustrated in Figure 1.13. The control of such digital actuator needs to consider the neutral stable zone or dead zone (deadband). The presence of the neutral stable positions is due to stronger friction forces than the holding force. When the mobile part is

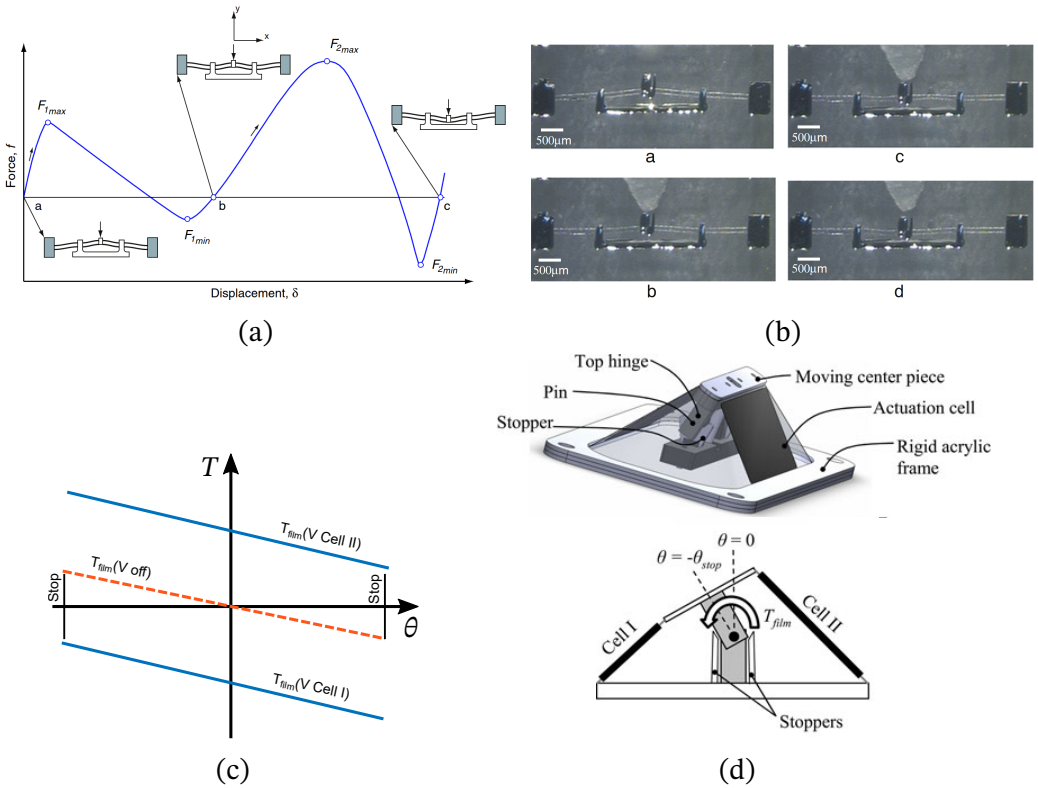

Figure 1.12: Type 1 examples. Tristable mechanisms by [WCP14]. (a) Force diagram. (b) Prototype. Bistable digital actuator by [CP12] (c) Force diagram. (d) Prototype.

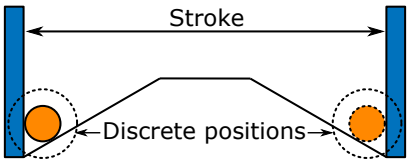

Figure 1.13: Type 2. Stable and neutral stable positions inside the digital actuator stroke and its discrete positions.

inside the dead zone, the holding force is unable to displace it to a stable position. Another reason for this type of actuators is the trade-off between the force needed to switch the mobile part and the passive holding force to maintain the stable positions. Given that the actuator needs to overcome the passive holding force each time it is going to be switched, then it could be beneficial to reduce the holding force in exchange for efficiency. Other possible trade-off is the length of the stroke: larger strokes need stronger holding forces to ensure the stability of the whole stroke. Sometimes, only a holding force system can be used for a given application (e.g. a magnetic holding force is to be used), but the stroke of the actuator is too large to make it a fully stable digital actuator. In this case, a compromise can be made and a dead zone is to be tolerated. Other times, physical limitations and geometric constrains do not allow the optimal design of the holding function, e.g., distance of the permanent magnets to the mobile part due to unwanted interaction of the magnets with other parts of the system (a hall effect sensor, for example).

The work of [MKD17] belongs to this type of digital actuator. Their plunge was switched between two stable discrete positions. The magnetic force to ensure the stability of those discrete positions was not enough to displace the plunge if its position was $\delta = 3.5$ m[2], as shown in Figure 1.14a.

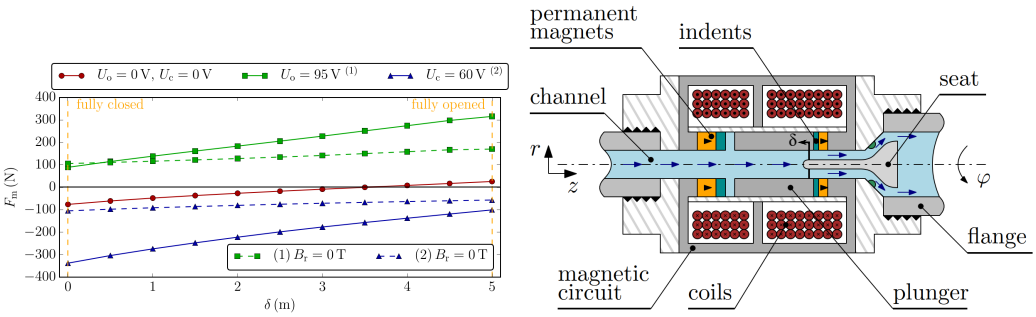

(a) (b)

Figure 1.14: Type 2 example, a stable and neutral stable discrete positions in a digital valve. (a) Force diagram defining two stable positions and a neutral unstable position. (b) Digital valve schema by [MKD17].

1.2.4.3.3 Type 3: Stable and unstable positions If there are stable and unstable discrete positions on the digital actuator stroke, the actuator is of type 3. Usually this type of digital actuators have one stable position (but could have more) and they are activated to accomplish a function for a short period of time in its unstable discrete position, to then return to their stable position. The

[2]This value seems large for the proposed valve, maybe there was an error with the figure units and it was intended as cm instead of m

use of springs attached to the mobile part to define the stable actuator, or the gravitational force, are the common methods for these actuators. A monostable digital actuator with one unstable position and a monostable actuator with two unstable positions are presented as examples in Figure 1.15.

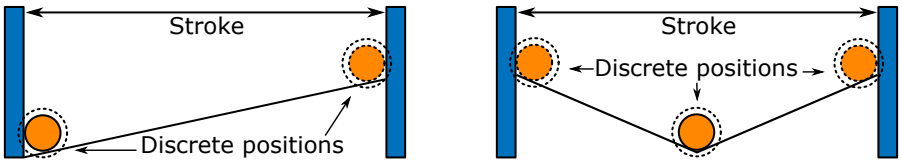

(a) (b)

Figure 1.15: Type 3. stable and unstable discrete positions. (a) A monostable with one unstable discrete position. (b) A monostable with two unstable discrete positions.

In the work of [MKD17], they presented a monostable actuator with one unstable discrete position (Figure 1.16a). The digital valve was in the open state by default thanks to a spring attached to the actuating rod. To close the valve, the electromagnetic force was used and kept active while the valve should remain close. Once the electromagnetic force turned off, the spring restored the open state. The work of [Li+17] presented an electrostatic force switch for RF applications. The switch was a monostable digital actuator that was in default in the transmission state. If a switching voltage of 18.3 V was applied to the attracting electrodes, the membrane of the switch was pulled down and the non-transmission state was engaged (as the membrane is electrically grounded). The displacement of the membrane was 3 µm. Once the voltage was switched off, the springs of the system returned the membrane to its transmission state.

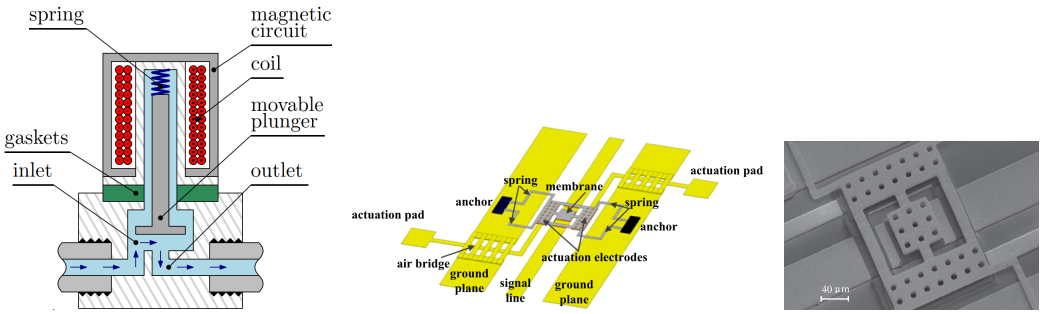

(a) (b) (c)

Figure 1.16: Type 3 examples. (a) A monostable with one unstable discrete position digital valve. Spring plus electromagnetic force for opening and closing respectively [MKD17]. (b) A monostable with two unstable discrete position digital switch. Spring plus electrostatic force with (c) prototype [Li+17].

1.2.4.3.4 Type 4: Discrete positions and stabilization with locking actuators If locking actuators are used to stabilize a discrete position of the mobile part of the main actuator, then it is of type 4. The locking systems discussed above are classified here, to recall, the advantages of these systems are a precise stable position against a large neutral stable stroke, minimizing the energy consumption of the main actuator's movement. Higher holding forces than the passive methods but, more power consumption, more control signals and a harder integration. The examples presented in Figure 1.10 and explained in the locking systems are valid in this category.

Discussion

The presented way to obtain a discrete actuator was to add a holding function to an analog actuator to create the stable positions of the mobile part. As seen in the holding function section, the most common solution are compliant structures (springs, buckled beams or membranes). The inverse process is also possible: if we add a digital actuator to an analog system, as a stepper motor to the lead screw nut actuator, the rotation of the lead screw becomes a step by step output, or a digital multistable actuator. Other way to obtain a digital actuator is by integration: some actuation technologies allow the assembly of multiple identical actuators to form an actuator system. Every actuator can exert a force and to generate a simple motion. If the actuators are integrated in a serial configuration, the stroke of the new actuator is the sum of the strokes of each single actuator. If each actuator is controlled in a digital way, then the resulting actuator system is a multi-discrete digital actuator.

For [Miy11], the concept of digital actuation has several advantages compared with the analog actuator as follows: stability at each state without the need for a feedback loop; high task repeatability; mechanism simplicity and minimal supporting devices. [PDD07] states that the actuator's reliability and efficiency are greatly improved and the resolution of discrete systems increases with the number of discrete states.

To summarize this section, the characteristics of digital actuators:

- Have a stroke divided in well-defined stable states that are repeatable, thanks to a holding force function.
- They use pulsed power to switch between their stable states, who are preserved mostly by passive holding forces.
- Can operate without a position sensor. As their stable states are repeatable and well-defined. If the initial state is known, the history of the command determines the mobile part position.

- They can, therefore, be controlled in open loop.
- Their integration into a system trades the sensor for the holding function of the actuator.
- Require high precision in their manufacturing process. The precision of their structure usually defines their stable states and the quality of the holding force function. Any error in the manufacture process will deteriorate the digital actuator performance. The errors can not be corrected with closed loop control techniques.

The differences between analog and digital actuators are summarized in Table 1.1:

Table 1.1: Comparison between analog and digital actuation

Properties	Analog actuators	Digital actuators
Stroke	Continuous	Discrete
Energy supply	Continuous	Pulsed
Manufacturing constraints	Low	High

1.3 Actuation application to planar motion

The application of the actuation systems covered in Chapter 2 are focused in the generation of motions in a plane or "planar motion". This is the motion needed mostly in conveyance systems and is the motion that this dissertation will exploit. A planar motion capability is defined as an actuation system that can translate an object in two dimensions and rotate it about an axis perpendicular to the translation plane [Pal10]. Among the planar motion actuating systems, there are two different systems used in the microfactory to accomplish different tasks: the positioning systems and the conveyance or transportation systems. The difference between them is the number objects in motion and their requirements in resolution, repeatability, speed and stroke requirements.

1.3.1 Positioning systems

Positioning systems (positioners) seek to place an object very precisely and accurately in space. This translates to a need of the smallest resolution possible. Positioners are required in precision engineering for machining, in measurement for scanning probe microscopes, in biology for cell manipulators or in optics for optic fiber alignment [MFM17; Wan+18a]. The size of the system

is not a determinant factor for this classification, i.e., a macro-system can be a micropositioning system. The resolution of the motion is the discriminator: if the system can achieve unit or sub-unit resolutions, then it is a unit positioning system, e.g., if a system can perform nanometer or sub-nanometer steps then it is a nanopositioner [MFM17]. Micro, nano and sub nanometer positioners usually have a compliant structure attached to the actuator system to exploit their well modeled behavior and good repeatability [Ken10]. These systems are usually called "flexure-based". The use of this structures carries some trade-offs in their design and a stroke limit not extendable by modular designs. The trade-offs to be done in these systems are between the stroke and bandwidth and between the stroke and resolution of the device [MFM17]. As the stroke becomes larger, the resolution and speed tend to degrade, linked to fact that larger structures are difficult to model, control and implement. Also, inchworm devices would need more steps to cover the larger stroke. The stroke and bandwidth of the positioner evolve in different directions. This relationship is presented in Figure 1.17 following the work of [Ken10]. The stroke (range in Figure 1.17) decreases as a function of the resonant frequency (directly linked with the bandwidth) for piezoelectric positioners with compliant structure outputs.

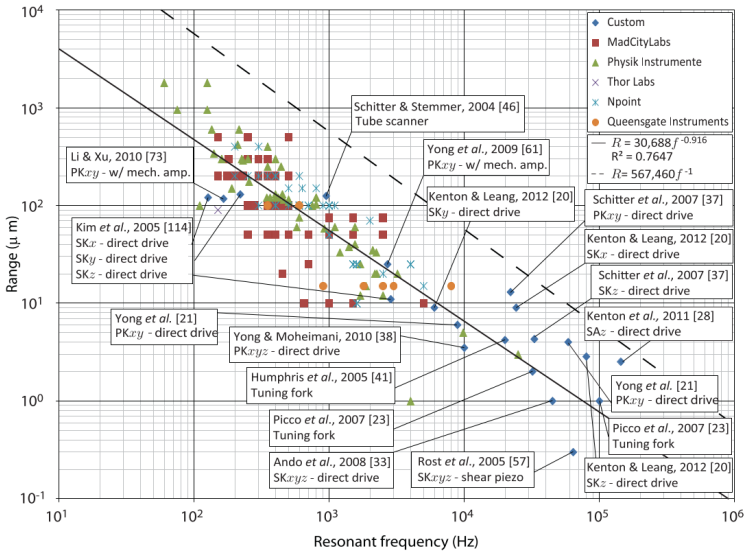

Figure 1.17: Trade-off between range and bandwidth (resonant frequency) for piezo positioners. Solid line is the fitted tendency and dashed line the theoretical maximum [Ken10; Yon+12].

The work of [Wan+18a] is a clear example of a piezo flexure-based positioning system (further explained in Section 2.1.4). It used one piezo stack actuator with a displacement amplifier for the x-axis displacement and an identical second one for the y-axis displacement (Figure 1.18). Both piezo actuators outputs were injected to a double parallelogram mechanism based in flexure elements that

displaced the moving stage of the positioning system (Figure 1.18a). The system generated a stroke of 55.4 µm × 53.2 µm with a resolution of 8 nm. The step response in closed loop (with a PID) is illustrated in Figure 1.18b. Figure 1.18c presents a common test for positioners: following a reference circle and multiple successive resolution steps to evaluate the trajectory and positioning error of the device.

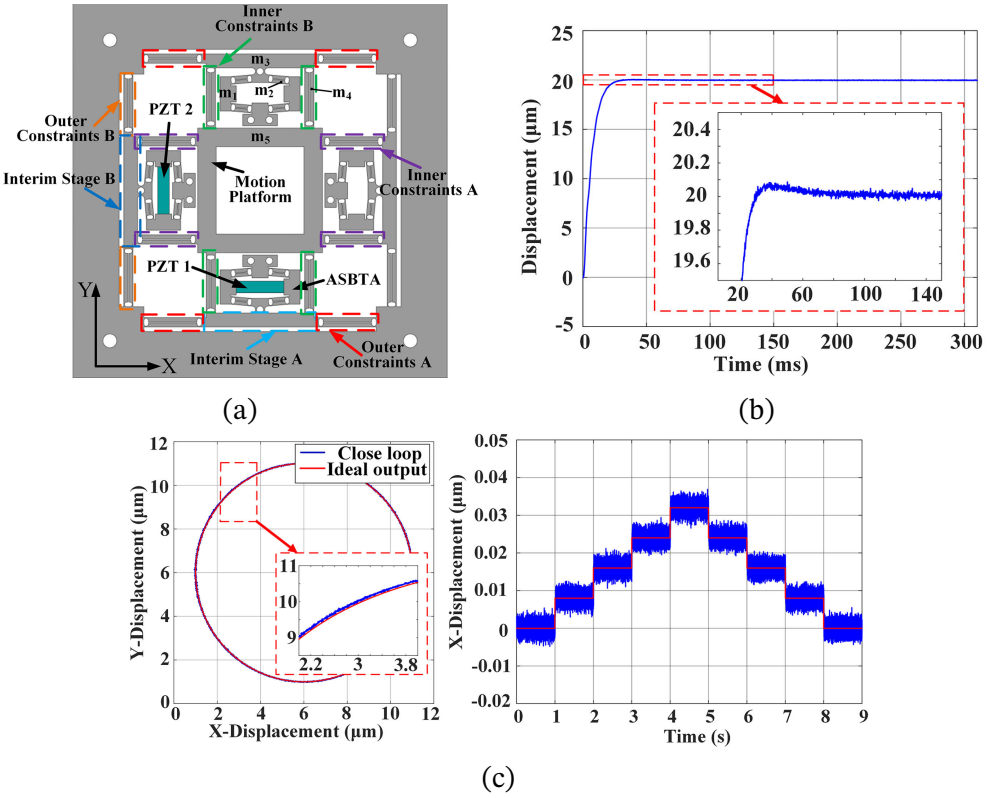

Figure 1.18: Piezo nanopositioner with compliant structure example [Wan+18a]. (a) System schema. (b) Closed loop output to a step and pulsed input. (c) Typical test for a positioner: a circular motion and consecutive step ladder, up and down.

The work of [CHL13] presented a microfabricated digital positioning system based in 4 bistable electrothermal actuators controlled in open loop with flexure elements (Figure 1.19a). The system generated a 12 µm × 12 µm stroke with a theoretical resolution of 1.5 µm (Figure 1.19b). The resolution could be increased by the use of more bistable modules in the system (two additional actuators would yield a 750 nm resolution). The experimental resolution was 3.8 µm with repeatability of 100 nm.

The work of [NK13] is an example of a 3 DoF Lorentz force electromagnetic micropositioner without a flex-based structure. The stroke in x, y, and the rotation about the vertical axis were 15.24 cm, 20.32 cm and 12°, respectively. The resolution in the plane was 8 µm with repeatability of 6 µm. The resolution in rotations around the vertical axis was 100 µrad. This work could have a larger

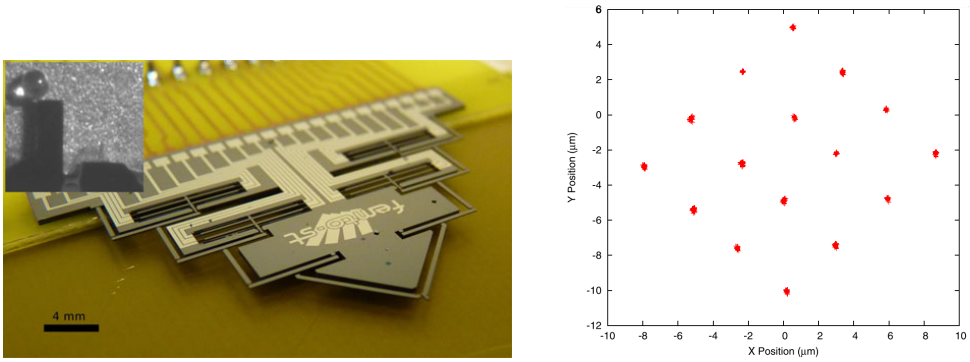

(a) (b)

Figure 1.19: Digital electrothermal positioner with compliant structure example [CHL13]. (a) System picture. (b) Attainable positions and repeatability.

stroke, as it only needs the permanent magnet stator to expand and the cables of the control system linked to the mover to follow it. This different architecture for a positioner trades precision and resolution for more DoF and larger strokes.

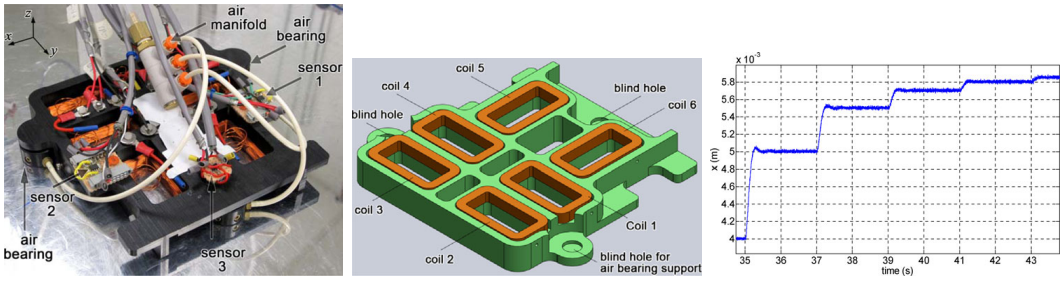

(a) (b) (c)

Figure 1.20: 3 DoF electromagnetic micropositioner [NK13]. (a) System schema. (b) Mover coils (c) Consecutive decreasing value of steps response in closed loop.

1.3.2 Conveyance systems

Conveyors are motion systems of a broader manufacturing system that bring the raw material to the workspace, move the in-process pieces between machining and sensing stations and, finally, dispatch the manufactured good to the shipping area. Their main requirements are:

- Maximize the conveyed load.
- An adaptive maximal speed in function of the carried object fragility.
- To be as energy efficient as possible.
- To be flexible, i.e., being able to change of configuration easily to adapt to the manufacturing process changes.
- Being modulable to cover the workspace efficiently, and adapt to the path of the conveyed objects.

- Have a minimal trajectory error.
- Reduce the final position error of the carried object within a tolerance imposed by the different machining/sensing stations.
- Being able to avoid obstacles and collision.
- Being easily maintained or replaced without the associated cost of down-time work.

The classical conveyor solutions based in a centralized control and linear translation lines (as belt conveyors) causes a reprogramming of the entire system during any layout reconfiguration, as well as mechanical rearrangement and purchase of additional components [Fir+18]. They also perform simple linear translation and need extra systems to rotate or classify items [Uri+19]. In contrast, decentralized control and actuation structures (as modular arrays) divide the labor homogeneously. A breakdown of a control unit does not imply the breakdown of the system, thereby increasing robustness, scalability, reconfigurability and maintenance [Fir+18]. Modular conveyors in which each module can perform planar motion are called “smart conveyors”.

A good macro-size example of a smart conveyor is “celluveyor”, from Cellumation ([Uri+16; Uri+19], Figure 1.21). The celluveyor is made of hexagonal modules with dimensions 150 mm × 200 mm × 300 mm, each module has three wheels independently driven by electric motors achieving planar motion. Each wheel can carry up to 15 kg. Several objects can be moved by friction simultaneously and independently of each other as long as they are flat-bottomed. A commercial macro-size solution by Swisslog is the AutoStore modular smart conveyor system with multiple mobile robots in a grid to pick up items in a warehouse (Figure 1.22). The robots use electric motors to move in a 2D grid and pick up object in a third dimension, they can not rotate objects but carry up to 30 kg with outputs of 350-650 orders per hour in a 5000-300 000 object warehouse [Swi20].

(a) (b)

Figure 1.21: Small scale modular conveyor system based in three DC motor powered wheels [Uri+16; Uri+19]. (a) Hexagonal cell. (b) Conveyor array.

Modular smart conveyors able to operate in the micrometer range are the fo-

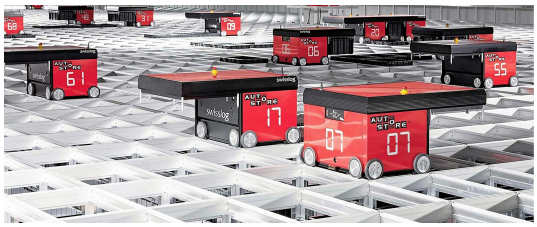

Figure 1.22: Swisslog AutoStore smart conveyor for warehouses [Swi20].

cus of the state of the art, presented in Chapter 2. There, the solutions comparable with the studied system of this dissertation will be analyzed.

Discussion

To summarize this section. The positioner systems usually have a shorter stroke, a slower speed and fewer degrees of freedom than the conveyance systems. On the other hand, their focus is in precision, accuracy, resolution of their output and minimal cross-coupling or straightness error. Conveyance systems are focused in covered active area, maximal carried load, maximum speed, energy efficiency, modularity, flexibility, ease of integration and autonomous operation to serve the surrounding systems. Conveyors normally have more degrees of freedom with larger strokes, higher speeds, bandwidths and forces than positioning systems. The use of closed loop control for both type of systems depends on their open loop performance. In the high precision exigence domain of positioners, the use of closed loops are common, as they increase precision and accuracy as a function of the sensing system. On the other hand, sensing errors and bias will feedback into the control system and could generate position errors in closed loop. Closed loops are also applicable to conveyors, enhancing precision and performance, but, in the densely packed world of conveyors, sensors for the closed loop could be too expensive to install (specially for large conveyance areas) or could complicate the integration of the conveyor into the already complex manufacturing system. An open loop/closed loop performance comparison should be done before deciding the control strategy for positioners and conveyors.

Positioners and conveyors could coexist in a manufacturing system. Positioners would place the pieces in the exact locations for the machining/sensing stations actions and conveyors would transport the worked pieces between the stations with a tolerated accuracy. The number of parts to transport and the motion requirements, as explained in this section, indicate which system is needed in which situation.

This dissertation's state of the art (Chapter 2) presents planar motion systems (including positioners) with special focus in conveyance system devices with

micrometer resolution, i.e., microconveyance systems.

1.4 Actuator arrays for complex applications

An array is an ordered series or arrangement of elements in a particular way. An array system performs complex tasks by combining and coordinating multiple actions of individual elements. These simple elements are easier to build, control, integrate and maintain than an equivalent monolithic complex system. [CHL13] is a good example of an array of digital electrothermal actuators that form a positioner system (Figure 1.19). The array idea could be extended to other applications. [Wan+07] designed an array of digital electrostatic actuators as an optical display (Figure 1.23). The actuators were stable-unstable actuators that blocked the light from an incident beam in the default state and open completely with 38 V, allowing the light to pass. The beam is directed towards the actuator array with a lens array. The optical display is designed to achieve high definition quality images in open loop with a pixel size of 125 µm and working frequency of at least 15.36 kHz. This yielded rise times of 10 and 20 µs (opening/closing) and settling times of 2 ms. They also measured some lifetime estimators, actuating the system more than 7.6×10^9 times at resonant frequency without a drop in performance.

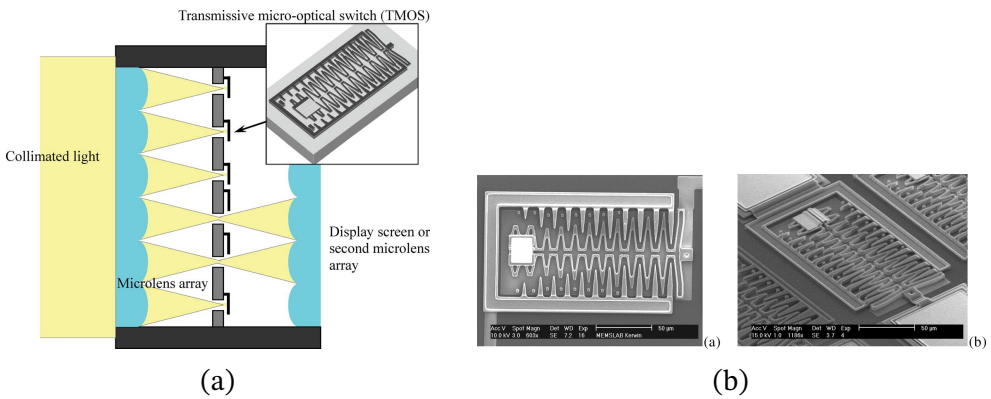

Figure 1.23: Digital electrostatic optical switch for MEMS display [Wan+07]. (a) System schema. (b) Microfabricated prototype.

[Fan+15] developed a digital loudspeaker array with 256 membrane piezoelectric actuators (Figure 1.24). The digital output of the actuators are superposed to construct an analog sound. The resonant frequency of each actuator was numerically designed at 25 kHz with a stroke of 4 µm. The system size was 6 cm × 6 cm and it correctly reproduced static and dynamic waves.

Adaptive optics is a method for real-time compensation of dynamic aberrations in imaging systems using deformable mirrors and used in life science

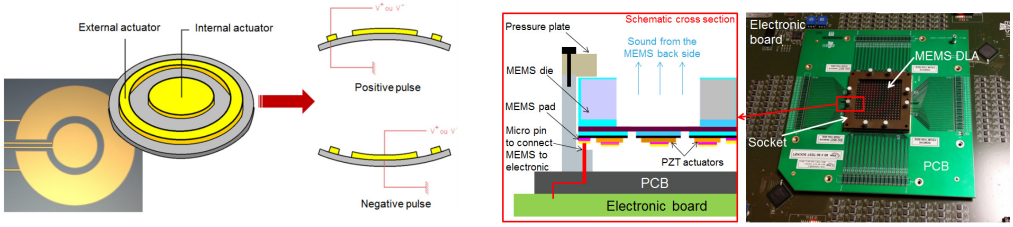

(a) (b)

Figure 1.24: Digital piezoelectric loudspeaker array [Fan+15]. (a) digital piezoelectric actuator. (b) Microfabricated prototype.

microscopy and laser shaping optics. The high cost of the available deformable mirrors creates a need for low-cost yet high-performance and easy to integrate alternatives [Boo07]. The work of [Ban+19] presented an array of 37 analog electrostatic actuators in a deformable mirror developed for applications in adaptive optics microscopy that tries to meet this need (Figure 1.25). The stroke of the actuator was 15 µm using a high voltage of 375 V. The array achieved a maximum root-mean-square error of 0.21 µm for all their tests.

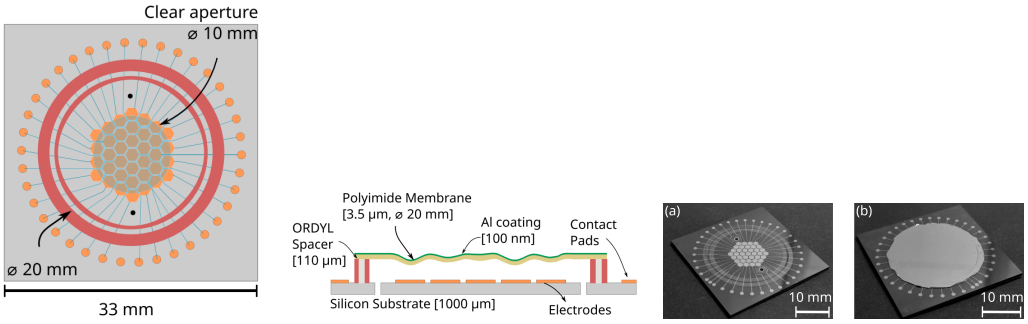

(a) (b) (c)

Figure 1.25: Electrostatic actuator array for a deformable mirror [Ban+19]. (a) Array schema. (b) Microfabricated prototype.

In the area of tactile displays, [Xu+20] presented a digital 5×5 array of Shape Memory Alloy (SMA) actuators with springs to stimulate the human skin at 15 Hz (Figure 1.26). Each actuator moved a pin upwards to give a stimulus to the human skin. The array could then transfer multiple letters, or messages if actuated constantly, at a sensible frequency. The spring returned the pin to the down position when the actuator was switched off. Each SMA actuator generated a force of 100 mN with a maximum stroke of 320 µm. Once the spring was added, it generated 32 mN and 23 µm at 1 Hz but reduced to 7 mN and 13 µm at 15 Hz due to cooling problems. This performance was still above the sensibility of human skin, so still applicable.

Multiple solutions presented in the state of the art, in Chapter 2, profit from the idea of arrays to extend its active area in a modular way. Hence, the arrays

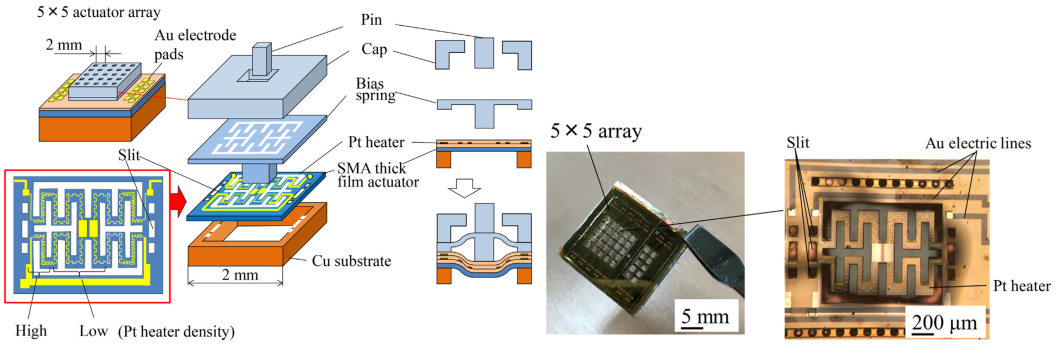

(a) (b)

Figure 1.26: SMA film actuator array with bias spring for tactile display [Xu+20]. (a) Array schema. (b) Microfabricated prototype.

fulfill the requirement of the microfactory of modularity and flexibility. This dissertation uses an actuator array to increase the DoF of the system and thus perform planar motion with a simpler elementary actuator design. The way in which this work exploits this idea is presented with the principles of the studied system, in Chapter 3.

1.5 Context: the microfactory environment

This dissertation is a contribution to the miniaturization of manufacturing systems, more precisely, the control of a conveyor system directed towards a microfactory. The microfactory is a proposed solution to the need of miniaturization of manufacturing systems. The questions of why to miniaturize the manufacturing systems is addressed in this section.

1.5.1 The need of miniaturize the manufacturing systems

The increased demand by consumers for compact, intelligent and multi-functional products like smartphones, smartwatches, personal computers, wearable technology, headphones, cameras, remote access keys, and energy harvesters can only be met by packaging more and more sensors, actuators and processors into the products. Miniaturization has been the industries' answer to this new paradigm of market demand [Hsu02]. Miniaturization is the idea to downscale a system or component in size to satisfy, principally, space and functionally requirements. A larger number of functional components such as sensors, actuators and processors can be integrated after being miniaturized. The execution of miniaturization produced an unexpected range of applications and performance improvements to numerous industries.

The miniaturization concept initiated with the transistor, in 1947. That crucial breakthrough lead to the integrated circuit concept that allowed computer to perform more operations more efficiently. The computing power saw then an exponential leap in performance that, in junction with the computing application to many research and industrial fields, created an enormous and increasing demand for computing power. This demand has been covered by miniaturization of the transistor. This leads to a larger number of them integrated in less space, increasing the operative capabilities of the computer.

In the transportation industry (automobile, train, aeronautical and spatial industries), the idea of miniaturization has given smaller and smarter sensors and actuators, such as gyroscopes and very precise fuel injectors, These sensors and actuators control more processes more precisely inside the system, making the transportation systems more efficient.

In the biological and biomedical industry, miniaturization has produced a paradigm shift where medicines can be delivered to precise parts of the body, and precise operations in a distance-controlled way.

The main interest and advantages of miniaturization ([Hsu02; Tri97]) are:

- Faster dynamics due to low mechanical inertia. An advantage for precision movements and for rapid actuation.
- Small size and low mass, leading to new implementation environments (such as medical and aerospace) and more functional components in a single device.
- Higher dimensional stability at high temperatures because of low thermal expansion.

To produce miniature components for small scale and compact products, the miniaturization of the manufacturing systems (the microfactory) is proposed as a solution [Mis+02; OMA04; Jär+15; Zha+17]. The idea of implementing manufacturing machines proportional to the size of the goods produced was born in Japan in 1991 and was called “microfactory” in 1999 [Mis+02; OMA04]. Thus, the microfactory is defined as “a small-size production system suitable for the manufacture of small products with micro and/or macro-sized features. It is the philosophy of downscaling the production equipment closer to the size of the produced goods” [Jär+15]. Microfactories are also called “desktop”, “palmtop” or “mobile” factories [Jär+15].

1.5.2 The challenges of microfactories

Downscaling a system is not straightforward when the dimensions get smaller than the milli and micrometer scale. There are multiple challenges to overcome

to miniaturize manufacturing systems.

Linked to the manufacturing process

First, the size of the microfactory limits the size of the products that can be manufactured. Second, the small and lightweight machines are more sensible to external vibrations, heat and inertia changes that are not solvable with heavy frames as in macro machines. Third, the components of the machines and products tend to be fragile and sticky. Forth, as the factory downscales, the space is reduced and the density of the factory increases, reducing accessibility and visibility of the workspace [Jär+15].

Small scale physics

When in the sub millimeter and micrometer range, the tools to design and simulate the produced parts deviate from the macro scale behavior. For example, for liquids flowing in capillary tubes and channels, surface tension becomes a dominant force, and the traditional fluid dynamic approach requires significant modification. The friction and adhesion forces become predominant and electromagnetic forces decrease rapidly with size [Hsu02; Tri97].

1.5.3 The benefits of microfactories

Microfactories are often characterized by modularity, reconfigurability and mobility. As the machines are smaller, they usually consume less energy and raw material, and create less material waste. They require less factory floor space, reducing the energy used for illumination, air-conditioning and heating. They also produce less waste heat. The energy comparison between an actual size factory and a scaled factory, with scaling factor of $1/S$ is presented in Table 1.2 ([Jär+15]). In this table, operating energy is proportional to moving the pieces and parts of the equipment. Illumination and heating are affected by the space needed for the equipment and the number of operators. Process energy is the energy to machine the pieces of the product. This dissertation contribution is in the operating energy category.

The small size of machines and factory reduce the vibration and noise which are beneficial for workers and the factories' neighbors. Reduce the investments in land space, buildings and power sources. The transfer distances of pieces are shorter. A piece-by-piece process decrease the statistical likelihood of faults [OMA04].

Table 1.2: Energy saving effect when scaling a factory with a factor $1/S$ ([Jär+15])

Energy category	Consumption in factory (%)	Energy scaling estimation
Operating	13	$1/S^3$
Illuminating	23	$1/(1.5 \cdot S^3)$
Air conditioning	56	$1/(3 \cdot S^3)$
Processing and others	8	1

1.5.4 Microfactories examples

The authors in [Neu+10] studied the integration of piezoelectric sensors and actuators in metallic structures to obtain smart products that could, for example, monitor themselves. The addition of piezo elements is usually made by polymer adhesives, but the adhesive does not have advantageous mechanical properties like a high elastic modulus (2.5 GPa against 70 GPa of the aluminum). Their solution was to integrate piezo elements in a mechanical assembly using a microfactory. For this, aluminum pieces were machined to obtain parallel microcavities of size 0.325 mm × 0.35 mm × 10 mm with a pitch of 0.5 mm. The cavities were covered with a dielectric layer of SiCN. Then, bar-shaped piezoceramic microparts with dimensions of 0.285 mm × 0.26 mm × 15 mm were inserted in the cavities (Figure 1.27a). The microfactory had three units: the manipulator for assembly that used a electrostatic gripper, the rotary table conveyor that had four arms and the manipulation unit for the rotation of the piezoceramics that used a needle-type vacuum gripper (Figure 1.27b). Both manipulators had 3 DoF piezo stage positioning systems for their grippers and task execution. The achieved workspace was 10 mm × 8.24 mm in translation and of ±10° in rotation. The conveyor was a rotary stage with a resolution of 0.01° and maximum speed of 65 ° s^{-1}. The conveyor had four identical arms. Each arm had two vacuum interfaces, one to clamp the work piece carriers and one to clamp the work pieces on the carriers. Work piece carriers were standard, so they could be easily changed for different parts. The parts were successfully assembled with assembly clearances of ±0.015 mm.

[Sil+11] assembled a 78 mm × 12 mm gas sensor composed of two plastic frames, a detector and an exciter (Figure 1.28a). The whole microfactory had dimensions of 610 mm × 300 mm × 500 mm (Figure 1.28b). The H-Scara robot had a 4 DoF closed loop electro-pneumatic positioner and the dispenser had a 3 DoF closed loop motor positioner system. The sensors were a pair of cameras for the H-Scara and hall sensors for the dispenser. The H-Scara put the elements together with a vacuum gripper and the dispenser glued them with a pressure

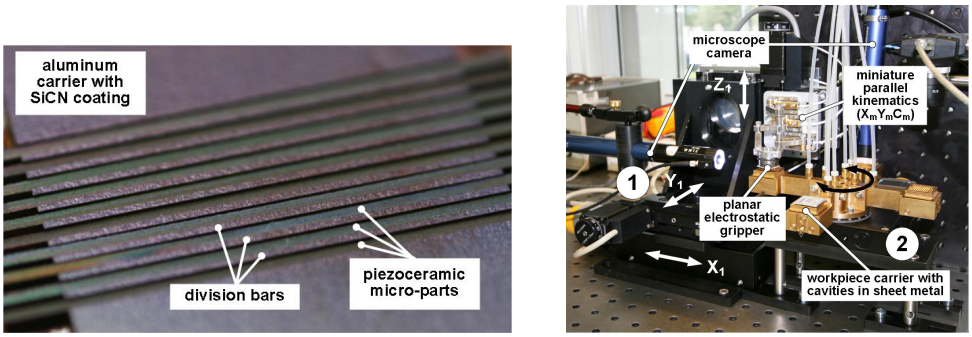

(a) (b)

Figure 1.27: Piezo-metal module fabricated in a microfactory by [Neu+10]. (a) Product. (b) Microfactory: (1) assembly manipulator. (2) conveyor.

valve to finish the assembly. The conveyance of the pieces to the H-Scara and to the dispenser was done with a belt conveyor. The use of computer vision to detect and sort the elements of the assembly was successful under their controlled conditions.

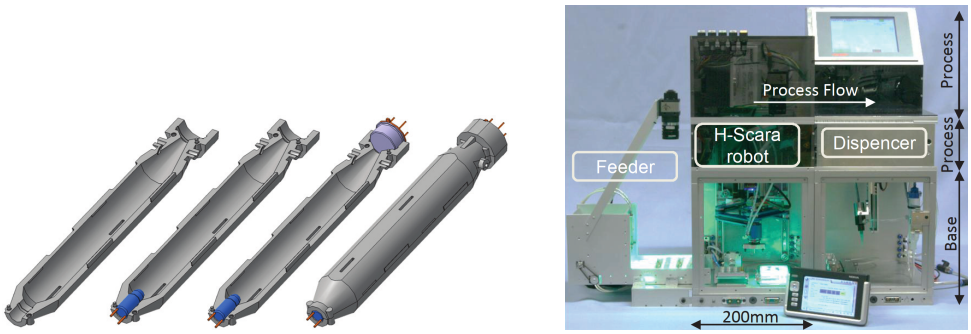

(a) (b)

Figure 1.28: Commercial gas sensor fabricated in a microfactory by [Sil+11]. (a) Product. (b) Microfactory.

In [Zha+17], the authors presented a modular microfactory composed of five stations: two manipulators, a laser micromachining station, a camera-based inspection station and a conveyor (Figure 1.29). The conveyor had 1 DoF with a DC motor with a encoder for closed loop control. It actuated a plate of ⌀ 30 cm with four slots for the conveyed parts. The accuracy of position was 0.0001 rad, meaning errors of 12.5 µm for the x-axis and 0.625 nm in the y-axis. The manipulators were 3 DoF mechanisms actuated with DC motors with compliant structures. The trajectory error obtained was less than 168 µm. The laser machining station achieved a laser position error of 2.5 µm. Finally, the camera inspection station had an auto-focus function to evaluate the pieces with the maximum resolution. The microfactory occupied 50 cm × 50 cm × 46 cm and weighted 15 kg. The microfactory wrote 550 µm inscriptions in ⌀3 mm spheres of different colors with success.

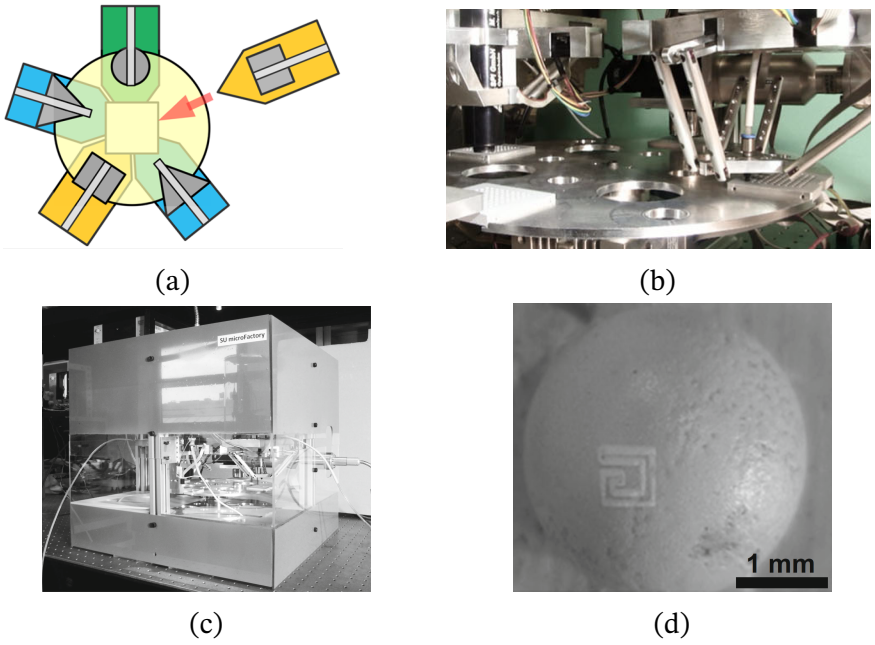

(a) (b)

(c) (d)

Figure 1.29: Five module microfactory of [Zha+17]. (a) Microfactory schema. (b) Modules picture. (c) Microfactory picture. (d) processes pieces.

The LFDA Xanthia modular microfactory of Ginolis Ltd [Gin20] was designed for the production automation of microparts, medical device components, such as point-of-care diagnostics, microfluidic devices, insulin pumps, drug delivery applications and test cartridges (Figure 1.30). Each module has cameras for computer vision control and guidance of the robot arms that perform the manipulation of the parts. The conveyance system based in belt and motors uses magnetized carriers to move components along a glass platform. This makes the conveyor liquid resistant. The core module has a size of 695 mm × 920 mm × 700 mm, it is able to manipulate 0.5 kg with an accuracy of 0.05 mm and precision of 0.01 mm [Gin18].

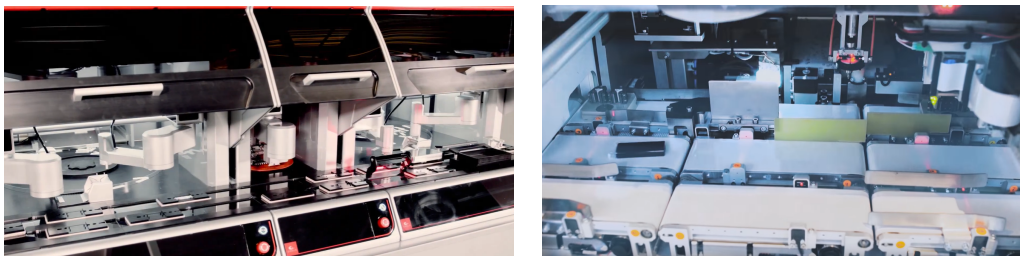

(a) (b)

Figure 1.30: LFDA Xanthia modular microfactory [Gin20]. (a) Microfactory modules with robot arms manipulators and a frontal conveyor common to all modules. (b) Multi conveyors inside larger modules.

JOT Automation Ltd is a Finnish industrial automation company that offers a range of modular microfactory stations. Their stations are manipulators, assem-

bly lines, conveyors and machining stations for microcomponents and electronics, supplying customers producing smartphones, tablets, smart watches, computers, smart wearables, displays, ebooks, navigation systems, headphones, speakers, TVs, LEDs, remote access keys, cameras, energy harvesters and solar panels. This demonstrates that the benefits of the microfactory is starting to appeal to the industry. The Jot V4 Assembly Cell from JOT Automation is a modular desktop platform for precision assembly. It has a size of 495 mm × 610 mm × 1030 mm handling 1 kg. It uses four cameras for computer vision control of its robotic arms (Yamaha SCARA robots). The Yamaha SCARA robots are a family of manipulators with high precision performance, e.g., the YK120XG, compatible with the Jot V4, has a repeatability of ±0.01 mm in the translation axes and 0.004° in the rotation axes with maximum speed of 3.3 m s^{-1} and 1700 ° s^{-1}. As the Ginolis solutions, the conveyance system between stations are miniature belt conveyors [Jot20].

1.5.5 The need addressed in this dissertation

Microfactories are a proposed solution to the need of miniaturize the manufacturing systems. Current microfactories produce a large range of products for multiple industries. These products need to be properly sorted, conveyed and aligned in each step of its manufacture and assembly process. This is the task of the microconveyor of such microfactory. Current solutions based in miniature belt conveyors and serial processes with microgrippers are not efficient nor flexible to the increasing demand on those manufacturing systems [LA12]. An additional flexibility level to reconfigure the microfactory and to execute parallel procedures would enhance the microfactory potential. Planar motion microconveyors contribute to this additional flexibility.

In all microfactory examples presented, the conveyance system was a miniature version of classical conveyors systems such as DC driven plates or belt conveyors. These solutions have the same characteristics as their macro versions: they are simple, unidirectional, and well controlled. The modularity of the presented microfactory comes mostly from their multipurpose stations compatible between them but still linearly (always following a single DoF). This shows that the idea of microfactory and modular, adaptive manufacturing is not yet completely integrated and the research and economical potential of this subject.

1.6 Scope and context of this dissertation

This dissertation is part of the "Tridimensional microconveyance systems for the microfactory" (ALVEO) research project, funded by the national research agency of France: Agence National de la Recherche (ANR). The ALVEO project is aligned on the *third challenge* of the *second axis* of the 2015 ANR action plan, called "Challenge: Stimulate the industrial renewal" (f.r Stimuler le renouveau industriel), "Axis: Fabric of the future, system, product, process" (f.r Axe 2, Système, produit, process), respectively. ALVEO's objective is to develop tridimensional microconveyance systems for the microfactory. For this, two challenges inside the project are defined: the technological challenge relative to the design and fabrication of the microconveyors; and a control challenge relative to ensure the best conveyance performance with these systems. This dissertation contributes to the control challenge of the ALVEO project.

This dissertation builds on the works of Laurent Petit ([Pet09]), who developed the idea of a digital electromagnetic actuator based in the Lorentz force actuation equipped of permanent magnets as holding function; Pengfei Huyan ([Huy15]), who fabricated the first digital actuator array; and Zhichao Shi ([Shi17]), who built a digital actuator array with microfabrication techniques.

With the concepts and context presented in this chapter, the scope of this dissertation can be set.

The **research question** of this work is: How to exploit an array of digital electromagnetic actuators as a conveyance system to transport objects between different machining/quality stations of a microfactory, efficiently in terms of consumed energy, displacement time, final position and trajectory error, and avoiding collisions with obstacles or other transported objects?

The road-map of this research project is explained in the conclusion of Part I.

This thesis is then placed in the microfactory environment, using the physics, control and pathfinding theories in a mechatronic system such as the microconveyor. This research is linked to five mechatronic topics: 1. *Digital actuation*. 2. *Planar motion actuation systems*. 3. *Actuator arrays for complex applications*. 4. *Electromagnetic-mechanic modeling*. 5. *Trajectory generation and control*.

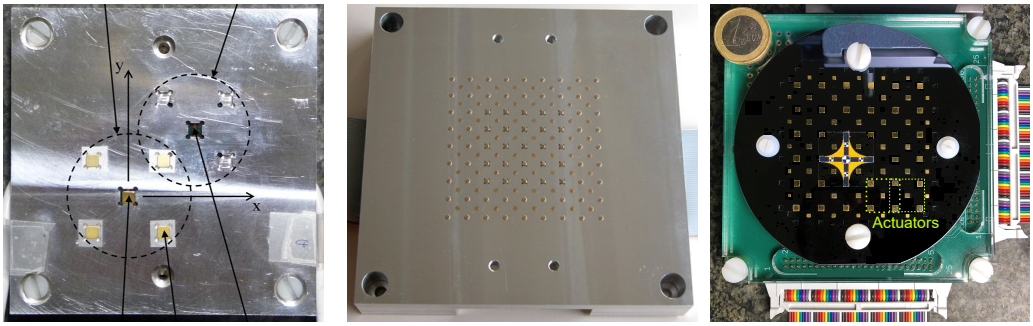

(a) (b) (c)

Figure 1.31: (a) Electromagnetic digital actuator by [Pet09]. (b) Digital actuator array by [Huy15]. (c) Digital actuator array by [Shi17]

Chapter 2

State of the art

This chapter presents the state of the art in three domains. The first state of the art domain is planar motion devices with a focus in modular smart conveyors able to operate in the micrometer range. The presented systems are grouped by the physical principle of their actuator's driving function. These physical principles are electrostatic, electrothermal, electrowetting, piezoelectric, pneumatic and electromagnetic principles. The presented solutions are compared and set as a benchmark to evaluate this dissertation's contribution. This state of the art is linked to the first three topics of this dissertation: 1. *Digital actuation*. 2. *Planar motion actuation systems* and 3. *Actuator arrays for complex applications*.

The second domain focuses on contact mechanics, composed of collision and friction phenomena modeling. This domain, linked to topic 4. *Electromagnetic-mechanic modeling*, sets the analytic bases for the modeling of this dissertation's system, as its conveyance principle is based on a friction stick-slip phenomena.

Finally, the third domain, linked to the considered application, is on pathfinding. This section defines the pathfinding problem and shows multiple ways to solve it. This will set the bases for the control of the conveyed objects on this dissertation's system, as each object needs to be moved to a precise position, avoiding obstacles and potential collisions with them or other conveyed objects. This section is linked to topic 5. *Trajectory generation (pathfinding)*.

2.1 Actuator driving functions by energy type: from actuation principles to motion applications

This section presents the state of the art of the actuators aimed at motion applications. The actuators are divided by the type of energy they use to generate their driving force. These energies types are: electrostatic, electrothermal, electrowetting, piezoelectric, pneumatic and electromagnetic. Each energy type subsection

explains the physical principle exploited by the actuators to generate the driving forces, their advantages/disadvantages and their scaling laws. Then, multiple examples of the use of these actuators in motion devices are presented. The presented devices use or apply the concepts of digital actuation, positioners and conveyors (Chapter 1).

2.1.1 Electrostatic actuators

The electrostatic actuators accumulate electrostatic energy and convert it into mechanical work. Electrostatic actuators are composed by two conducting bodies (electrodes) at different electric potential levels. The electrodes accumulate charge for a period of time, increasing the electrostatic energy and generating a force when the charge reaches a level where the electrostatic force overcomes the mechanical load. The accumulation of charge follows the capacitor effect, i.e., the ratio between charge (q) and potential (V) is the capacitance $C = q/V$. The energy stored between the electrodes U_e is the work W needed to move a charge dq from an electrode to the other under the presence of a potential $v(q)$. As more charge is moved, the potential $v(q)$ increases until a final charge of the electrodes Q is reached at a potential V. This can be expressed as [Bor08]:

$$U_e = W = \int_0^Q v(q)dq = \int_0^Q \frac{q}{C}dq = \frac{Q^2}{2C} = \frac{QV}{2} = \frac{CV^2}{2} \tag{2.1}$$

This equation is independent of the geometry of the electrodes as it is an expression of the capacitance C. For a parallel plate electrode capacitor, the electric energy U_e is:

$$U_e = \frac{CV^2}{2} = \frac{\epsilon_0 \epsilon abV^2}{2d} \tag{2.2}$$

With ϵ_0 the permittivity of free space, ϵ the permittivity of the material between the electrodes, d the separation between electrodes, a the length of the electrodes in the x-axis and b the length of the electrodes in the z-axis (Figure 2.1a, b not represented).

The derivation of U_e with respect to a and d gives the electrostatic forces [LC18]:

$$F_x = \frac{\partial U_e}{\partial a} = \frac{\epsilon_0 \epsilon bV^2}{2d} \tag{2.3}$$

$$F_y = \frac{\partial U_e}{\partial d} = -\frac{\epsilon_0 \epsilon abV^2}{2d^2} \tag{2.4}$$

To maximize the electrostatic force, the area between the electrodes could be maximized with a comb-drive actuator. Their force equation changes depend-

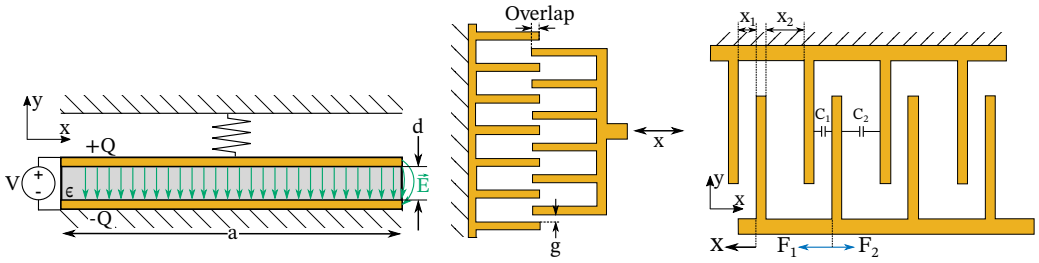

Figure 2.1: (a) Electrostatic principle. (b) Lateral motion comb-drive actuator. (c) Transverse motion comb-drive actuator.

ing on the generated movement. When the movement changes the overlap of the combs, the movement is called lateral (Figure 2.1b). When the movement changes the distance between the combs, the movement is called transversal (Figure 2.1c). The force equations for both movements are [LC18]:

$$F_{lateral} = \frac{netV^2}{g} \tag{2.5}$$

$$F_{trans} = -\frac{n\epsilon A}{2}\left[\frac{(x_1+x_2)(x_2-x_1+2x)}{(x_1-x)^2(x_1+x)^2}\right] \tag{2.6}$$

Where n is the number of comb pairs, t is the thickness of the plate, g is the gap spacing, ϵ is the permittivity of the medium, A is the overlapping area of each finger pair, x_1 and x_2 are the initial gap spacings and x is the changes in gap spacing. Electrostatic force scales with a factor $\propto S^2$ [Tri97].

Electrostatic actuators are often characterized by low power consumption and a high switching speed. Actuation voltages range from 9 to 250 V. Only small deflections can be achieved at a low voltage, which is restrictive in some applications. Electrostatic actuators suffer from a problem known as “pull-in”, where the movable parts stick to the fixed parts when actuation voltages reach a high value. The fabrication of electrostatic actuators is highly compatible with microfabrication techniques of Integrated Circuits, thus an advantage [LC18].

[SZF18] designed a 1 DoF repulsive electrostatic actuator and applied it to move a micromirror for laser steering (Figure 2.2). The 25 mm × 10 mm pattern had the advantage of no pull-in instability and low hysteresis. The pattern directed the electric field through the substrate, so its properties are independent of electrode geometry or layer alignment, and limited only by the dielectric strength of the substrate. The actuator weighted 135 mg, generated a force of 9.03 mN with 1000 V and showed a quadratic relationship between the applied voltage and force. The maximum displacement was 511 µm at a resonant frequency of 29 Hz and the actuator had a bandwidth of 43 Hz. The energy efficiency of the

actuator was 0.72%. Finally, a 290 mg 1 DoF micromirror system for laser beam steering was tested. 1000 V generated an angular displacement of 5.1° at 16 Hz (resonance). The actuator displacement was proportional to the voltage, so it could deflect to any intermediate angle.

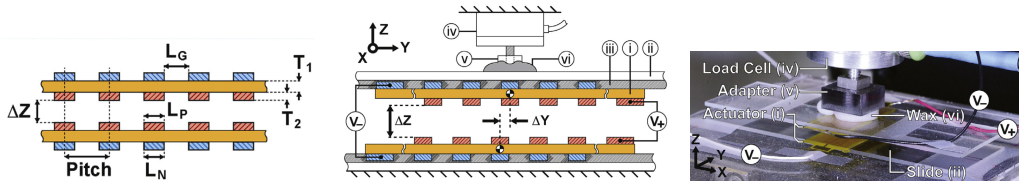

(a) (b) (c)

Figure 2.2: Electrostatic 1 DoF actuator by [SZF18] (a) Actuator schema and parameters. (b) Force generation installation. (c) Experimental test.

[DPS11] presented a modular digital electrostatic microconveyor based on comb-drive actuators (Figure 2.3). A 500 µm × 250 µm × 30 µm, 2 µg container with wings was bent by the comb-drives to make the container execute a 21 µm step in its ratchet rack guided path (Figure 2.3a). The comb actuators were arranged in different modules (straight, curve or T-junction). The maximum speed was 1 mm s^{-1} using 140 V at 50 Hz. Higher voltages of 160 V produced broken wings or pull-in of the comb electrodes. A lifetime test was performed at 140 V and 25 Hz reaching 4.5×10^5 cycles. The system had 1 DoF and the path of the conveyor must be defined beforehand in a given application.

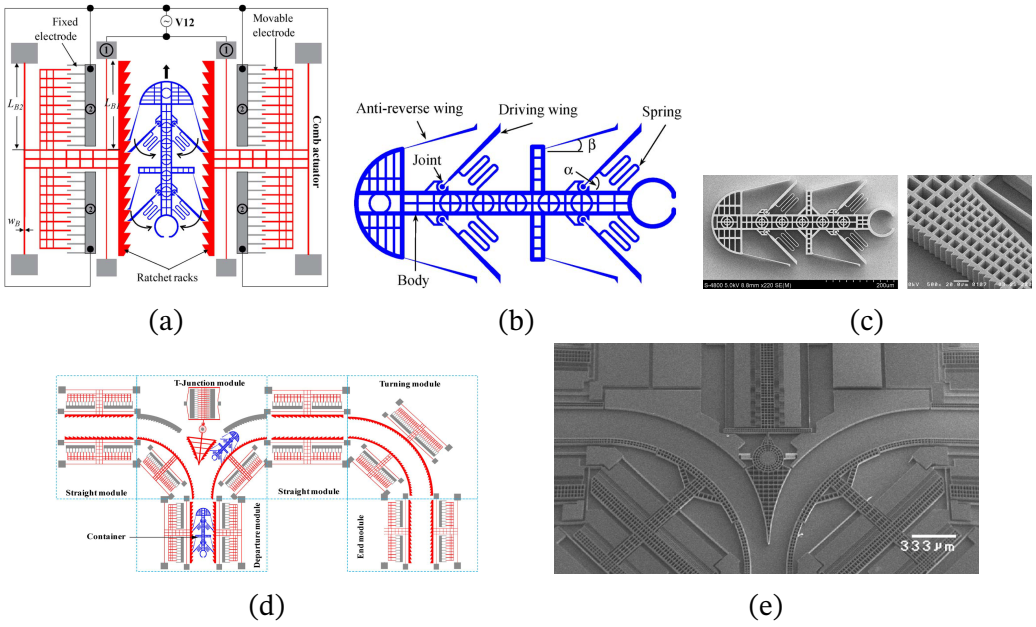

(a) (b) (c) (d) (e)

Figure 2.3: Modular digital electrostatic microconveyor by [DPS11]. (a) Working principle. (b) Container architecture. (c) Container prototype. (d) Conveyor modules schema. (e) Conveyor prototype.

[HYH15] developed a transparent planar electrostatic actuator aimed at interactive human–computer interfaces on flat panel displays (Figure 2.4). The actuator was an overlaid pair of films. The larger film fixed at the bottom was the stator and the smaller film placed on top was the slider. Between these two films were glass beads maintaining an air gap (Figure 2.4a). Each film had three-phase strip-electrodes for driving in two directions x and y using the synchronous electrostatic force principle. Three-phase voltage drove the actuator at speeds proportional to the excitation frequency (Figure 2.4c). The 132 mm × 132 mm, 10.9 g slider operated with a constant thrust force over the 264 mm × 264 mm workspace on the stator. The prototype could exert peak forces of 160 mN and average forces of 100 mN with 500 V. The maximum speed was 354 mm s^{-1}. The actuator conveyed up to 18 g with a 0.9 m s^{-2} acceleration. The authors demonstrated the capability to travel along straight and curved paths (2 DoF) and measured some rotation phenomena that was not controlled.

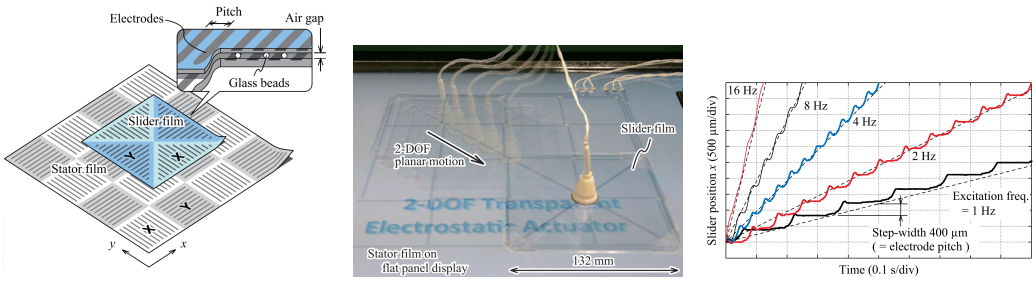

(a) (b) (c)

Figure 2.4: 2 DoF electrostatic conveyor by [HYH15] (a) System schema. (b) Prototype. (c) Displacement results.

[KLA18; KA19] designed a planar electrostatic microconveyor for assembly purposes and the associated trajectory algorithms (Figure 2.5). The stator was a PCB with embedded disc electrodes. The sliders were rectangular and hexagonal plexiglass layers with embedded disc electrodes. A liquid dielectric was used to reduce friction of the moving parts and a solid dielectric on top of the stator was used to isolate the electrodes from the user (Figure 2.5a). From the numerical simulations, the heavier movable slider was 265 mg and the system generated up to 2.29 µN forces with 225 V. No prototype or experimental values were reported The project seems in a study phase, with more emphasis on the optimization of geometrical parameters and distribution of electrodes. The principal subject of the articles were the trajectory algorithms and their implementation to the electrostatic conveyor.

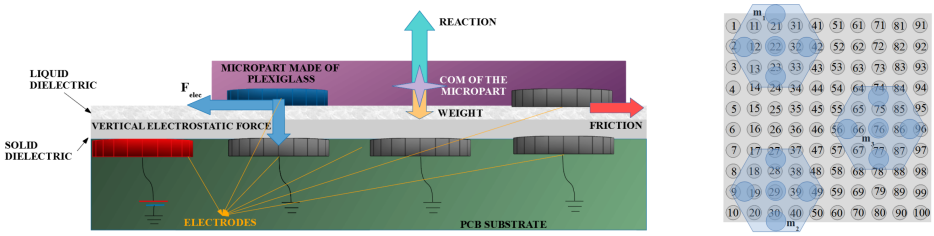

(a) (b)

Figure 2.5: Electrostatic conveyor by [KLA18; KA19]. (a) Conveyance principle. (b) Hexagonal conveyors.

2.1.2 Electrothermal actuators

Electrothermal actuators operate on the principle of Joule heating and differential thermal expansion [LC18]. An electrical current flows through the actuator and heat is generated following Equation (2.7) (considering the actuator as a ohmic resistance). The generated heat increases the temperature of the actuator following Equation (2.8). Finally, the increase in temperature expands the material by thermal expansion following Equation (2.9).

$$Q = I^2 R \tag{2.7}$$

$$Q = mc\Delta T - Q_{dis} \tag{2.8}$$

$$l = l_0(1 + \alpha\Delta T) \tag{2.9}$$

With Q the generated heat on the actuator, I the current flowing through the actuator, R the actuator's electrical resistance, m the mass of the actuator, c the actuator's specific heat capacity, ΔT the actuator's temperature change, Q_{dis} the dissipated heat to the environment by the actuator, l the current length of the actuator, l_0 the standard length of the actuator at a reference temperature and α the thermal expansion coefficient of the actuator. This principle is exploited in different architectures, as shown in Figure 2.6 and described in the next paragraph.

The U-shape actuator use differential arm expansion to produce movement (Figure 2.6a). When a current flows through the actuator, more heat is generated in the "hot arm" than in the "cold arm". This is because the cross-section of the arms are different, changing the resistance value. Different thermal expansion produces a bending moment and the structure deflects towards the cold arm (δ). Generally, a flexure is added to maximize the displacement. The deflection δ has a nonlinear dependence on the ratio between the lengths of the hot and cold arms, and on the width of the cold arm. The optimal flexure size was found to be approximately 14%–18% of the total arm length [PW19]. The size of the gap

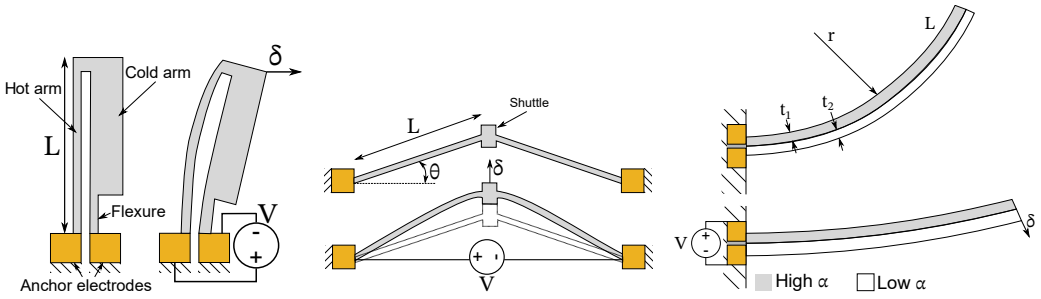

(a) (b) (c)

Figure 2.6: Electrothermal actuator types. (a) U-shape. (b) Chevron (or V-shape). (c) Bimorph.

between arms also has an influence: a larger displacement can be achieved with a smaller gaps [PW19].

The Chevron or V-shape actuator uses the total amount of thermal expansion in the structure (Figure 2.6b). The expansion is constrained to produce displacement in one linear direction. Two equal beams are connected in the apex (shuttle or tip) at a certain angle θ, and anchored at the other end. Several actuators can be connected in parallel to increase the force. The design parameters for chevron actuators are the beam length L and the pre-bending angle θ. The displacement of the tip is proportional to the temperature increase and the beam length. The tip displacement is inversely proportional to the beam width, but it is not related to the beam thickness. Larger displacement can be achieved with smaller pre-bending angles. However, there is a low critical limit for the angle below which the risk of out-of-plane buckling is high [PW19].

The bimorph actuator consists of two or more layers of dissimilar materials with different coefficient of thermal expansion and Young modulus (Figure 2.6c). The bimorph actuator is normally used for out-of-plane displacement because the different materials are deposited in layers on top of each other. Therefore, the bimorph actuators are preferred in applications where in-plane actuators cannot be used.

Electrothermal microactuators have a slow response time compared with piezo electric and electrostatic actuators. They require time to heat up and cool down, thus limiting their operating frequency to less than 1 kHz and consume more power than other solutions but generate large forces with large displacements at low voltages [LC18]. Electrothermal actuators do not involve electrostatic or magnetic fields for operation, therefore they are suitable for manipulation of biological samples and electronic chips. Unlike piezo and Shape Memory Alloys (SMA) actuators that experience significant hysteresis and require complex control, electrothermal actuators are easy to control.

Electrothermal actuators scaling laws are dependent of multiple physical

phenomena such as heat dissipation, heat generation and thermal capacity. Heat can be dissipated by conduction, convection or radiation. Heat generation in electrothermal actuators is produced by Joule effect, which depends on the electric current. Different assumption can be made for the current scaling such as constant current density, constant heat flow or constant temperature rise. The heat scaling laws are summarized in Table 2.1. Thermal capacity is dependent of the volume, so it scales $\propto S^3$.

Table 2.1: Scaling laws of physical phenomena influencing electrothermal actuators ([Tri97; For06]).

Heat flow dissipation		
Conduction S^1	Convection S^3	Radiation S^2
Joule heat generation		
Constant current density S^3	Constant heat flow S^2	Constant temperature rise S^1

In his doctoral dissertation, [Ell12] developed a digital electrothermal microconveyor based on lift and slide principle and a top view camera for closed loop control (Figure 2.7). His work is very near this dissertation's subject, thus described in detail next. The conveyed object was driven, then lifted to allow the mobile part of the actuator to return, and prepare another displacement step (Figure 2.7a). Each module (called pad) actuated in three axes (3 DoF) and weighted 0.25 µg. A four arm chevron electrothermal actuators was used for each actuation axis. The chevron had a length of 200 µm and pre-bending of 6° (Figure 2.7b). The chevron actuators generated forces of 80 µN and 3 µm strokes. The conveyor was formed with an 4×4 array of pads and lifters. Working at 12 V for the pads and 7 V for the lifters, the conveyor generated 320 µN conveyance forces and 12.8 µN lifting forces. The conveyor was tested in open and closed loop operation. For the open loop performance, the step size varied with the injected voltage: 0.28 µm at 7 V, 0.55 µm at 10 V and 0.89 µm at 12 V. Importantly, these step sizes did not change significantly with frequency up to 100 Hz. Repeatability was also measured: after 100 steps, a mean displacement at 12 V was 70.8 µm with a standard deviation of 10.1 µm in the x-axis and 64.9 µm with standard deviation of 10 µm in the y-axis. The straigtness errors for these test were 1.1 µm and 1 µm respectively. The maximum speed was 56.8 µm s^{-1}, with a straightness error speed of 10 µm s^{-1}. The average rotation achieved was 0.8° per step at 12 V, though position over the conveyance surface heavily influenced the results. For the closed loop performance: the maximum speed decreased to 46 µm s^{-1}, linked to a delay in image processing by the computer. The straightness error decreased

to 10% of the total displacement and its maximum speed decreased to 5 µm s^{-1}. The straight line trajectory was followed with a 2 µm delta. The system performed circular, square and cross-like trajectories as well. Finally, the conveyor moved a 78 µg salt crystal to validate its purpose.

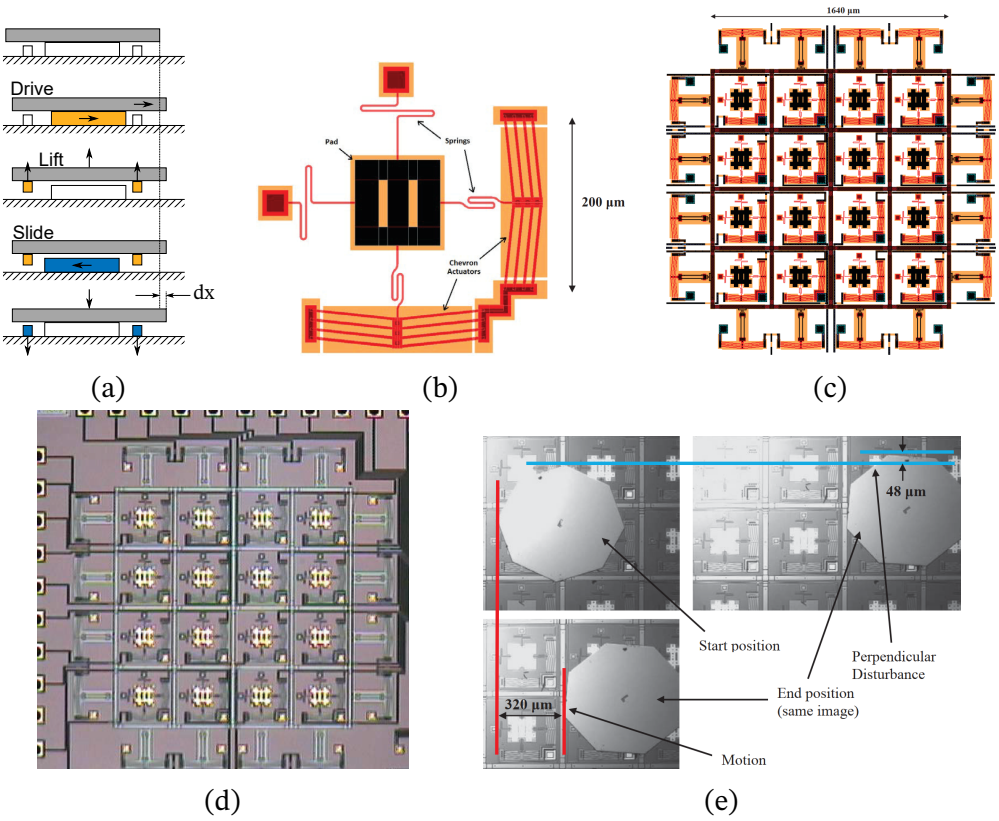

Figure 2.7: Electrothermal digital microconveyor by [Ell12] (a) Drive, lift-slide principle. (b) Module. (c) 4 × 4 array conveyor. (d) Microconveyor prototype. (e) Conveyance test.

[Hus+18] designed a 12 mm × 11 mm digital electrothermal 1 DoF micromover for robotic tasks (Figure 2.8). The mover consisted of three subsystems, each integrating two U-shape actuators and compliant structures (Figure 2.8a). Subsystem 1 was a bistable actuator displacing the mover through subsystem 2, the transmission clamp. Subsystem 3 was a clamp to hold the position of the mover while subsystems 1 and 2 reset their states for a new displacement. Each U-shaped actuator operated at 20 V for 20 ms generated 200 µm displacements and 10 mN forces. The microfabricated prototype executed 12 steps in both directions, generating a total displacement of 120.67 ± 0.08 µm, that translated to a step size of 10.06 ± 0.09 µm (Figure 2.8c).

[Zha+19] built a 10 mm × 10 mm 4 DoF microrobot aimed for micromanipulation tasks in microfactories such as pick and place as well as applying controlled forces (Figure 2.9). Four in-plane electrothermal actuators drove the end-effector through a series of compliant structures and springs. The chevron actuators

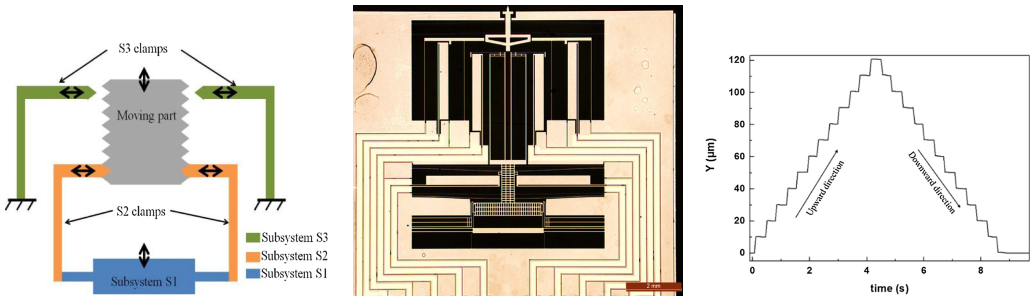

(a) (b) (c)

Figure 2.8: Electrothermal digital 1 DoF micromover by [Hus+18] (a) Working schema. (b) Prototype. (c) Displacement results.

operated at 10 and 15 V generating millinewton forces. Higher voltages generated beam buckling. The force transmitted to the effector diminished due the compliant structures to 55 µN for the pitch, 120 µN for the yaw and 1 mN for the x and y directions. The maximum force of the effector was 45 µN. The resulting workspace was 16 µm × 20 µm × 118 µm. The resolution changed with the position and the total displacement of the effector. The resolution along the x and y axes ranged between 20 nm for a step displacement and 120 nm for a 15 µm displacement. The resolution saturated with the displacement at around 70 nm for x translation and 80 nm for y translation. The yaw and pitch resolutions showed similar phenomena: 0.2 to 0.4 mrad for the pitch and 0.15 to 0.2 mrad for the yaw (maximum rotations of 6 and 8 mrad, respectively). The repeatability followed a similar behavior, with ranges between 20 and 150 nm for x and y translation, and between 0.15–0.26 mrad for pitch and yaw.

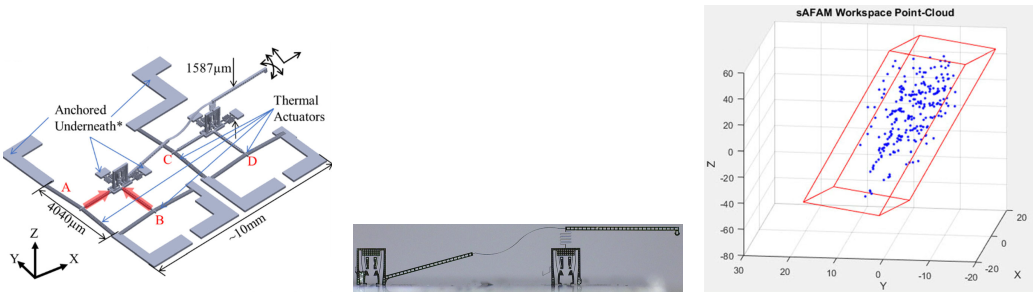

(a) (b) (c)

Figure 2.9: Electrothermal digital micropositioner by [Zha+19] (a) Working schema. (b) Prototype. (c) Working space.

2.1.3 Electrowetting actuators

Electrowetting (EW) is the manipulation of small amounts of liquid (drop or droplet) on solid surfaces. Electric fields are used to modify and control the

wetting and capillary properties of the drop. Wetting is the ability of the drop to maintain contact with the solid surface. Adhesive forces between the drop and surface cause the drop to spread across the surface. Cohesive forces within the drop cause the drop to avoid contact with the surface. The principal cohesive force of the drop is its surface tension γ, which is determined by intramolecular forces such as Coulomb electric interaction and van der Waals interactions. The balance of cohesive and adhesive forces determines a contact angle θ between liquid and surface, providing a measure of the wettability of the drop. Capillarity is the ability of a liquid to flow in narrow spaces even in opposition to external forces like gravity. Wetting and the surface forces of the drop are responsible for capillary effects. The classic electrowetting technique of a drop on a metal contact is rarely used today, instead, a dielectric (usually hydrophobic) layer between the electrode and the drop is used to protect the electrode from corrosion and the drop from contamination. This is called electrowetting on dielectric (EWOD) [MH19] and in this dissertation EW and EWOD are used to denote electrowetting.

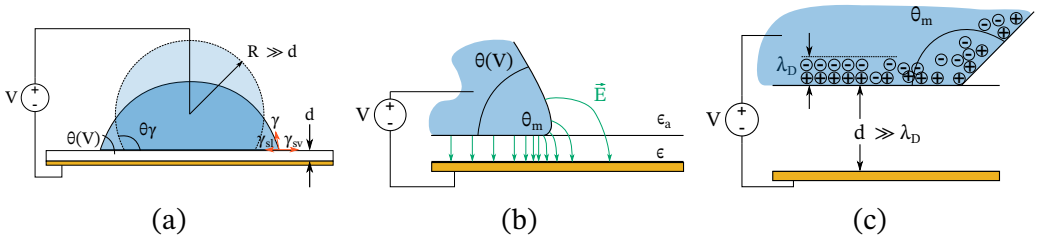

Figure 2.10: Electrowetting on dielectric phenomenon (a) Macroscopic level. (b) Microscopic level. (c) Molecule level.

Electrowetting is an equilibrium between the drop, the surface, the vapor around the drop and the electric energy of the electric field, so the total energy of the system $\left(E_{tot} = E_{surf} + E_{el}\right)$ tends to a minimum at each working point. This means that the infinitesimal change in energy of the system is zero ($\delta E_{tot} = 0$) once the equilibrium attained. The free energies of the system are the surface energies E_{surf} (due to surface tensions) and the electric energy of the capacitor formed by the dielectric and the drop E_{el}. The surface energies depend on the areas and the surface tensions between: the surface and the liquid drop γ_{sl}; the surface and the vapor around the drop γ_{sv}; the liquid drop and the vapor γ. The sum of these surface energies is then $E_{surf} = A_{lv}\gamma + A_{sl}(\gamma_{sl} - \gamma_{sv})$, as represented in Figure 2.10a (with A area). For an infinitesimal change in the contact line between the drop and surface, dx, the change in surface energy is $\delta E_{surf} = dx(\gamma_{sl} - \gamma_{sv} + \gamma\cos(\theta))$. θ is the angle between the drop and surface under a given condition. If no external influence of the system is present, then the only forces are the surface tensions and $\theta = \theta_\gamma$ [MH19]. At equilibrium,

$\delta E_{surf} = 0$, implying that:

$$\cos(\theta_\gamma) = \frac{\gamma_{sv} - \gamma_{sl}}{\gamma} \tag{2.10}$$

For the electric energy, the drop and electrode are supposed as a parallel plate capacitor [1], with a uniform electric field of strength V/d and a capacitance per unit area $c_d = \epsilon\epsilon_0/d$. This corresponds to an electrostatic energy per unit area of the drop–substrate interface of $E_{el}/A_{sl} = -c_d V^2/2$ [MH19]. Hence, $\delta E_{el} = -dxc_d V^2/2$.

Building the total energy change $\delta E_{tot} = \delta E_{surf} + \delta E_{el}$:

$$\delta E_{tot} = dx\left(\gamma_{sl} - \gamma_{sv} + \gamma\cos(\theta(V)) - \frac{c_d V^2}{2}\right) = 0 \tag{2.11}$$

As the equilibrium criteria imposes that this change in energy is zero and replacing θ_γ, we obtain the Young–Lippmann equation:

$$\cos(\theta(V)) = \cos(\theta_\gamma) + \frac{c_d V^2}{2\gamma} = \cos(\theta_\gamma) + \eta \tag{2.12}$$

With η the EW number that measures the relative strength of the electrostatic energy and surface tension. Normally, the liquid for the EW is chosen to maximize the surface tension, thus minimizing η (such as metallic liquids like Hg) [MH19]. This is because, as seen in Equation (2.12), the EW technique can only increase the angle of the drop. Thus, a maximum surface tension will form the lowest natural angle of the drop and give the largest stroke for this kind of actuator. All known applications of EW work in the Young-Lippmann equation regime [MH19]. If the voltage is increased from a certain threshold, the contact angle is no longer dependent on the applied voltage, and the drop angle saturates.

To transport the drop in space, the EW technique needs channels and electrodes defining the possible paths for the drop. The drop will follow the energized path thanks to an electric force generated by the electric field, which translates to a difference in pressure around the drop [Ten+20]:

$$F = \gamma\cos(\theta(V)) = \Delta P_L h \tag{2.13}$$

The pressure differential can be computed also by the Young-Laplace equation [MH19]:

$$\Delta P_L = 2\gamma\kappa = \gamma\left(\frac{1}{R_1}\right)\left(\frac{1}{R_2}\right) \tag{2.14}$$

[1] The capacitance calculus requires the field and charge distribution, which depends on the geometry of the electrodes. For scales of the drop $\gg d$, the border phenomena can be neglected and the dielectric layer and the electrode on the surface form a parallel plate capacitor [MH19].

With ΔP_L the Laplace pressure differential around the drop to move, γ the surface tension, h the high of the droplet relative to ground (gravity effects), κ the mean curvature of the drop shape which takes the form $f(R_1, R_2)$ for two principal radii shapes [MH19].

The scaling laws for electrowetting are dependent on the surface tension and the gravity effect on the droplets. Surface tension has a scaling of S^1 because it depends upon the length of the wet interface [Tri97]. The gravity effects on the droplet scales as S^3. To link both forces, the Eötvös (E_o) or Bond (B_o) dimensionless number measures the importance of gravitational forces compared to surface tension forces:

$$E_o = B_o = \frac{\Delta\rho g L^2}{\gamma} \tag{2.15}$$

With g the gravitational acceleration, $\Delta\rho$ the difference in densities between the liquid droplet and the surrounding vapor, γ the surface tension and L the radius of the droplet. If $B_o < 1$ the surface tensions dominate over gravitational effects. For this to happen, L must be less than $L_c = (\gamma/\Delta\rho g)^{1/2}$. This value of L_c defines the radius for which the drop is equally influenced by gravity and tension forces. Under L_c the surface tensions dominate. For a water droplet in air, $L_c = 2.7\,\text{mm}$, for a silicon oil droplet in air L_c =1.5 mm.

Multiple droplet motions are realizable with EWOD: transfer, oscillation, capillary bridge, permeation and bouncing [Ten+20]. Oscillations are obtained with AC voltages, making the drop vibrate and could be useful for micromixing liquids in a controlled way. Capillary bridges are a special case of translation where two drops are made to touch or disengage to connect a circuit. Permeation is the control of the drop to penetrate a solution and activate a reaction with its diluted activators. Bouncing is an extreme application of AC voltage to make the drop bounce off the surface. This dissertation focuses on the translation manipulation with EWOD.

[WDM17] presented a bistable actuator based in EWOD and the surface tension of the drops holding function (Figure 2.11a). The authors used a GaIn alloy liquid metal diluted in a electrolytic aqueous solution to obtain a very sensible drop to electric field and actuate the switch with low voltages (10 V), which is a novelty for this kind of systems. The switch used an electrode under each drop and another electrode next to each drop to control the switch action (Figure 2.11b). Their work focused on parameter evaluation against performance, studying the impact of different component's concentration in the liquid drop, the scale of the system and electrode separation (up to 23 mm). The potential applications mentioned were field-programmable gate arrays, reconfigurable antennas, and soft memory storage devices. The system worked as expected but

the frequency limit of the switch (AC transmission) was not evaluated and could be limited by the inertia of the liquid.

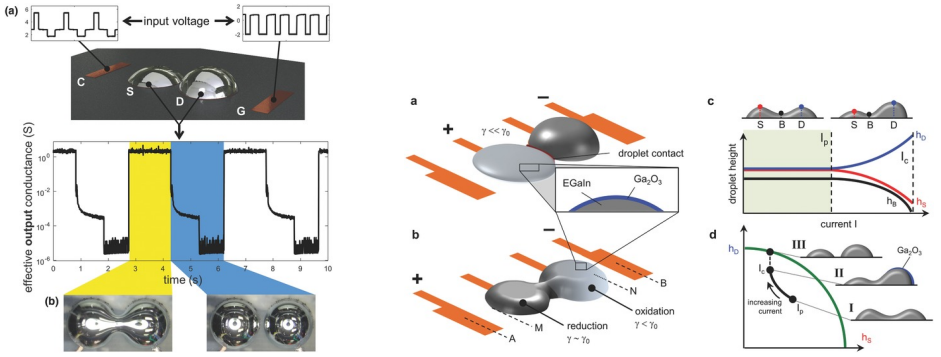

(a) (b)

Figure 2.11: Bistable electrical switch (EWOD digital actuator) by [WDM17]

[Rib+19] reported an bistable optical shutter using opaque ionic liquid microdroplets that could block visible and mid-infrared wavelengths (Figure 2.12). The system had a transmission hole that was blocked with the drop, that absorbed the incoming light in the close state. The minimum operating voltage was 22.5 V achieving a settling time of 1 s. Increasing the voltage to 25 V decreased the settling time to 300 ms. A minimum settling time of 100 ms was possible with higher voltages, but degradation of the system's layers was noticeable with this performance level. Because of the transmission state was a hole, no insertion losses were present in the system. The system achieved 78 dB attenuation levels and 99.999% transmission efficiency. The system worked continuously with incoming intensities of 5 mW or up to 3 hours with 100 mW, which is extremely high power absorption for this kind of devices.

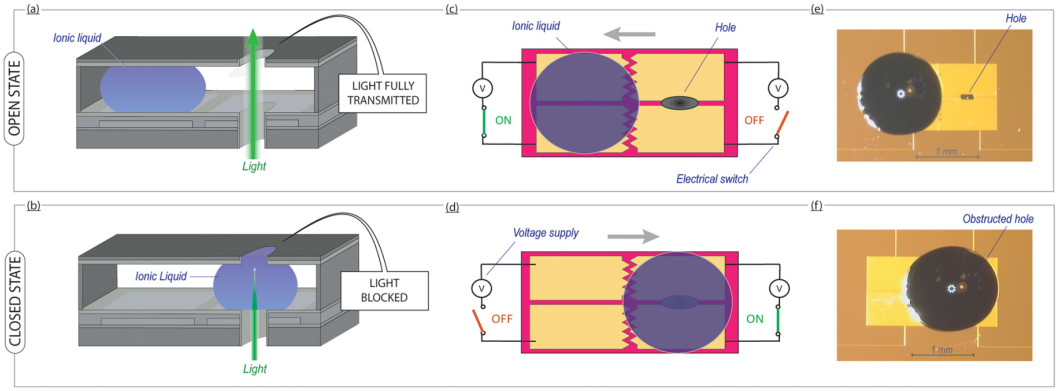

Figure 2.12: Bistable optical shutter using opaque ionic liquid microdroplets [Rib+19]

[MK06] designed a microconveyor based on EWOD driving four drops carrying an object in a synchronized way (Figure 2.13a). The 5 mm × 4 mm × 0.5 mm

conveyor could move forwards and backwards with operating voltages of 100 V DC and 80 V AC at 1 kHz using 6 µL droplets. The system achieved 2.5 mm s^{-1} speeds. The conveyor moved a payload of 180 mg.

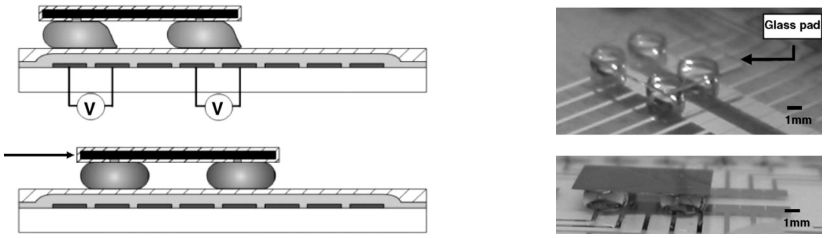

(a) (b)

Figure 2.13: EWOD microconveyor by [MK06]. (a) Principle schema. (b) Prototype.

The same conveyance idea was used by [Nie+18] (Figure 2.14a). The authors integrated a triboelectric nanogenerator device to the system to supply the conveyor and achieve an embedded system. The generator used tribo-electrification between a nano treated Kapton film and four pieces of Al foil to generate the driving voltages of the system (each of sizes 10 cm × 8 cm). This power supply could generate up to 3500 V but the hold of this voltage was not reported. The electrode separation, that indirectly defines the step of the conveyor, was 0.5 mm for a total one dimensional stroke of 25 mm. The conveyor used four 70 nL droplets to carry a 6 mm × 8 mm plate. The maximum load was 500 mg and maximum speeds was 1 m s^{-1}.

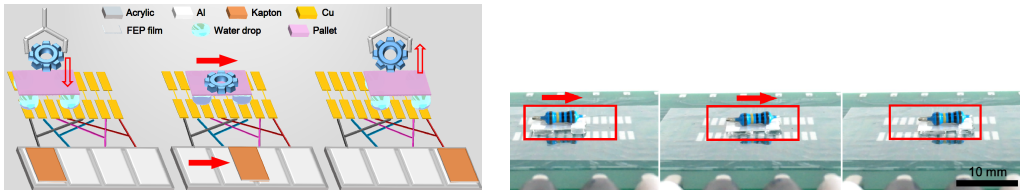

(a) (b)

Figure 2.14: EWOD microconveyor by [Nie+18]. (a) Principle and materials. (b) Prototype in motion

The doctoral dissertation of [Geu18] treated about an EWOD microconveyor (Figure 2.15). Her work focused in the modeling of the droplets and their interaction with the driving electrodes. She developed a capacitance-based model to predict the driving forces on the droplet and evaluated multiple geometrical parameters of the electrode and their impact in the transport of the droplets. Her findings were that electrodes with a small width compared to the length allowed for a fine positioning accuracy. Puzzle-shaped and serrated electrodes were more usable for a full electrode array than square-shaped electrodes. The electrodes

needed to be symmetrical and the geometry of the electrode edge should differ centrally from on the outsides, to ensure the alignment of the droplets in the path. She also demonstrated circular motions of the droplets in closed electrode paths, which is a novelty for this kind of conveyors. Her microconveyor obtained speeds of 2 mm s^{-1} for an actuation voltage of 250 V. For an increased actuation voltage of 300 V, the speed increased to 3.93 mm s^{-1}. Steps of 1/3mm were executed.

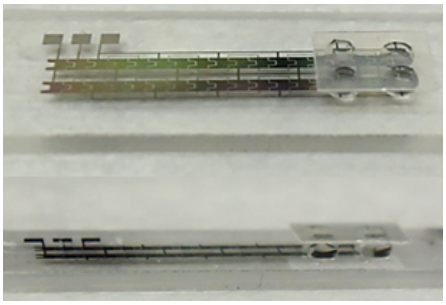

Figure 2.15: Miniaturized conveyor driven by EWOD [Geu18]. 2 µL droplets carrying a platform.

Discussion

Electrowetting applications are a growing interest in microdevices such as switches, micromixers, and microreactors, and even microconveyors. The references above did not report on the precision, accuracy or repeatable minimum step achievable for their devices. The speed of the conveyors were dependent on: the shape and separation of the electrodes ; the frequency and intensity of the electric field. The system of [Nie+18] achieved 1 m s^{-1} using 3500 V while [Geu18] achieved 4 mm s^{-1} with 300 V.

The EWOD technique has the advantage of an intrinsic holding function in the surface tension of the droplets, but the inertia of the drop is high compared to other actuation solutions. Yet, in smaller scales (read, nano) this technique could be very useful given the scaling laws of the phenomena. A downside of EWOD conveyors is the difficulty in assembling an array of electrodes to allow planar motion of the droplets and, thus, form a smart conveyor. They are still based in linear paths of electrodes and not smart surfaces.

2.1.4 Piezoelectric actuators

The piezoelectric effect is the ability of some materials to generate an electric charge in response to applied mechanical stress [Pon05]. If the material is not short-circuited, the applied stress induces a voltage at the ends of the material.

When the material is at rest, the electrical charge is balanced and neutral (Figure 2.16a). An external stress elastically deforms the crystal lattice of the material, displacing ions of the crystal cell towards the ends of the crystal cell. This creates a concentration of negative and positive charge at different ends of the crystal cell, i.e., an electric dipole moment (Figure 2.16b). Multiple dipoles of the material align together in domains called Weiss domains and create a polarization density inside the material ($\vec{P}$) (Figure 2.16c). This polarization creates a concentration of opposite charges at the ends of the material, i.e., an electric field along the material that can be measured as a voltage.

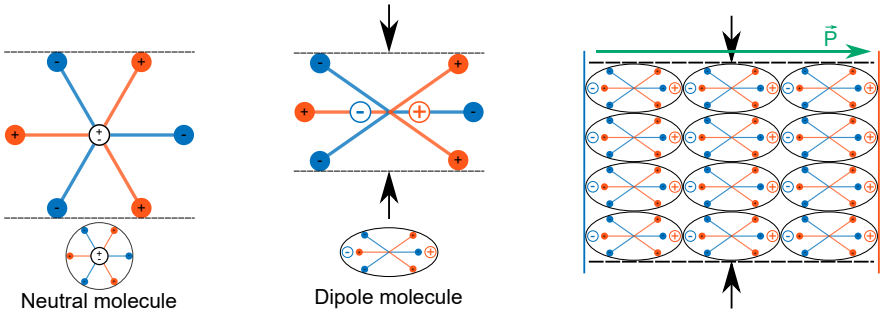

Figure 2.16: Piezoelectric effect. (a) Electrically neutral molecule. (b) Dipole. (c) Weiss domain polarization (adapted from [Zie19]).

The piezoelectric effect is reversible, i.e., an external applied electric field ($\vec{E}$) will cause mechanical deformation in the crystal following the same process [Pon05]. This is called converse or inverse piezoelectric effect and is the physical phenomenon exploited by piezoelectric actuators (Figure 2.17). Some piezoelectric materials are submitted under a strong electric field at high temperatures to align their electric dipoles and increase the converse piezoelectric effect. This process is called poling. Once its Weiss domains aligned, the material keeps these dipoles in place. A higher temperature than their Curie temperature, or very intense electric fields, can skew the Weiss domains or neutralize the electric dipoles, eliminating the poling. The most frequently used piezoelectric materials are piezoceramics, such as Lead zirconate titanate, also called PZT.

The relation between polarization density vs applied electric field and strain vs applied electric field of a ceramic piezoelectric is shown in Figure 2.18. The virgin material is submitted to a external electric field, aligning the dipoles of the ceramic and increasing the polarization density (Virginal curve in Figure 2.18). This causes a strain of the material until a maximum strain is attained (Figure 2.18b) with the maximum polarization density, P_S (Figure 2.18a). If the electric field is reduced, the strain and polarization decreases with different rate than the increasing path (hysteresis in both curves). When the electric field is

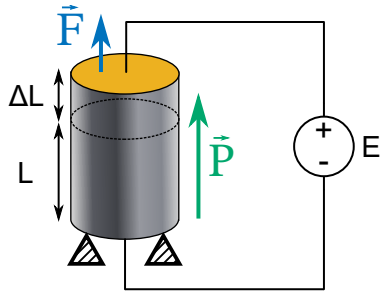

Figure 2.17: Converse or inverse piezoelectric effect.

zero, there is a remanent polarization density (P_r) and strain (S_r) in the material. The electric field can decrease to negative values to reduce the remanent strain. This is the normal working zone of the actuator and a linear model approximation is usually accepted in this zone. Outside this zone, the behavior is strongly non-linear and more complex models need to be used. The electric field needed to return the piezo material to its original length and polarization is noted E_C.

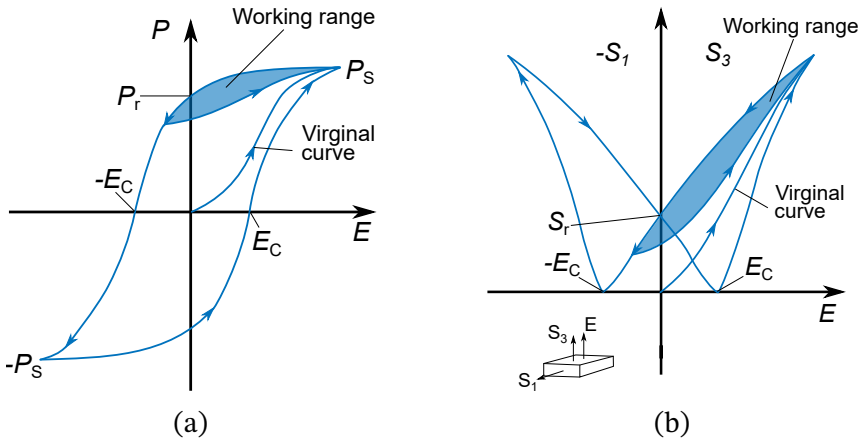

Figure 2.18: Ceramic piezoelectric response to an applied electric field. (a) Polarization of the material. (b) Strain of the material (adapted from [Jan04]).

For the working range presented in Figure 2.18, a linear model can be built for small changes in electric field and strain. The electric part of the model takes the applied electric field $\vec{E}$ and the polarization density $\vec{P}$ to build the electric displacement in a dielectric material $\vec{D} = \epsilon_0\vec{E} + \vec{P} = \epsilon\vec{E}$ (Gauss' law). The mechanical strain S follows Hooke's law $\vec{S} = s\vec{T}$, with s the compliance of the material and T the stress. Both mechanical and electrical models are linked in equations Equation (2.16) [Jan04]:

$$\mathbf{S} = \mathbf{s}^{\mathbf{E}}\mathbf{T} + \mathbf{d}^{\top}\mathbf{E} \tag{2.16}$$

$$\mathbf{D} = \mathbf{dT} + \epsilon^{\mathbf{T}}\mathbf{E} \tag{2.17}$$

With: $\mathbf{d}$ the piezoelectric charge constant that indicates the intensity of the

piezoelectric effect; $\mathbf{d}^\top$ its transpose; $\boldsymbol{\epsilon}^\mathbf{T}$ the dielectric constant for constant T and $\mathbf{s}^\mathbf{E}$ the compliance coefficient for constant E. The entities $\boldsymbol{\epsilon}^\mathbf{T}$ and $\mathbf{s}^\mathbf{E}$ are obtained experimentally for each actuator. This model is linear, does not consider creep, hysteresis nor logarithmic decay in parameters with temperature and age, as real piezoelectrics exhibit [Bor06]. The piezoelectric force scales with a factor of $\propto S^2$ [SYS18].

Piezoelectric actuators are characterized by noticeable exerted forces and high frequencies, but limited strokes. Different principles are then used to maximize their performance in the trade off between force, stroke and frequency (speed) [Bor06]. When using the natural resonance frequency of the actuators to increase the stroke and speed of operation, the actuation system is called resonant or ultrasonic. If the resonance frequency is not used, the system is called non-resonant or quasi-static [Pon05]. Non-resonant piezos can be divided in force-leveraged actuators and frequency-leveraged actuators [Bor06] (frequency in the sense of a series of steps, not resonance frequency). The leverage effect can be gained integrating multiple elementary piezo actuators or by external mechanisms, so another distinction can be made between internally leveraged actuators and externally leveraged actuators [Bor06]. A classification tree of piezoelectric actuators is presented in Figure 2.19 following the review works of [Bor06; Pen+15; LHM19; Tia+20].

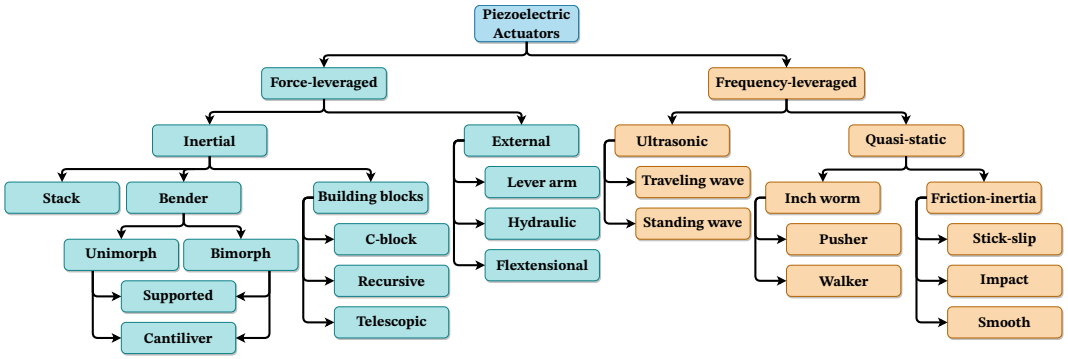

Figure 2.19: Classification tree of piezoelectric actuators following [Bor06; Pen+15; LHM19; Tia+20].

2.1.4.1 Force-leveraged piezo actuators

The most common internally force-leveraged actuators are stack and bender. Stacks apply important forces with micrometer strokes and low frequencies. Benders trade force to have larger strokes (a quadratic function of the length of the actuator). Different configurations of bender actuators are available, such as end supported or cantilever.

The externally force-leveraged actuators can be subdivided as lever arm, hydraulic amplified and flextensional actuators, depending in the mechanism to amplify the actuators stroke [Bor06]. Lever arm actuators amplify the stroke and reduce the generated force with a leverage system (fulcrum and leverage arm). In the hydraulic amplification a piezo actuator moves a piston, which pumps a fluid into another piston of a reduced section. The result is a very high stroke amplification, however, modeling and mechanical problems linked to fluids are present. Flextensional actuators have a flexible component that amplifies the stroke. It differs from the lever arm actuators approach, because of its closed-loop configuration, resulting in a higher stiffness but reduced amplification [Bor06]. Figure 2.20 presents two types of internally force-leveraged actuator (Figure 2.20a, Figure 2.20b) and an externally force-leveraged actuator (Figure 2.20c).

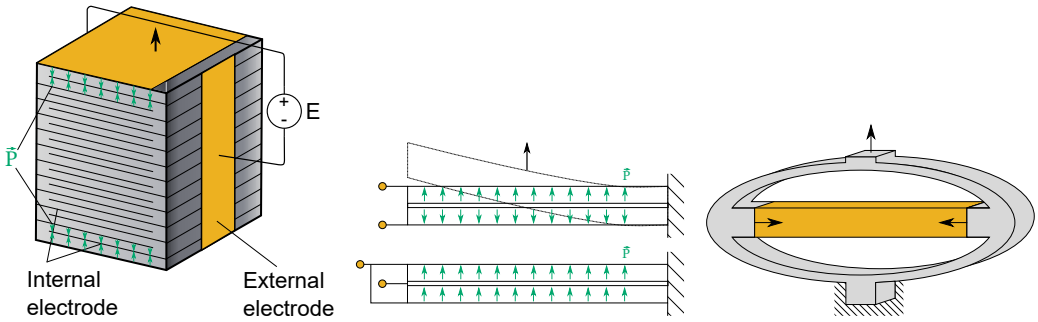

Figure 2.20: Some force-leveraged piezo actuators. (a) Stack. (b) Bender. (c) Stack and flexure amplification mechanism.

The work of [Wan+18a], presented in Section 1.3, used a piezo stack and flexure amplification mechanism for their positioning system (Figure 2.21). The authors compared the influence of an undesirable lateral stress in the classical bridge-type amplifier (BTA), a modified more robust but cumbersome version "compound" bridge-type amplifier (CBTA) and their arch-shape bridge-type amplifier solution (ASBTA) (Figure 2.21a). This lateral stress generates unwanted cross-coupling and damaging shear stress to the piezo actuator. Compared to the robust CBTA solution, their ASBTA was more compact, had similar lateral stiffness and a higher first vibration frequency. One ASBTA per axis, needing 0-100 V, were coupled to a double parallelogram mechanism based in flexure elements as motion stage. The 160 mm × 160 mm × 12 mm positioning system (Figure 2.21b) generated a stroke of 55.4 µm × 53.2 µm with a resolution of 8 nm. The cross-coupling rate were 0.42 and 0.45 % for the x and y-axis, respectively. The settling time was 3.5 s for a 50 V input step. Their FEA model correctly predicted the resonant frequencies of the system, which should be avoided to precisely control the position and cross-coupling of the stage. To improve the

linearity and repeatability, the authors implemented a PID controller to reduce the hysteresis of the piezo actuators. The closed loop system followed sinusoidal, triangular and circular trajectories of amplitude 20 µm with an error of less than 0.6 µm. Finally, a groove scratching application of the stage was tested, achieving multiple 1 µm width groves with 40 nm precision.

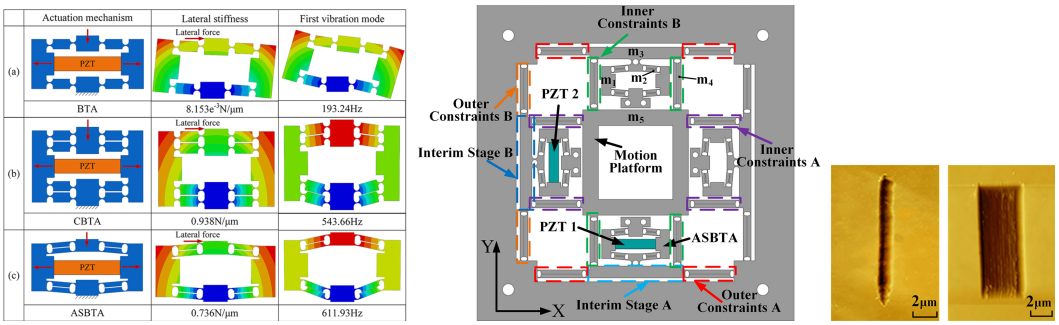

(a) (b) (c)

Figure 2.21: Piezo micro/nanopositioner with flexure compliant structure [Wan+18a]. (a) Flexure amplification mechanisms evaluated. (b) System schema. (c) Microgrooves obtained.

2.1.4.2 Frequency-leveraged piezo actuators

The frequency-leveraged actuators can be divided into ultrasonic (or resonant) actuators and quasi-static actuators. Ultrasonic actuators use high forces to generate mechanical waves as vibrations in a stator and transfer them, through friction, to a moving object, or rotor. They are divided into standing and traveling wave ultrasonic devices, both able to generate linear and rotational motions. The quasi-static actuators use the inchworm, inertia or stick-slip drive to perform displacement steps of the moving part, i.e., they are digital actuators (Figure 2.22).

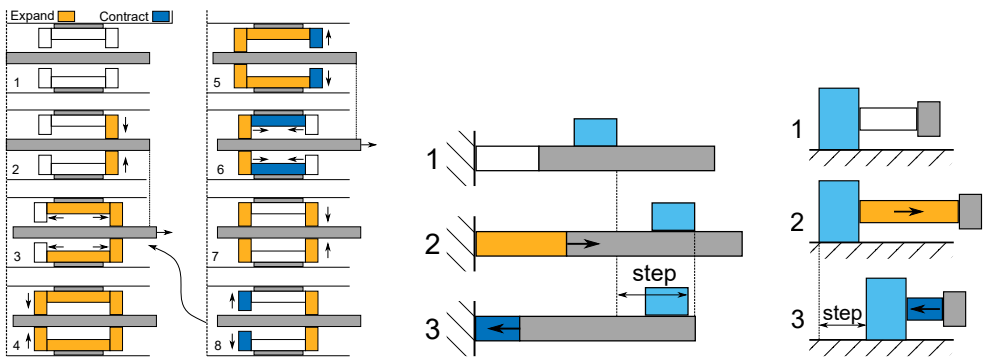

(a) (b) (c)

Figure 2.22: Quasi-static piezo actuators. (a) Inchworm pusher. (b) Friction stick-slip. (c) Inertia smooth.

[Tia+18] presented a 100.6 mm × 74.6 mm × 7 mm four-foot inchworm actuator (Figure 2.23a). Each foot could move in both horizontal and vertical directions generating an elliptical walking movement in 2 DoF (Figure 2.23b). The central piezo and the feet piezo are synchronized to generate the inchworm motion. The system was driven with 100 V sinusoidal signals at 41 Hz, generating steps of 4.4 µm. The system achieved 1641 mm s^{-1} and 1.18 N with 250 V. The speed was linear against input voltage. A perfect synchronization of the feet is needed to actuate optimally, any vibratory or load unbalance will affect the actuation step. A cross-coupling of 5.24% was measured.

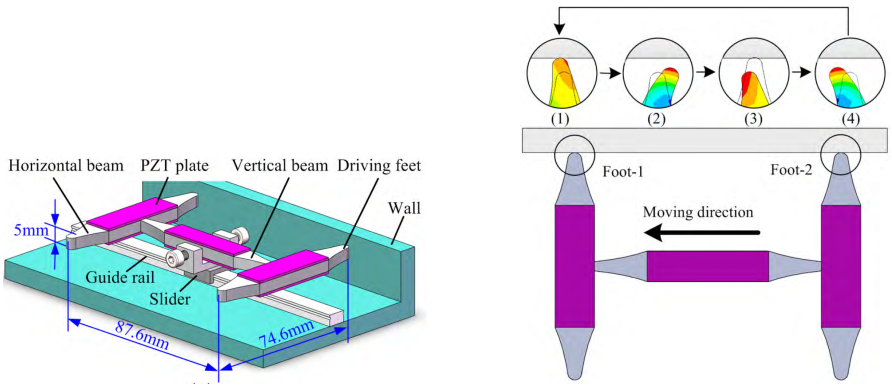

(a) (b)

Figure 2.23: Four feet inchworm by [Tia+18]. (a) System schema. (b) Inchworm motion.

[Wan+18b] presented a 120 mm × 75 mm × 18 mm rotational inchworm based on wedge block clamping (Figure 2.24a). As shown in Figure 2.24b, the piezo pushed the rotor away from a curved surface, allowing an opposite wedge to move by the tension of a spring. The system entered a new equilibrium point between the piezo force and the spring force. Then the piezo was contracted to allow the pushing surface to be displaced by another spring and set a new rotation step. The piezo and flexure mechanism produced up to 7.17 N m. The resolution was 0.567 µrad in a 5° stroke. With a driving signal of 150 V at 1 Hz, the maximum velocity was 511.7 µrad s^{-1}, when the driving signal was 90 V at 128 Hz the velocity was 43.96 mrad s^{-1}. The speed was linear against the input voltage. Frequencies higher than 128 Hz negatively impacted the performance of the actuator.

[RHL09] developed a 2 DoF digital piezo conveyor aimed at moving the end-effectors of a microassembly device (Figure 2.25). The authors deformed a piezo layer in two dimensions with four electrodes (Figure 2.25b). The digital inchworm motion is presented in Figure 2.25a, the actuator was deformed to move the object in a direction by friction (stick) and then quickly restored to the neutral position to slip through the contact base and obtain a displacement

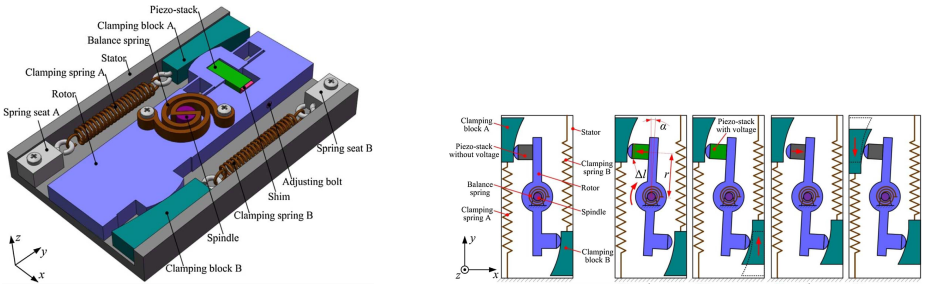

(a) (b)

Figure 2.24: Rotational inchworm by [Wan+18b]. (a) System schema. (b) Inchworm motion.

(slip). They assembled three actuators in a glass bar to form a linear and rotation conveyor (Figure 2.25d). With a 150 V at 500 Hz sawtooth signal they obtained a maximum step of 200 nm. When the voltage decreased to 75 V the step was 70 nm. The step of the system had a constant efficiency of 70% (the ratio between step and applied voltage). Rotational steps of 0.0025° with 150 V, 0.0015° with 100 V, and 0.001° with 75 V were obtained with an uncertainty of 10%. They found a linear relation between speed vs frequency and speed vs voltage amplitude between 35-150 V and up to 10 kHz. The maximal speed was 1.8 mm s^{-1} and 20 ° s^{-1} with 10 kHz and 150 V. The maximal force was 150 mN. An accuracy of 5 nm for a 100 nm reference was measured.

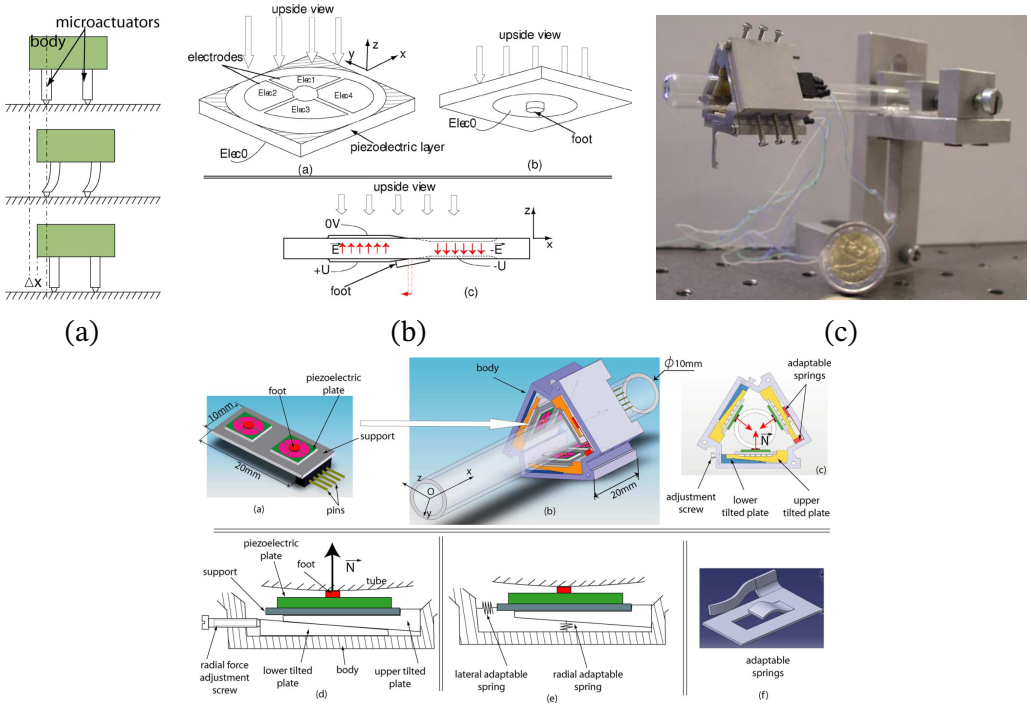

(d)

Figure 2.25: 2 DoF piezo stick-slip inchworm conveyor by [RHL09]. (a) Inchworm schema. (b) 2 DoF piezo actuator. (c) Prototype. (d) Conveyance explanation.

[IM18] presented a microlinear ultrasonic motor aimed at auto-focus systems and small endoscopes (Figure 2.26). The authors added four piezoactuators to a 2.6 mm × 2.6 mm × 2.2 mm phosphor-bronze cuboid to deform its shape in a circular motion using two resonant frequencies of the system. The first resonant frequency produced steps of 32.6 nm and the second resonant frequency 5.5 nm. The speed settling time was 15 ms for a 56 mm s^{-1} reference. The maximum force and velocity were 140 mm s^{-1} and 20 mN, using 150 V at 522 kHz. The motor needed 273 mW, obtaining an efficiency of 0.16%. The minimum operating voltage of the motor was 40 V. A 2 DoF system using the same technique had been demonstrated by [MT09].

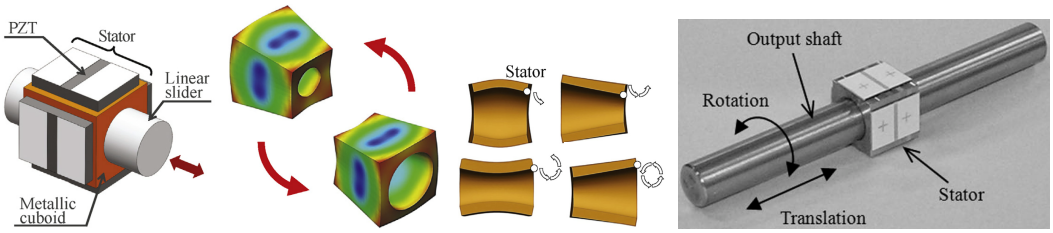

(a) (b) (c) (d)

Figure 2.26: Microlinear ultrasonic motor by [IM18]. (a) Schema. (b) Second resonant mode. (c) Force transmission cycle. (d) 2 DoF concept by [MT09].

[Gab+19] presented a non-contact planar motion stage using langevin piezo actuators. The actuators resonated with a ⌀ 150 mm metallic annulus in a traveling wave motor configuration (Figure 2.27a). The ultrasonic vibrations in the annulus created an air layer with a dynamic acoustic pressure field able to levitate and move a planar object. Three of these acoustic actuators were used to levitate a silicon wafer of ⌀ 300 mm and 128.7 g. The system was controlled with a H_∞ closed loop using three laser sensors, so only reflective objects could be controlled. The system had a working space of ± 5 mm and 90°. The rise time (from 10% to 90%) was 2 s which suggested a bandwidth of 0.175 Hz. The mean position error was 0.4 mm. Disturbances in the object's position are observed in their system. This could be caused by the saturation of the actuators as the controller commands a power above the actuator's working limit.

[FL12; LF13] presented a 3 DoF modular resonant conveyor (Figure 2.28). They used three piezo stack actuators in each axis to generate planar motions. The actuators were coupled to a double parallelogram structure that transferred the vibrations to a hexagonal shape, generating forces in the x and y axes. The system was controlled in closed loop with a computer vision that detected the type, number, position and orientation of the parts on the conveying system. The authors did not mention trajectory control. The conveyor generated accelerations of 40 m s^{-2} in the xy plane. Speeds of 83 mm s^{-1} were measured. A maximum po-

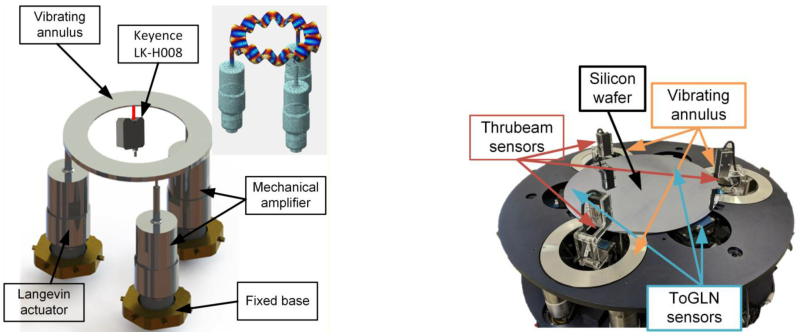

(a) (b)

Figure 2.27: Ultrasonic planar motion stage by [Gab+19]. (a) Langevin actuators forming a vibration annulus. (b) Three annulus forming the planar motion stage.

sition deviation of ± 0.3 mm and an orientation deviation of 30° were measured.

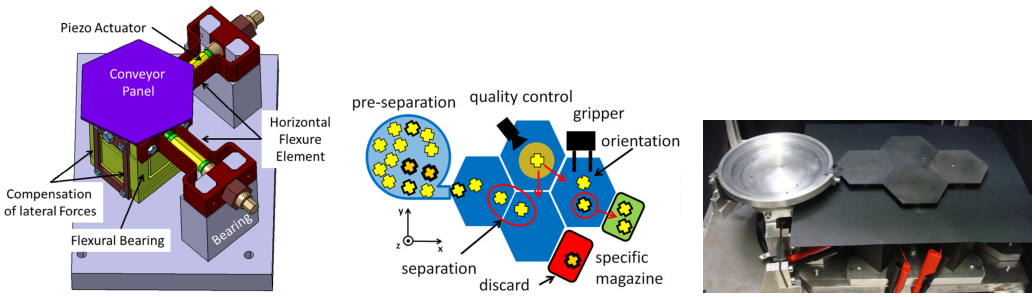

(a) (b) (c)

Figure 2.28: Modular resonant conveyor by [FL12; LF13]. (a) Module schema. (b) Conveyor schema. (c) Prototype.

[FAO12] developed two hybrid piezo and electromagnetic inchworm smart conveyors (Figure 2.29). Both systems had two U-shaped electromagnets that acted as fixing actuators (or locks) with a ferromagnetic surface. The four piezo actuators executed steps in 3 DoF in synchrony with the electromagnetic actuation. Each leg had springs to smooth the operation of the system. The difference between the two solutions were their joints between sections to allow the planar movement. The “C” type was slower, more compact and precise (35 mm × 35 mm × 25 mm, 10 nm position resolution). The “G” type was larger, less precise but faster (50 mm × 50 mm × 25 mm, 2.7 times faster than C type). Both systems required 100 V to operate. The maximum speed for the G type without slip was 20.1 mm s^{-1}. If the frequency of the driving signal surpassed 180 Hz (the fixing time of the electromagnets), a slip appeared. This increased the speed to almost 50 mm s^{-1} at 500 Hz but decreased the precision. The position repeatability varied with the speed of the system with a maximum standard deviation of 2% of the wished position without slip. Then the precision kept 4%

until 400 Hz. The G type could carry a 140 g load and, in open loop, achieved a repeatability of 3%. The step size was around 100 µm before slide, decreasing quadratically against frequency until 400 Hz. The research team designed a second generation system with the same principle in [Sho+16]. This time an octagon of 100 g, 86 mm × 86 mm × 11 mm with three electromagnets and six piezos was developed (Figure 2.29b). The step size was 62 µm at 120 V with a resolution of 10 nm, precision of 1% and a maximum speed of 5 mm s^{-1} all until 100 Hz. The carried load was 150 g.

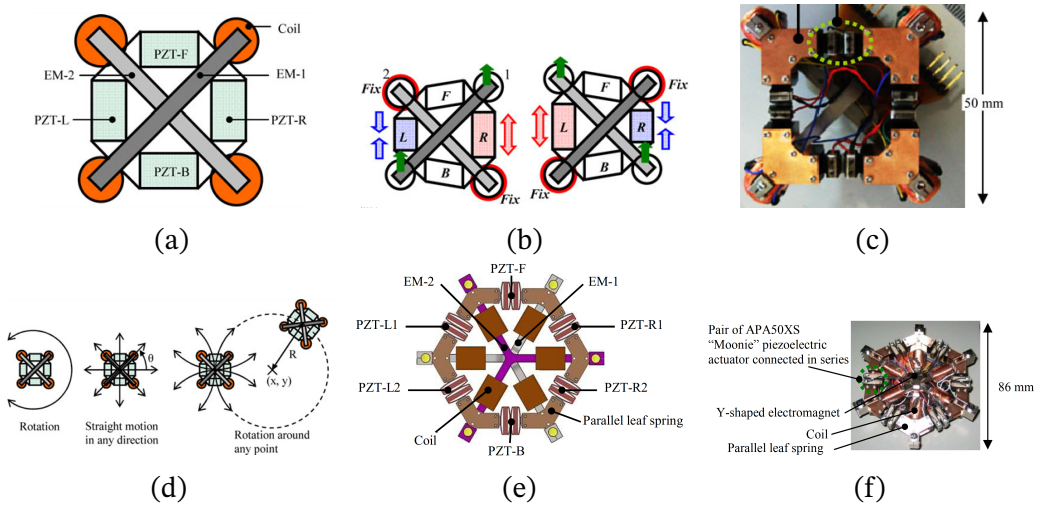

Figure 2.29: Piezo and electromagnetic inchworm conveyor by [FAO12; Sho+16]. (a) 1st gen. schema. (b) Inchworm motion. (c) 1st gen. prototype. (d) 3 DoF of the conveyor. (e) 2nd gen. schema. (f) 2nd gen. prototype.

2.1.5 Pneumatic actuators

Pneumatic actuators are a type of fluid-based actuators that use gases (most commonly compressed air), as medium to generate a force through a difference in pressure. The physical phenomena involving fluids, their flow due to pressure differences and the transmitted forces are described by the Navier-Stokes equations. Considering that the density of the flowing fluid involved is constant, that the internal forces of the fluid are independent of temperature and that the fluid is incompressible, these equations take the form [ŁK16]:

$$\frac{\partial \vec{u}}{\partial t} - \frac{\mu}{\rho}\nabla^2\vec{u} + (\vec{u}\cdot\nabla)\vec{u} + \frac{1}{\rho}\nabla p = \vec{f} \tag{2.18}$$

$$\nabla\cdot\vec{u} = 0 \tag{2.19}$$

With $\vec{u}$ the flow velocity, ρ the fluid density, μ the fluid dynamic viscosity, p the pressure and $\vec{f}$ the external forces. Each application of pneumatic actuation solves these complex equations by simplifications, assumptions and approximations depending on the geometry and working conditions of the system. In the context of conveyance devices, pneumatic conveyors use compressed air injected onto the conveyed object trough well-defined holes, called nozzles. The injected air collides with the conveyed object or creates a pressure field that lifts and/or displaces the object around the nozzle-equipped area. A proper control of the active nozzles and the air pressure injected by each one produces the control forces of the conveyor. This conveyance solution offers non-contact, non-magnetic actuation and fast conveyance speeds thanks to high air pressures, but does not have an intrinsic holding function, the modeling of the system is complex and the energy consumption is higher than other solutions. The fluid forces scale with a factor $\propto S^2$ [GC15].

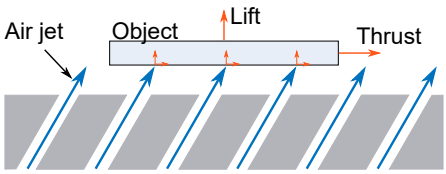

Figure 2.30: Inclined air-jets pneumatic conveyor (adapted from [ZEN16]).

[Yah+12; Lau+14] developed a modular microfabricated tilted air jet conveyor (Figure 2.31). Each module could generate four directional air jets named north, south, west and east, thanks to four nozzles. All directional nozzles were connected in series to generate the same direction, e.g., all north nozzles were connected to the same air-pressure source. The authors built a 8×8 array with dimensions of $8.9\,\text{mm} \times 8.9\,\text{mm}$. An object of ⌀3 mm and weighing 2 mg was conveyed using 20 kPa air pressure. Then, the authors used a ⌀5 mm, 19.43 mg object for the positioning and speed trials. The paths generated by a step response in pressure had a significant deviation, explained by the authors as a dependency in the air jet angle on the position of the array. This was because the serial connection of the pressure circuit. The maximal speed was $140\,\text{mm}\,\text{s}^{-1}$. The minimal step (resolution) was 0.3 µm with a pressure pulse duration of 5 ms. However, the standard deviation of the steps were around 15% of the step size. The authors characterized the step size vs pulse duration relation of the system and used it as model-based controller in closed loop. The sensor was a camera on top of the system. When in closed loop, the system reached a positioning repeatability of 17.7 µm.

[Gue+17] designed a modular pneumatic conveyor based on $75\,\text{mm} \times 75\,\text{mm}$ unidirectional 3D printed blocks (Figure 2.32). Each block upper surface con-

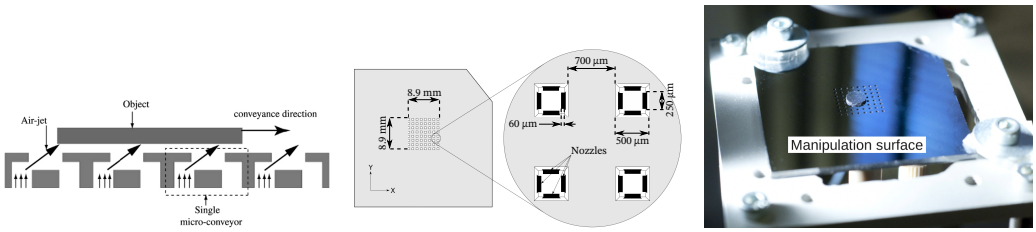

(a) (b) (c)

Figure 2.31: Modular pneumatic microconveyor by [Lau+14; Yah+12]. (a) Array principle. (b) Array schema. (c) Microprototype.

tained an array of 128 tilted holes (45°) with the same angular orientation (Figure 2.32b). The idea was to reduce a conveyance need to a block arrangement problem that could be solved as a topology optimization problem of the blocks. This topology optimization relied on a physical model of the pneumatic block. The physical model achieved a mean relative prediction error of 3.5% of the displacement value in a linear movement and 5.7% in a circular movement. The authors conveyed ⌀150 mm glass wafers for their tests. The maximum speed was $0.3\,\mathrm{m\,s^{-1}}$. The conveyance surface was 675 mm × 1275 mm.

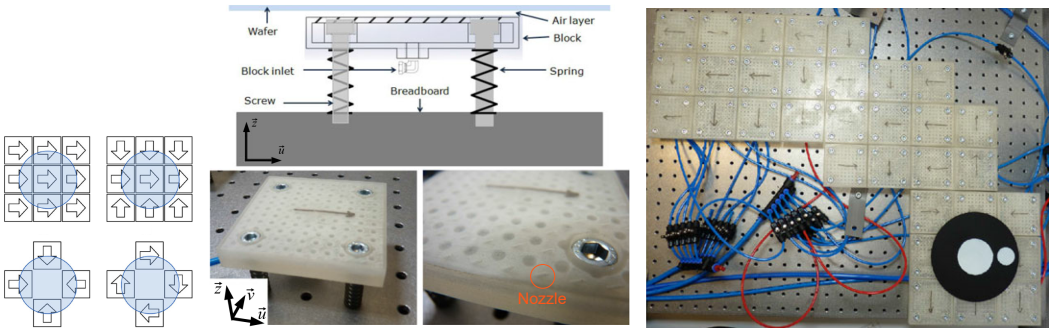

(a) (b) (c)

Figure 2.32: Modular pneumatic microconveyor by [Gue+17]. (a) Array configurations for simple, guided, centering and rotation motions. (b) Module prototype and schema. (d) Prototype.

[FNU18] proposed a pneumatic conveyance method by switching positive and negative pressure air flow in the nozzles (Figure 2.33). The advantages of this method were a constant speed of the carried object, the discharged compressed air could be recovered, consuming less air, and the air pressure did not accumulate in the center portion of the carried object preventing bending. The disadvantage was that a position measurement of the object was needed to control the positive/negative pressures of the corresponding nozzles (Figure 2.33b). The authors built a 750 mm × 170 mm, 0.3 MPa pneumatic conveyor, using a 90 mm × 100 mm × 2 mm, 139 g metallic plate as object. As the object was metallic, they implemented Eddy current and photo sensors to measure the object's

position. The system attained speeds of 70 mm s^{-1}. The authors did not measure the step size, repeatability nor accuracy.

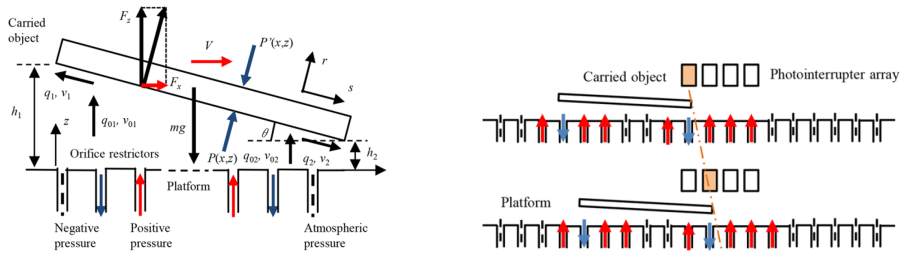

(a) (b)

Figure 2.33: Pneumatic conveyor by [FNU18]. (a) Pneumatic actuator array. (b) A pneumatic soft actuator. (c) Conveyor prototype.

[Che+18; LCZ20] presented a 228 mm × 204 mm modular air conveyor based on 128 actuating cells (Figure 2.34). Each 10 mm × 10 mm cell had two pairs of inlet/outlet nozzles to the air to flow thanks to positive and negative pressure, respectively. These pressures form an horizontal flow which generates a viscous force at the boundary with the carried object (Figure 2.34c). The entering air flow also generates the lifting force to the object. The object was a plate of ⌀80 mm, 16.9 g. The maximum speed was 80.1 mm s^{-1} using 16 L min^{-1}. An H_∞ controller achieved a position error of 0.2 mm, independently of the mass of the conveyed object. A PID controller achieved rise time of 3.6 s.

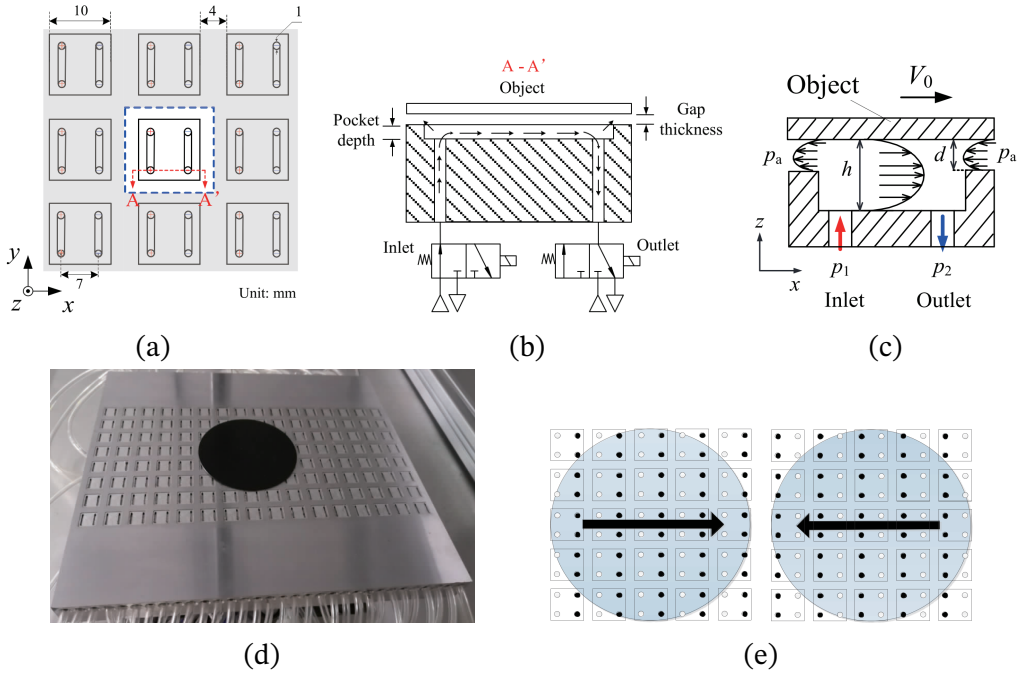

(a) (b) (c)

(d) (e)

Figure 2.34: Pneumatic microconveyor by [LCZ20]. (a) Pneumatic cell array. (b) A pneumatic cell schema. (c) Working principle. (d) Conveyor prototype. (e) Two direction control example.

Pneumatic soft actuators

Pneumatic pressure can be used to actuate a system by deforming an elastic material. The material contacts the movable part, transferring the force of the fluid. Once the desired deformation of the actuator is reached (determined by the deformability of the actuator) the pneumatic pressure can be turned off and the actuator will return to a default position given by the elastic forces of the material. This forms a type 3 digital actuator. This kind of pneumatic actuators using elastic materials and hollow deformable structures are called soft actuators.

[DSX16] designed a modular soft table conveyor based on 3D printed pneumatic soft actuators (Figure 2.35). The prototype was an array of 5×5 actuators. The system carried a smartphone for 21 mm in 40 s (average speed of 0.525 mm s^{-1}) using 17 kPa. The displacement step varied between 1-1.3 mm. The rotation speed was 1 ° s^{-1}. The out-of-plane displacement was 4 mm. A design constrain is that the smallest transportable object must be twice the size of the actuator.

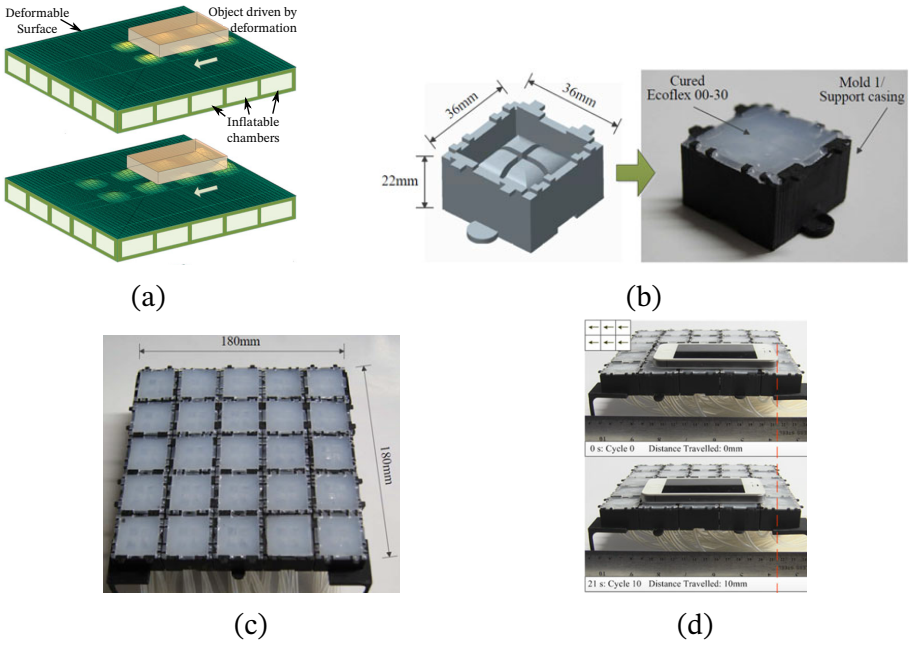

Figure 2.35: Modular pneumatic soft actuator conveyor by [DSX16]. (a) Array principle. (b) Module prototype. (c) Array prototype. (d) Conveyance test.

[WT18] presented a flexible sheet actuator that generated bidirectional traveling waves by pneumatics (Figure 2.36). The actuator used inflatable chambers in a sheet to produce a traveling wave in the sheet, thus, conveying an object in 2D (Figure 2.36a). The prototype had a surface of 180 mm × 180 mm, used 100 kPa at 0.5 Hz. The prototype carried a 200 g object with speeds of 2.5 mm s^{-1} (2D) up to 4 mm s (1D). But a more radical usage with 100 kPa at 3.3 Hz yielded speeds of 28.6 mm s^{-1} in a exclusively 1D prototype. The position precision was

not studied.

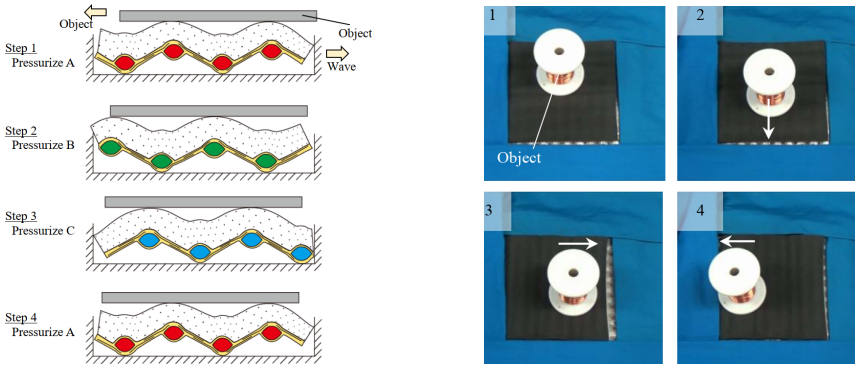

(a) (b)

Figure 2.36: Pneumatic traveling wave conveyor by [WT18]. (a) Array principle. (b) Conveyance test.

[Rob+19] used 16 one DoF soft pneumatic actuators arranged in a 4×4 array to obtain a 16 DoF object manipulator surface (Figure 2.37). The system had an area of 110 mm × 93 mm. Each soft actuator had a sensor for a closed loop control and used a maximum 30 kPa. This pressure generated actuator deformations of 1 cm and forces of 2.3 N. The authors validated multiple applications of the system as force modulator and haptic device. In the object manipulation application, the average linear velocity of a ball-shaped object was 27.5 cm s^{-1}, while for a "large, heavy, rectangular" object it was 0.7 cm s^{-1}.

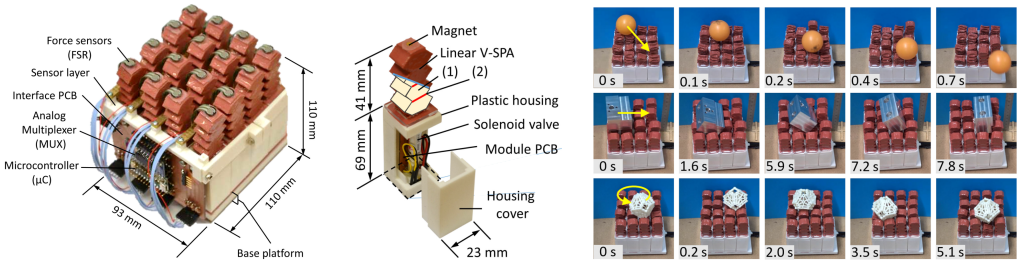

(a) (b) (c)

Figure 2.37: Pneumatic soft-actuator conveyor by [Rob+19]. (a) Pneumatic actuator array. (b) A pneumatic soft actuator. (c) Conveyor prototype.

2.1.6 Electromagnetic actuators

Electromagnetic actuators exploit the interaction between moving charged particles and magnetic fields that produces a force on the particle. This fundamental electromagnetic force follows the empirical Coulomb-Lorentz's equation [Fur01]:

$$\vec{F} = q(\vec{E} + \vec{v} \times \vec{B}) \tag{2.20}$$

with q the charge of the studied particle, E electric field intensity, v the velocity of the particle and B magnetic flux density. Equation (2.20) can be generalized for thin wires of length l carrying an electrical current I (Equation (2.21)):

$$\vec{F} = I \int_{wire} \mathrm{d}\vec{l} \times \vec{B}_{\text{ext}} \tag{2.21}$$

The electromagnetic force depends then on the entities $\vec{E}$ and $\vec{B}$. These entities arise from electromagnetic field and waves that are modeled by the Maxwell equations, presented here in differential form [Fur01]:

$$\nabla \times \vec{H} = \vec{J} + \frac{\partial \vec{D}}{\partial t} \qquad \nabla \cdot \vec{B} = 0 \tag{2.22}$$

$$\nabla \cdot \vec{D} = \rho \qquad \nabla \times \vec{E} = -\frac{\partial \vec{B}}{\partial t} \tag{2.23}$$

With E electric field intensity (V/m), D electric flux density (C/m^2), H magnetic field intensity (A/m) and B magnetic flux density (T). J, the free electric current density (A/m^2) and ρ, the free charge density (C/m^3), are the sources of the fields. The constituent equations of the Maxwell theory are:

$$\vec{B} = \mu_0(\vec{H} + \vec{M}) \tag{2.24}$$

$$\vec{D} = \epsilon_0(\vec{E} + \vec{P}) \tag{2.25}$$

Where M is the magnetization vector accounting for the density of magnetic dipole moment in the material studied (A/m) and P the polarization density vector accounting for the density of electric dipole moment in the material (V/m).

Equations (2.22) to (2.25) model the behavior of electromagnetic waves and fields generated by electric charges, currents and magnetic dipoles and thus model the magnetic field generated by currents and permanent magnets. The equations also describe the interaction between permanent magnets, permanent magnets and electric currents and electric currents. All those cases are the interactions exploited by electromagnetic actuators, and thus, the Maxwell equation and the Lorentz force represent the standard model for these devices. A general schema for a linear electromagnetic actuator is presented in Figure 2.38. A current-carrying wire (I) immersed in a perpendicular magnetic field B suffers an induced electromagnetic force F_{em} that causes the wire to move with a speed u, following Equation (2.21).

[Pir+13] developed a modular reconfigurable planar electromagnetic microconveyor (Figure 2.39). The idea was to insert the planar conveying actuators

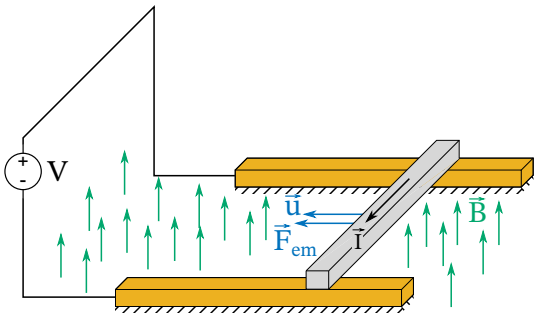

Figure 2.38: A linear electromagnetic actuator schema (adapted from [Bor08]).

in a 1 cm^3 block (Figure 2.39a). The authors used electro-permanent magnets to design a linear motor able to slide the blocks on an arrangement of the same blocks and change the topology of the block distribution, thus, the conveyor (Figure 2.39b). Using the electro-permanent magnets, a strong connection without any power consumption is achieved between the blocks. This means that after the system had formed its optimal configuration it could perform its conveying function using no other resources for the linkage. The authors also proposed a reconfiguration algorithm to form any 2D shape required for the conveyor. The electro-permanent magnet was a coil with an AlNiCo core which could be magnetized to attract or repulse other coils with an injected current, making it a bistable system. The linear motor used the mover block as rotor and the static blocks (forming the conveyor) as stator. The rotor was composed of two cylindrical 1 mm × 1 mm neodymium magnets. The stator part consisted of three ⌀2 mm × 3 mm electro-permanent magnets per block. The maximum speed of the sliding block was 16.4 mm s^{-1}. The holding force of the electro-permanent magnets saturated to 45 mN for a 16 V, 25 µs pulse. The energy consumption was 13 mJ for the magnetic circuit, meaning an efficiency of 7.8 mJ mm^{-1}. The authors developed and simulated the reconfiguration algorithms to achieve an objective topology from different starting states. The reconfiguration time depended strongly on the difference between the goal and starting state of the conveyor.

[Xu+19b; Xu+19a] presented a 6 DoF magnetic levitated (maglev) positioning system using four linear maglev actuators (Figure 2.40). Each actuator was a side of a square. Each actuator used a Halback permanent magnet array and a pair of driving coils to generate the levitating and driving Lorentz forces (Figure 2.40a). The minimum steps of the system were 3 µm for the xy plane, 1 µm for the z axis and 50 µrad for the rotation around the axes. The root-mean-square (RMS) errors of translation in the x, y and z axes were 1.36 µm, 1.08 µm and 0.64 µm respectively. The RMS error of rotation around these axes were 20.45 µrad, 21.63 µrad and 9.29 µrad. The workspace of the positioner was 20 mm × 20 mm × 4 mm

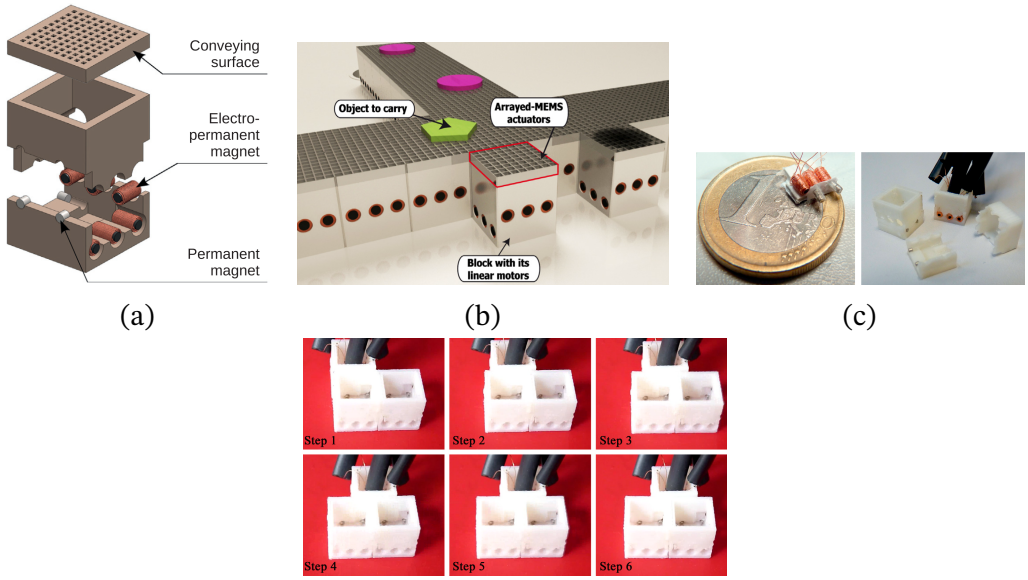

(a) (b) (c)

(d)

Figure 2.39: Modular electromagnetic microconveyor by [Pir+13] (a) Working schema. (b) Prototype. (c) Displacement results.

and could rotate in a range of 0.05 rad × 0.05 rad × 0.2 rad. The system took 0.5 s to adjust to a 2 kg sudden load with a PID controller. A maximum trajectory error, evaluated ina circular trajectory, of 1.8% of the circle radius was reported.

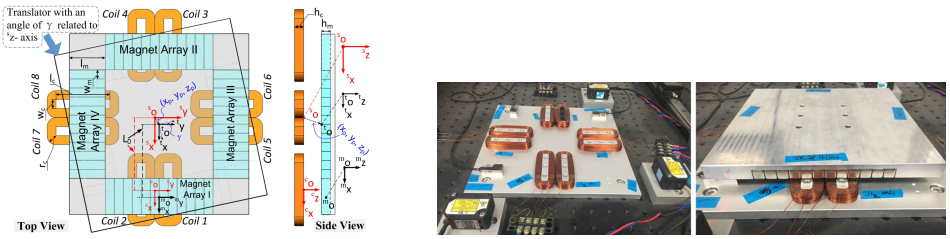

(a) (b)

Figure 2.40: 6 DoF electromagnetic positioner by [Xu+19b; Xu+19a] (a) Working schema. (b) Prototype.

[LSK19] built a 6-DoF magnetic levitation (maglev) system, based on four Lorentz repulsive levitation actuators using two driving coils each (Figure 2.41). All actuators had an air-core coil dedicated to levitate the mover. Two of the four had another air-core coil at 90° from the levitating coil to drive the mover in the x direction. The other two actuators were identical but directed in the y direction (Figure 2.41a). The position measurement of the mover was done by four eddy-current sensors and four laser sensors, fixed to the stator. The prototype had a 50 mm × 50 mm × 2 mm travel range. The mover had four 20 mm × 20 mm × 20 mm NdFeB permanent magnets and weighted 468 g. Using a PID controller, the system had a settling time in the x and y directions of

310 ms and 282 ms in the z direction, without overshoot nor steady state error. A current of 2.8 A is needed for stable levitation, i.e. a power need of 62.7 W. The position noise in the z-axis had a standard deviation of 8 µm, whereas the position noises in the x and y axes had a standard deviation of 176 µm. Releasing a sudden load of 100 g on the system, the controller took 133 ms to adjust. The maximum trajectory error in a circular motion was 189 µm.

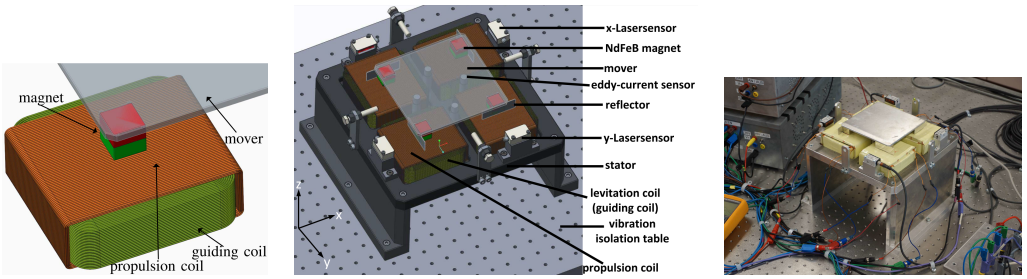

(a) (b) (c)

Figure 2.41: 6 DoF electromagnetic positioner by [LSK19] (a) Single levitation actuator. (b) Positioner schema. (c) Prototype.

[ZTP19] built a 6+2 DoF magnetically levitated parallel actuated dual-stage (maglev-PAD) positioner (Figure 2.42). This dual-stage motion system consisted of a 6 DOF maglev primary stage for coarse positioning and a 2 DOF planar motion flexure-based secondary stage for fine positioning. The coarse-fine positioning was realized through a parallel actuation concept (Figure 2.42a). The coarse stage used four Halbach permanent magnet arrangements and four driving coils generating levitating and driving Lorentz forces. The fine stage was serially connected to the primary stage by a flexure-based structure and used another set of permanent magnets and four coils (Lorentz force) to adjust the position of the end-effector in the xy plane. The authors tested a reference ⌀1 mm circular trajectory obtaining a position root-mean-square (RMS) error of 32 µm for the primary stage and 5 µm for the secondary stage. For a 2 mm linear motion, the RMS errors in the x, y and z directions were less than 1 µm. The minimum step of the primary stage was found at 500 nm with an error of 1 µm, thus the secondary stage compensated this with a 150 nm step with a 75 nm RMS error.

[Aro+19] developed an 3 DoF analog electromagnetic microconveyor based on the Lorentz force principle. The conveyor used a 150 mm × 150 mm stator with a 5 × 5 matrix of two driving coils (one for each actuation direction). The mover was composed of a cross-shaped platform with two permanent magnet arrangements per actuation direction. The interaction between the permanent magnets and the driving coils generated the 3 DoF movements of the mover. The mover had a size of 68 mm × 68 mm × 0.5 mm and a mass of 3.6 g. A glass layer separated the stator from the mover. The repeatability for a 69.48 mm dis-

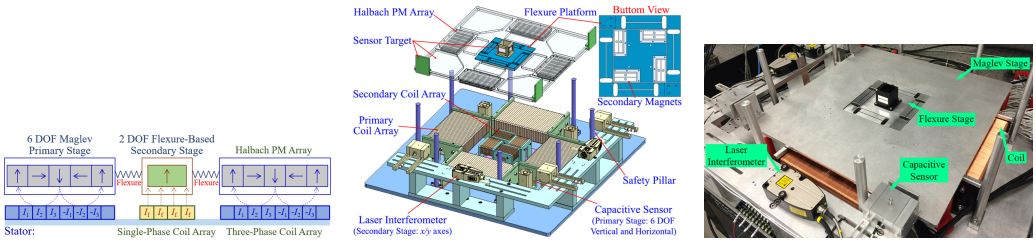

(a) (b) (c)

Figure 2.42: 6 DoF electromagnetic positioner by [ZTP19] (a) Working schema. (b) System architecture. (c) Prototype.

placement was 6.8 µm with an straightness error of 65.0 ± 3.7 µm. To reduce the straightness error, the authors used both driving coils to produce driving and holding forces, reducing the straightness error to 7.53 µm with 0.1 A. This increased energy consumption. The maximum speed was 12 mm s^{-1}. A hysteresis of 0.25 mm was observed for a forward-backward movement. An average maximum rotation angle of 12.4° was measured.

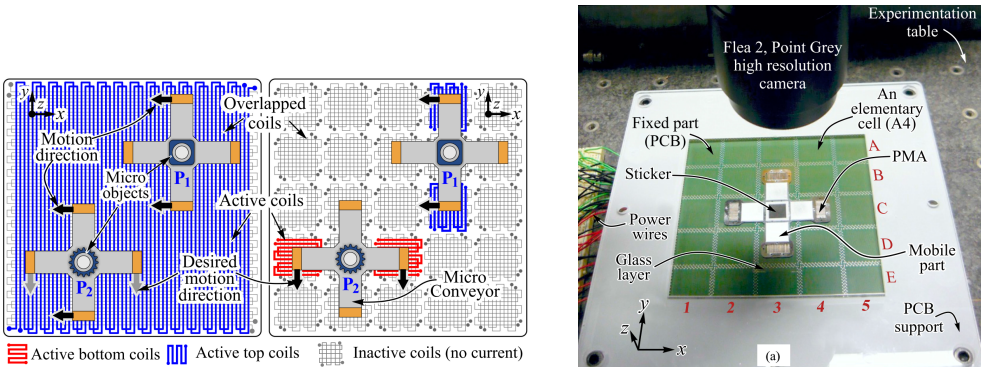

(a) (b)

Figure 2.43: Electromagnetic microconveyor by [Aro+19] (a) Working schema. (b) Prototype.

Meissner–Ochsenfeld effect applications

The Meissner–Ochsenfeld effect is the exponential expulsion of a magnetic field from a “type I” superconductor boundary towards its interior when it is cooled below its critical superconductive temperature (“type II” superconductors or high temperature superconductors are presented afterwards). The theory that explains the Meissner effect is incomplete, as there is only a phenomenological explanation based on the London equation, a fundamental part of the Bardeen–Cooper–Schrieffer theory. There is not a scientific-method proven hypothesis of the governing quantum phenomena [Hir12]. The London equation originates from the idea that a superconductor’s electron would accelerate constantly under an electric

field $\vec{E}$, as there is no resistance [Tin96]. This yields London's first equation:

$$\frac{\partial \vec{J}}{\partial t} = \frac{n_s e^2}{m}\vec{E} \tag{2.26}$$

With e the charge of the electron, m the mass of the electron and n_s the number of electrons in the superconductor. Applying the curl operator at both sides of Equation (2.26), together with Maxwell's equation $\nabla \times \vec{E} = -\frac{\partial \vec{B}}{\partial t}$ and knowing that the $\nabla\times$ and $\frac{\partial}{\partial t}$ are linear operators, we obtain:

$$\frac{\partial}{\partial t}\left(\nabla \times \vec{J} + \frac{n_s e^2}{m}\vec{B}\right) = 0 \tag{2.27}$$

So

$$\nabla \times \vec{J} = -\frac{n_s e^2}{m}\vec{B} \tag{2.28}$$

Which is London's second equation. Finally, taking the curl operator from both sides of Maxwell's equation $\nabla \times \vec{B} = \mu_0 \vec{J}$ and substituting Equation (2.28), we obtain the Helmholtz form of the London's equation which describes the Meissner effect:

$$\nabla^2 \vec{B} = \frac{\mu_0 n_s e^2}{m}\vec{B} \Rightarrow \lambda = \sqrt{\frac{m}{\mu_0 n_s e^2}} \Rightarrow \nabla^2 \vec{B} = \frac{1}{\lambda^2}\vec{B} \tag{2.29}$$

With λ the characteristic length scale over which external magnetic and electric fields are exponentially suppressed inside the superconductor. λ is called the London penetration depth and changes for each superconductor (typical values vary from 15 to 110 nm [Kit04]). As shown in Figure 2.44, an external applied magnetic field $\vec{B}_a$ on a superconductor induce circulating currents that oppose the buildup of magnetic field in the conductor (Lenz's law). In a solid material, this is called diamagnetism, and a perfect conductor (superconductor) behaves like a perfect diamagnet. The induced currents meet no resistance, so they persist in whatever magnitude necessary to cancel the external field. The interaction between the applied external magnetic field and the opposing magnetic field creates the repealing force used by the Meisnner effect devices. The induced currents adapt to changes of the external magnetic field to preserve the equilibrium, e.g., the mass of the conveyed object, or the distance of the external field magnet, making it an intrinsic control system. Nevertheless, this phenomenon has a limit: the Meissner state breaks down when the applied magnetic field is too strong or the temperature increases above the critical superconducting threshold [The18]. The highest critical temperature of type I superconductors is 23.2 K for Nb_3Ge [Roh94]. The Meissner effect has a scaling factor of S^2 [KKF90].

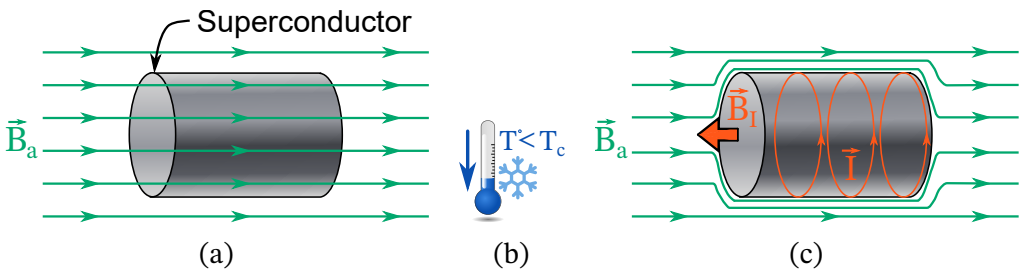

Figure 2.44: Meissner effect on type I superconductors. (a) external magnetic flux density $\vec{B_a}$. T_c (b) Cooling below T_c. (c) Supercurrent generated field.

Type II or High critical temperature superconductors The type II superconductors (type II SC) have higher critical temperatures T_c than type I superconductors. The T_c of a type II superconductor ranges from 30 to 125 K [Roh94]. This is important as they expand the applicability of this technology because it can be cooled with liquid nitrogen (boiling point 77 K) instead of liquid helium (boiling point 4.25 K). Type II SC also present the Meissner effect, but differently. Type II SC allow the penetration of the external magnetic field through fine volumes of the SC acting as normal conductors. The volumes, called cores, are contoured by super-currents, or current vortex, that limit the penetration only to those volumes and expel the magnetic field from the rest of the superconductor, as shown in Figure 2.45. Type II SC behave as type I below a certain temperature and low external field. Then they enter their vortex state above the T_c of any type I SC and keep the Meissner effect. As their critical temperatures are approached, the normal cores are more closely packed and eventually overlap as the superconducting state is lost. When in the vortex state, type II SC try to preserve the configuration of the penetrating magnetic field, creating a "pinning" force that holds the source of the external field in its position relative to the SC.

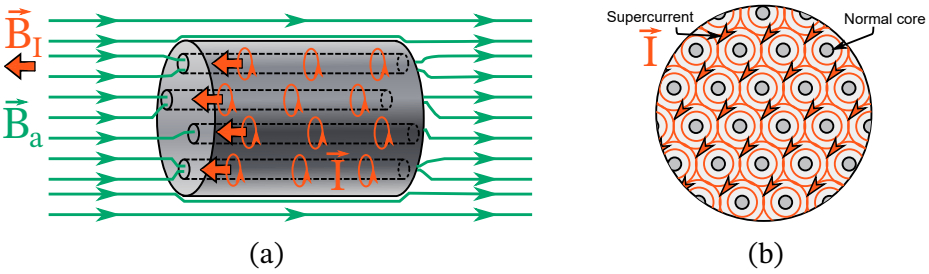

Figure 2.45: Meissner effect on type II superconductors. (a) The external field penetrates along a number of conducting volumes. (b) Vortex super-currents contouring the volumes.

Meissner effect conveyors

Some electromagnetic systems use the Meissner–Ochsenfeld effect to levitate a conveyed object on its active area and avoid friction phenomena (contactless actuation). The Meissner effect intrinsically maintain the equilibrium levitation and thus the levitation control is simplified. This contrast with the complex control needed for Lorentz force levitation, where high currents are needed to obtain a stable levitation. The Meissner effect devices need very low working temperatures, even if they use type II SC such as $YBa_2Cu_3O_{7-x}$ ($T_c = 92\,K$) or $GdBa_2Cu_3O_{7-x}$ ($T_c = 95\,K$). This restriction can be used in its advantage if applied under cryogenic, vacuum or clean environments as these environments tend to already have refrigeration units.

In [KKF89], the authors developed a microconveyor using only the Meissner effect as levitation and driving force (Figure 2.46). The slider was a 84 mg, 2 mm × 2 mm permanent magnet. The driving force is obtained by controlling the superconducting state by temperature or injected current. The active area was 5 cm^2. The conveyor obtained levitation forces of 0.82 mN and driving forces of 0.3 mN. The current to switch between normal and superconducting states of the stator affected multiple superconductors at a time due to the electromagnetic field of the current, affecting the conveyance control. For this reason, the same authors changed to a Lorentz force conveyance drive coupled with a Meissner levitation in [KKF90]. This time, the permanent magnet slider had 9 mg, 1 mm × 4 mm reaching speeds of 7.17 mm s^{-1}, needing 176 mW at 0.4 A. They could levitate a 200 mg object but could not convey it with the Lorentz force without breaking the superconducting state of the stator. They state that the Meissner effect driving force was about 1/10 of the levitation force. The principal problem was the observed hysteresis on both the levitation height and the conveyance direction. Figure 2.46 shows the principle of the proposed Meissner effect conveyor.

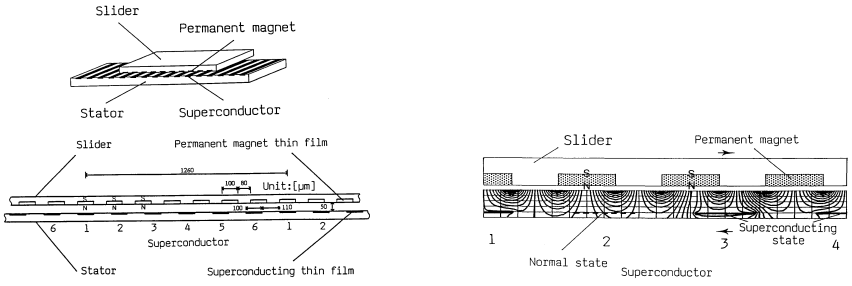

(a) (b)

Figure 2.46: Meissner effect microconveyor by [KKF89]. (a) Conveyor scheme. (b) magnetic flux density lines explaining the slider levitation.

The work of [Iiz+94] used the pinning force of the type II SC to have a more stable levitation of the object in their microconveyor (Figure 2.47). This pinning force added a drag force to the conveyed object. They used Lorentz force to drive the object, installing two layers of coils on top of the superconductors, one for xy displacements and another for rotations. The displacement could be analog/continuous or step by step digital (45° or 320 µm per step) depending on the control of the Lorentz currents. The system presented hysteresis due to the non-linear nature of the pinning effect. The system, in a vacuum environment, conveyed a 9 mg, 3 mm × 3 mm slider up to 9 mm s^{-1} and 3.5 rpm using 5.85 W at 0.5 A.

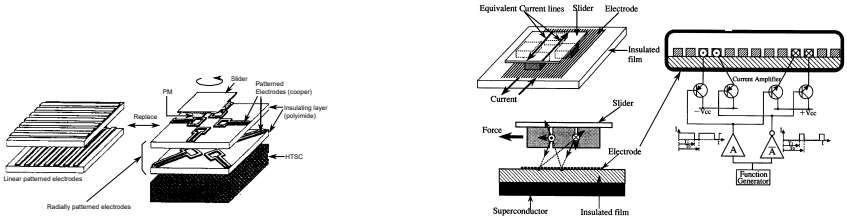

(a) (b)

Figure 2.47: Micromotion stage by [Iiz+94; IF97]. (a) Conveyor scheme with interchangeable Lorentz force layers for $x - y$ displacement or θ rotation. (b) Lineal electrode schema.

In their subsequent work [IF97], the authors improved the fabrication of the linear electrode patter and implemented a two-level control circuit for the displacement of the slider. The system improved its step accuracy (100 µm accuracy) and executed microsteps (40 µm accuracy) reaching a speed of 28 µm s^{-1} for a 38 mg slider.

[ISF09] implemented the Meissner levitation effect with Lorentz driving forces (Figure 2.48). The authors used magneto-impedance sensors between a 380 mg slider and the electrodes to control the position of the slider in closed loop. They used the $GdBa_2Cu_3O_{7-x}$ superconductor as it has a higher critical current value than $YBa_2Cu_3O_{7-x}$ (110 kA cm^{-2} against 513 A cm^{-2}) as well as a higher critical temperature (95 K against 92 K). The control loop needed a parameter identification study to determine the magnetic flux that effectively changed the output voltage of the sensors under such low temperatures. The system achieved speeds of 104 mm s^{-1} in open loop and a position accuracy of 100 µm.

[KSO16] presented a conveyor system based in a GdBCO[2] (type II SC) mover and an array of coils and permanent magnets as the stator (Figure 2.49a). The coils were used to control the rotation and translation of the mover and the

[2]This formula could not be found to detail its critical temperature and other characteristics, maybe it is a wrong spelling of the $GdBa_2Cu_3O_{7-x}$ superconducting formula.

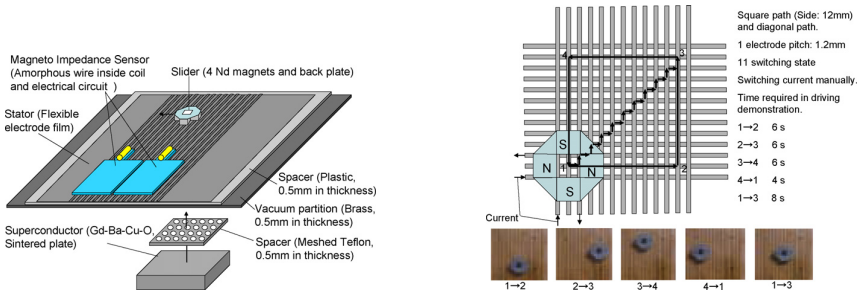

(a) (b)

Figure 2.48: Meissner effect levitation plus Lorentz force microconveyor by [ISF09]. (a) Conveyor scheme. (b) Conveyor displacements.

permanent magnets increase the conveyance surface of the system by providing a sliding surface for the mover (Figure 2.49b). This macro size system attained maximum levitation forces of 8 N and speeds of 1.1 m s^{-1} but only in a single cell of the proposed array. The prototype was a principle demonstration and not a complete conveyor, but in [KOS16] the concept evolved to a conveyor able to carry objects along walls (against the force of gravity) using the pinning force of the SC (Figure 2.49c). This time they used a full coil stator to increase the pinning force. They achieved a maximum vertical displacement of 11.5 mm with movers of ⌀60 mm, 270 g and ⌀46 mm, 180 g. They also achieved horizontal displacements while in a wall position of 46 mm. This feature of wall conveyance can be only achieved with attracting/repulsing forces such as the pinning force and maglev forces.

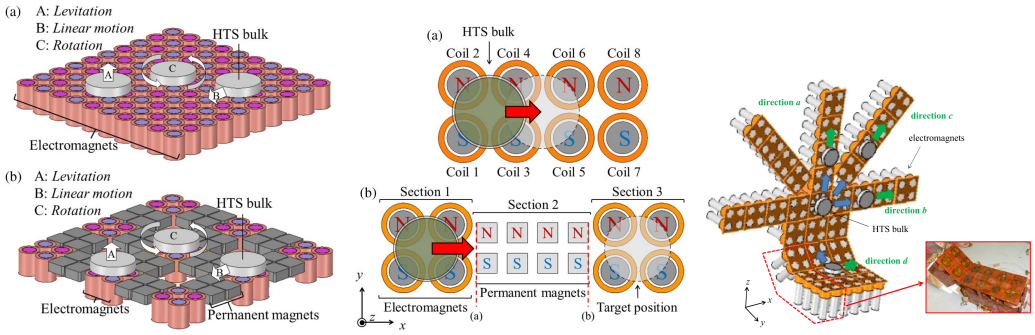

(a) (b) (c)

Figure 2.49: Proposed conveyor by [KSO16; KOS16]: (a) Planar motion conveyor with permanent magnets. (b) Lorentz force driving function. (c) Wall conveyor using the pinning force.

2.1.7 Overview and comparison of the presented conveyors

The motion devices presented in this section included positioners and conveyors, mainly micro-electro-mechanical-systems (MEMS) for micrometer planar mo-

tion. A physical principle and performance comparison of the different solutions in the state of the art allow a discussion of the advantages and disadvantages of each type of actuator in the microconveyance application and set a benchmark to which compare the system developed in this dissertation.

The advantages and disadvantages of the presented actuation physical principles are:

- Electrostatic systems have high displacement forces, a scalability advantage and easy construction with microfabrication techniques, but require high voltages to operate, produce short strokes and present their characteristic "pull-in" failure.
- Electrothermal systems generate large strokes with important forces but have slow response times, consume more power than other actuation principles and thermal saturation could stop their operation.
- Electrowetting systems have an intrinsic holding function in the form of surface tension and have excellent scalability properties but require high forces to displace the droplets due to their high inertia and are limited to actuate along predefined electrode paths.
- Piezoelectric systems can achieve long range motions with sub-micrometer accuracy and high speeds but need high working voltages, are sensible to temperature and aging, present strong non-linearities like hysteresis and creep in their displacement and, thus, require robust control techniques to operate.
- Pneumatic systems are fast and non-contact solutions but require constant energy input to hold a position, high fluid pressures, complex fluid models and control schemes to predict and control their behavior and are not simple to integrate due to their pipework.
- Pneumatic soft actuator systems are intrinsically digital actuators (Type 3), with modulable force and stiffness, and a relatively high force output. This make them safe to operate with humans and adaptable to a wide range of applications. On the other hand, they need high fluid pressures, complex fluid and material models and are not simple to integrate due to their pipework.
- Electromagnetic systems present large strokes with medium forces compared with the previous actuation principles; have slower response times than piezoelectric or electrostatic actuators but faster than electrothermal actuators; are relatively easy to build; could generate levitation and driving forces but do not scale as well as other principles below the millimeter size.
- Electromagnetic Meissner effect systems have an intrinsic repulsion force between their operation parts that can grow exponentially. This can be

exploited as holding force to design stable digital actuator systems. Their principal drawback is their need of very low operation temperatures (special and expensive refrigerants needed). Also, the Meissner effect works poorly as driving function, normally being coupled with a Lorentz electromagnetic principle to increase performance.

For the performance comparison, microconveyor platforms can be evaluated with multiple criteria. Contact solutions present less energy consumption and higher precision whereas levitation solutions offer higher speeds, and no contamination or degradation of the object through friction. The modular and planar motion capabilities increase the flexibility of the conveyor, as explained in Chapter 1, thus, the architecture (array/modular) and DoF of the conveyor are evaluating criteria. The actuation principle is relevant to compare the proposed solution against the state of the art as well as influence the complexity of integration and needed control of the conveyance system.

The criteria chosen for the comparison of the state-of-the-art solutions (Table 2.2) are then: contact or contact-free conveyance (C or CF), modular architecture (array), number of DoF, actuation principle (A.P: digital or analog), control needed (open or closed loop), size of the conveyance surface (active surface), conveyed object size and mass, maximum speed, resolution, precision and force. Other important criteria were listed in the description of each system, such as maximum step stroke, maximum operation frequency, accuracy and energy consumption.

2.2 Contact Mechanics

The digital actuator treated in this dissertation is driven by electromagnetic forces and the holding forces are generated by magnetic interaction. The other forces present in the actuator are friction and collision phenomena. The collision forces arise from the impact of the mobile part with the actuator's fixed part and friction is due to their relative motion. Both of these forces are part of the contact mechanics domain [Pop17]. The detailed force analysis of the actuator will be addressed in Chapter 3, where a dynamic model of the system is developed. This section presents a state of the art in the contact mechanics treating the collision and friction modeling.

2.2.1 Collision

The mobile part of the digital actuator collides with the limiting cavity that defines its stroke. The collision phenomenon is studied by normal direction (or

Table 2.2: Microconveyors: Literature comparison by actuating principle.

Ref.	Contact	Array	DoF	A.P	Control	Surface (mm)	Object (mm)	Speed (mm s^{-1})	Resolution (µm)	Precision (µm)	Force (mN)
Electrostatic conveyors											
[DPS11]	C	Yes	1	Digital	Open	6 width	0.5 × 0.25, 2 µg	1	21	-	-
[HYH15]	C	Yes	2	Analog	Open	264 × 264	132 × 132, 11 g	354	400	-	100
Electrothermal conveyors											
[Ell12]	C	Yes	3	Digital	Both	16 × 16	0.8 × 0.8, 78 µg	0.057	0.28	1	0.32
[Hus+18]	C	No	1	Digital	Open	0.12	-	0.029	10	0.1	10
Electrowetting conveyors											
[MK06]	C	No	1	Digital	Open	-	5 × 4, 180 mg	2.5	-	-	-
[Nie+18]	C	No	1	Digital	Open	25	6 × 8, 500 mg	1	500	-	-
[Geu18]	C	No	1	Digital	Open	-	-	4	333	-	-
Piezoelectric conveyors											
[Tia+18]	C	No	2	Digital	Open	-	-	1641	4.4	-	1180
[RHL09]	C	No	2	Digital	Open	-	-	1.8	70×10^{-3}	5×10^{-3}	150
[Gab+19]	CF	Yes	2	Analog	Closed	10 × 10	ø300, 129 g	2	-	400	-
[LF13]	C	Yes	3	Analog	-	-	-	83	-	300	-
[FAO12]	C	No	3	Digital	Open	-	50 × 50,140 g	20	70	3%	-
[Sho+16]	C	No	3	Digital	Open	-	86 × 86,150 g	20	62	10×10^{-3}	-
Pneumatic conveyors											
[Lau+14]	CF	Yes	3	Analog	Closed	9 × 9	ø5, 19.4 mg	140	300	17.7	-
[Gue+17]	CF	Yes	3	Analog	Closed	75 × 75	ø150	300	-	93	-
[LCZ20]	CF	Yes	3	Analog	Closed	228 × 204	ø80, 17 g	80	200	-	-
Pneumatic soft actuator conveyors											
[DSX16]	C	Yes	3	Digital	Open	180 × 180	Smartphone	0.53	1000	-	-
[WT18]	C	Yes	2	Digital	Open	180 × 180	200 g	2.5	-	-	-
[Rob+19]	C	Yes	16	Analog	Closed	110 × 93	-	70	-	-	2300
Electromagnetic conveyors											
[Pir+13]	C	Yes	2	Analog	Open	-	-	16.4	-	-	45
[Aro+19]	C	Yes	3	Analog	Closed	150 × 150	68 × 68, 3.6 g	12	-	7	-
[KKF90][a]	CF	Yes	2	Both	Open	50 × 50	1 × 4, 9 g	7.2	-	-	-
[ISF09][a]	CF	Yes	2	Both	Open	180 × 180	380 g	104	-	40	-
[KOS16][a]	CF	Yes	3	Analog	Open	Macro	ø60, 270 g	1.1	-	-	-

[a]System using the Meissner effect. Low temperatures needed to work (less than 130 K)

perpendicular stresses) contact mechanics [Pop17]. When an object with a given velocity impacts another, a contact force is produced by the material stiffness and the inertia of the moving objects upon each other. The contact-impact process presents very short duration, large contact force, rapid dissipation of the energy and high acceleration and deceleration of the contacting bodies [SSB18]. The contact-impact process is divided into two phases: compression and restitution. At the beginning of the contact process, the start of the compression phase, the contact force increases with the deformation of the objects until a maximum value at the end of the compression phase. In this maximum deformation instant, the objects' velocities are null. The restitution or expansion phase follows, where the energy that is stored in the objects' materials during the compression phase drives the bodies apart. The restitution phase ends when the two bodies are separated. Some energy of the impact is dissipated though internal damping, vibrations, heat and sound [SSB18]. Figure 2.50 represents a contact-impact phenomenon of a sphere with an initial speed u exerting a force F onto a static plane. The indentation or penetration of the sphere in the plane is denoted δ with the deformed materials generating an opposing force F_n.

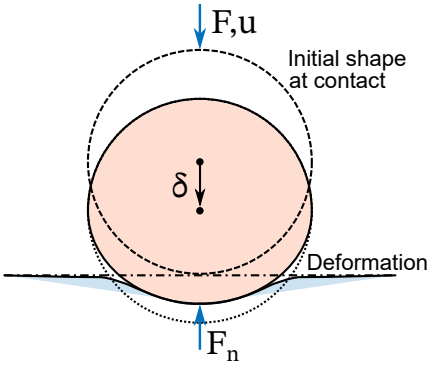

Figure 2.50: Contact-impact of a sphere and a plane

The first studies of contact-impact were done by Heinrich Hertz, who assumed elastic-only regimes for the deformation of the materials. He related the contact force to a nonlinear power function of indentation and material properties as [Pop17]:

$$F_n = K\delta^n \tag{2.30}$$

Where K is the contact-stiffness parameter and n the nonlinear power exponent. Both are determined from the material and the geometrical properties of the local region of the bodies in contact. Analytical expressions of K exist for simple geometrical shapes like spheres or planes. The equivalent or effective properties of the two bodies in impact are: radius of the contact zone R_*; Young modulus

E_* and mass m_* [SSB18; Str18]:

$$R_* = \left({R_1}^{-1} + {R_2}^{-1}\right)^{-1} \tag{2.31}$$

$$E_* = \left[(1-{\nu_1}^2){E_1}^{-1} + (1-{\nu_2}^2){E_2}^{-1}\right]^{-1} \tag{2.32}$$

$$m_* = \left({m_1}^{-1} + {m_2}^{-1}\right)^{-1} \tag{2.33}$$

With ν the Poisson's ratio of the materials. Other parameters are: Y the yield strength and ρ the material density. For the contact-impact between a sphere and a plane [SSB18]:

$$K = \frac{4\sqrt{R_*}}{3E_*} \tag{2.34}$$

For the contact-impact between two planar surfaces [SSB18]:

$$K = \frac{40a}{19E_*} \tag{2.35}$$

With a half the width of the contact line.

Hertz studied only perfectly elastic impacts, thus, his model do not account for the energy dissipation in the contact. The energy dissipation factor was studied by different authors. The first and most widely used model was developed by Kelvin and Voigt. Their model takes the Hertz theory and includes the energy dissipation as a linear spring and a linear damper element. The spring and damper are combined in parallel, giving a contact force as [Gol01]:

$$F_n = K\delta + D\dot{\delta} \tag{2.36}$$

Where the parameter D represents the force-dissipation (energy-dissipation) coefficient of the spring-damp and $\dot{\delta}$ the indentation velocity. The linear Kelvin–Voigt model does not reproduce the non-linearity of the whole contact process and, thus, is only suitable for contacts at low speeds [Mac+12]. It also states the non-realistic scenario where the contact force at the beginning of the contact is not continuous (due to the damping component) and an attracting velocity at the end of the restitution phase [Mac+12]. For this reason, Hunt and Crossley developed a model with Hertz theory combined with a nonlinear visco-elastic element that depends on the penetration depth [HC75]:

$$F_n = K\delta^n + \chi\delta^n\dot{\delta} \tag{2.37}$$

Where χ is the hysteresis (or hysteretic) damping factor. This factor is a function of the initial indentation speed $\dot{\delta_0}$, the already mentioned contact-stiffness parameter K and the coefficient of restitution c_r (explained further below).

From the model of Hunt-Crossley, multiple authors have adjusted the elastic assumptions, the damping factor or the hysteresis damping factor expression to adapt their models to different conditions, regimes, shapes and materials [Mac+12; SSB18; Pop17]. Table 2.3 presents some of these contact-force models using the presented entities. Figure 2.51 presents the different force and speed prediction of these models as a function of indentation.

Table 2.3: Different contact-force models [SSB18]

Contact-force model	Law	n	m	χ
Hertz	$F_n = K\delta^n$	$\frac{3}{2}$	-	-
Kelvin–Voigt	$F_n = K\delta^n + D\dot{\delta}$	1	-	-
Hunt–Crossley	$F_n = K\delta^n + \chi\delta^m\dot{\delta}$	$\frac{3}{2}$	$\frac{3}{2}$	$\frac{K}{\dot{\delta}_0}\frac{3(1-c_r)}{2}$
Herbert–McWhannell	$F_n = K\delta^n + \chi\delta^m\dot{\delta}$	$\frac{3}{2}$	$\frac{3}{2}$	$\frac{K}{\dot{\delta}_0}\frac{6(1-c_r)}{(2c_r-1)^2+3}$
Lee–Wang	$F_n = K\delta^n + \chi\delta^m\dot{\delta}$	$\frac{3}{2}$	$\frac{3}{2}$	$\frac{K}{\dot{\delta}_0}\frac{3(1-c_r)}{4}$
Lankarani–Nikravesh	$F_n = K\delta^n + \chi\delta^m\dot{\delta}$	$\frac{3}{2}$	$\frac{3}{2}$	$\frac{K}{\dot{\delta}_0}\frac{3(1-c_r{}^2)}{4}$
Gonthier	$F_n = K\delta^n + \chi\delta^m\dot{\delta}$	$\frac{3}{2}$	$\frac{3}{2}$	$\frac{K}{\dot{\delta}_0}\frac{1-c_r{}^2}{c_r}$
Flores	$F_n = K\delta^n + \chi\delta^m\dot{\delta}$	$\frac{3}{2}$	$\frac{3}{2}$	$\frac{K}{\dot{\delta}_0}\frac{8(1-c_r)}{5c_r}$
Gharib–Hurmuzlu	$F_n = K\delta^n + \chi\delta^m\dot{\delta}$	$\frac{3}{2}$	$\frac{3}{2}$	$\frac{K}{\dot{\delta}_0}\frac{1}{c_r}$
Hu–Guo	$F_n = K\delta^n + \chi\delta^m\dot{\delta}$	$\frac{3}{2}$	$\frac{3}{2}$	$\frac{K}{\dot{\delta}_0}\frac{3(1-c_r)}{2c_r}$
Ristow	$F_n = K\delta^n + \chi\delta^m\dot{\delta}$	$\frac{3}{2}$	1	Empirical
Shäfer	$F_n = K\delta^n + \chi\delta^m\dot{\delta}$	$\frac{3}{2}$	1	Empirical
Bordbar–Hyppänen	$F_n = K\delta^n + \chi\delta^m\dot{\delta}$	$\frac{3}{2}$	0.65	Empirical

A critical parameter for the contact forces is the coefficient of restitution c_r. This coefficient characterizes the energy transformed to internal energy of deformation during the compression phase which is recoverable during the restitution phase [Str18]. Three expressions for this coefficient exist, depending on the physical magnitude used. The square of coefficient of restitution is called energetic. It is the ratio of elastic strain energy released at the contact point during restitution to the energy absorbed by internal deformation during compression [Str18]:

$$c_r{}^2 = \frac{W_n(\delta_f) - W_n(\delta_c)}{W_n(\delta_c)} \tag{2.38}$$

With $W_n(\delta_f)$ the contact force work during the restitution phase and $W_n(\delta_c)$ the contact force work during the compression phase. The kinetic c_r, first expressed by Poisson, can be derived from the energetic expression with the momentum of the objects at the end of impact p_f and the momentum of the objects at maximum

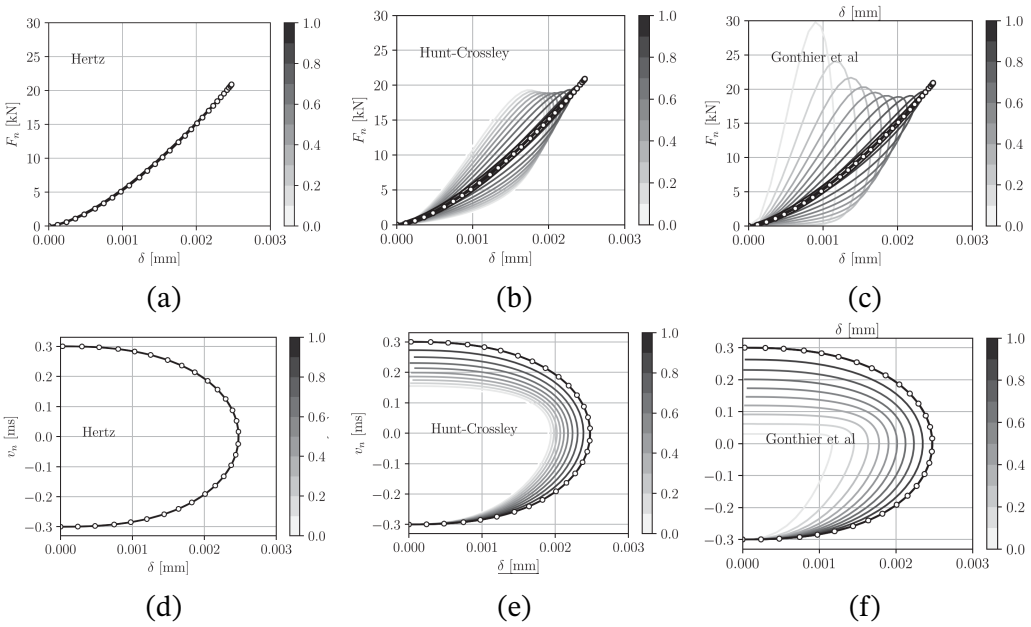

Figure 2.51: Contact forces vs deformation for different coefficient of restitution (a) Hertz model. (b) Hunt-Crossley model. (c) Gonthier model. Impact of the coefficient of restituion to the post-impact speed. (d) Hertz model. (e) Hunt-Crossley model. (f) Gonthier model ([SSB18]).

indentation p_c [Str18]:

$$c_r = -\frac{p_f - p_c}{p_c} \tag{2.39}$$

Finally, the kinematic c_r, first described by Newton, can be defined as the ratio of final velocity of the objects after impact V_f to the initial impact velocity V_0 [Str18]:

$$c_r = -\frac{V_f}{V_0} \tag{2.40}$$

Analytical expressions of c_r are derived for different collision regimes assumptions. The simplest case where energy is conserved is called purely elastic regime. This assumption holds at very low impact speeds. The opposite case is the fully plastic regime, where impact speeds are important and energy is lost to deformation. The elastic behavior is supposed non-existent. The intermediate regime, elasto-plastic, is the more common case in real impacts were both phenomena interact. Finally, material behavior generalizations and geometrical approximations are always present. The most usual derivation scenario for the c_r are identical sphere-sphere impact or sphere-plane impacts with identical material properties, to simplify an already complex problem.

Johnson derived an expression for fully plastic impacts approximating the mean pressure in the impact zone as $\bar{p} \approx 3Y_d$, with Y_d the dynamic yield strength

of the material. For the sphere-sphere impact [Joh85]:

$$c_r{}^2 = \frac{3\sqrt{2}\pi^{5/4}}{5}\left(\frac{3Y_d}{E_*}\right)\left(\frac{m_* V_0{}^2}{6Y_d R_*^3}\right)^{-1/4} \tag{2.41}$$

For a sphere-plane impact [Joh85]:

$$c_r = 1.718\left(\frac{\bar{p}^5}{E_*{}^4\rho}\right)^{1/8} V_0{}^{-1/4} \tag{2.42}$$

Thornton developed an expression for elasto-plastic impacts tending to unity when the impact speed tends to zero (perfectly elastic impact). The parameter p_Y is the pressure at maximum deformation, which can be approximated in different forms depending on the contact model. For sphere-sphere impacts [Tho97]:

$$c_r = \left(\frac{6\sqrt{3}}{5}\right)^{1/2}\left[1-\frac{1}{6}\left(\frac{V_f}{V_0}\right)^{1/2}\right]\left[\frac{V_f/V_0}{V_f/V_0+2\sqrt{6/5-(1/5)(V_f/V_0)^2}}\right]^{1/4} \tag{2.43}$$

With final speed or yield speed V_f:

$$V_f = \left(\frac{\pi}{2E_*}\right)^2\left(\frac{8\pi R_*{}^3 p_Y{}^5}{15m_*}\right)^{1/2} \tag{2.44}$$

For a sphere-plane impact [Tho97]:

$$c_r = \frac{331}{250}\left(\frac{30m_* V_f{}^2}{\pi^5 R_*{}^3\rho}\right)^{1/8}(V_0)^{-1/4} \tag{2.45}$$

Stronge derived expressions of c_r for sphere-sphere and sphere-plane impacts in the elasto-plastic and fully plastic regimes. For the elasto-plastic sphere-sphere impact [Str18]:

$$c_r{}^2 = \left(\frac{1944R_*{}^3 Y^5}{5\pi E_*{}^4 m_* V_0{}^2}\right)\left(\frac{5\pi E_*{}^4 m_* V_0{}^2 - 729R_*{}^3 Y^5}{1215R_*{}^3 Y^5}\right)^{3/4} \tag{2.46}$$

For the elasto-plastic sphere-plane impact [Str18]:

$$c_r{}^2 = \left(\frac{4050Y^5}{137E_*{}^4\rho V_0{}^2}\right)\left(\frac{548E_*{}^4\rho V_0{}^2 - 6075Y^5}{10125Y^5}\right)^{3/4} \tag{2.47}$$

Wier and Tallon developed expressions for the kinematic c_r assuming the Hertz theory and linear elasticity in the materials. They scaled the impact speed to the velocity and propagation of the impact's waves. Their expressions of c_r

are function of impact speed, geometric and material properties of the objects involved. Under purely elastic impact, they obtained an expression tending to unity for low-speed impacts [WT05]:

$$c_{r\text{elastic}} = \exp\left(\frac{-3\sqrt{2(1-\nu)}\rho^{3/10}V_0^{3/5}}{5{E_*}^{3/10}}\right) \tag{2.48}$$

For elasto-plastic impacts:

$$c_r = 3.1\left(\frac{Y}{1}\right)^{5/8}\left(\frac{1}{E_*}\right)^{1/2}\left(\frac{R_1}{R_*}\right)^{3/8}\left(\frac{1}{V_0}\right)^{1/4}\left(\frac{1}{\rho}\right)^{1/8} \tag{2.49}$$

The term R_1/R_* arises because of the different possible geometries after separation (and penetration) depending on the materials' different hardness and shape. For impacts in which either one surface is plane, or both surfaces suffer plastic deformation, the ratio R_1/R is neglected [WT05].

When the particles in collision are made of different materials or shapes, a composite coefficient of restitution is needed. For dissimilar elastic bodies [Str18]:

$$\frac{{c_{r_*}}^2}{E_*} = \frac{c_{r_1}(1-\nu_1^2)}{E_1} + \frac{c_{r_2}(1-\nu_2^2)}{E_2} \tag{2.50}$$

With c_{r_i} the coefficient of the i-th body. The composite coefficient of restitution for dissimilar elasto-plastic or plastic deformation is [Str18]:

$$\frac{{c_{r*}}^2}{k_*} = \frac{{c_{r1}}^2}{k_1} + \frac{{c_{r2}}^2}{k_2} \tag{2.51}$$

With $k_* = k_1k_2/(k_1+k_2)$ the equivalent deformation curvature of the bodies in impact. $k_i \propto aE_i$ for elastic deformation or $k_i \propto R_iY_i$ for plastic deformation.

Figure 2.52 compares different models of coefficient of restitution and their impact in the contact mechanics models.

The coefficient of restitution also depends on the number of impacts on the impact zone [WT05]. Weir and Tallon proposed a recurrent analytic expression for c_r that correctly predicted their experimental measures. The measures tended towards a stable value, higher than the first impact values (noted sub 1):

$${c_{r,n+1}}^{8/3} = {c_r}^{8/3} + c_{r,1}\left[1 - 2.7\left(\frac{V_1\sqrt{\rho}}{\sqrt{E}}\right)^{3/5} - {c_{r,n}}^2\right] \tag{2.52}$$

2.2.2 Friction

Chapter 3 will explain how the friction forces play an important role in the working principle of the treated digital actuator. Friction forces are due to the

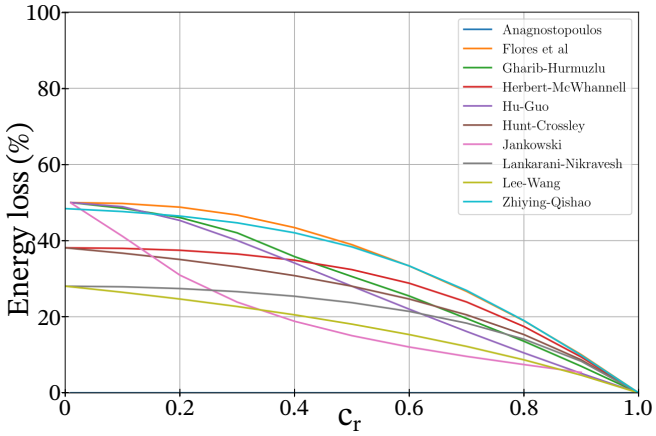

Figure 2.52: Coefficient of restitution models comparison for energy loss at impact ([SSB18]).

relative motion between: the mobile part and the actuator's fixed part. In this section, the variables influencing the friction forces are described. Then, multiple dry friction models are presented, explained and compared.

2.2.2.1 Friction variables

Friction is dependent on both normal and tangential direction forces in contact mechanics [Pop17]. Friction is influenced by multiple physical phenomena, generating a very complex multi-physical process to understand, model and control [Vak+18] (Figure 2.53). Also, microscale friction is highly stochastic in nature [KV19].

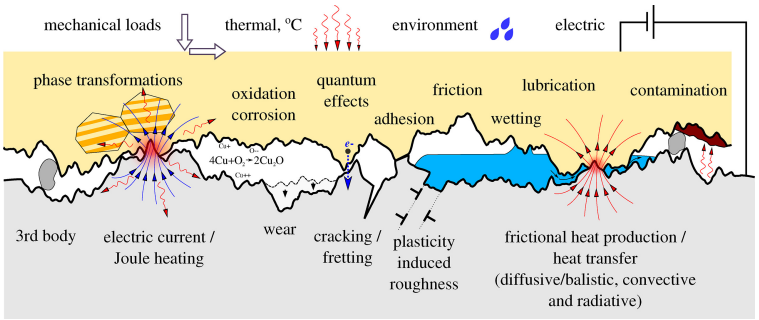

Figure 2.53: Contact phenomena influencing friction ([Vak+18]).

The most important variables for the friction force between two objects are their relative pressing force (normal force), speed and displacement. The interaction of these variables and how they are used to model the friction forces will be treated in detail on the friction modeling subsection, below. Other important variables affecting friction like the contact time and direction, surface roughness, temperature and number of cycles are treated in Appendix B.1.

2.2.2.2 Friction modeling

Coulomb friction law was the predecessor for all the friction models. This model involves a single parameter, the coefficient of friction μ: the fraction of the normal force between the objects (F_N) transformed to friction resistance (F_f). However, the Coulomb model fails to describe multiple friction behaviors, notably the stick-slip phenomena (important for the operation of this dissertation's system), and presents a discontinuity for the friction force at zero velocity. This discontinuity is an important issue for dynamic modeling and simulations because it introduces a numerical instability in the system's response [Mar+16]. For this reason, multiple friction models have been proposed to better predict, control and compensate friction in mechanic devices.

Friction is a complex, nonlinear phenomenon and its modeling depends upon the scale of interest: from macroscopic behavior, to millimeter devices and microscopic phenomena, to nanometer range, where atomic effects are dominant and the continuum physics breaks. In this nano scale quantum theories must take the relay [Vak+18]. The scale of interest in this dissertation is the macro to milli/microfriction behavior. For this scale, the observed friction behaviors to be modeled are presented in Figure 2.54, which are explained next.

Friction presents two regimes: pre-sliding, where adhesive forces between asperities are dominant, and thus, the friction force is primarily a function of displacement; and sliding, where the applied force makes the asperities break and form in a continuous process, transforming the friction force in a velocity function rather than a displacement one. The transition from pre-sliding to sliding is a "criticality" that depends on many factors such as the relative velocity and acceleration of the sliding objects and determines the stick-slip behavior [Al-10]. In the pre-sliding regime, small displacements generate hysteretic rate-independent (velocity does not influence) curves, this is called "non-local memory" (Figure 2.54b). The hysteresis shape depends on the distribution of the asperity heights, the tangential stiffness, and the normal stiffness of the contact [Al-10]. In the sliding regime, the friction force at constant velocity starts from a maximum at a low velocity (normally at zero), then decreases to a local minimum for a given velocity, and then increases with higher velocity (steady state in Figure 2.54c). This curve is called Stribeck effect. If the velocity is not steady (acceleration), the maximum friction force (or break-away force) changes with the acceleration value, as well as presenting a hysteresis loop for velocity reversal (dynamic in Figure 2.54c). This is called rate-dependent breakaway force and friction lag (detailed in Figure 2.54d).

The models attempting to describe friction phenomena are divided into static

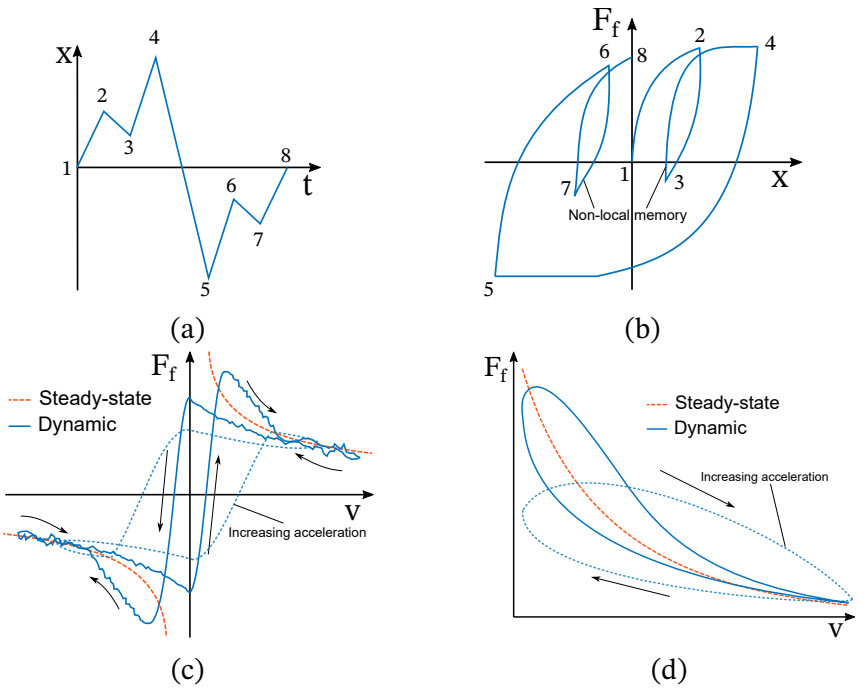

Figure 2.54: Friction phenomena (a) Wished displacement vs time. (b) Non-local memory. (c) Stribeck effect for different accelerations (rate-depenent break-away force and friction lag). (d) Friction lag for different accelerations.

and dynamic models. Appendix B.1 lists and explains multiple static and dynamic models found in the literature with their equations, advantages and drawbacks. Generally, static models describe the steady-state behavior of friction force, while the dynamic models capture hysteresis behaviors by using extra state variables (as steady-state and dynamic in Figure 2.54). Nevertheless, some static models approximate dynamic phenomena and some dynamic models do not model all hysteresis behaviors.

Figure 2.55 presents three static friction models: the Bo-Pavelescu, Bengisu-Akay and Wojewoda models. The first only captures the stribeck effect, the second one the Stribeck effect and a finite slope at null velocity and the third the Stribeck effect, finite slope, friction hysteresis and randomness.

Figure 2.56 presents three dynamic friction models: the LuGre, GMS and Generalized models. The LuGre model is derived from the Dhal model, the first reported dynamic model, and included the Stribeck effect. The LuGre model considers friction as the interaction of elastic bristles. The GMS proposed multiple mass-spring elements to characterize the friction behavior of a system by identification. The number of mass-spring systems depends on the precision wished and the identification process. The Generalized model is a theoretical, physical model of the contact as: a set of stochastic distributed asperity masses and an elastic non-dissipative counter profile. All the Generalized model's parameters are material properties or stochastic distributions.

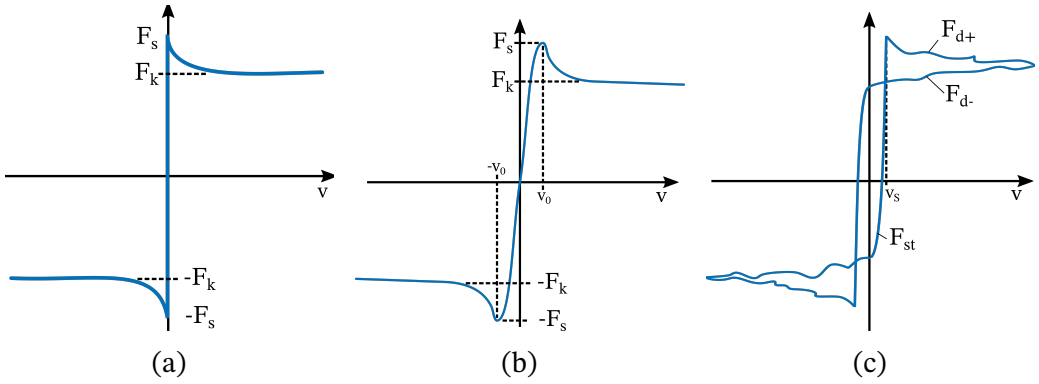

Figure 2.55: Static friction models (a) Stribeck effect by Bo-Pavelescu. (b) Bengisu-Akay. (c) Wojewoda. (Adapted from [Mar+16; BA94; Woj+08]).

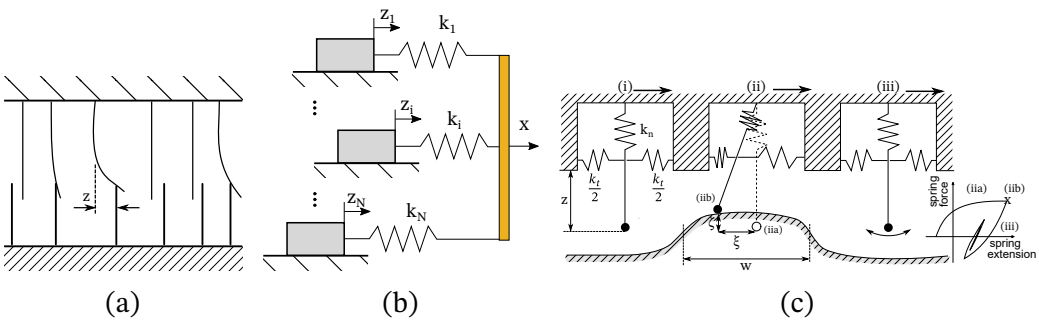

Figure 2.56: Dynamic friction models (a) LuGre [Can+95; Ols+98]. (b) GMS [LSA02; ALS05]. (c) Generalized friction model [Al-+04; DAV10].

As stated above, please refer to Appendix B.1 for a deeper study of the static friction models (Bo-Pavelescu, Bengisu-Akay, Seven parameter and Wojewoda) and the dynamic models (Dahl, LuGre, Leuven, GMS and Generalized).

Comparison between models This subsection compares the friction models in terms of their friction behavior capabilities, needed parameters and their accuracy to predict a system's behavior. Table 2.4 compares the friction behavior capabilities of the presented models. A relation between friction behaviors and number of parameters can be seen: the most complete models need the most parameters. Static friction models need less parameters and are faster in simulation but do not model all friction behaviors. A compromise is then needed depending on the accuracy, simulation time and control schema of each system. For the difference in output between the models and accuracy, multiple models are compared in Figure 2.58 and Figure 2.60. The simulation scenario is a Rabinowicz test: a mass on a conveyor belt attached to a spring (Figure 2.57). For Figures 2.58a and 2.58b the conditions are $m = 1\,\mathrm{kg}$, $v = 0.1\,\mathrm{m\,s^{-1}}$, $k_s = 2\,\mathrm{N\,m^{-1}}$. For Figure 2.60 the conditions are $m = 20\,\mathrm{kg}$, $v = 0.5\,\mathrm{m\,s^{-1}}$, $k_s = 10\,\mathrm{N\,m^{-1}}$. For Figure 2.59 the conditions are the same for their GMS experiment explained

earlier. From the dynamic friction comparison (Figure 2.58b and Figure 2.59), the most accurate models are the GMS and the Generalized friction models. From the static friction model comparison (Figure 2.58a), the Karnopp, Bengisu & Akay and Awrejcewicz models predict very similar results, avoiding simulation oscillations and predicting stick-slip phenomena. The Bengisu & Akay model, being the simplest of the three, predicted similar behaviors to the LuGre and Gonthier dynamic models (Figure 2.60a and Figure 2.60b) accurately predicting the oscillation lag when the spring reached its maximum length.

Table 2.4: Studied friction models comparison (see Appendix B.1).

Model	Stick-slip	Finite slope	Non-local memory	Rate-dependent break away force	Friction lag	Parameters
Bo-Pavelescu	✓	-	-	-	-	3
Bengisu-Akay	✓	✓	-	-	-	4
Seven parameter	✓	✓	✓	-	✓	8
Wojewoda	✓	✓	-	✓	✓	10
Dahl	-	✓	✓	✓	-	3
LuGre	✓	-	✓	✓	✓	6
Leuven	✓	✓	✓	✓	✓	8
GMS	✓	✓	✓	✓	✓	3× element + 2
Generalized	✓	✓	✓	✓	✓	Variable

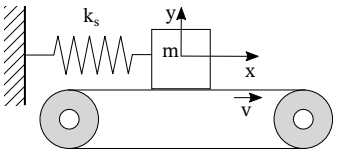

Figure 2.57: Rabinowicz test for friction models

2.3 Pathfinding

Pathfinding (or path planning) is the geometric problem of determining a feasible path, from a start location to a goal location, through an environment with obstacles. The feasibility of the path depends on the characteristics of moving entity (the *agent*), such as size or DoF of its movement. This problem is seen in, for example, GPS navigation, robotics, video games, traffic control, and decision-making [VV15; Sha15]. Generally, the quality of the solution path is a cost function of the cost and time to perform the path, plus the cost and time to calculate it (time and space complexity, respectively). The optimal solution is then the minimum of this cost function.

This dissertation divides the pathfinding problem (and the algorithms to solve it) by different relations of the agent and its environment (Figure 2.61):

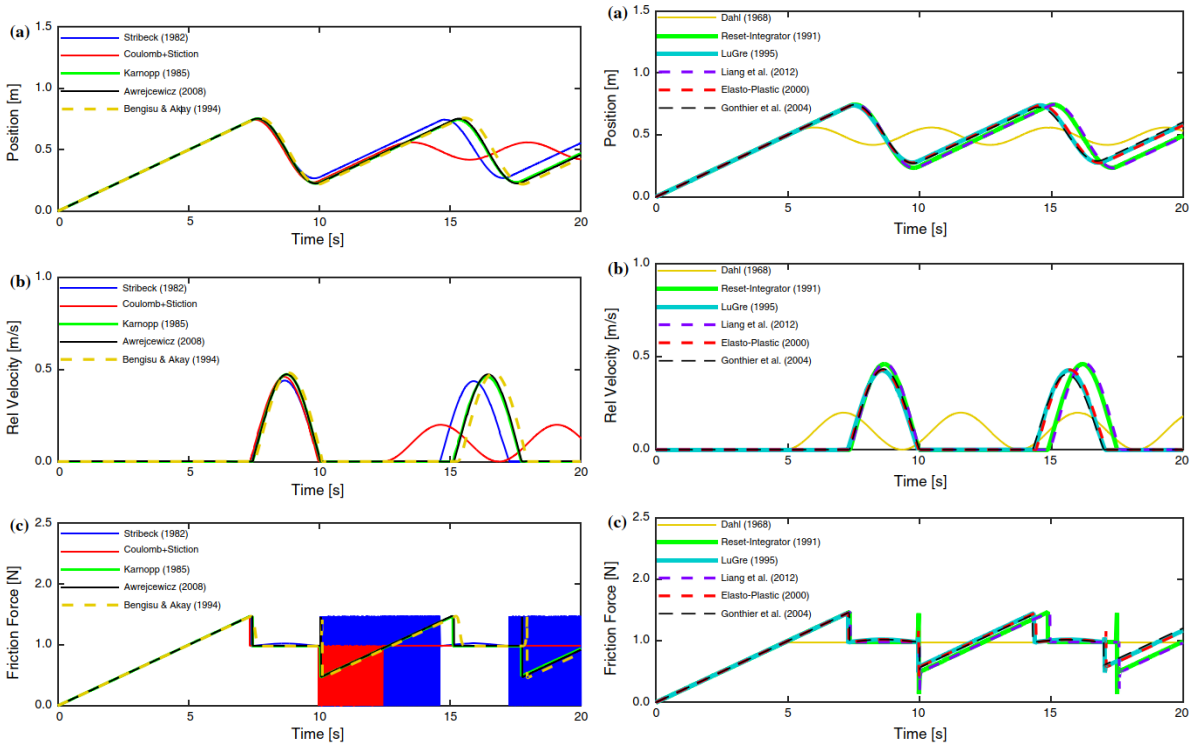

(a) (b)

Figure 2.58: (a) Static friction models with stiction comparison. (b) Dynamic friction models comparison [Mar+16].

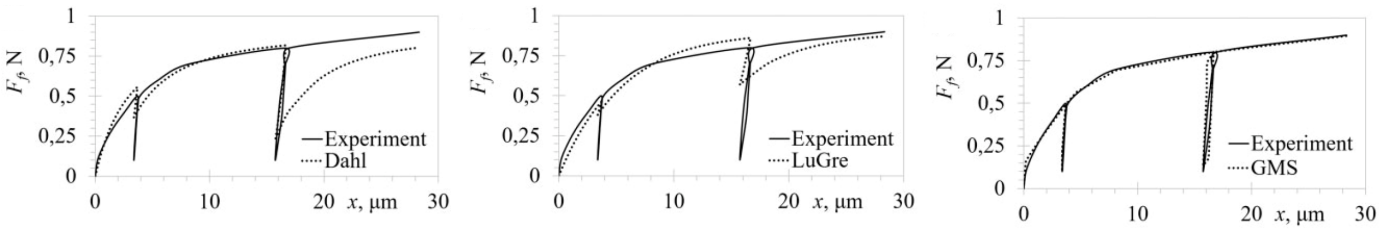

Figure 2.59: Dynamic friction models comparison by [KZ19].

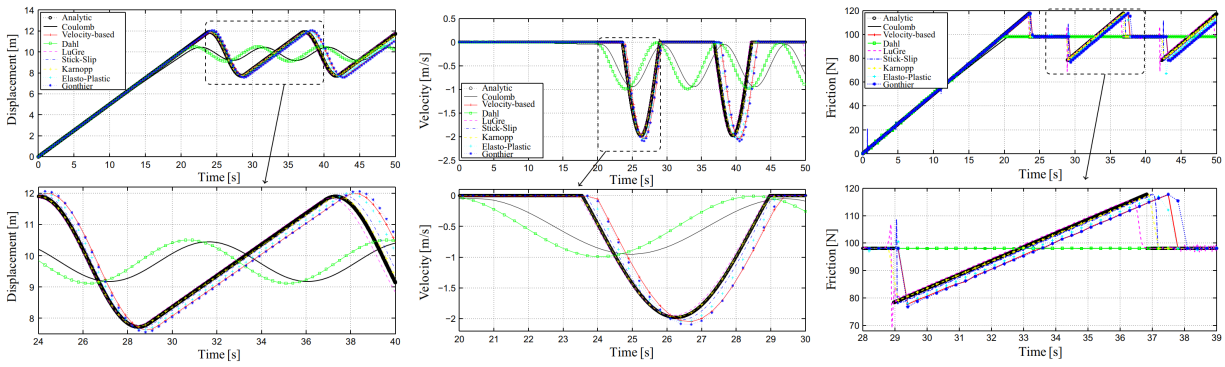

(a) (b) (c)

Figure 2.60: Friction models accuracy comparison (a) Position vs time. (b) Velocity vs time. (c) friction force vs time [Pen+16].

- Evolution of the environment though time: if the environment remains unchanged in time, the pathfinding problem is called *static*. If the environment changes through time, e.g., moving obstacles, changing terrain or conditions, the problem is called *dynamic*.
- Evaluation of the environment: if the algorithm explores all possible path alternatives and select the best one, it is called *exact*. If the algorithm tries to reduce the number of possibilities to obtain a faster yet acceptable solution, it is called *heuristic*.
- Representation of the environment: the simplification of the real world into an abstract object plays a crucial role in the strategy to solve the problem. The environment can be discretized in a set of possible reachable positions and possible connections or transitions between these positions, called *a graph* or *grid*. The environment can also be represented by two *space* sets. One free, movable space, and a forbidden space represented by enclosed *polygons* or *polyhedra*. The algorithms use one or the other representation to solve the problem.
- The number of agents for which to find a path: if a single agent is present, the problem is called *single-agent*. If there are multiple agents with different start/finish objectives and representing movable obstacles to one another, the problem is called *multi-agent* (MAPF).
- Agent knowledge about the environment: if the agent knows the environment, obstacle location and its changes though time, the problem is called *informed*. If the agent only knows about its immediate surroundings and discovers the environment as it advances, the problem is called *uninformed*.

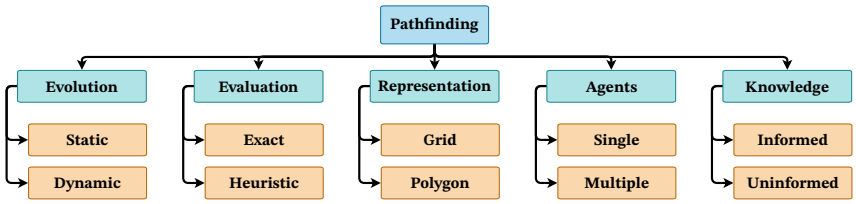

Figure 2.61: Classification tree of pathfinding problems/algorithms following.

An important property of the solution algorithms is its *completeness*. An algorithm is said to be *complete* if it is guaranteed to find a solution in finite time, if one exists. It is to report failure if there is no solution. Another concept is *resolution completeness*. A planner is *resolution complete* if it is complete for the resolution of a discretized representation of the problem, such as the resolution of a grid representation. Finally, a planner is *probabilistically complete* if the probability of finding a solution, if one exists, tends to 1 as the planning time goes to infinity [LP17].

There is no single planner applicable to all pathfinding problems. To solve these different pathfinding problems, multiple algorithms have been proposed in the literature. They use different methods to solve the problem, depending on its representation of the free space and approach to link the start and goal locations. Next, some of these algorithms, divided by the method they use, are presented, classified and explained. Appendix B.2 explains in detail all the studied pathfinding algorithms.

2.3.1 Grid methods

These methods discretize the free space into a grid (vertex or nodes connected through edges) and search the grid for a path from the start node to a goal node. The grid approximates the start, goal and obstacles locations to the nearest nodes (Figure 2.62). Grid methods are relatively easy to implement and can return optimal solutions but, for a fixed resolution, the memory required to store the grid, and the time to search it, grow exponentially with the number of dimensions of the space. This limits the approach to low-dimensional problems [LP17]. Normally, the algorithms present a solution for a given grid discretization. This is known as the resolution of the grid.

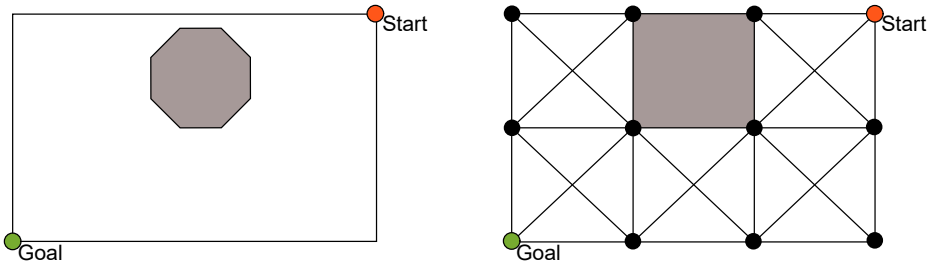

(a) (b)

Figure 2.62: Grid representation of an environment in $\mathbb{R}^2$. (a) Environment. (b) 8-connect grid approximation. Adapted from [Nas12].

2.3.1.1 Dijkstra

Dijkstra's algorithm (or Uniform Cost Search) [Dij59] finds the shortest path between nodes in a graph (grid). It associates a cost to the connections between the nodes (edges) to find the least expensive path (optimal path) between a given start node and all other nodes in the grid. It can also be used for finding the shortest paths from a single node to a goal node by stopping the algorithm once the shortest path to the goal has been determined. Dijkstra evaluates all the nodes in the grid until finding the solution, affecting its execution time in dense grids or high DoF problems.

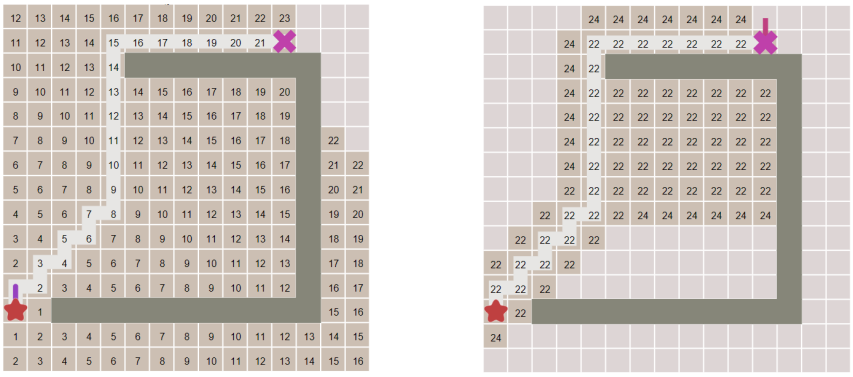

(a) (b)

Figure 2.63: Same solution for the same problem, but different number of nodes evaluated for (a) Dijkstra (b) A*. The numbers in the cells represent the cost from start to the cell for (a) and the total path cost on (b). Unnumbered cells are non-evaluated nodes. The clear cells are the solution path [Pat16].

2.3.1.2 A*

A*, developed by [HNR68], can be seen as an improved Dijkstra's algorithm (Figure 2.63). A* uses an heuristic function to guide the node exploration. Every node n is assigned a distance from the start node $g(n)$ plus the heuristic function value, an assumption of the remaining distance to the goal $h(n)$, forming the total value function $f(n)$.

$$f(n) = g(n) + h(n) \tag{2.53}$$

The node with lower $f(n)$ is expanded, i.e., the connected nodes are evaluated. Once the goal is chosen for expansion, A* halts and the found path to the goal is returned. If $h(n)$ is *admissible*, i.e., it never overestimates the actual cost from n to the goal, then A* is guaranteed to return an optimal solution if one exists [HNR68; Sha15]. This also means that A* is resolution complete. A* is optimal in the number of expanded nodes. That is, any other equally informed search algorithm will have to expand all the nodes expanded by A* before identifying the optimal solution [HNR68; Sha15].

The most commonly used heuristic functions $h(n)$ are: the Manhattan distance, the total difference between the coordinates of the node and goal; the Euclidean distance, the straight-line distance between the node and goal; and the Move distance, the length of the path between the node and goal nodes following a 8-connected grid map. As A* does not pre-process the obstacles of the environment, these distances do not consider them for their value.

2.3.1.3 Theta* (Θ*)

Theta* (Θ*), developed by [Nas+07; Nas+10], is an any-angle path planning algorithm based on A*. Any-angle means that the algorithm uses the grid to link the start-goal nodes, but once the path is set, it is optimized. The optimization uses straights not contained in the grid edges to join grid nodes and form a shorter path than the grid edges path. This produces optimal or near-optimal paths in the free space rather than optimal paths on the grid, which can be badly set for the problem. Θ* finds near-optimal paths in free space with execution times comparable to A*. Θ* records the parent nodes that are in line of sight, linking them if: they belong to the grid solution path, skipping the nodes in between; and the linking path is collision free (Figure 2.64b). This produces a shorter path than A*. As A*, Θ* is complete.

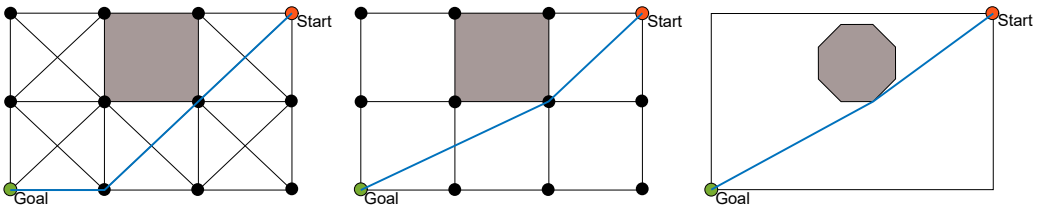

(a) (b) (c)

Figure 2.64: Grid-based solutions of Figure 2.62. (a) A* solution with grid nodes and edges. (b) Θ* solution with grid nodes and free-space straights (any angle solution). (c) Real shortest path. Adapted from [Nas12].

2.3.2 Sampling methods

Sampling methods rely on a random or deterministic function to choose a sample from the state space; a function to evaluate whether the sample is in the free space; a function to determine the "closest" previous free-space sample; and a local planner to try to connect to, or move toward, the new sample from the previous sample. This process builds up a graph or tree representing feasible paths. Sampling methods are easy to implement, tend to be probabilistically complete, and can solve high DoF planning problems. The solutions tend to be satisfying, not optimal, and it can be difficult to characterize the computational complexity [LP17]. Two major classes of sampling methods are rapidly-exploring random trees (RRTs) and probabilistic roadmaps (PRMs).

2.3.2.1 Rapid-exploring Random Trees (RRTs) & variants

RRT algorithm were developed by Steven M. LaValle ([LaV98; LK01a; LK01b]) by randomly building a space-filling tree. The tree is constructed from the start

point and by samples drawn randomly from the search space (nodes). As each sample is drawn, a connection (branch) is attempted between it and the nearest existing sample of the tree. If the branch passes entirely through free space, the new sample is added to the tree. The length of the branch between the tree and a new sample is limited by a growth factor, to avoid sample overshooting. If the random sample is further than this grow factor, the new sample is redefined as the maximum distance from the existing tree to the far sample, along their connecting line (ϵ in Figure 2.65a). The random samples control the direction of the tree growth while the growth factor determines its rate. The tree tends to grow towards unexplored areas of the space by its stochastic construction (Figure 2.65).

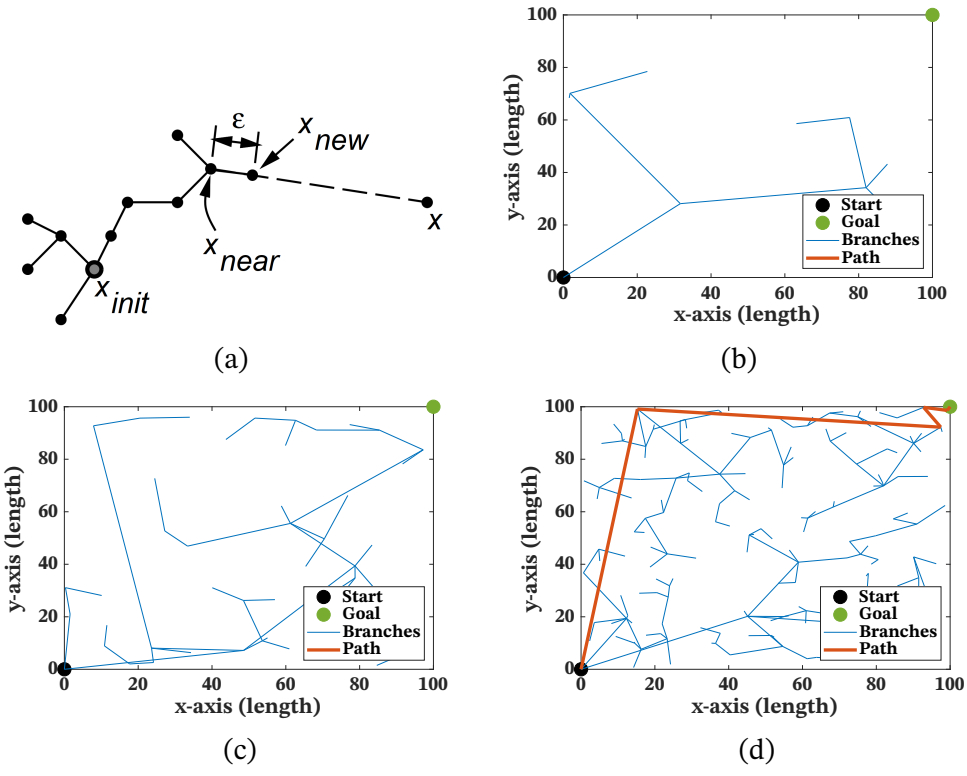

Figure 2.65: RRT evolution. (a) Growing the tree ([LK01b]). (b) RRT with 10 iterations. (c) 50 iterations. (d) Success with 184 iterations.

The RRT algorithm approaches then the goal location but, depending on the sample method, it sometimes never reaches the exact value. A goal region is then defined as the objective. RTTs can be applied to nonholonomic and high DoF problems, but they converge almost surely to a non-optimal path. The performance of the RRT algorithm depends heavily on the choice of sampling method, distance measure, and local planner [LP17]. To enhance the RRT algorithm performance, multiple modifications have been proposed in the literature.

RRT* RRT*, developed by [KF11], continually rewires the search tree to ensure that it always has the shortest path from the start to each node in the tree (Figure 2.66). It allows exact paths from any node to any other node. The solution approaches the optimal solution as the number of samples increases (asymptotically optimal). RRT* is probabilistically complete. To rewire the tree, the algorithm uses the nodes inside a radius of the new sample to find the shortest one to the start by hierarchy.

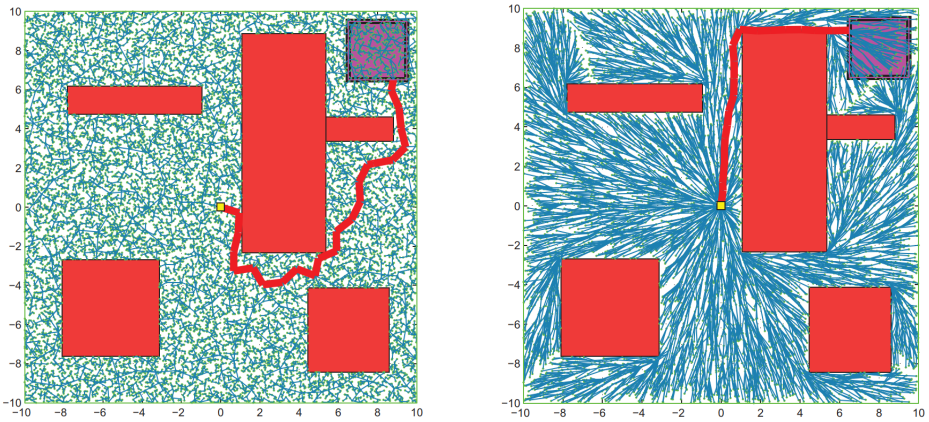

(a) (b)

Figure 2.66: RRT and RRT* comparison by [KF11] (a) RRT (b) RRT*.

2.3.3 Virtual potential fields methods

Virtual potential fields create forces on the robot that pull it toward the goal and push it away from obstacles (Figure 2.67). The approach is easy to implement, even for high-degree-of-freedom systems, and fast to evaluate [LP17; Ras+17]. With sensors, the method can handle dynamic problems. The drawback is local minima in the potential function: the robot may get stuck in configurations where the attractive and repulsive forces cancel but the robot is not at the goal state [LP17]. The goal location is given a low potential value, and obstacles high values. The actuating force can be defined as the negative of the potential gradient, plus a damping factor to avoid oscillations near the goal location. Another option is to use the negative gradient potential as speed input of the agent, eliminating oscillations directly. Potential fields can be used in conjunction with multiple other techniques to avoid prevent the agent from getting stuck in local minima.

[Ras+17] developed a controller for autonomous vehicle path planning including the potential field method. The authors added the potential field of obstacles and road limits in the objective function of the optimal controller problem. Their controller found an optimal path in terms of obstacle avoidance, road respect and optimal vehicle dynamics. They applied their controller to multiple

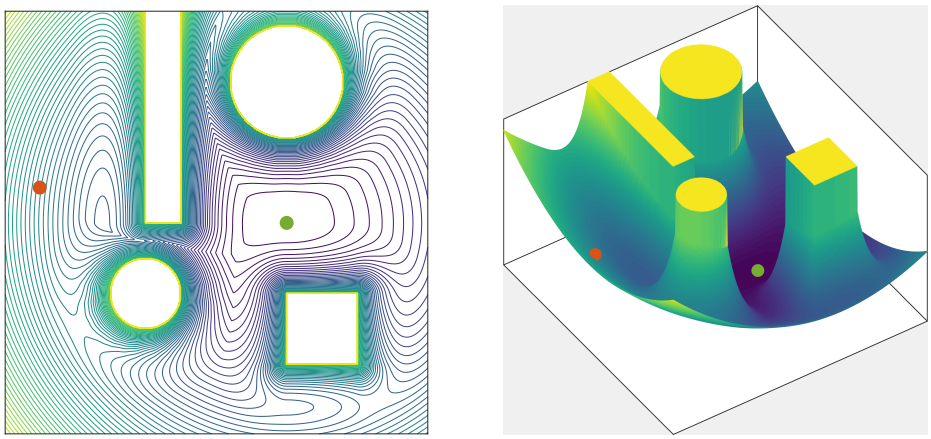

(a) (b)

Figure 2.67: Virtual potential field. (a) Contour plot of the potential field to solve a pathfinding problem with obstacles, start (orange) and goal (green) positions. (b) 3D representation.

simulations, evaluating the differential obstacles speed (moving cars), inter-car spacing, size of the obstacles and road changes. They obtained good behaviors, although a quadratic approximation had been necessary to reduce the computational time, inducing small errors against the exact nonlinear and long solution (Figure 2.68).

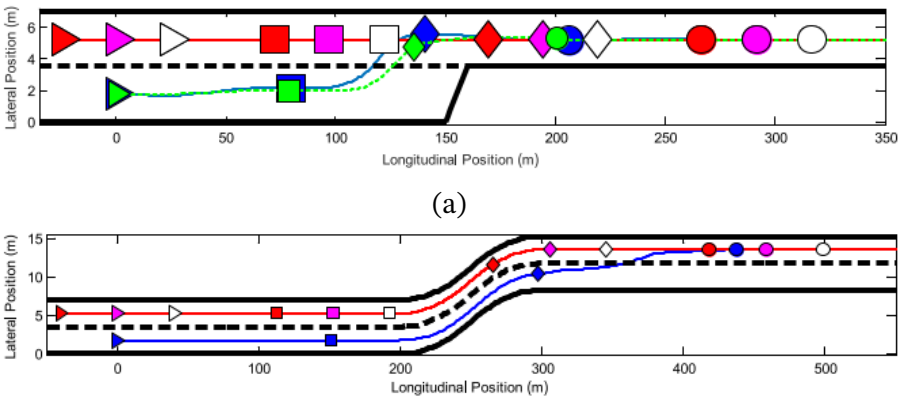

(a)

(b)

Figure 2.68: Potential field method in a dynamic environment: autonomous vehicle. (a) Highway insertion. (b) Line insertion [Ras+17].

[OMS19] presented a hybrid path planning algorithm combining membrane-inspired evolutionary algorithms (generic algorithm) with potential fields. Their approach could solve static and dynamic problems. It used parallel computation to speed up their solutions for complex problems. Their algorithm outperformed other state-of-the-art potential field algorithms using soft computation, as the "parallel evolutionary artificial potential field" (PEAPF), the "pseudo-bacterial potential field" (PBPF), and the "bacterial potential field" (BPF).

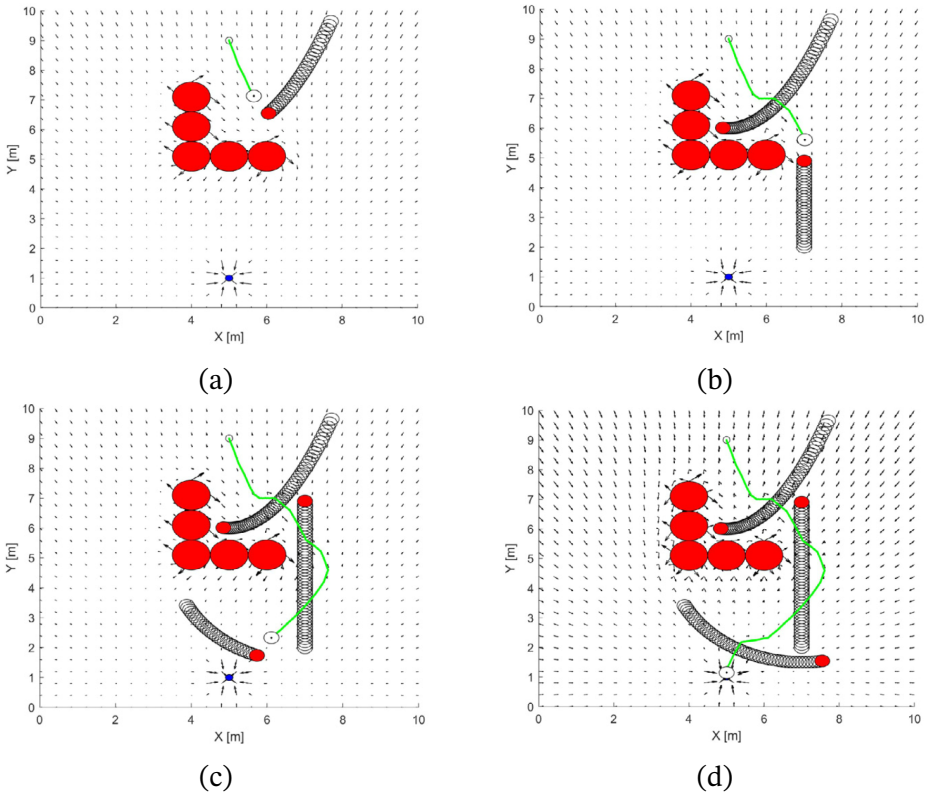

Figure 2.69: Membrane generic algorithm plus potential field method in a dynamic environment by [OMS19]. (a)-(d) Temporal evolution.

[NKD19] presented another hybrid approach with a potential field to find possible paths and a multi-objective enhanced genetic algorithm to optimize the paths and select the best one in terms of path length, smoothness, and safety in a continuous environment. The generic algorithm minimally modified the potential field solutions to avoid generating infeasible paths. The proposed algorithm could solve the multi-agent problems (four agents in their test). The the proposed method was compared against A*, PRM, and B-RRT in 12 environments, outperforming them.

2.3.4 Multi-agent pathfinding (MAPF)

On the problem of multi-agent pathfinding (MAPF), graph-based methods have been proven to be effective [YL16]. The main approach of these methods have been using A*-based algorithms [Gol+12; Gol+14]. Some examples are: Cooperative A* (CA*), Hierarchical Cooperative A* (HCA*) and Windowed Cooperative Hierarchical A* (WHCA*) by [Sil05]; M* by [WC11]; Operator Decomposition A* (ODA*) by [Gol+12]; Enhanced Partial Expasion A* (EPEA*) by [Gol+14]. The branching factor for any A*-based search in the MAPF problem is exponential in the number of agents. This may lead to optimal solutions, but with very long

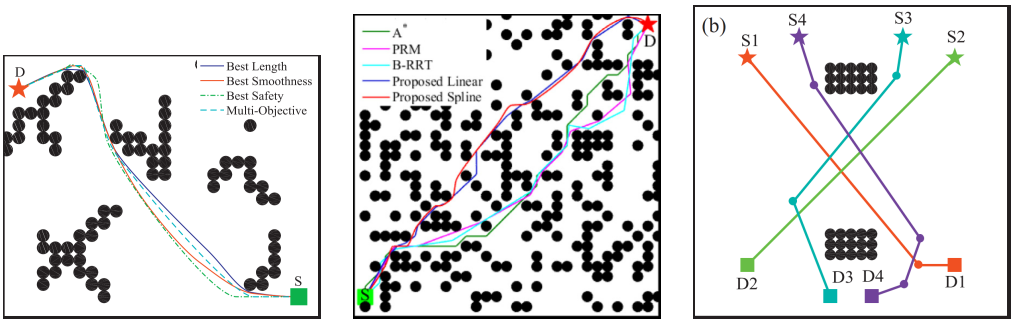

(a) (b) (c)

Figure 2.70: Generic algorithm plus potential field method in static and multi-agent environments by [NKD19]. (a) Potential field path enhancement (b) Static performance. (c) Multi-agent performance.

runtimes.

2.3.4.1 Increasing cost tree search (ICTS)

A novel formalization and optimal algorithm of the MAPF problem was presented in [Sha+13; Sha15]. ICTS construct a tree of the cost of the paths of all agents as nodes. The tree grows to explore all possible path solutions of the problem and calculate the cost of each solution (node grow). Once the tree constructed (and pruned if equivalent or useless nodes are found), another algorithm searches this coast tree to find the optimal node. ICTS proved to have a higher success rate vs number of agents than A*-based solutions with comparable execution times. Only on specific situations, ICTS was significantly slower than A*-based solutions, but always found optimal solutions.

2.3.4.2 Conflict-based search (CBS) & Improved CBS (ICBS)

The CBS method [Sha+15; Sha15] decomposes the MAPF into a number of constrained single-agent problems, finding an optimal solution. CBS grows a tree of constraints and find paths that are consistent with these constraints. If these paths have conflicts, and are thus invalid, the conflicts are resolved by adding new constraints. CBS works in two levels. At the high level, conflicts are found and constraints are added. The low level finds paths for individual agents that are consistent with the new constraints. A generalized version of CBS (MA-CBS), presented on the same references, outperformed A*-based solutions and ICTS.

An improved version of CBS, ICBS, enhanced runtime and conflict management to further add to the performance of CBS [Boy+15]. Heuristics for the high level search have been added to CBS improving the runtime and expanded nodes [Li+19].

2.3.5 Discussion & Network map of the pathfinding algorithms

This dissertation's digital actuation array produces displacement steps, thus the displacement evolution in space is well represented by a discrete state-space, or a grid. Therefore, a grid-based method would be ideal for the pathfinding problem of the conveyed object on the digital actuator array. This dissertation pathfinding problem, as explained in detail in Chapter 6, is set as an informed semi-static single-agent problem as a first step towards a general solution.

Following the description of the presented solutions (Figure 2.71), this dissertation adapts an A* algorithm for the digital actuator array. A* have been proven to be more efficient than RRTs to solve UAV navigation problems, under the condition of a good grid-environment representation [ZK18]. A* is chosen because it is the base of other performance-enhancement algorithms like any-angle, real-time, any-time and even MAPF solutions. Following this argument, an any-angle pathfinding algorithm, Θ*, is adapted to exploit and evaluate the any-angle generation capabilities of the digital actuator array (this capability is explained in Chapter 3, Section 3.1).

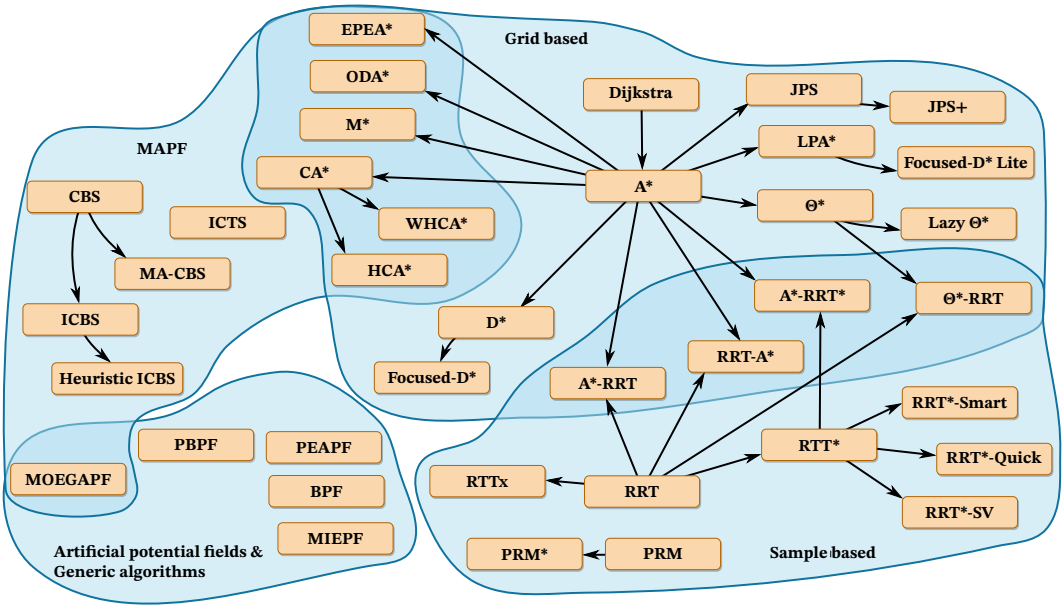

Figure 2.71: Pathfinding algorithm network

Summary and conclusion of Part I

Chapter 1 introduced the concept of *digital actuator*, the discretization and holding functions it needs to operate and the advantages/drawbacks of digital actuation against analog actuation. Examples of digital actuators exploiting material properties, electromagnetic circuits and locking systems as holding functions were presented. A classification of digital actuators by the number and nature of their discrete positions was presented with examples for each type. Then, the planar motion systems *positioners* and *conveyors* were defined. Positioners and conveyors were differentiated by their requirements and examples of each one were presented. Afterwards, the idea of arranging multiple actuators in an array to obtain a system able to accomplish complex tasks was presented. Examples of positioners, loud-speakers, adaptive optic mirrors, displays, and tactile interfaces, were presented. Later on, this dissertation's application context, the microfactory, was explained in detail. This section went from the need of miniaturize the manufacturing systems to the place of microfactories in this challenge, along with microfactory examples from the research and industrial fields. Chapter 1 finished with the scope and context of this dissertation as part of the "Tridimensional micro-conveyance systems for the micro-factory" (ALVEO) research project, funded by the national research agency of France: Agence National de la Recherche (ANR). ALVEO's objective is to develop tridimensional micro-conveyance systems satisfying the needs of the microfactory environment.

The **research question** of this work is: How to exploit an array of digital electromagnetic actuators as a conveyance system to transport objects between different machining/quality stations of a microfactory, efficiently in terms of consumed energy, displacement time, final position and trajectory error, and avoiding collisions with obstacles or other transported objects?

Chapter 2 presented the state of the art related to: micro planar motion systems (divided by physical principles of their actuators), contact mechanics modeling and pathfinding. The first section, micro planar motion systems, explained and exemplified electrostatic, electrothermal, electrowetting, piezoelectric, pneu-

matic and electromagnetic systems. The section discussed the advantages and drawbacks of each physical principle and synthesized a comparative table to evaluate this dissertation's final solution. The second section, contact mechanics, presented the theories and modeling of two crucial phenomena of this dissertation's system: collisions and friction phenomena. The final section, pathfinding, presented the vast approaches developed in the literature to solve the conveyance problem: efficiently move one or multiple objects between desired positions avoiding collisions.

Following these concepts and literature review, this dissertation proposes the following solution road-map for ALVEO's objective:

- Use a modular array of digital electromagnetic actuators based on the Lorentz force principle. The modular design ensures the flexibility, reconfigurability and mobility needed for the microfactory. The digital actuation provides repeatable positions, low energy consumption and ease of integration thanks the open-loop control. The Lorentz electromagnetic principle enables large strokes with medium forces and response times compared with other actuation principles.
- Develop a dynamic model that predicts the acceleration, speed, position and energy consumption of the conveyed objects on the array. The digital actuator array is based on Lorentz electromagnetic force, stick-slip conveyance and a limiting cavity for the mobile parts. This means that the dynamic model would be a multi-physical model integrating electromagnetic, collision and friction modeling.
- Use the dynamic model as a feed-forward, open-loop control in each conveyance step. The feed-forward will be nested in a trajectory control loop of the objects guided by pathfinding trajectory algorithm.
- Develop grid-based pathfinding algorithms for the digital actuator array. Grid-based algorithms are chosen because of the digital actuation of the array. This means that the system evolves in a step by step manner, making the grid representation a good approximation of reality. Two trajectory algorithms are developed: A* and Θ* algorithms. These algorithms are grid-optimal, thus ensuring efficiency in terms of consumed energy, displacement time, final position and trajectory error, and avoid collisions with obstacles or other transported objects. Θ* is also an any-angle algorithm, fully exploiting the motion capabilities of the array.

Part II

Dynamic Model: development, validation & application

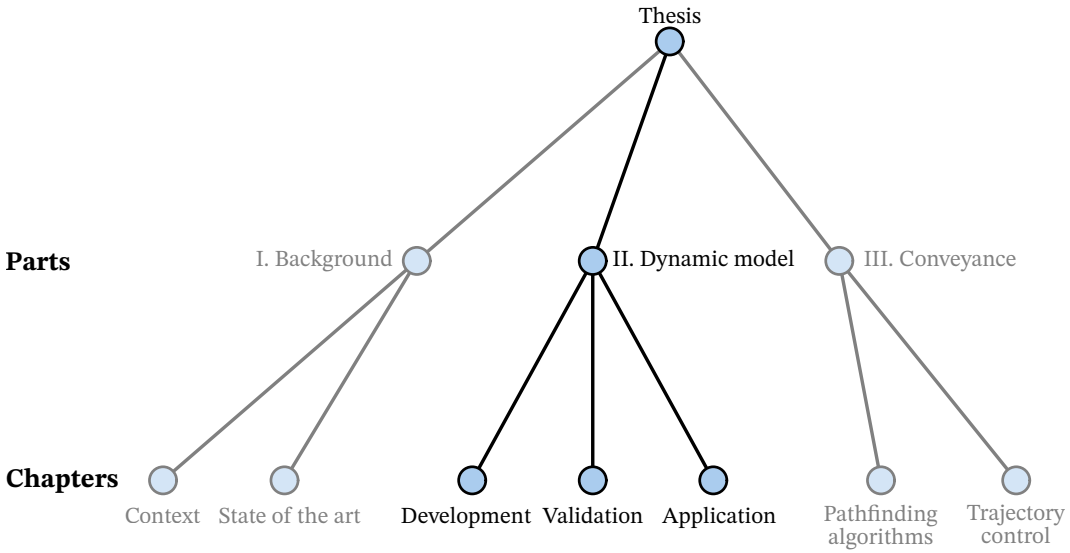

Chapter 3

Digital microconveyor: Principles & Model

This chapter presents the digital microconveyor studied in this thesis. The chapter is divided in three sections.

The first section explains: the conveyor principles from its elementary digital actuator to the digital actuator array used as conveyor; the conveyance strategy used to transport objects; the role of the digital actuator conveyor to satisfy the microfactory environment; and the prototype used for the concept demonstration and experimental tests.

In the second section, a dynamic model of the prototype is built from analytical principles, considering magnetic, electromagnetic, friction and collision phenomena. Then, an identification process is presented to determine the model parameters by experimental tests.

The third section is about the assumptions, hypotheses and neglected phenomena of the developed model.

3.1 Principles

The basic component of the conveyor is the elementary digital actuator (digital actuator or EDA from now on). Multiple digital actuators are arranged in an array to form the digital actuator array (array or DAA from now on). A 2×2 array is used to explain the array's principle and conveyance strategy. The role of the digital actuator conveyor to satisfy the microfactory environment is then exemplified. Finally, the prototype used for the concept demonstration and experimental tests is presented.

3.1.1 Elementary digital actuator (EDA) principles

The elementary digital actuator (EDA) is composed of five gold-coated NdFeB permanent magnets in a silicon structure (Figure 3.1). The permanent magnet at the center of the digital actuator is called mobile permanent magnet (MPM), with dimensions of 2 mm × 2 mm × 1.2 mm. The MPM lies in a square cavity of dimensions 2.2 mm × 2.2 mm × 1 mm, i.e. slightly larger than the MPM cross section. The stroke of the digital actuator in both x and y directions is defined by the gap between the MPM and the cavity (0.2 mm). The other four permanent magnets, named fixed permanent magnets (FPMs), are fixed around the square cavity. The magnetization of the MPM and FPMs are directed along the z-axis in opposite directions to obtain an attracting magnetic force between them. This configuration creates five equilibrium positions for the MPM: each corner of the cavity, giving a digital actuation nature to the elementary digital actuator; and the center of the square cavity. On this last position, the four attracting magnetic forces due to the FPMs cancel and the net force on the MPM is zero. Because this last equilibrium position is unstable, it is not considered as a valid state of the actuator in the normal operation of the system.

To actuate the digital actuator, two wires are placed under the cavity for each displacement axis (a pair of actuating wires). There are two wires per axis to maximize the generated electromagnetic force. When an electrical current passes through the wires, a Lorentz force appears between the MPM and the wires. The wires placed along the x-axis switch the MPM in the y-axis and vice versa. The wires and their currents are named by its actuating axis, i.e. the x wires, carrying the x current (I_x) are the ones actuating the MPM in the x-axis as shown in Figure 3.1. A current used to generate a displacement is named *driving current* ($\mathrm{I_d}$). The two pairs of actuating wires can be activated simultaneously. When both pairs generate displacements in their respective axis, moving the MPM in a diagonal, both are considered to be carrying driving currents. If one of the actuating wires is used to generate a force towards the silicon wall, the current is called *holding current* ($\mathrm{I_h}$). The holding current can be used to ensure that the MPM's stays in contact with the silicon wall along an axial movement, improving the straightness of the resulting displacement.

To avoid electrical contact between the x and y wires, they are placed in different layers of a multi-layer printed circuit board (PCB). The separation between the PCB layers is 100 µm. This circuit layer distance was chosen as small as possible to obtain a similar behavior for each axis ($\mathrm{d_3}$). Finally, a glass layer is placed between the MPM and the circuit board to avoid their direct contact and give the MPM a plane surface to slide between the discrete positions.

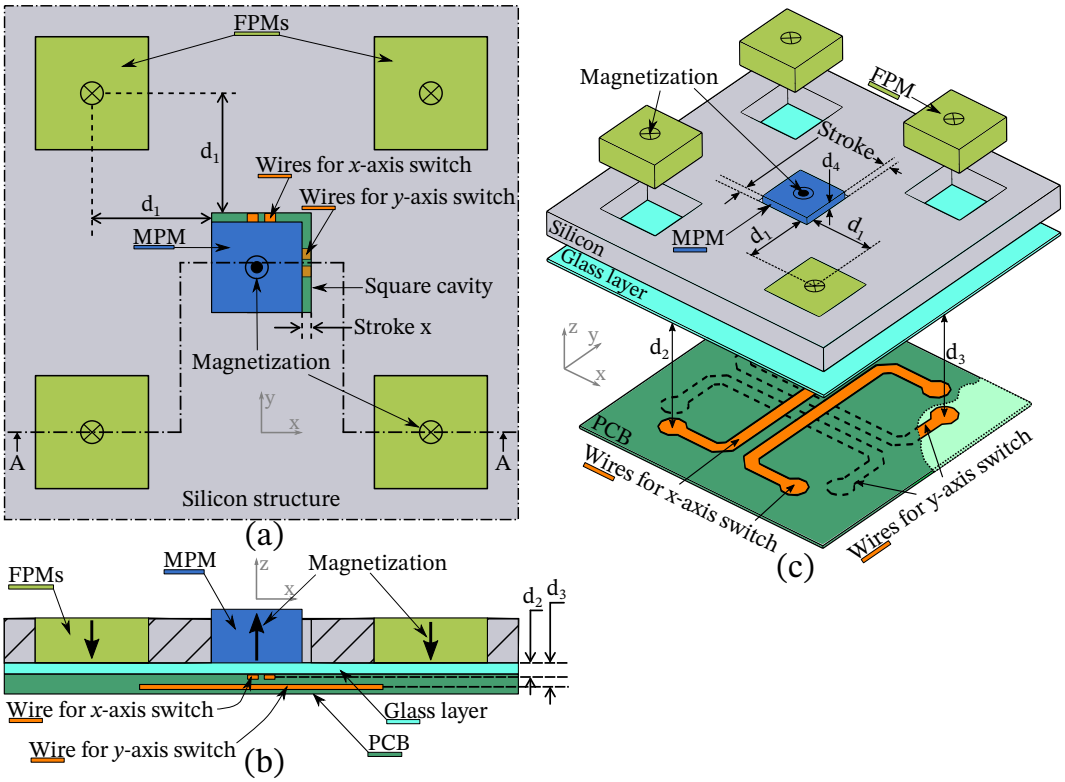

Figure 3.1: Square Elementary Digital Actuator (EDA) views (a) Top. (b) Front (A-A cut). (c) Isometric.

The elementary digital actuator characteristics are presented in Table 3.1. The design parameters d_2, stroke and d_1 were determined thanks to the actuator's analytical model (explained in Section 3.2). The distance d_2 influences the electromagnetic force generated on the MPM. This force is maximized by minimizing d_2. For this, a 100 µm-thick glass layer between the MPM and the circuit board was used. The actuator's stroke should be large to exploit the benefits of Lorentz actuation principle, but it needs to be short to keep the displacement resolution fine and avoid undesired MPM rotations. A 200 µm stroke was chosen as compromise following the results of previous single EDA prototypes [Pet+15]. To determine d_1, the model was used to calculate the magnetic force on the MPM at its discrete positions (without a conveyed mass). To ensure the digital nature of the actuator, the magnetic holding force needs to be as strong as possible, but, a too strong magnetic force would impose a high driving current to overcome the magnetic force and actuate the MPM. The distance d_1 was then chosen to ensure that the MPM will return to its discrete position even if it was at 15% of the stroke value from a discrete position (30 µm for a 200 µm stroke). Finally, to ensure that the MPM is the only contact point with the rigid conveyed object, they are thicker than the FPMs along the z-axis by 0.2 mm (d_4). The digital actuator has then 2 DoF: the x and y-axis switching.

Table 3.1: Elementary Digital Actuator (EDA) Characteristics

Element	Dimensions (mm)	Mass	Material	Mag. (T)
MPM	$2.0 \times 2.0 \times 1.2$	34 mg	NdFeB	1.22
FPM	$2.2 \times 2.2 \times 1.0$	45 mg	NdFeB	1.43
Structure	$9.6 \times 9.6 \times 1.0$	104 g	Silicon	–
Glass layer	$4.0 \times 4.0 \times 0.1$	64 mg	Glass	–
Variable	**Distance between**			**Value (μm)**
d_1	Cavity and FPMs			2600
d_2	MPM and *x* wire			185
Stroke	Stroke in both axes			200
d_3	MPM and *y* wire (wire separation)			253
d_4	MPM and FPM thickness (*z*-axis)			200

3.1.2 Digital actuator array (DAA) principles

The digital actuator array (DAA) consists of a matrix of elementary digital actuators (EDAs). Adjacent actuators share a pair of FPMs to decrease the array size. The array combines individual actions of each actuator to obtain complex tasks. The smallest square-matrix DAA capable of planar motion is a 2×2 array (Figure 3.2). The "stick-slip" strategy to convey an object on top of the array, using the DAA collaborative actuation, is presented in Figure 3.3. The conveyed object is placed on top of the MPMs (Figure 3.3 (a)). At the first step, the MPMs are switched simultaneously to displace the object (Figure 3.3 (b)). During this step, the friction force between the MPMs and the conveyed object accelerates the object until the MPMs reach their discrete position (thus called "stick"). Once the MPMs stop, the dynamic friction due to the relative movement between the moving object and the static MPMs acts as a brake to the object until it stops, reaching a *displacement step*. The second phase, "slip", resets the configuration for a new displacement step: each MPM is individually switched back to return to its initial position (Figure 3.3(c)-(d)). The friction force between a single MPM and the object is lower than the opposition force of all the other MPMs. During the steps represented in Figure 3.3(c) and Figure 3.3(d), the MPMs slide without moving the object (thus called "slip" phase). When all the MPMs are back to the initial position, a new displacement step can be executed (Figure 3.3(a)). The current used to return the MPMs to the initial position is called *return current* (I_r).

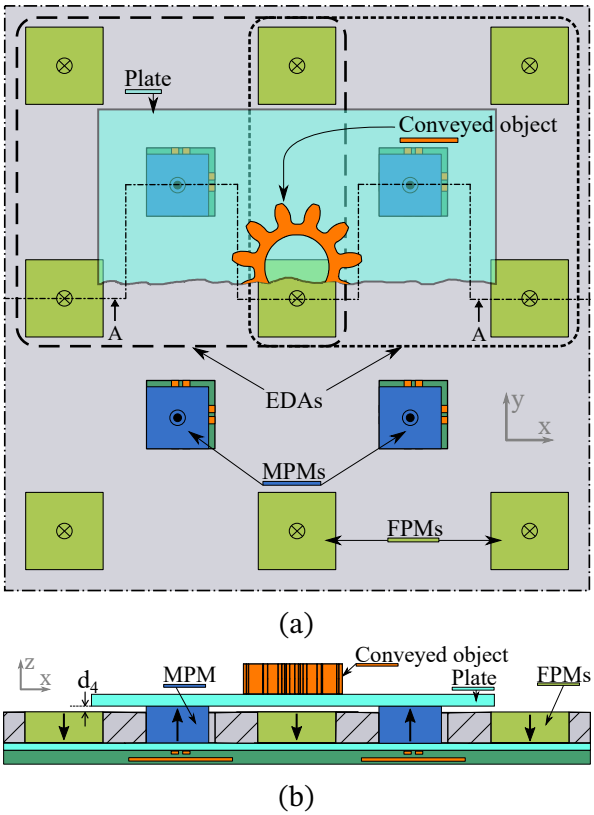

Figure 3.2: 2 × 2 DAA. (a) Top view. (b) Front view (A-A cut).

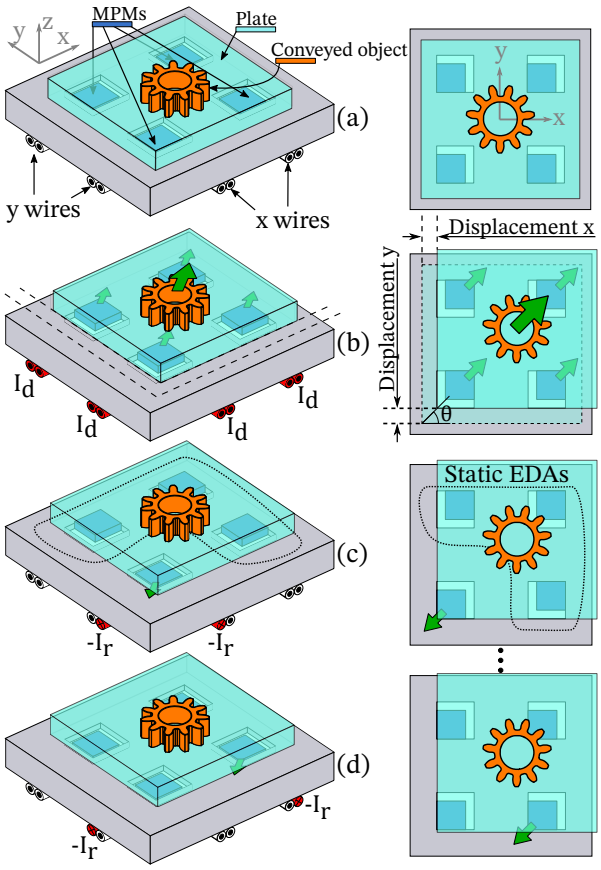

Figure 3.3: Stick-slip conveyance principle of the DAA (one displacement step represented): (a) Initial state. (b) Simultaneous MPM displacement. (c) to (d) Return of the MPMs to the initial position.

3.1.3 Digital actuator array: a smart surface microconveyor

The 2×2 DAA can be extended to any $n \times m$ matrix. Modules of different matrix sizes can be assembled to obtain a "smart surface" conveyor (an array of arrays). The DAA would then convey objects between the microfactory stations. The DAA modular assembly, planar motion capability and independent control of the sub-matrix in the smart surface responds to the needs of flexibility, reconfigurablility and parallel procedures needed in the microfactory, as discussed in Section 1.5 (Context: the microfactory environment).

Figure 3.4 exemplifies this flexibility and reconfigurability. A microfactory with four stations is first arranged in a square configuration (Figure 3.4a). The DAA transports different objects in parallel. If the stations' location change inside the square area of the array, there is no need to change the conveyor configuration, as the DAA can reach any point on its smart surface. If the factory is re-arranged with a station outside the conveyor's area, the DAA can be modified to a shape that serves the configuration. A reduced DAA area (Figure 3.4b), or a larger square area (if the factory constrains allows for it) are solutions to the new configuration.

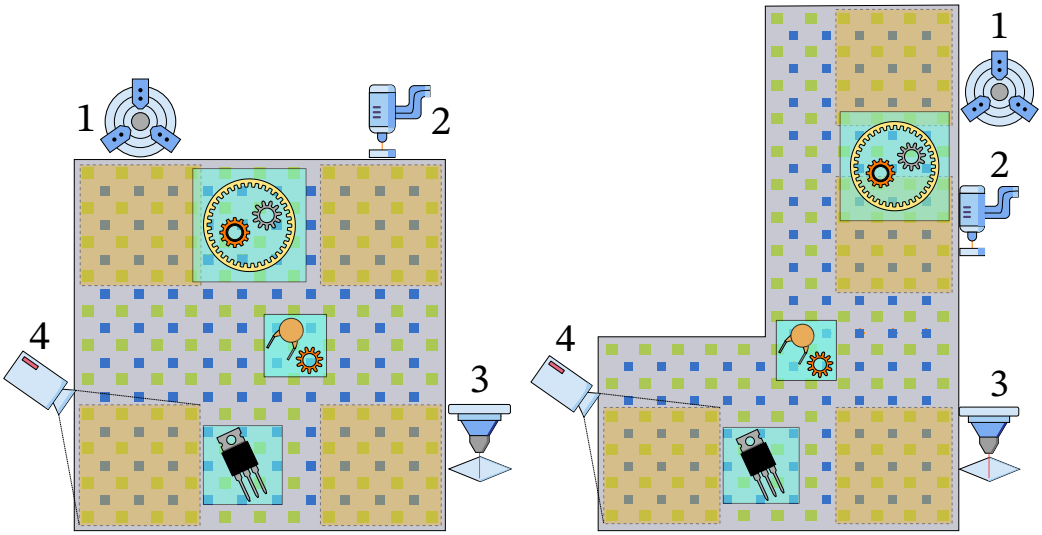

Figure 3.4: DAA serving a turning (1) 3D printing (2) laser cutting (3) and quality (4) stations. Microfactory configurations: (a) Square. (b) L-shape.

3.1.4 Prototype

A prototype 5×5 DAA was microfabricated to be evaluated as a microfactory conveyor (Figure 3.5). This was part of the doctoral thesis of Zhichao Shi under the ANR "READMI" project [Shi17]. Apart from the already explained MPMs

and FPMs, there are additional permanent magnets at the perimeter of the array's active area. These magnets, called Balancing Mobile Permanent Magnets (BMPMs), try to balance the magnetic force on the MPMs, i.e., that all MPMs have the same magnetic force on their cavities (Figure 3.5a). The BMPMs are aligned with the MPMs, have a magnetization of 1.17 T (repelling the MPMs) and a size of 1.5 mm × 1.5 mm × 1.0 mm. Their distance to the active area is 1.4 mm. The prototype's active area is 50 mm × 50 mm. Four non-magnetic screws fix the array, underlying glass layer and PCB to a laser-cut acrylic base. These screws tune the array's flatness (Figure 3.5b). The acrylic base is screwed to the flat working table. The control signals for the x and y axes are connected to dedicated ports at the bottom and right sides of the array, respectively (x-axis and y-axis inputs in Figure 3.5b).

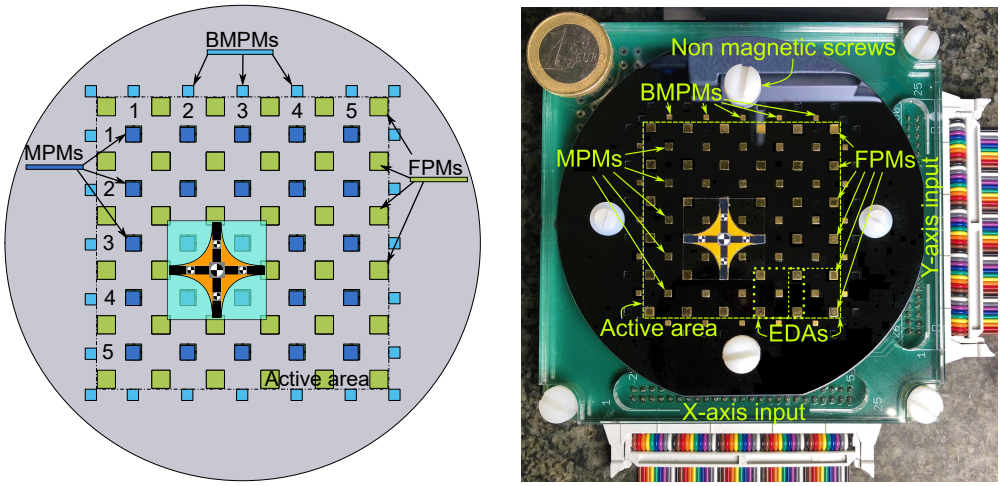

(a) (b)

Figure 3.5: 5 × 5 DAA prototype (a) Schema. (b) Real.

The prototype was fabricated on a ⌀ 100 mm, 1 mm thick, 1-20 Ω cm silicon wafer with a ⟨100⟩ crystal orientation. The wafer was covered with a 12 µm-thick positive photoresist resin (AZ4562 and developed in AZ400K, both by Microchemicals GmbH). This thickness protected the non-etching silicon areas while allowing for an easy resin removal after the etching process [Shi17]. An Inductive-Coupled Plasma Deep Reactive Ion Etching (ICP-DRIE) and Bosch process were used to etch the magnet cavities through the silicon thickness. The Bosch process was based on alternating etching and passivation steps: dry etching with sulfur hexafluoride (SF_6) and passivation with the deposition of octafluorocyclobutane (C_4F_8) polymer [Her+19].

Figure 3.6 is a scanning electron microscopy (SEM) image of a MPM cavity (cut view). The image shows that the vertical sidewall has an angle of 89.4° (the design parameter was 90°). A measurement of nine cavities and the distances

between them was conducted in a “MarVision MS222” machine with a resolution of 0.5 µm. The maximum error between the design parameters and the prototype measurement was 3 µm with a standard deviation of 1 µm [Shi17].

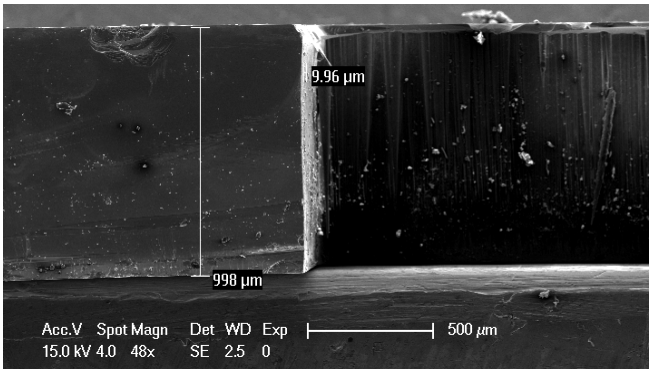

Figure 3.6: SEM front view (cut view) of a magnet cavity [Shi17].

3.2 Dynamic Model

A dynamic model of the array was developed to predict the acceleration, speed and displacement (kinematics) of the MPMs and conveyed object.

The dynamic model assumes that all EDAs in the DAA are homogeneous and distribute the mass of the conveyed object equally. Then, the displacement step is the sum of the efforts of each actuating EDA on the conveyed object.

The model calculates the MPM and conveyed object kinematics as a function of the system variables: intensity and duration of the currents in both actuation axes; number of acting EDAs; and mass of the conveyed object. Three different types of forces act on the system: magnetic forces due to the interaction between the permanent magnets; electromagnetic forces due to the interaction between the MPMs and the control currents; and friction forces between the mobile and fixed parts (Figure 3.7). Each force is calculated at each time-fixed simulation step, as well as the total force acting on the MPM and its share of the conveyed object. The MPM acceleration is calculated at each simulation step using Newton’s Second Law under constant mass assumption. Equation (3.1) states Newton’s Second Law for a single MPM (m_{MPM}) carrying its share of the conveyed object’s mass (m_{object}). The coordinate system origin is placed at the center of the EDA cavity and at the contact point between the MPM and the glass layer separating it from the PCB (gray arrows in Figure 3.7).

$$\sum \vec{F} = \left(m_{MPM} + \frac{m_{object}}{N_{MPMs}} \right) a_{MPM} = \vec{F}_{em} + \vec{F}_{m} + \vec{F}_{f1} + \vec{F}_{f2} + \vec{F}_{f3} \qquad (3.1)$$

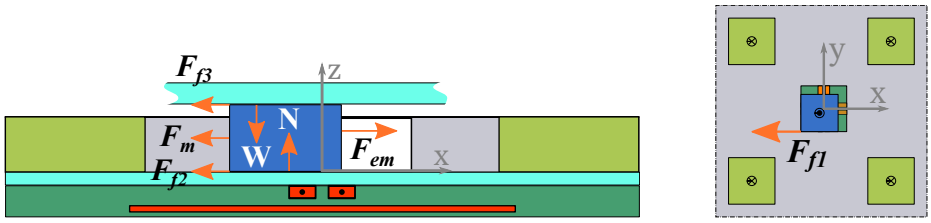

(a) (b)

Figure 3.7: EDA's free body diagram (a) Side view. (b) Top view.

With N_{MPMs} the number of MPMs carrying the object, $\vec{F}_{em}$ the electromagnetic force driving the MPM, $\vec{F}_m$ the magnetic force on the MPM, $\vec{F}_{f1}$ the friction forces between the MPM and silicon cavity, $\vec{F}_{f2}$ the friction force between the MPM and bottom glass layer and $\vec{F}_{f3}$ the friction force between the MPM and carried object. This $\vec{F}_{f3}$ is the driving force of the carried object. The MPM acceleration a_{MPM} is integrated to obtain the MPM's speed and position.

First, the magnetic flux density (B-field) of a cuboid permanent magnet is derived, as it will characterize both the electromagnetic and magnetic force on the MPM. Then, the system's forces (electromagnetic, magnetic and friction) analysis are presented. Finally, the collisions and rebounds of the MPM as it reaches its discrete position are studied.

3.2.1 Rectangular cuboid magnetic flux density

The magnetic flux density (B-field), $\vec{B}$, of all rectangular cuboids (rectangular parallelepipeds or orthogonal parallelepipeds) magnets, such as the MPM, FPMs and BMPMs, can be derived from the Maxwell equations assuming magnetostatic conditions. This is, the time-dependent terms in Maxwell's equations, presented in Equation (2.22), are neglected. This means that the currents and magnetic flux densities are assumed static and constant. The magnetostatic equations, in differential and integral form, are [Fur01]:

$$\nabla \times \vec{H} = \vec{J} \qquad \oint_C \vec{H} \cdot d\vec{l} = \int_S \vec{J} \cdot d\vec{s} \tag{3.2}$$

$$\nabla \cdot \vec{B} = 0 \qquad \oint_S \vec{B} \cdot d\vec{s} = 0 \tag{3.3}$$

With H the magnetic field intensity (A/m) and B the magnetic flux density (T). J, the free electric current density (A/m^2), is the source of the magnetic fields. The constituent equation of the magnetostatic Maxwell theory is:

$$\vec{B} = \mu_0(\vec{H} + \vec{M}) \tag{3.4}$$

Where M is the magnetization vector accounting for the density of magnetic dipole moment in the material studied (A/m).

The *charge model* is used to reduce the cuboid magnet into a "magnetic charge" distribution that generates its external magnetic flux density field (also called Coulomb approximation). For this, all permanent magnets are supposed perfectly cuboid, their magnetization vector confined to their volume V, falling abruptly to zero outside of this volume, and in free space ($\vec{B} = \mu_0 \vec{H}$). This yields [Fur01]:

$$\vec{B}(\vec{r}) = \frac{\mu_0}{4\pi} \int_V \frac{\rho_m(\vec{r'})(\vec{r} - \vec{r'})}{|\vec{r} - \vec{r'}|^3} dv' + \frac{\mu_0}{4\pi} \oint_S \frac{\sigma_m(\vec{r'})(\vec{r} - \vec{r'})}{|\vec{r} - \vec{r'}|^3} ds' \tag{3.5}$$

With μ_0 the permeability of free space ($4\pi \times 10^{-7}$ N A^{-2}), $\vec{r}$ the position vector of the observation point and $\vec{r'}$ the position vector of the source point.

The charge model uses the following equations to translate the magnet's magnetization vector $\vec{M}$ into surface (σ_m) and volume (ρ_m) charge densities [Fur01]:

$$\sigma_m = \vec{M} \cdot \hat{n} \tag{3.6}$$

$$\rho_m = -\nabla \cdot \vec{M} \tag{3.7}$$

With $\hat{n}$ the unit surface normal vector of the magnet geometry.

For a perfect cuboid magnet with dimensions $(x_2 - x_1), (y_2 - y_1), (z_2 - z_1)$ (Figure 3.8a):

$$\hat{n} = \begin{cases} \pm\hat{x} & x = x_1, x_2 \\ \pm\hat{y} & y = y_1, y_2 \\ \pm\hat{z} & z = z_1, z_2 \end{cases} \tag{3.8}$$

Applying Equation (3.6) and Equation (3.7) to $\hat{n}$, and assuming a perfectly aligned magnetization along the z-axis, we obtain $\rho_m = 0$, $\sigma_m = M$ for $z = z_2$ and $\sigma_m = -M$ for $z = z_1$, as illustrated in Figure 3.8.

Substituting σ_m in Equation (3.5), the magnetic flux density field of the cuboid magnet is obtained, illustrated in Figure 3.9 and expressed in cartesian components as [Fur01]:

$$\begin{aligned} B_x(x,y,z) = \frac{\mu_0 M}{4\pi} \sum_{k=1}^{2} \sum_{m=1}^{2} (-1)^{k+m} \\ \times \ln \left[\frac{(y - y_1) + \sqrt{(x - x_m)^2 + (y - y_1)^2 + (z - z_k)^2}}{(y - y_2) + \sqrt{(x - x_m)^2 + (y - y_2)^2 + (z - z_k)^2}} \right] \end{aligned} \tag{3.9}$$

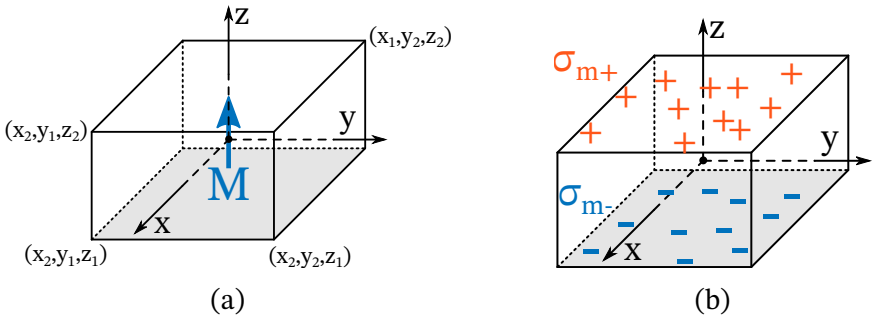

Figure 3.8: Cuboid magnet representation. (a) Coordinate system and magnet dimensions. (b) Charge model.

$$B_y(x,y,z) = \frac{\mu_0 M}{4\pi} \sum_{k=1}^{2} \sum_{m=1}^{2} (-1)^{k+m} \times \ln \left[\frac{(x-x_1) + \sqrt{(x-x_1)^2 + (y-y_m)^2 + (z-z_k)^2}}{(x-x_2) + \sqrt{(x-x_2)^2 + (y-y_m)^2 + (z-z_k)^2}} \right] \tag{3.10}$$

$$B_z(x,y,z) = \frac{\mu_0 M}{4\pi} \sum_{k=1}^{2} \sum_{n=1}^{2} \sum_{m=1}^{2} (-1)^{k+m+n} \times \tan^{-1} \left[\frac{(x-x_n)(y-y_m)}{(z-z_k)\sqrt{(x-x_n)^2 + (y-y_m)^2 + (z-z_k)^2}} \right] \tag{3.11}$$

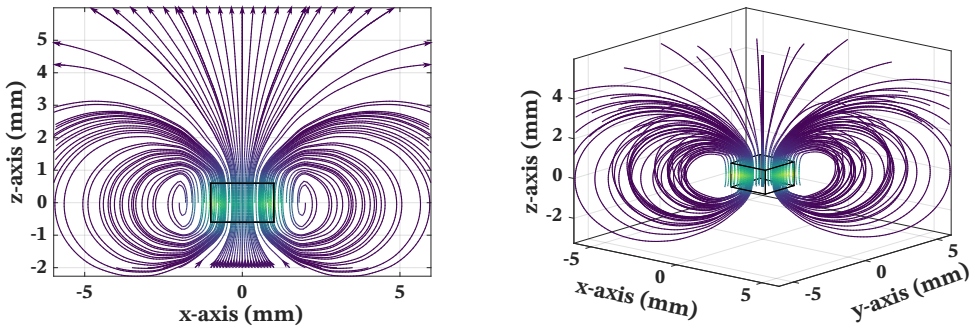

Figure 3.9: Magnetic flux density (B-field) contour lines of a cuboid permanent magnet (a) *zx* or *zy*-plane projection. (b) 3D view.

3.2.2 Electromagnetic force modeling

Lorentz's electromagnetic force equation is used to model the electromagnetic driving force on the MPM by the actuating wires ($\vec{F}_{em}$). The Lorentz's equation for a charged particle under the magnetic flux density field of the MPM ($\vec{B}_{MPM}$)

is Equation (3.12) [Fur01][1]:

$$\vec{F}_{em} = q\left(\vec{v} \times \vec{B}_{MPM}\right) \tag{3.12}$$

With q the elementary charge element in the wire and v the velocity of this elementary charge.

Equation (3.12) can be generalized for electrical currents considering ρ_u charges per unit volume moving with velocity $\vec{u}$. This gives a volume current density $\vec{J} = \rho_u \vec{u}$. The force on each charge follows Equation (3.12) and therefore the force per unit volume due to the MPM's magnetic flux density ($\vec{B}_{MPM}$) is [Fur01]:

$$\vec{f} = \vec{J} \times \vec{B}_{MPM} \tag{3.13}$$

The total force is then the integral of $\vec{f}$ over the conductor's volume

$$\vec{F}_{em} = \int_v \vec{f} dv \tag{3.14}$$

Equation (3.14) is simplified to Equation (3.15) considering thin conducting wires of length l porting a current I:

$$\vec{F}_{em} = I \int_{wire} d\vec{l} \times \vec{B}_{MPM} \tag{3.15}$$

The electromagnetic force depends then on the current intensity of the wires, the length of the wires and the magnetic flux density of the MPM.

The current intensity is the control variable of the system. The wire length and geometry are described in Figure 3.10.

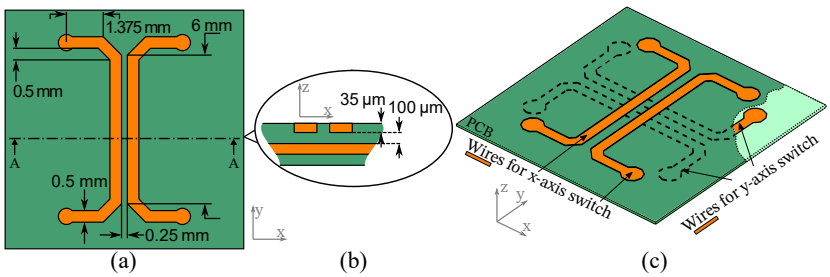

Figure 3.10: PCB geometry. (a) Top view. (b) A-A cut front view. (c) Isometric view.

Using the previously derived expressions for the magnetic flux density of the MPM ($\vec{B}_{MPM}$, Equations (3.9) to (3.11)), the electromagnetic force can be

[1]Note that the Coulomb contribution of the fundamental Coulomb-Lorentz electromagnetic force (Equation (2.20), Section 2.1.6) is neglected as the external electric field intensity (E), is zero in this scenario.

obtained. Figure 3.11 presents the MPM's B-field components in both 2D (fixing $y = 0$) and 3D space for both actuating wires.

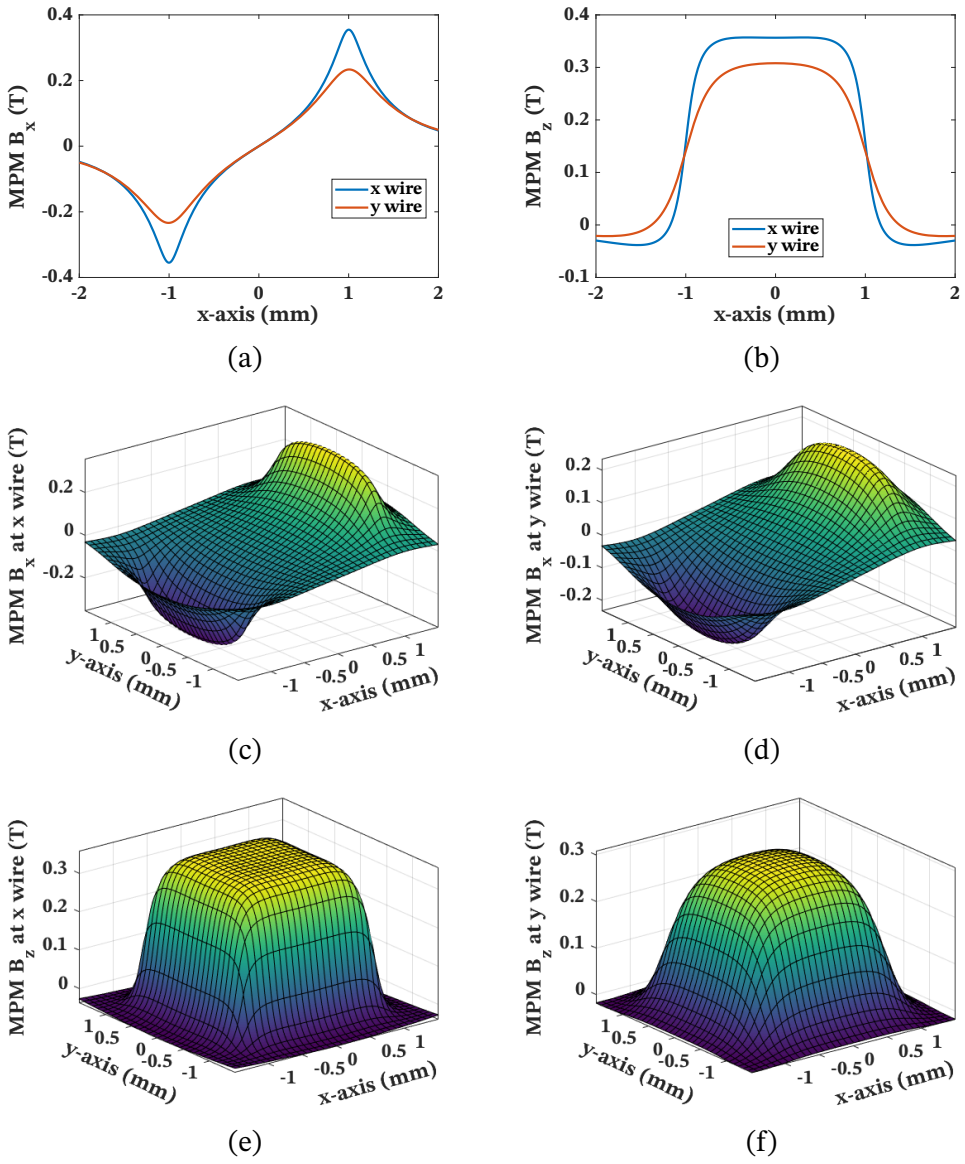

Figure 3.11: MPM B-field. (a) x-axis component $\vec{B}_x(x)$ on x and y wires. (b) z-axis component $\vec{B}_z(x)$ on x and y wires. (c) x-axis component $\vec{B}_x(x, y)$ on x wire. (d) x-axis component $\vec{B}_x(x, y)$ on y wire. (e) z-axis component $\vec{B}_z(x, y)$ on x wire. (f) z-axis component $\vec{B}_z(x, y)$ on y wire. The B-field y-axis components $\vec{B}_y$ are symmetrical to the x-axis components.

The difference of the B-field on the x and y wires observed in Figure 3.11 is explained by the different distance between the wires to the MPM. The x wire is closer to the MPM than the y wire (d_2 and d_3, respectively). This will generate a difference in the electromagnetic driving force between the wires.

With the components of B_{MPM}, Equation (3.15) can be obtained for both actuation wires. Figure 3.12 presents the electromagnetic force components for

the x and y wires using I =1 A on each wire. The coordinate system origin is at the EDA's cavity center.

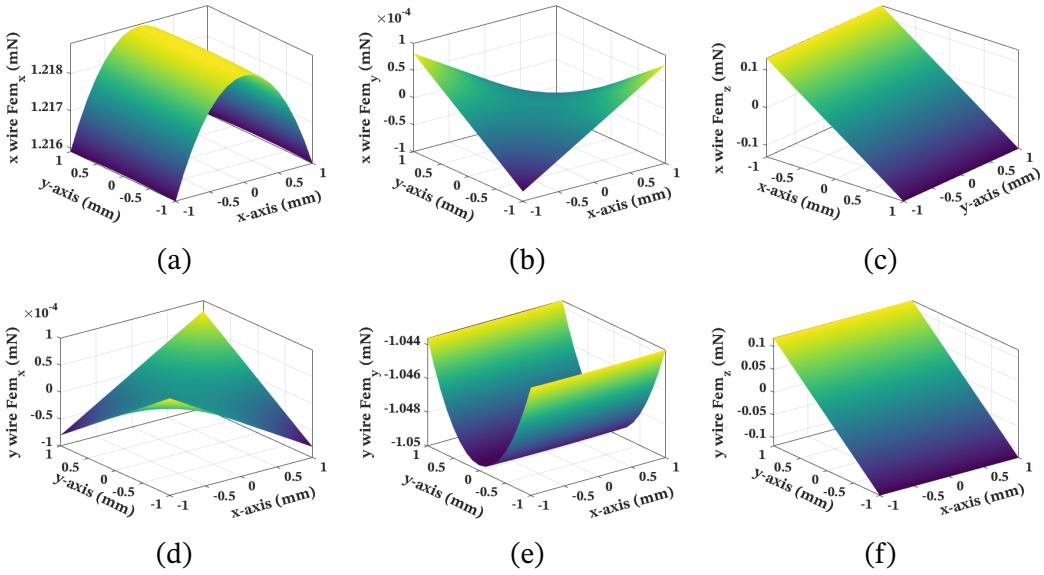

Figure 3.12: Electromagnetic force. (a) x-axis component $\vec{F}_{emx_x}(x,y)$ on x wire. (b) y-axis component $\vec{F}_{emx_y}(x,y)$ on x wire. (c) z-axis component $\vec{F}_{emx_z}(x,y)$ on x wire. (d) x-axis component $\vec{F}_{emy_x}(x,y)$ on y wire. (e) y-axis component $\vec{F}_{emy_y}(x,y)$ on y wire. (f) z-axis component $\vec{F}_{emy_z}(x,y)$ on y wire.

The $\vec{F}_{em}$ on the x wire is divided in its cartesian components. The x component ($\vec{F}_{emx_x}$, Figure 3.12a) drives the MPM in the x-axis direction. The y component is very weak (note the 10^{-4} in Figure 3.12b), indicating a very low cross-coupling between the axes. The z component is not negligible. It generates an upward (z-axis) force along half of the actuator's stroke and a downward (-z-axis) force along the other half of the stroke. This changes the normal force between the MPM and the glass layer, affecting the friction force between them. The $\vec{F}_{em}$ on the y wire is symmetrical to the x wire but with a slightly smaller magnitude. This is due to the difference in distance between the MPM and the wires (d_2 and d_3).

3.2.3 Magnetic forces modeling

The charge model of a cuboid magnet also gives an expression for the magnetic force between two such magnets. One "influenced" permanent magnet suffers a magnetic force due to another "source" permanent magnet's magnetic flux density following Equation (3.16) [Fur01]:

$$\vec{F}_m = \int_V \rho_m \vec{B}_{ext} dv + \oint_S \sigma_m \vec{B}_{ext} ds \tag{3.16}$$

With ρ_m the volume charge density of the influenced magnet, σ_m the surface charge density of the influenced magnet and $\vec{B}_{ext}$ the external magnetic flux density, the B-field generated by the source permanent magnet onto the influenced permanent magnet.

Equation (3.16) is not always possible to implement analytically. In the studied case, it would mean to integrate Equations (3.9) to (3.11) in two or/and three dimensions (rather than along the wire length for the electromagnetic force), which has no analytical solution. An alternative is to divide the surface S of the influenced magnet into p areas ΔA and evaluate the magnetic force of this area unit under $\vec{B}_{ext}$ (the source permanent magnet B-field). This process yields the discrete version of the charge model magnetic force, Equation (3.17) [Fur01].

$$\vec{F}_m = \sum_n \rho_m(x_n)\vec{B}_{ext}(x_n)\Delta V_n + \sum_p \sigma_m(x_p)\vec{B}_{ext}(x_p)\Delta A_p \tag{3.17}$$

As previously deduced, $\rho_m = 0$ for the cube magnet. Therefore, the discrete equation for the magnetic force between two cuboid permanent magnets is:

$$\vec{F}_m = \sum_p \sigma_m(x_p)\vec{B}_{ext}(x_p)\Delta A_p \tag{3.18}$$

Figure 3.13 illustrates this discrete magnetic force equation.

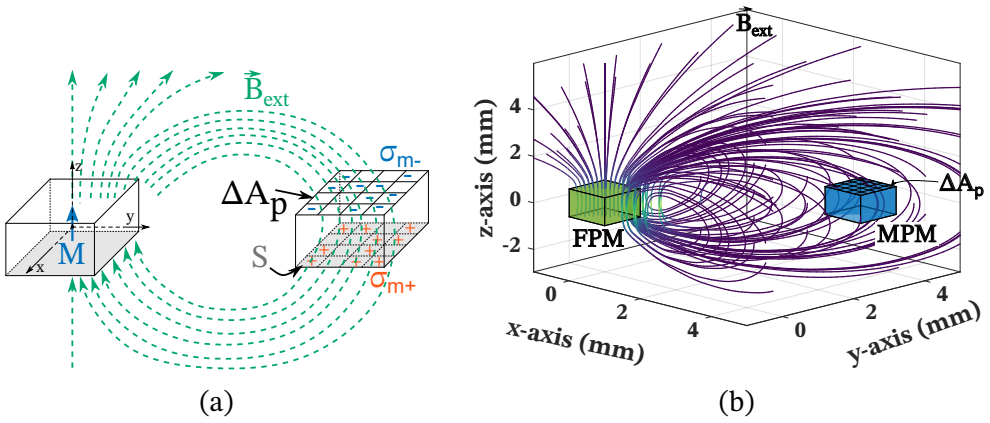

(a) (b)

Figure 3.13: Discrete magnetic force process. (a) Schema. (b) Analytical.

To compute the total magnetic force on the MPM due to the FPMs ($\vec{F}_m$), the B-field of all four FPMs is used as $\vec{B}_{ext}$ in Equation (3.18). This produces the magnetic attraction presented in Figure 3.14. The figure shows the five equilibrium positions of the MPM inside the cavity (corners plus center) and the digital nature of the EDA actuation (magnetic holding function). The magnetic force components are presented as a function of the MPM's x-axis position. The y-axis is symmetrical to the x-axis. At a discrete position, the MPM suffers a

0.426 mN force along the x and y axes.

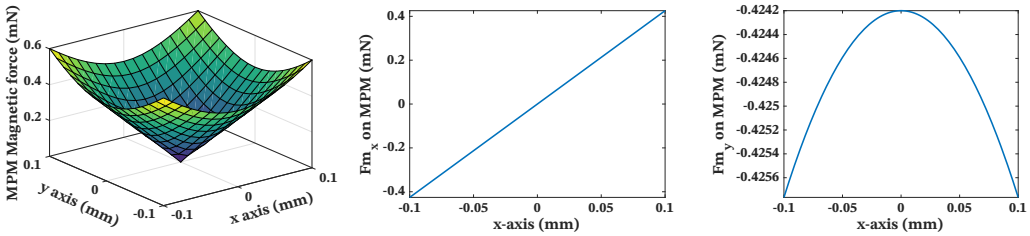

(a) (b) (c)

Figure 3.14: Magnetic force on the MPM cavity due to the FPMs (a) Magnetic force magnitude surface. (c) x-axis magnetic force component. (d) y-axis magnetic force component.

3.2.3.1 Magnetic homogeneity of the DAA

The presented analytical solution computes the magnetic force on the MPM due to the FPMs of one EDA. The next step is to consider the entire DAA system with all its permanent magnets. This is important as the magnetic force acts as the holding force of the MPMs in its discrete positions and influences the interaction of the MPM with its driving current. If each EDA of the DAA behaves equally, i.e, the DAA is homogeneous, the dynamic model can be equally applied to every EDA of the DAA. Therefore, the magnetic homogeneity of the DAA is studied next.

The analytical expression of magnetic force (continuous or discrete) can only be evaluated when the external magnetic flux density ($\vec{B}_{ext}$) can be deduced. This is only possible for very basic, regular and symmetric geometries. The cube geometry of the presented EDA has a discretized analytical solution, but, if the geometry of the magnets change for other EDA designs, an analytical solution could not exist. These other geometries might require software approximations. A general software approximation will allow to adapt the dynamic model to other EDA geometries.

To evaluate the magnetic homogeneity of the DAA, a model was built with the semi-analytical software Radia, developed by the European Synchroton Radiation Facility (ESRF). The Radia software uses the boundary integral method, in contrast to other software that use finite element methods [CEC98; ECC98]. In Radia, magnetized objects are modeled as equivalent magnetic charges. The magnet's pole are subdivided in area elements (as with the discrete analytical solution presented). The magnetic field and its integral along a straight line can be computed for each field source, at any point, using analytical formulas [Le +16]. The advantages and drawbacks of Radia over finite element methods are

[CEC98; ECC98]:

- Geometries opened to infinity are easily simulated, as it does not need parametrization of the free space.
- The precision of the results only depends on the refinement of subdivision of the poles and magnets. With the finite element codes, one needs to mesh the whole space (including air) up to infinity and the estimation of the dominant source of errors is difficult (pole, magnet, air, boundary condition at infinity etc.)
- The field integral of magnetic devices matches the analytical solutions [ECC98]. The accuracy of the field integral from a finite element code is very sensitive to the truncation at infinity, the step of the numerical integration in addition to the precision required for the computation of the field at each point.
- As a drawback, Radia presents discontinuities of the field inside the magnets, at the border between individual volumes introduced by the subdivision. This originates from the assumption of a uniform magnetization in each individual volume.

Radia was used by [Kit+19] to simulate and measure the magnetic field of an undulator prototype for generating terahertz radiation from electron beams. The magnetic field was measured by using a Hall probe. Radia was used to optimize the prototype's design (Figure 3.15).

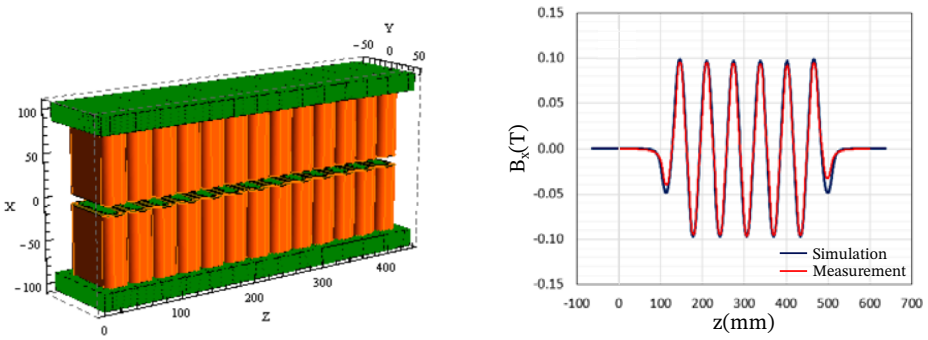

(a) (b)

Figure 3.15: THz undulator by [Kit+19]. (a) 3D RADIA model (b) The horizontal magnetic field results.

Radia was also used on [Le +16] to design a prototype of high gradient quadrupoles for the European Synchrotron Radiation Facility. The quadrupoles are key components for the coming generation of storage ring based light sources.

These two works underline the efficacy of Radia as a design and analysis tool for magnetic devices, such as the treated microconveyor.

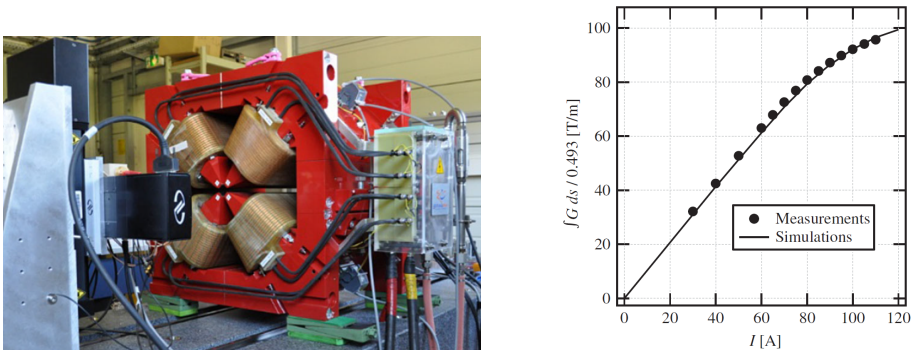

(a) (b)

Figure 3.16: High gradient quadrupole electromagnet by [Le +16]. (a) Prototype (b) Magnetic gradient results.

The magnetic homogeneity of the DAA can be evaluated with the dispersion of the magnetic force on the MPMs. A smaller dispersion translates to a better homogeneity. The developed Radia model considers all the DAA's permanent magnets (MPMs, FPMs and BMPMs). The magnetic force exerted on each MPM due to all permanent magnets is computed with the Radia model. All MPMs were placed at the same discrete position inside each cavity (lower left corner) and the magnetic force along the x-axis was computed. As the array is symmetrical, the y-axis force follows the same behavior.

Figure 3.17 presents the heatmap of the x-axis magnetic force for all EDAs in the 5×5 array. Each cell in the heatmap represents an EDA in the given row and column, and the cell's value is the magnetic force of that EDA. The heatmap evaluates the dispersion of the magnetic force spatially. The heatmap shows that the array columns 1 and 5 contain the extreme values of the set while columns 2 through 4 (forming a 3×3 DAA considering both the x and y axes) are more balanced. The reason for the inhomogeneity of columns 1 and 5 is their placement at the array's perimeter, were only the additional BMPMs compensate the magnetic force generated by the rest of the array. This indicates that larger arrays with more rows and columns of EDAs provide a larger internal homogeneous zone.

The raincloud plot [All+19] (Figure 3.18) presents the data of the heatmap (dots) with its statistical box plot (percentiles) and probability distribution of the data assuming normal distribution. The mean value of magnetic force was 0.422 mN for the 5×5 DAA, with a standard deviation of 0.26 mN. The raincloud revealed the two extreme groups of columns 1 and 5, explaining the high standard deviation value. Inside the area of columns 2 to 4 (3×3 DAA), the mean value of magnetic force was 0.442 mN with a standard deviation of 0.03 mN. This magnetic force standard deviation is 6.6% of the mean value which translates to

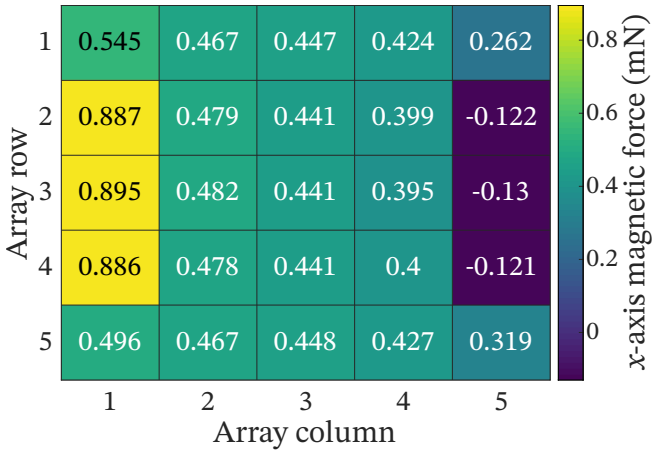

Figure 3.17: x-axis magnetic force heatmap of a 5×5 DAA.

a homogeneous behavior.

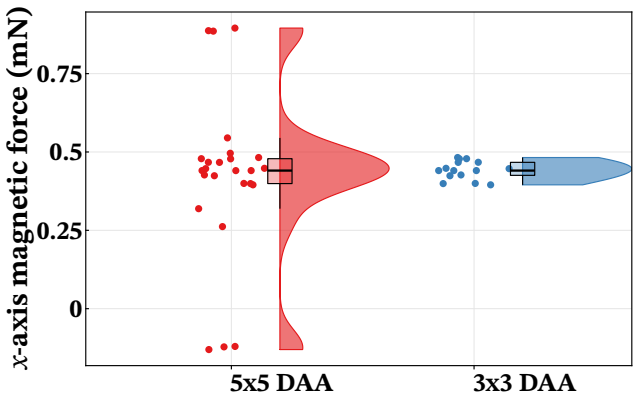

Figure 3.18: Raincloud plot of the x-axis magnetic force homogeneity of the 5×5 and 3×5 DAA.

3.2.4 Friction modeling

The friction model needs to reproduce the "stick-slip" conveyance strategy used by the DAA. Also, the dynamic model needs to be nested into a pathfinding algorithm, thus, the friction model should be lightweight and fast in simulation time and resources.

Section 2.2.2 showed that static friction models need less parameters and are faster in simulation than dynamic models but do not model all friction behaviors. Dynamic friction models are more accurate and reproduce complex friction phenomena but are heavier in simulation time, parameter identification and implementation.

From the static friction model comparison (Figure 2.58a), the Karnopp, Bengisu & Akay and Awrejcewicz models predicted very similar results, avoiding

simulation oscillations and predicting stick-slip phenomena. The Bengisu & Akay model, being the simpler of the three, predicted similar behaviors to the LuGre and Gonthier dynamic models (Figure 2.60a and Figure 2.60b) accurately predicting the oscillation lag and stick-slip when the spring reached its maximum length.

Given the mentioned needs for the microconveyor dynamic model and the performance comparison presented, the Bengisu & Akay model was chosen to model the friction phenomena between the MPM, the silicon cavity walls, the glass support and the conveyed object ($\vec{F}_{f1}$, $\vec{F}_{f2}$ and $\vec{F}_{f3}$ in Figure 3.7).

The Bengisu & Akay model is constituted by two equations (one for a finite velocity slope at zero and another to describe the Stribeck effect) [BA94]:

$$\vec{F}_f = \begin{cases} \left(-\frac{F_s}{v_0^2}\left(\|v\| - v_0\right)^2 + F_s\right)\mathbf{sgn}(v) & \|v\| < v_0 \\ \left(F_k + (F_s - F_k)e^{-\zeta(\|v\| - v_0)}\right)\mathbf{sgn}(v) & \|v\| \geq v_0 \end{cases} \tag{3.19}$$

With v the speed of the MPM, F_s the static friction value, F_k the kinetic or dynamic friction value (the settling friction when v tends to ∞), v_0 the transition speed value between the static and kinetic friction and ζ the decay factor for the dynamic friction.

3.2.4.1 Static friction identification

The friction model parameters are identified with two different experimental setups. The first setup uses the inclined plane technique to find the static friction coefficient (F_s) between the MPM and silicon wafer and between the MPM and glass layer.

Figure 3.19 presents the inclined plane experimental setup. A Newport SR50CC rotation stage is fixed on one z-axis stage. The evaluated material is fixed on the rotation stage base (silicon or glass in Figure 3.19). The MPM is placed on top of the evaluated material. To ensure a horizontal plane for the rotation stage, a laser is fixed on a second z-axis stage 1.2 m away from the rotation stage. The laser passes through a small aperture aiming a mirror fixed on the rotation stage base. If the reflected laser beam passes through the small aperture again, the rotation stage base is assumed to be parallel to the working table. The rotation stage has an angular step of 0.001°. The rotation stage rotates the base until an angle θ in which the gravitational force overcomes the static friction and the MPM slides. At this point, the static friction coefficient (mu_s) can be calculated as $\mu_s = \tan(\theta)$.

The MPM-silicon (μ_{s1}) and MPM-glass (μ_{s2}) static friction coefficients were

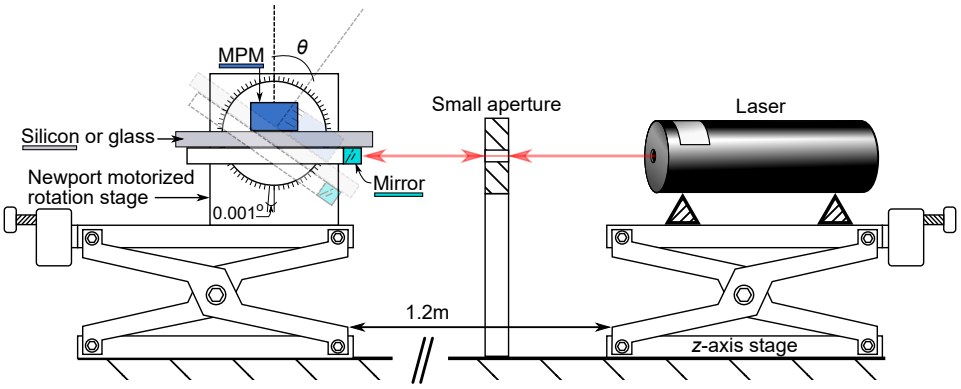

Figure 3.19: Static friction identification by inclined plane technique. Experimental set-up schema.

measured with two different MPMs and in two different contact zones of the evaluated materials. The mean value of the friction coefficient, ± standard deviation, are condensed in Table 3.2, with n the number of test per condition.

Table 3.2: Experimental results (mean ± standard deviation) of the MPM-silicon and MPM-glass static friction coefficients.

	MPM-silicon μ_{s1}		MPM-glass μ_{s2}	
	Magnet 1	Magnet 2	Magnet 1	Magnet 2
Zone 1	0.263 ± 0.054, $n = 14$	0.244 ± 0.037, $n = 28$	0.319 ± 0.04, $n = 12$	0.388 ± 0.052, $n = 17$
Zone 2	0.276 ± 0.035, $n = 19$	0.267 ± 0.032, $n = 10$	0.343 ± 0.071, $n = 13$	0.404 ± 0.033, $n = 16$
Mean ± std	0.260 ± 0.04		0.368 ± 0.06	

The mean value ± standard deviation were $\mu_{s1} = 0.260 \pm 0.04$ and $\mu_{s2} = 0.368 \pm 0.06$. The raincloud plot (Figure 3.20) presents the experimental data (dots) with its statistical box plot (percentiles) and probability distribution of the data assuming normal distribution.

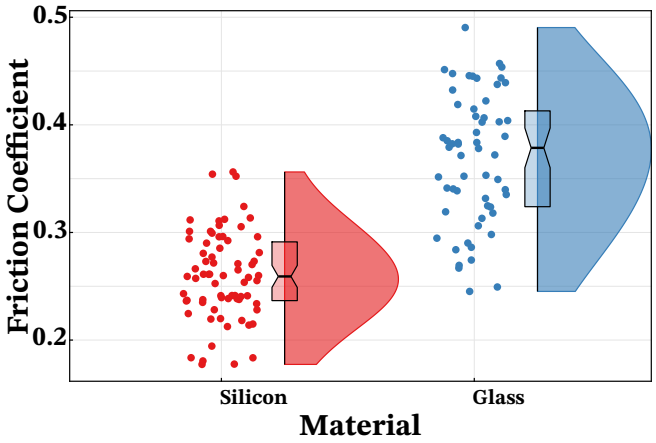

Figure 3.20: Raincloud plot of the static friction coefficient between MPM-silicon nad MPM-glass.

From Figure 3.20, the MPM-silicon static friction data had a lower mean value and a more concentrated distribution (lower standard deviation) than the MPM-glass static friction, even if there were some data points on the extremes of the distribution. The standard deviation of the friction coefficient was significant for both results. The standard deviation percentage of the mean value was 15.4% for MPM-silicon and 16.3% for MPM-glass.

3.2.4.2 Dynamic friction identification

The dynamic friction identification process uses the experimental setup explained in detail in Section 4.1. This setup uses a camera on top of the DAA to measure the conveyed object displacement as a function of the driving current in the wires. The identification idea is to measure the displacement of a conveyed object under multiple driving currents, which translate to multiple speeds of the MPM and conveyed object. In parallel, a dynamic model with a classic Coulomb friction model is constructed. Using the experimental displacement, speed and energy measurements, an optimal Coulomb friction coefficient is determined for each speed value of the conveyed object, so that the Coulomb dynamic model matches the experimental data with a minimum root-mean-square error. This process yields a friction coefficient as a function of speed, which is used to identify the parameters of the Bengisu & Akay model.

A 411 mg, 20 mm × 20 mm × 0.13 mm glass sheet was used as conveyed object on a 2 × 2 DAA system. The glass sheet was moved along the x-axis, y-axis and xy-plane using currents from 2 to 9 A with a fixed pulse width of 200 ms. The pulse width was chosen longer than the system kinematics (movement plus rebound phenomena) to include the collision, rebound and consequent speed direction change of the MPMs on the friction identification.

Figure 3.21 presents the dynamic friction identification results. The experimental results showed an increase in the friction coefficient as a function of speed until 0.1 m s^{-1}, where the friction coefficient was almost 1. After 0.1 m s^{-1}, the friction coefficient slightly decreased for two data points. In the increasing friction zone, the identified Bensigu & Akay model correlated with the experimental data before 0.055 m s^{-1}. After this value, the correlation decreased. To obtain a better correlation with the experimental data, and include the static friction coefficient in the model, this thesis proposes a modification of the increasing friction function of the Bengisu & Akay model ("modified increase" in Figure 3.21). This modification follows the equation:

$$\vec{F}_f = \left(\frac{F_s}{v_0^2} \|v\|^2 + F_s \right) \mathbf{sgn}(v), \|v\| < v_0 \tag{3.20}$$

Replacing the first equation of Equation (3.19).

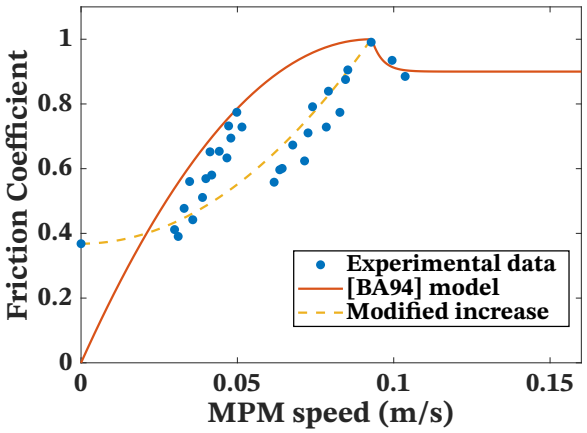

Figure 3.21: Experimental results of the dynamic friction coefficient between MPM and glass with the identified Bengisu & Akay model [BA94] and a modified incremental friction function.

The Begisu & Akay had a root-mean-square error (RMSE) of 0.175 and a mean-absolute error (MAE) of 0.101. The proposed modification had a RMSE of 0.148 and MAE of 0.081 (errors calculated without the static friction value)[2]. The proposed modification better fits the measurements and includes the static friction coefficient to the model, but adds a discontinuity at $0\,\mathrm{m\,s^{-1}}$ (speed direction change). This discontinuity is acceptable as the dynamic model will be executed in a DAA displacement step by step basis. In that case, the only change in speed sign (which could trigger the model oscillations due to the discontinuity) are only possible during the rebounds of the MPM, but as the sign change occurs instantly at the collision, with a non-zero value, then the model never passes through the discontinuity. This means that there are no model oscillations with the proposed modification and the step-by-step modeling solution.

3.2.5 Collision and rebound effect modeling

Because of the digital principle of the system, the MPM impacts the cavity walls when reaching its discrete positions. The collision and rebound of the MPM due to this impact were modeled implementing the classic equations of elasto-plastic collisions in one dimension [SK58] (Equation (3.21) and Equation (3.22)).

$$v_a = \frac{m_\mathrm{a} u_\mathrm{a} + m_\mathrm{b} u_\mathrm{b} + m_\mathrm{b} c_r \left(u_\mathrm{b} - u_\mathrm{a}\right)}{m_\mathrm{a} + m_\mathrm{b}} \tag{3.21}$$

[2]The root-mean-square error (RMSE) and mean-absolute error are presented and discussed in Section 4.1.5

$$v_b = \frac{m_a u_a + m_b u_b + m_a c_r (u_a - u_b)}{m_a + m_b} \tag{3.22}$$

With v_a and u_a the speed of the MPM after and before collision, respectively. v_b and u_b the speed of the structure after and before collision, respectively. m_a and m_b the mass of the MPM and structure, respectively. We suppose that the structure is static before and after the collision ($v_b = u_b = 0$) given its large mass compared to the one of the MPM ($m_b \gg m_a$).

The coefficient of restitution (c_r) for the collision between the MPM and the structure is modeled following the work of Weir & Tallon for elasto-plastic impacts [WT05]:

$$c_r = \alpha \left(\frac{Y}{1}\right)^{5/8} \left(\frac{1}{E_*}\right)^{1/2} \left(\frac{R_1}{R_*}\right)^{3/8} \left(\frac{1}{v}\right)^{1/4} \left(\frac{1}{\rho}\right)^{1/8} \tag{3.23}$$

With v the impact speed, Y yield pressure, E_* the equivalent Young modulus and ρ the density of the material in collision (in our case NdFeB into silicon). The term R_1/R_* arises because of the different possible geometries after separation (and penetration) depending on the materials' hardness and shape. For impacts in which either surface is plane, or both surfaces suffer plastic deformation, the ratio R_1/R is neglected [WT05]. Finally, α is a coefficient dependent of the impact theoretical shape and energy transmission. Weir & Tallon worked with sphere-sphere impacts, deducing $\alpha = 3.1$. The collision between the MPM and structure is a plane-plane impact, resulting in $\alpha = 1$ [WT05].

3.2.6 Dynamic model parameters & flowchart

The parameters of the dynamic model and some characteristic values of the EDA are synthesized in Table 3.3.

Figure 3.22a presents the flowchart of the dynamic model. The information needed for the model are the EDA and DAA characteristics (Table 3.1, geometry, magnetization, PCB, etc). The inputs of the dynamic model are: the current profile in both actuating wires (current intensity as a function of time); mass of the conveyed object; and number of actuating EDAs. The core of the model is Newton's second law to compute the total exerted force onto the MPM and the energy transferred to the conveyed object by friction. This computation considers the MPM and object acceleration, speed and position at each time-fixed simulation step to update the friction, magnetic and electromagnetic forces. The model's outputs (Figure 3.22b) are: the MPMs and conveyed object displacement, speed and acceleration along the three axes (x,y,z); the system forces through time; the mechanical energy generated; and the electrical energy injected.

Table 3.3: Parameters of the Dynamic Model and Characteristic values of the Elementary Digital Actuator.

Symbol	Variable/Conditions	Value	Unit
$\vec{F}_{mx}$	x-axis magnetic force at a discrete position	0.43	mN A^{-1}
$\vec{F}_{emx}$	x-axis electromagnetic force at cavity's center	1.22	mN A^{-1}
$\vec{F}_{emy}$	y-axis electromagnetic force at cavity's center	1.05	mN
v_0	Transition speed	93.0	mm s^{-1}
ζ	Decay factor	300	s mm^{-1}
$\vec{F}_{f1}$	Friction force MPM-silicon at 50 mm s^{-1}	0.11	mN
$\vec{F}_{f2,f3}$	Friction force MPM-glass at 50 mm s^{-1}	0.50	mN
Y	Yield pressure	165	MPa
E	Equivalent Young modulus	35.7	GPa
ρ	MPM Density	7.01	g cm^{-3}
m_a	MPM mass	34.0	mg
m_b	Silicon structure mass	104	g
c_r	Coeff. of restitution at 0.1 m s^{-1}	0.4	-

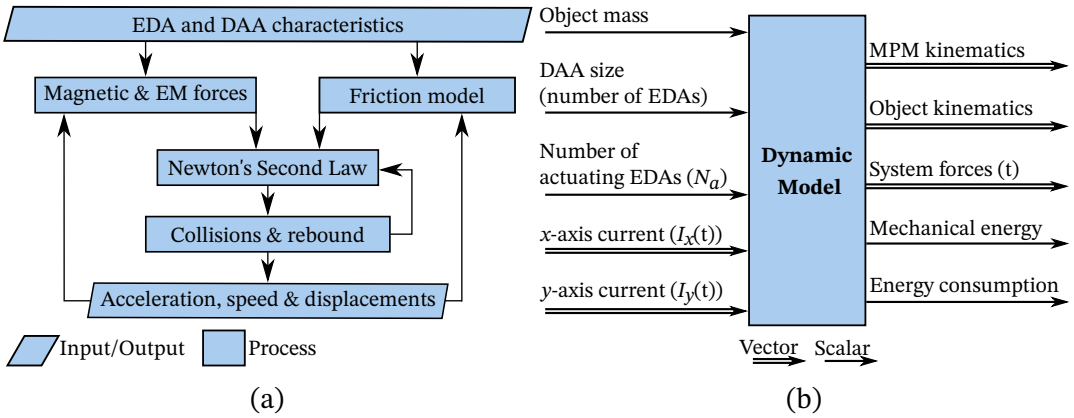

Figure 3.22: Dynamic model (a) Flowchart. (b) Input-Output.

The dynamic model assumes that all EDAs in the DAA are homogeneous and distribute the mass of the conveyed object equally. Then, the displacement step is the sum of the efforts of each actuating EDA on the conveyed object. This assumption allows the dynamic model to operate in a step by step basis. The uncertainties and neglected phenomena of the dynamic model are discussed in Appendix C. The next chapter will treat the experimental validation of the dynamic model for multiple DAA configurations, varying all the system inputs and evaluating all the DAA outputs.

Chapter 4

System Characterization & Model Validation

This chapter presents the characterization of the EDA and DAA and its comparison with the developed dynamic model.

The first section (Section 4.1) presents the materials used to measure the inputs and outputs of the EDA and DAA.

The subsequent sections present the methods & results of the experimental tests and its comparison with the developed dynamic model. The first set of tests (Section 4.2) study the kinematics of the EDA: the displacement through time of the MPM and conveyed object. Both kinematics are coupled, as the MPMs carry the conveyed object through contact friction. Once the kinematics of both bodies are explained together, the kinematics section uncouples this relation to present the influence of the driving and holding currents on the mobile and conveyed object separately. The second set of tests (Section 4.3) study the most important system variable: the object displacement as a function of the DAA inputs. This variable is crucial as it will be used by the trajectory algorithm to plan the conveyance of the object on the DAA. These tests study the influence on the conveyed object of: the driving and holding current intensities; the driving current pulse duration; and the number of actuating EDAs. Bi-dimensional displacements of the conveyed object (xy displacements and object rotations) and the conveyable mass on the system are also tested.

The results and model correlation are summarized and discussed in the final section (Section 4.4), with Table 4.2 synthesizing the results.

4.1 Materials

This section presents the experimental conditions, materials, sensors, set-ups and protocols used to measure the inputs and outputs of the EDA and DAA.

4.1.1 Conditions

All experimental tests were done in the same room and on the same experimental table. The test were executed on different days and with changing intervals of time between them, along a year of experimentation. The following ambient conditions were not controlled nor registered through the experiments: electromagnetic interference, room temperature nor humidity. The DAA's flatness, or parallelism in respect to the flat working table, was measured. This condition is important as an inclination would foment larger displacements in a direction and, oppositely, limit displacements against the inclined plane. Non-magnetic screws, fixing the DAA to its base, were used to alter the DAA inclination. To measure the DAA flatness, a 60 mm Mitutoyo grade 2 gauge (± 1 µm) was used as reference plane to measure the distance between its upper face to a point in the silicon structure of the DAA (Figure 4.1a). Eight measure points were taken, as showed in Figure 4.1b. The largest difference between any two points was 0.09 mm. This means that the DAA is slightly inclined diagonally towards the bottom right corner and could add some variability to the experimental results. This was the best flatness attained by manually tuning the nonmagnetic screws. A bi-dimensional bubble level placed at the center of the DAA evidenced this inclination. Figures 4.1c to 4.1f present the distance of the bubble to the control line of the level. The images were taken with the method explained in the next section. The flatness condition was measured before the first experimental test was executed. All experimental tests were assumed to be under this flatness condition.

Table 4.1: Bubble level measure results. Image resolution for measurement: 0.694 µm/pixel.

$+x$ (µm)	$-x$ (µm)	$\lvert\Delta x\rvert$ (µm)	$+y$ (µm)	$-y$ (µm)	$\lvert\Delta y\rvert$ (µm)
1258.8	1571.2	312.5	1775.3	1106.9	668.4

4.1.2 Imaging system calibration

To avoid any measuring system perturbation on the DAA behavior, two imaging systems were used as measure devices (contactless measure). The first one,

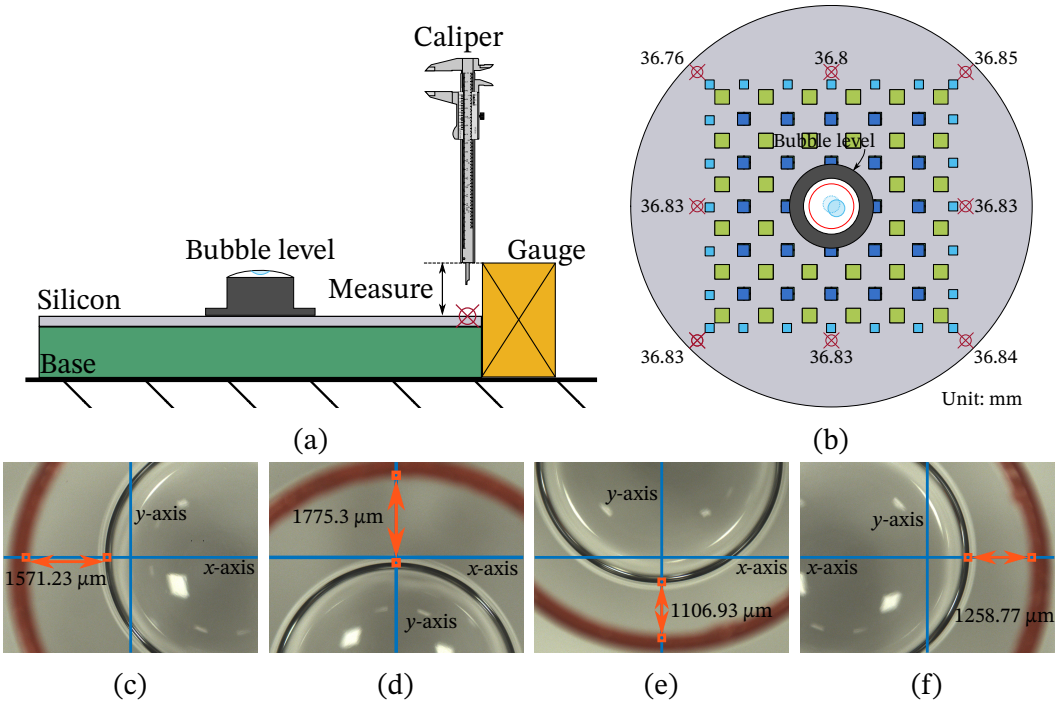

Figure 4.1: Flatness condition. (a) Experimental setup. (b) Caliper results. (c) to (f) Bi-dimensional bubble level results.

a Grasshopper3 GS3-U3-32S4C camera, took static photos of the system and measured the conveyed object displacement. The second one, a Photron FastCam SA1.1 camera, captured video at 15 kHz. This frequency is needed to measure the kinematics (displacement through time) of the conveyed object and MPMs. Both cameras were placed on top of the DAA. To calibrate both cameras, a 25 mm × 25 mm fixed frequency dot target by Edmund Optics was used (C/N 59209, Figure 4.2a). The target has an array of 62.5 µm diameter dots spaced 125 µm apart from each other. The tolerance of the target is 1 µm for both the dot diameter and space between dots. An image of the target was taken at focal distance and, using the known distance between the dots, the pixel per distance size of the images was deduced (Figure 4.2b).

The static camera (Grasshopper3), with a fixed optic system, obtained an image with a 0.694 µm/pixel resolution. The dynamic camera (Photron FastCam), with a variable optic system, obtained images with resolutions between 2.45 and 16.1 µm/pixel.

The target image also helped to detect and evaluate the deviation of the camera axis to the z-axis of the system. Deviations generate aberrations and distortions in the target image. When the camera image was the sharpest and less distorted, the camera was fixed and assumed perpendicular to the DAA's active surface.

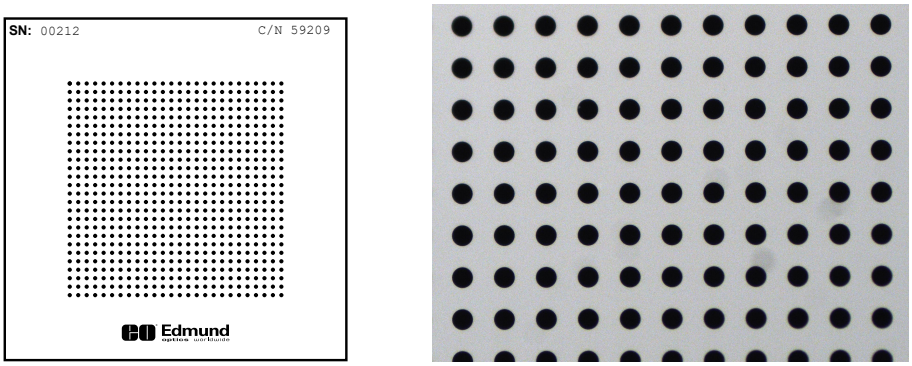

(a) (b)

Figure 4.2: (a) C/N 59209 fixed frequency dot target by Edmund Optics. 25 mm × 25 mm dot area, 125 µm dot to dot (center to center) separation, 62.5 µm dot diameter. (b) Grasshopper3 GS3-U3-32S4C image with 0.694 µm/pixel resolution.

4.1.3 Signal flux

The material and signal flux involved in all the experimental measurements are schematized in Figure 4.3. The system was controlled with a developed LabVIEW interface (Figure 4.3 (1)), connected to a National Instruments PCI6733 input/output board (Figure 4.3 (2)) that sent the control voltages to the voltage-to-current converters (current sources). The voltage signal shape were reproduced by the converters. The maximal output power of the converters was 100 W (Figure 4.3 (3)). The current signals were injected in the actuators wires (Figure 4.3 (4)). The displacement and dynamics of the conveyed object and MPMs were measured using two cameras placed on top of the array. To measure the displacement of the object (a static measure once the displacement step is done), a Grasshopper3 GS3-U3-32S4C was used (Figure 4.3 (5)). The kinematics of the MPM and object (a dynamic measure of displacement through time) were measured with a Photron FastCam SA1.1 camera (Figure 4.3 (6)).

The conveyed objects were glass plates with sticker targets on top of them to measure their displacement with the cameras. Some measurements included plastic pieces to increase the weight of the conveyed object without interacting with the magnets. Multiple configurations of the DAA were tested: 2×2, 3×3, 4×4 and 5×5. The object changed for every DAA configuration. The smallest and lightest object weighted 202 ± 1 mg and had a size of 20 mm × 20 mm × 0.1 mm. The largest object was 50 mm × 50 mm × 0.13 mm. The heaviest object weighted 8901 mg. Each experimental point was measured 20 times to obtain a mean value as well as a standard deviation, represented by the error bars in the figures ahead.

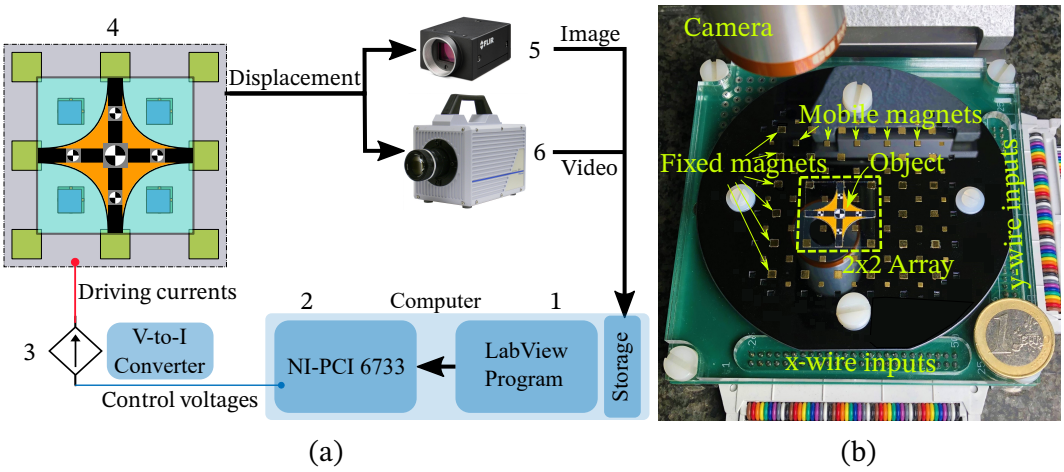

Figure 4.3: Control scheme of the digital actuator array. (a) Schema with: 1. Computer with Labview interface, 2. National Instruments PCI6733 DAQ, 3. Multiple voltage-controlled current sources, 4. The array system, 5. Grasshopper3 GS3-U3-32S4C camera, 6. Photron FastCam SA1.1 camera. (b) Real system.

4.1.4 V-to-I converters characterization

The DAA control variables are the injected currents in each EDA. These currents are a function of the control voltage generated by the LabView interface on the computer and the intrinsic behavior of the V-to-I converters. It is important to characterize the converters to be sure that the commanded current is indeed the injected value to the system.

The converters have a maximum supply power (P_{max}) of 100 W. Assuming each EDA's actuating wires as pure resistors (R), the maximum output current follows the equation $I_{max} = \sqrt{P_{max}/R_{eq}}$, with R_{eq} the equivalent resistance of the connected DAA. The equivalent resistance determines then the maximum current.

The converters were characterized measuring four times the output current to the DAA against the control voltage injected from the computer. Two DAA were used: a 2×2 and a 3×3 DAA. The R_{eq} of the 2×2 DAA was measured at 1.2 Ω and 2.5 Ω for the 3×3 DAA. These values translate to maximum currents of 9.13 A and 6.32 A respectively. The results are presented in Figure 4.4.

From Figure 4.4, the experimental results followed the power relation of the converters. The experimental point outside the power limit did not follow a linear relation and presents the higher standard deviation. Inside the linear relation of the converters, the experimental results had an error of less than 0.05 A with negligible standard deviation. All experimental tests were executed on the linear power relation of the converters.

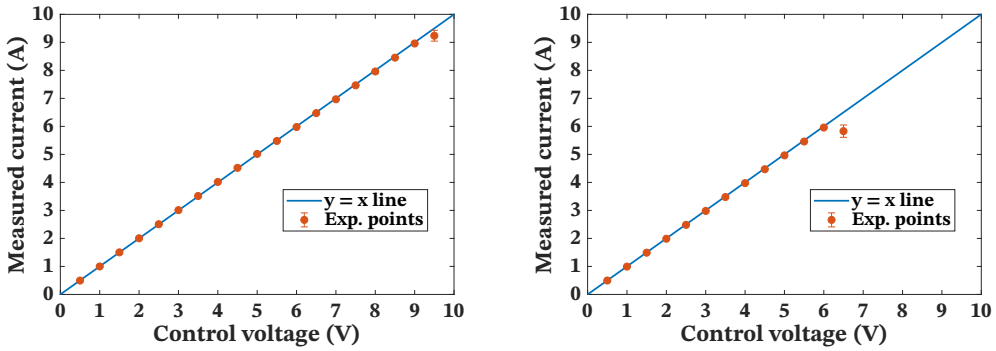

(a) (b)

Figure 4.4: V-to-I converters characterization. (a) 2×2 DAA results and ideal response (the $y = x$ line). (b) 3×3 DAA results and ideal response.

4.1.5 Model evaluation: Root-mean-square error (RMSE) and Mean-absolute error (MAE)

Two metrics are used to evaluate the performance of the dynamic model: root-mean-square error (RMSE) and the mean-absolute error (MAE). Equations (4.1) to (4.2) present the mathematical expressions of both errors. e_i is defined as $e_i = y_i - \hat{y}_i$, with y_i the i-th experimental measure and $\hat{y}_i$ the model prediction for that y_i (both share the coordinate x).

$$MAE = \frac{1}{n}\sum_{i=1}^{n} ||e_i|| \tag{4.1}$$

$$RMSE = \sqrt{\frac{1}{n}\sum_{i=1}^{n} {e_i}^2} \tag{4.2}$$

From Equations (4.1) to (4.2), the MAE is simple to interpret and can be directly applied to the data and model from which it was computed. The MAE gives the same weight to all errors, while the RMSE penalizes variance as it gives errors with larger absolute values more weight (given its quadratic term). When both metrics are calculated, the RMSE is by definition never smaller than the MAE [CD14].

When the error distribution is expected to be Gaussian and there are enough samples, the RMSE has an advantage over the MAE to illustrate the error distribution, but the RMSE is more sensible to outliers than the MAE [CD14].

This dissertation uses both RMSE and MAE to assess the dynamic model performance, as they are the basic elements of the advice of [CD14]: "As every statistical measure condensing a large number of data into a single value, these metrics only provide one projection of the model errors, emphasizing a certain aspect of the error characteristics of the model performance. A combination of

metrics, including but certainly not limited to RMSEs and MAEs, are required to assess model performance."

4.2 Kinematics results

The experimental results presented in this section are the MPM and object displacement though time (kinematics) as a function of the driving and holding current variables. These kinematics are the lower level physical events that occur on the DAA while conveying objects. The dynamic model tries to predict these kinematics events as they are the basis of the DAA behavior.

The Photron FastCam camera, at 15 kHz frames per second, was used to record these fast kinematic events (dynamic measure). The image processing software "Tracker", by Doug Brown [BC11; Bro20], was used to extract the kinematics information from the videos. In this section, only the root-mean-square error is used as model metric because, as the physical phenomenon studied is displacement though time, any outlier on the kinematic results would mean a discontinuity in motion. Given that the RMSE effectively penalizes such events, the RMSE is a better metric to this physical phenomena than the MAE.

The following results will be presented: the kinematics of the MPM and the conveyed object; the driving current intensity influence on the kinematics of the MPM and conveyed object; and the influence of the holding current on the MPM kinematics.

4.2.1 EDA kinematics

The MPM and conveyed object kinematics one EDA and at different current intensities is studied. Driving currents were injected into the x and y wires of a 2×2 DAA for 100 ms to ensure that the pulse was longer than the response time of the system. Figure 4.5 presents a comparison between the dynamic model and the experimental results for different I_x and I_y driving current intensities.

From Figure 4.5b, the MPM moved forward from 0 to 3 ms. During this time, it transferred energy to the object by friction, accelerating the object forward with it. At 3 ms the MPM reached the stroke distance (200 μm). At this point, the MPM collided and rebounded with the silicon cavity wall, generating an opposing friction force on the conveyed object. This resulted in an inflection point in the object displacement curve (rebound and its effects are noted with squares on Figure 4.5b). After the first rebound, the electromagnetic and magnetic forces drove the MPM towards the stroke value, which was the desired discrete position. These forces decelerated the rebounding MPM and forced it to change speed sign

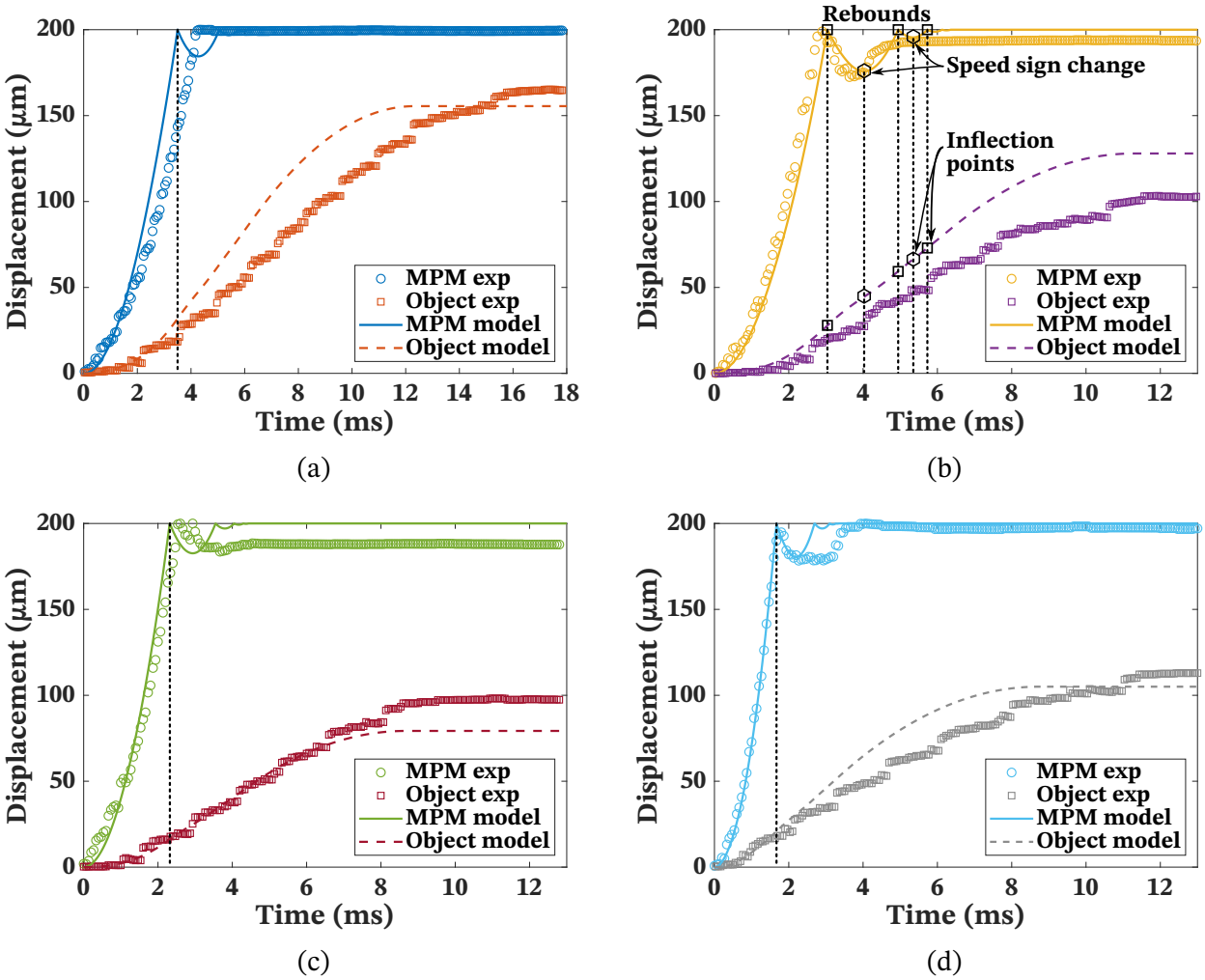

Figure 4.5: MPM and object kinematics along the x-axis of a 2×2 DAA for (a) 1.5 A I_x. (b) 2 A I_x, 2 A I_y. (c) 3 A I_x. (d) 5 A I_x.

towards the discrete position. This speed sign change also changed the friction force towards the conveyed object, once more dragging it forward, resulting in a second inflection point on the conveyed object's curve (MPM speed sign changes and its effects are noted with hexagons on Figure 4.5b). The electromagnetic and magnetic forces caused a second MPM-cavity wall collision and rebound, with a smaller amplitude. This process repeated until the MPM rested in the discrete position. When the MPM finally stayed stationary, the remaining kinetic energy of the object was dispersed by friction until the object stopped. This cycle represents one displacement step.

From Figure 4.5, the MPM kinematics predicted by the dynamic model were very close to the experimental results. For all the MPM kinematics test, the dynamic model obtained a root-mean-square error (± standard deviation) of $5.72 \pm 0.89\,\mu$m, which corresponds to 2.9 % of the actuator stroke. The largest source of incertitude were the collision and rebound kinematics. In Figure 4.5a,

no rebound was measured from the collision (marked with a dotted line on Figure 4.6a) and the MPM rested at the discrete position. The dynamic model predicted a single rebound before resting at the discrete position. In Figure 4.5b the rebound was well predicted in both amplitude and duration. In Figure 4.5c the rebound amplitude was well predicted, but the MPM did not return to the discrete position. This could have been by a larger portion of the object resting on the studied EDA, increasing the friction force on the MPM. In Figure 4.5d the rebound amplitude was well predicted but the experimental rebound was slower than predicted.

From Figure 4.5, the object kinematics predicted by the dynamic model had a root-mean-square error of $7.38 \pm 3.32\,\mu m$ for all the kinematic tests, which corresponds to 3.7 % of the actuator stroke (summarized in Table 4.2). The model predictions were, in general, faster than the experimental results.

The dynamic model predicted then the MPM and object kinematics with low root-mean-square errors.

4.2.2 Driving current intensity influence

Reading Figure 4.5 from (a) to (d), the driving current intensity influence on the MPM and object kinematics can be seen. To have a clearer view of the influence, the MPM and object kinematics are studied separately. The same experimental procedure of the last subsection was used. A single MPM is used for Figure 4.6a and a 2×2 DAA is used for Figure 4.6b.

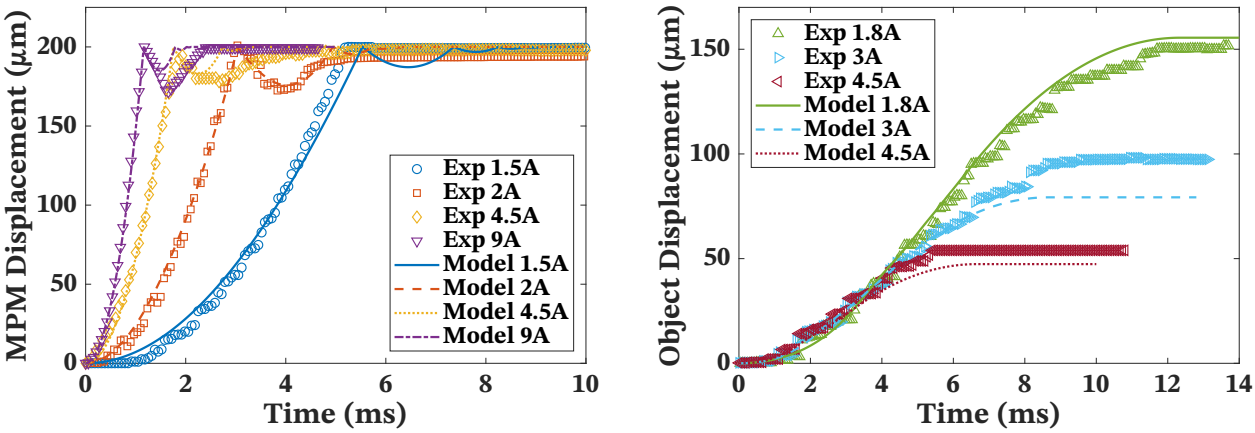

(a) (b)

Figure 4.6: EDA kinematics (displacement vs time) along the x-axis for different I_x values. (a) MPM. (b) Conveyed object.

From Figure 4.6a, the final MPM displacement value was 200 μm, independent of the current intensity, demonstrating the digital nature of its actuation

principle. The settling and rise time of the MPM varied with the value of current intensity. As the current intensity increased the kinematics of the MPM were faster, shortening both the rise time and the settling time. The rise time was defined as the time needed for the output to reach from 10% to 90% of its final value. The settling time was defined as the time needed by the output to stay within 2% of its final value. MPM rising times between 0.8 and 3 ms were measured, with settling times between 2.4 and 5.1 ms.

From Figure 4.6b, the final object displacement value varied with the current intensity (between 50 and 150 μm). This displacement range was due to the fact that the object is carried by the MPMs and then slides on top of them with different kinetic energies for different speeds of the MPMs (Equation (3.19)). Object rising times between 3.7 and 7.5 ms were measured, with settling times between 5.4 and 11.7 ms.

For all the MPM kinematic tests, the mean root-mean-square error ($\pm$ std) was 5.72$\pm$0.89 μm (which corresponds to 2.9 % of the actuator stroke). For the conveyed object tests, the mean root-mean-square error was 7.38$\pm$3.32 μm (which corresponds to 3.7 % of the actuator stroke). The dynamic model predicted then the MPM and object kinematics with low root-mean-square errors.

4.2.3 Holding current influence

This subsection studies the influence of the holding current on the MPM kinematics. A 5 A driving current was injected into the x-axis wires for 100 ms to ensure that the pulse was longer than the response time of the system. Different holding current intensities were injected into the y-axis wires while the driving current was activated to study its influence on the MPM's kinematics. Driving currents are noted as positive values and holding currents are noted as negative values in this dissertation. Figure 4.7 presents a comparison between the dynamic model and experimental results of this test.

From Figure 4.7, the kinematics of the -1 A holding currents was slightly slower than the non-holding test. For both of these tests, the dynamic model correctly predicted the behavior. The -3 A holding test resulted in an even slower kinematics. The slower kinematics with increasing holding current intensity is explained by the increased friction force between the MPM and the cavity wall generated by the holding current: the holding current increases the normal force between these bodies. The dynamic model predicted a faster kinematics for this last test than the experimental results before the collision. After the collision, the model and experimental results matched almost perfectly. The model error for these tests is included in the already presented root-mean-square error of

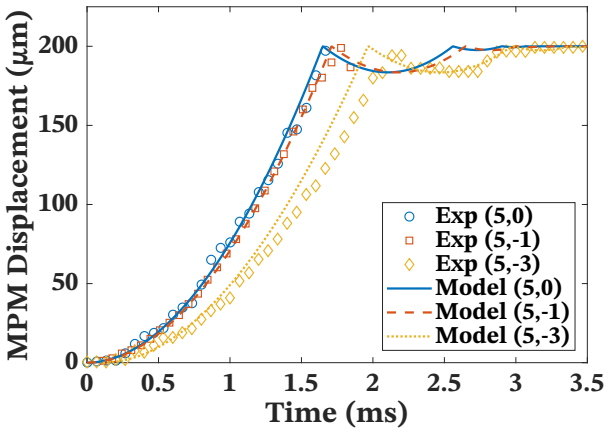

Figure 4.7: MPM kinematics along the x-axis for different (I_x, I_y) pairs. Experimental points after rebound of first two curves hidden for enhanced readability.

5.72±0.89 µm.

4.2.4 Coefficient of restitution results

This subsection compares the predicted and measured coefficient of restitution (c_r) of the MPMs when they impact the cavity wall. The MPM impact speed and rebound speed were measured for different driving and holding current intensities and conveyed mass. From the measures of the impact and rebound speed, the coefficient of restitution can be deduced (c_r =rebound speed / impact speed). Figure 4.8 presents the results against the MPM's impact speed.

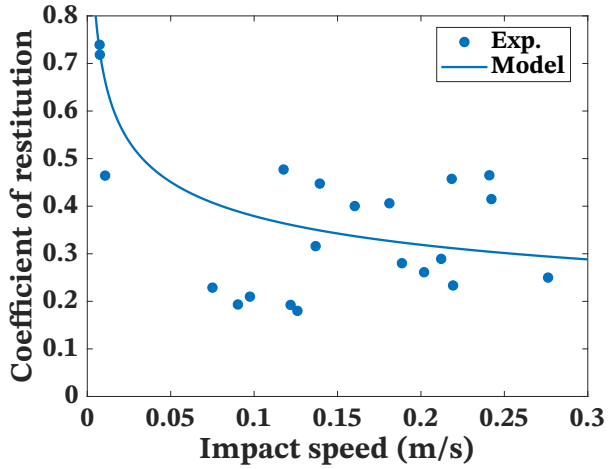

Figure 4.8: Coefficient of restitution vs impact speed of the MPM under multiple conditions.

From Figure 4.8, the c_r presented a high variation, even for similar impact speeds. This could be due to a non-controlled rotation of the MPM along its stroke, meaning that the impact would not be a single plane-plane collision with

the silicon structure. The leading edge would collide first and then the trailing edge, the last one accelerated by the driving force *and* the reaction force of the first impact.

The dynamic model accurately predicted two points at low impact speed, then behaved like an average value of the experimental results as the impact speed increased. The root-mean-square error of the model to all experimental points was 0.121, while the mean-absolute error was 0.103.

4.3 Conveyed object displacement results

The object displacement as a function of the DAA inputs (Figure 3.22b) is studied next. This variable is crucial as it will be used by the trajectory algorithm to plan the conveyance of the object on the DAA. The Grasshopper camera was used to measure the object's displacement: distance from its initial position, before the DAA's displacement step, to the final position, after the DAA's displacement step (static measure).

4.3.1 Driving & holding current intensities influence

Figure 4.9 presents the driving and holding current intensities influence on the object displacement of a 2×2 DAA. For Figure 4.9a and Figure 4.9b (x-axis and y-axis object displacement, respectively), a variable driving current intensity was injected in only one of the two pair of wires of each actuator at a time to obtain a linear motion of the MPM and the object along that axis only. A pulse duration larger than the system kinematics (50 ms) was selected. No holding current was used. For Figure 4.9c and Figure 4.9d, the same conditions and a -1 A holding current intensity with the same pulse duration were used.

From Figure 4.9a and Figure 4.9b (0 A holding current), the object displacement decreased as the driving current increased. The higher the injected current, the faster the MPM kinematics, reducing the displacement time and energy transfer through friction to the object. The model predicted this tendency correctly. The error bars decreased as the driving current increased. This is attributed to the important influence of the friction conditions at lower currents and its reduced influence with faster kinematics as the current increases.

The maximum experimental object displacement was (1.5 A, 179.3 µm) for the x-axis and (1.75 A, 204.5 µm) for the y-axis. At these points the energy transferred to the plate through friction was maximized though a slow MPM movement that prevents slipping phenomena of the actuation. These points are called *critical points* in Figure 4.9. The current value of the critical point along the y-axis was

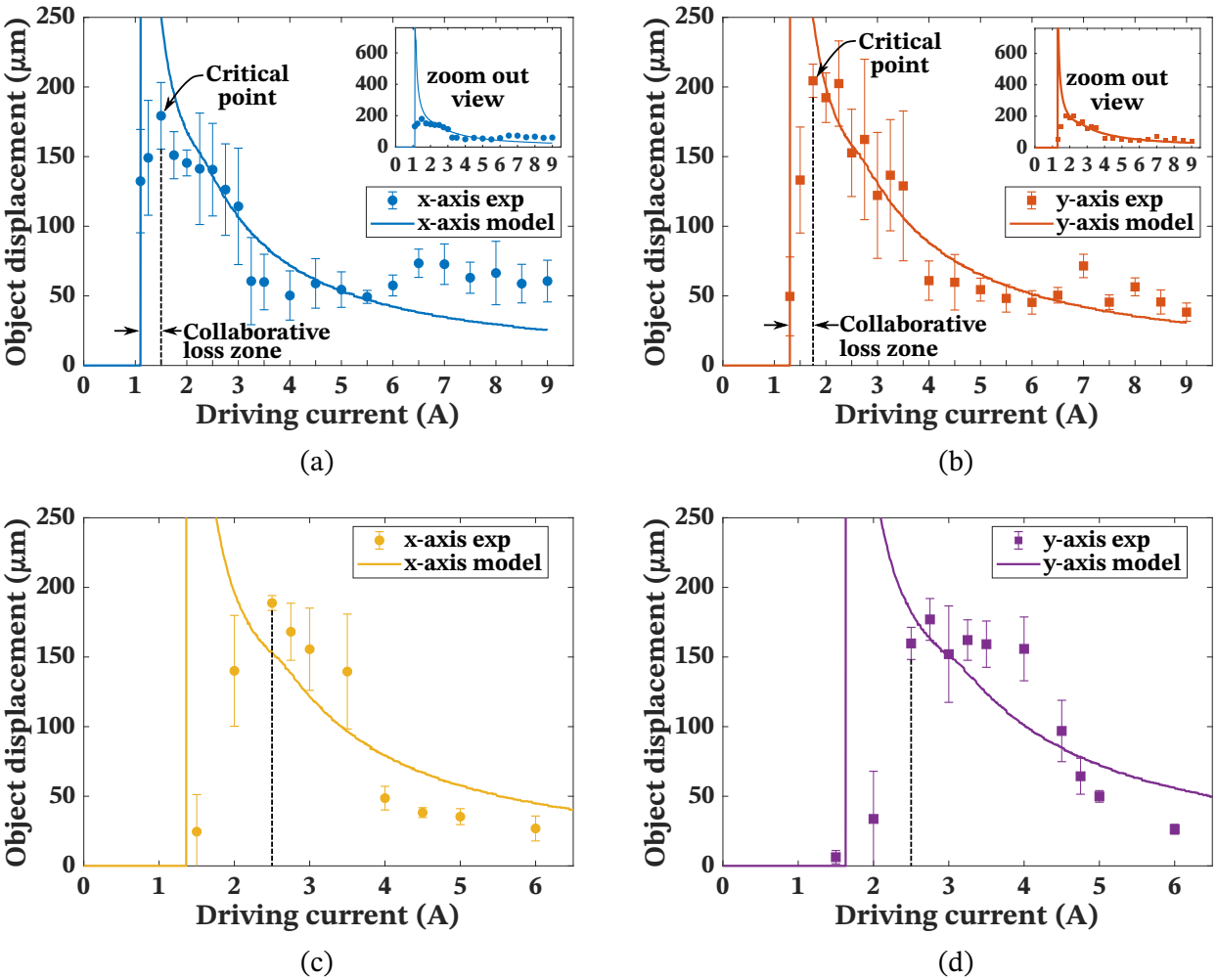

Figure 4.9: Conveyed object displacement vs driving current intensity on the 2×2 DAA. (a) x-axis no holding current. (b) y-axis no holding current. (c) x-axis $I_h = 1$ A. (d) y-axis $I_h = -1$ A.

higher than along the x-axis. This is explained by the difference in distance between the currents wires and the MPM (d_2 and d_3 in Table 3.1). The model predicted greater displacements with lower currents than 1.5 A or 1.75 A, but experimentally, another phenomenon was observed: the displacement decreased sharply as the collaborative effect of the array was lost due to the heterogeneous nature of friction. This zone of displacement collapse is called the *collaborative loss zone* in Figure 4.9. This collaborative loss zone was not predicted by the model as it considers all actuators perfectly homogeneous.

Inside the collaborative loss zone, the experimental displacements of the object started from current values of 1.1 A for the x-axis and 1.5 A for y-axis, in accordance with the model. Lower current values did not generate enough electromagnetic forces to overcome the magnetic holding and friction forces of the MPM and object. Without considering the collaborative loss zone, the model

predicted the x-axis measures with a root-mean-square error of 29.87 µm and a mean-absolute error of 24 µm. For the y-axis, the RMSE was 19.05 µm and MAE was 16 µm.

Figure 4.9c and Figure 4.9d (−1 A holding current), followed a similar behavior than the 0 A holding results, but with a shift towards higher driving currents. This is due to the higher driving current intensity to overcome the increased friction force generated by the holding current. The maximum displacements were (2.5 A, 188.8 µm) for the x-axis and (2.75 A, 177 µm) for the y-axis. The error bars of the −1 A holding results were, in average, smaller than the 0 A holding results. This is attributed to the reduced influence of the friction conditions as the holding current friction force becomes the larger influence.

The straightness error of all the experimental points of Figure 4.9 was measured. This error is attributed to the asynchronous movement of the MPMs due to the heterogeneity in friction, causing a torque to appear. Also, manufacturing and assembly errors like the misalignment between the wires and the actuators' axes could contribute to this error. Figure 4.10 presents the straightness error measurement of the results presented in Figure 4.9.

The mean straightness error of Figure 4.10a and Figure 4.10b (0 A holding results) were 13.3±6.8 µm and 10.5±5.4 µm, respectively. In both cases, the straightness error decreased as the driving current increased. The mean straightness error for Figure 4.10c and Figure 4.10d (−1 A holding results) were 4±3.5 µm for the x-axis and 8.4±6.5 µm for the y-axis. These results show that the holding current reduced the straightness error due to the higher frictional force between the MPM and silicon cavity.

For driving currents from 5 A to 9 A in Figure 4.9 and Figure 4.10, the influence of the different initial conditions of the MPMs such as position and friction heterogeneity are reduced against the rapid dynamic of the system, explaining the smaller error bars for both axes. This high current zone is then useful for repeatable and precise object displacement steps given the step low standard deviation and straightness error.

The driving and holding current intensities influence on the 3×3, 4×4 and 5×5 DAA systems were also evaluated, presenting similar behaviors to the 2×2 DAA. The results of these larger DAA systems are presented in Appendix D.2.1. Table 4.2, the synthesis of the experimental test, presents the results for these larger DAAs.

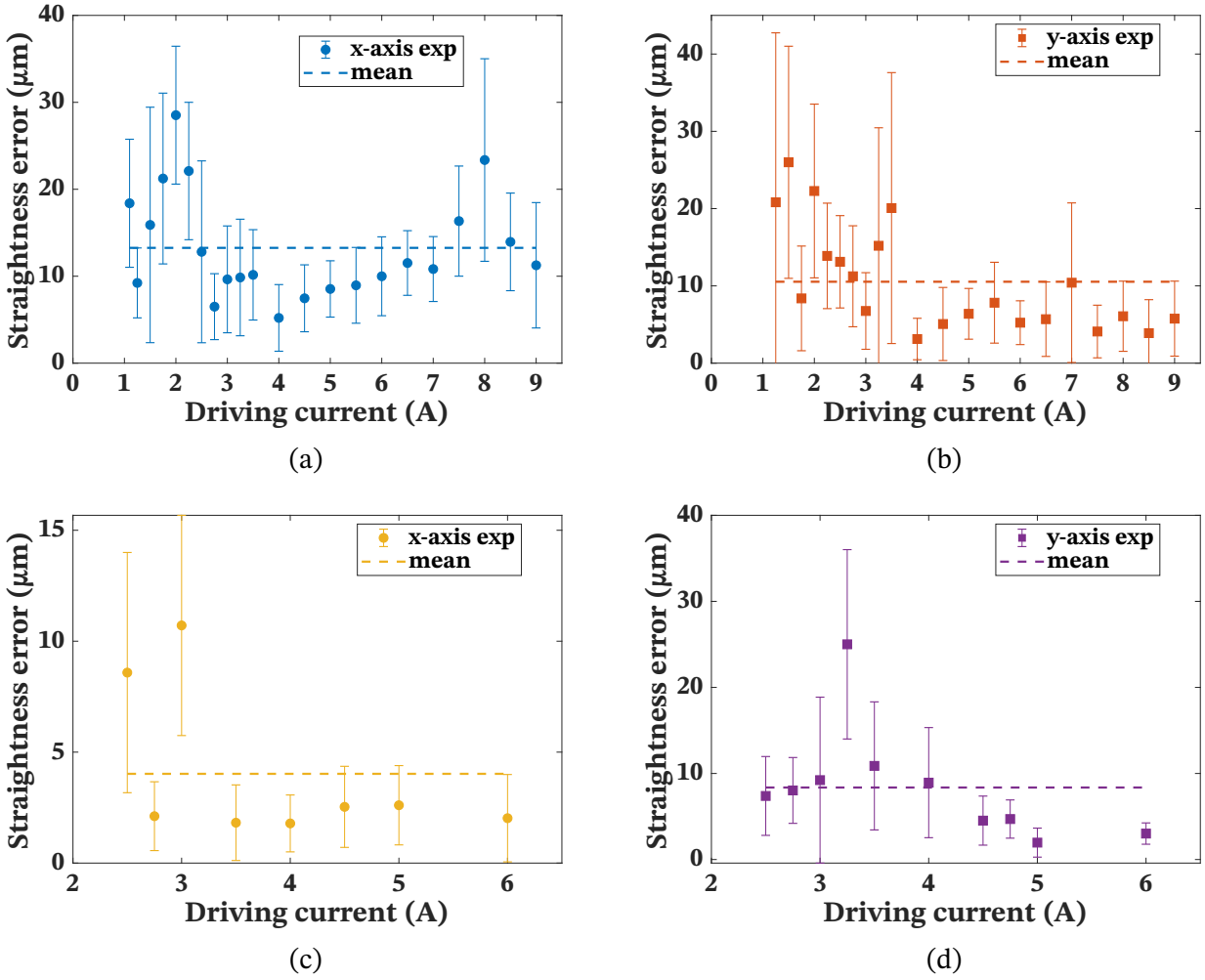

Figure 4.10: Conveyed object displacement straightness error (involuntary y-axis displacement) vs driving current intensity on the 2×2 DAA. (a) x-axis no holding current. (b) y-axis no holding current. (c) x-axis $I_h = -1$ A. (d) y-axis $I_h = 1$ A.

4.3.2 Driving current pulse duration influence

This test used a driving current pulse along the x-axis only. The pulse duration was varied to observe its influence on the displacement step of the conveyed object. Figure 4.11 presents the displacement step value as a function of the driving current pulse duration for current intensities of 2 A (Figure 4.11a) and 6 A (Figure 4.11b).

From Figure 4.11, a similar behavior was observed for the two driving current intensities: the model predicted an increasing object displacement as the pulse duration increased until a saturated displacement value. When the pulse duration was longer than the whole kinematics of the MPMs, including all rebounds, the pulse duration no longer influenced the object's displacement, explaining this saturation. Before this saturated value, the effect of the rebound of the MPMs on the object displacement were visible.

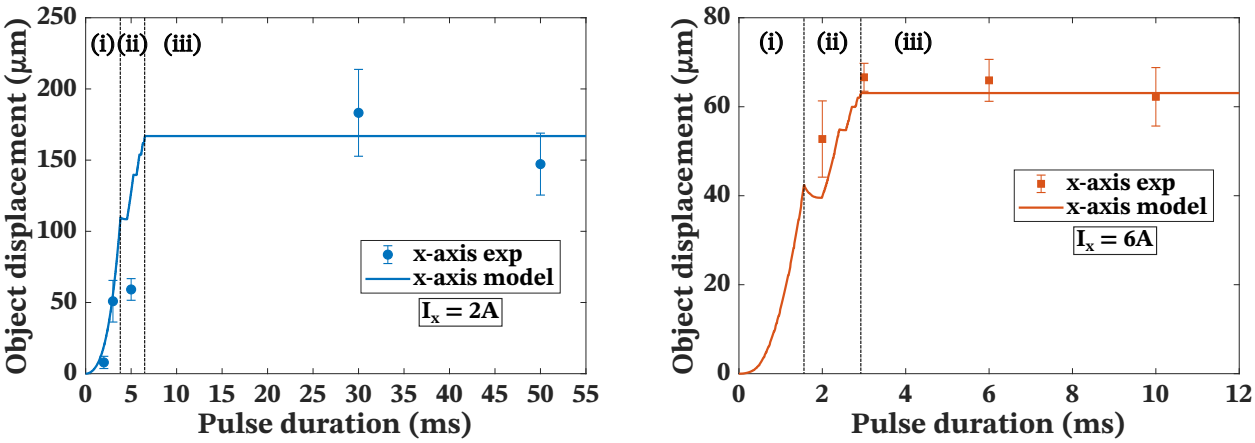

(a) (b)

Figure 4.11: Conveyed object displacement vs driving current pulse duration on the 2 × 2 DAA. (a) x-axis no holding current $I_x = 2$ A. (b) y-axis no holding current $I_x = 6$ A.

Focusing on Figure 4.11b, for pulses from 0 to 1.56 ms (zone (i)), the model predicted an increasing displacement as a function of the pulse duration. The movement of the MPMs stopped when the driving current was switched off. The EDAs stroke was not reached. The displacement of the object increased until a first local maxima (1.56 ms in Figure 4.11b). At this point, the stroke distance was reached, the driving current switched off and the magnetic holding force ensured that the MPMs stayed at the discrete position, protecting the object from a negative force due to a rebound of the MPMs. If the pulse time increased from 1.56 ms, the rebound of the MPMs affects the displacement of the object (zone ii). The rebound under these conditions is larger than the one presented in the kinematics results, as the driving current is switched off while the MPM rebounds, suppressing the force that drives the MPM towards the stroke value and increasing the rebound distance (shown as a valley after 1.56 ms in Figure 4.11b). If the pulse duration continued to increase, then the driving current reduces the rebound distance as it forces the magnet towards the stroke, helping the object's displacement, until a new rebound is generated. This explains the behavior between 1.56 ms and 2.93 ms in Figure 4.11b (zone ii). This process repeats, with decreasing rebound influence, until the saturated displacement value is attained (zone iii). The model predicted a saturation of the object's displacement for pulses longer than 6.51 ms for 2 A and 2.93 ms for 6 A. This is the minimal pulse duration for which the kinematics of the MPMs and the object, including all rebounds, are completed before the driving current is switched off and the pulse duration has no longer an impact on the object's displacement.

The model predicted the experimental measures of the 2 A test with a root-

mean-square error of 14.2 µm and a mean-absolute error of 13 µm. For the 6 A test the RMSE was 6.86 µm and the MAE was 5 µm.

4.3.3 Number of actuating EDAs influence

Another variable of the system is the number of actuating EDAs of the DAA. When all EDAs are activated, the DAA performs the maximum step displacement as all EDAs contribute to the movement. When the number of actuating EDAs decreases, the DAA performs a smaller displacement step, as the inactivated EDA acts like a friction brake. The DAA can operate until the number of inactivated EDAs reaches half of the total number of EDAs. At this point, the friction force of the inactivated EDAs and the displacement force of the actuating EDAs balance and the object does not move. To evaluate the influence of the number of actuating EDAs, a 4×4 and 5×5 DAAs were tested with a reduced number of actuating EDAs. For the 4×4 DAA, the number of EDAs was changed while the current conditions were kept constant. There were tests for the x-axis and y-axis without holding current and with -1 A holding current. The results are presented in Figure 4.12. For the 5×5 DAA test, four EDAs are inactivated symmetrically with respect to the object mass (the corners of the DAA). This means that 21 of the 25 EDAs were used along the y-axis. The driving current intensity was varied without holding current and with -1 A holding current (same test as in the driving current intensity influence, Section 4.3.1). The results are presented in Figure 4.13.

From Figure 4.12 the experimental results followed the theoretical explanation described earlier. The error bars with the -1 A holding current were larger than with 0 A holding current. This is attributed to the increased friction force of the holding test, added to the friction heterogeneity of the system. Also, the smaller displacement force of the degraded DAA resulted in some small displacements in each point, increasing the variability of the point. The model predicted the behavior of:

- The x-axis without holding (Figure 4.12a) with a root-mean-squared error of 7.63 µm and mean-absolute error of 6.65 µm.
- The y-axis without holding (Figure 4.12b), RMSE 9 µm and MAE 6.69 µm.
- The x-axis with holding (Figure 4.12c), RMSE 1.87 µm and MAE 1.68 µm.
- The y-axis with holding (Figure 4.12d), RMSE 9 µm and MAE 7 µm.

From Figure 4.13, the behavior of the system followed the results of the driving current intensity influence test (Section 4.3.1). The model predicted the y-axis without holding experimental results with a root-mean-square error of 23.22 µm and a mean-absolute error of 20.28 µm. For the y-axis with holding,

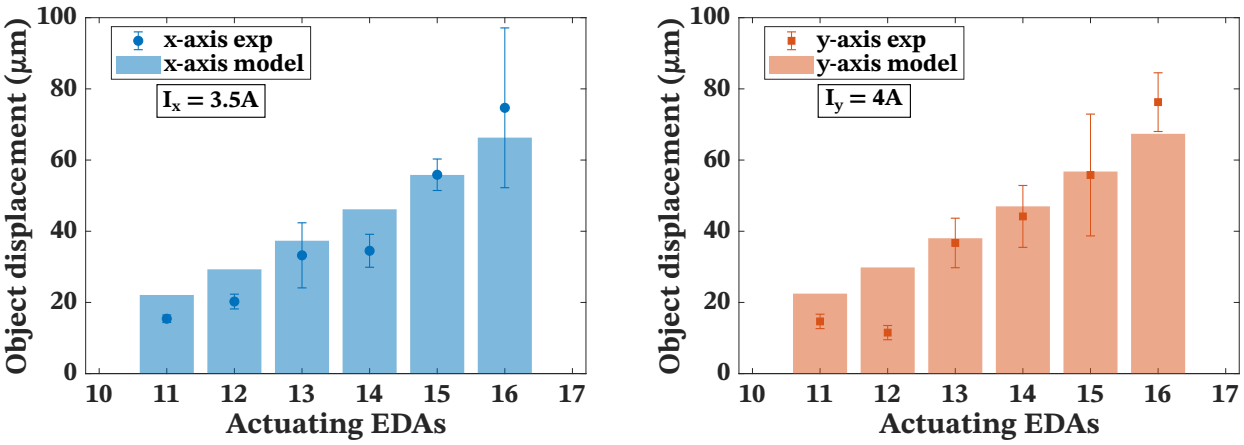

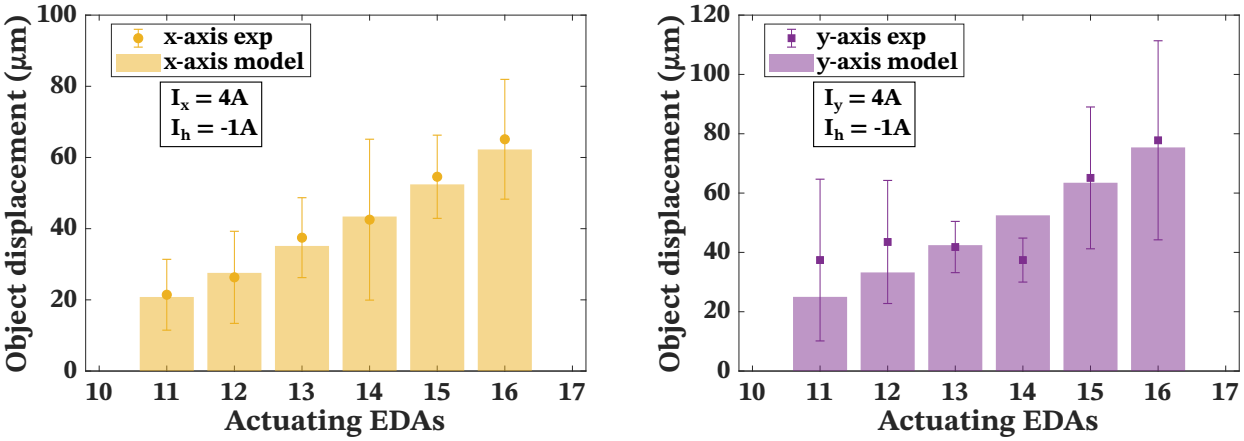

Figure 4.12: Conveyed object displacement vs number of actuating EDAs on a 4×4 DAA. (a) x-axis no holding current. (b) y-axis no holding current. (c) x-axis $I_h = -1$ A. (d) y-axis $I_h = -1$ A.

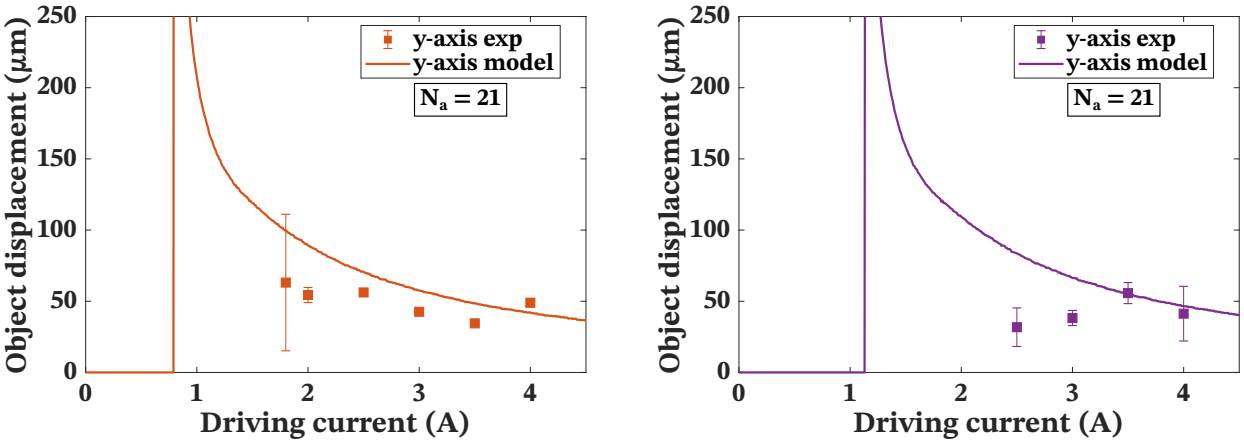

Figure 4.13: Conveyed object displacement vs driving current intensity with N_a =21 of 25 EDAs actuating on a 5×5 DAA. (a) y-axis no holding current. (b) y-axis $I_h = -1$ A.

the RMSE was 29.6 µm and the MAE error was 21.42 µm.

4.3.4 Bi-dimensional object displacement

One planar motion capability of the DAA is to displace objects on the xy plane. To evaluate this, independent driving currents were injected into both wires of each actuator of the 2×2 DAA to obtain an object displacement in both x and y axes (xy plane displacement by I_x and I_y). Each combination of I_x and I_y is called a current pair. The angle of the bi-dimensional movement to the x-axis was measured for multiple currents pairs (Figure 4.14). The pulse duration of

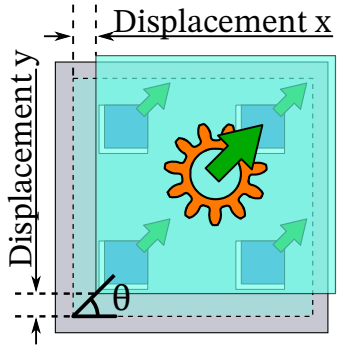

Figure 4.14: Angle of the bi-dimensional movement to the x-axis

the current pairs were larger than the kinematics of the MPMs as in Figure 4.6. The results are presented in two representations: a bubble chart (Figure 4.15a) and a bar plot (Figure 4.15b).

The bubble chart Figure 4.15a presents the experimental and model-predicted angle as a function of both I_x and I_y. The area of the bubble is proportional to the angle value. This representation allows to map, geometrically, the influence of the current intensity on the generated angle. The reported value of the bubble is the experimental angle in degrees.

The bar plot Figure 4.15b presents the experimental and model-predicted angle as a function of the injected currents pairs. Each current pair identification number is presented in the lower horizontal axis of Figure 4.15b. The experimental value is the mean of 20 measures per point with its standard deviation represented as error bars. This representation allows an easier evaluation of the model correlation with the experimental data.

From Figure 4.15a, along the axes I_x ($Iy = 0$) and I_y ($Ix = 0$), a 1D linear displacement along the correspondent axis was obtained, i.e., angles tending to 0° along the I_x axis (horizontal axis on Figure 4.15a) and angles tending to 90° along the I_y axis (vertical axis on Figure 4.15a). For similar values of I_x and I_y, similar displacements on both axes were observed, i.e, angles around 45° along the $I_x \approx I_y$ diagonal.

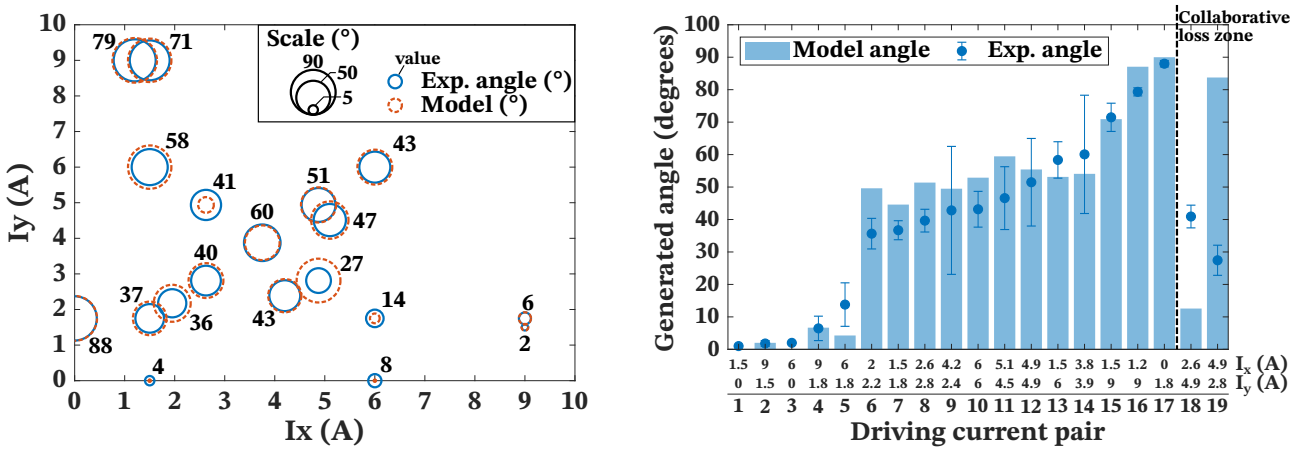

(a) (b)

Figure 4.15: Angle to the x-axis generated by the object's xy plane displacement on a 2×2 DAA. (a) Bubble chart of I_x vs I_y with the bubble diameter proportional to the angle (degrees). (b) Error bar plot between the experimental and predicted angle.

Figure 4.15b confirms that when one of the driving currents was zero ($I_x = 0$ or $I_y = 0$), a 1D linear displacement along the correspondent axis was obtained, i.e., an angle tending to 0° along $I_y = 0$ and 90° along $I_x = 0$ (pairs 1, 3 and 17 in Figure 4.15b). For similar values of I_x and I_y, similar displacements on both axes were obtained, i.e, angles tending to 45° (experimentally from 43.16° to 51.48° for pairs 10, 11 and 12 in Figure 4.15b).

For opposing magnitudes of I_x and I_y currents, e.g. pairs 4 or 15 in Figure 4.15b, antagonistic phenomena was observed: as shown in Figure 4.9, a low current generated a big displacement of the object, so the low current axis should generate a big displacement. On the other hand, the MPM moved quicker in the high current axis than in the low current axis. As the MPM arrived to its stroke in the high current axis, it contacted the wall's cavity, creating a friction force. The high current along such axis increased the mentioned friction force opposing and limiting the displacement along the low current axis. The dynamic model correctly predicted this antagonistic behavior for all experimental pairs except for pairs 18 and 19 (Figure 4.15b).

On pairs 18 and 19 of Figure 4.15b, the antagonistic phenomena described before was observed, but the current difference between the currents was smaller than for the other antagonistic pairs (2.07 for pair 18 and 2.31 A for pair 19). With this smaller current difference, as the MPM arrived to the stroke distance, the created friction force was not as overwhelming as the previous explained antagonistic phenomena and the system entered the "collaborative loss zone" explained before. This explains the divergence between the model and the experimental

results on these points.

The dynamic model predicted the experimental results with a root-mean-square error of 12.3° and mean-absolute error of 9.86°, excluding the collaborative loss points. The mean standard deviation for all the experimental points (angle repeatability, error bars) was 6.3°.

4.3.5 Conveyable mass

To evaluate the conveyable mass on the DAA, a glass plate with plastic masses was used as conveyed object. A 2×2 DAA was loaded with different masses, from 0.411 g to 8.901 g. Then the driving current on the x-axis (I_x) was increased until a displacement of more than 20 µm was observed. This displacement value was chosen to be sure that the DAA correctly executed the displacement step on its collaborative zone. The value of the driving current was considered as the minimum current intensity to obtain such displacement, and was compared to the value predicted by the model. Figure 4.16 presents the conveyed mass vs the minimum driving current intensity value. A linear regression of experimental results was done, including the 95% confidence intervals.

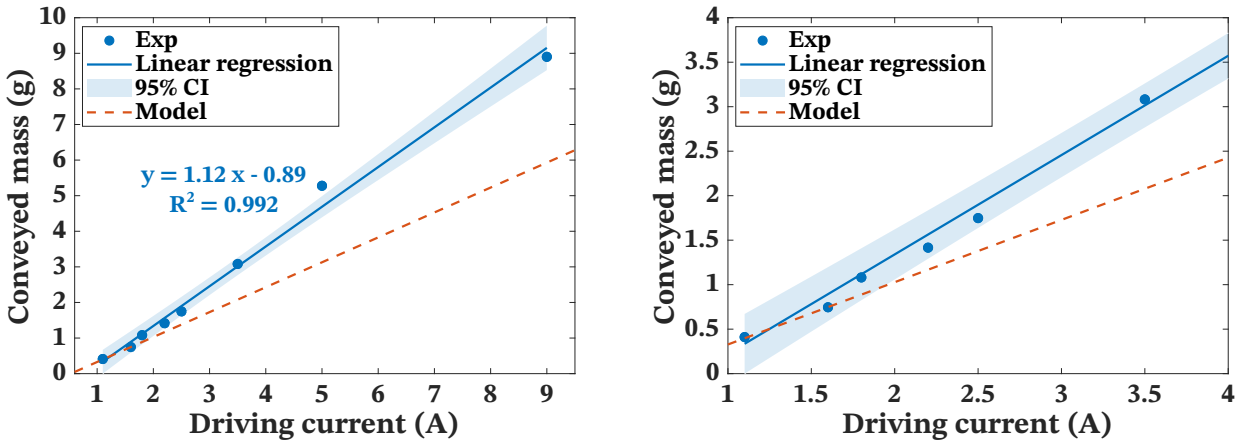

Figure 4.16: Conveyed mass vs minimum driving current intensity value on a 2×2 DAA. Linear regression of experimental results with 95% confidence intervals. (a) Complete mass range. (b) Figure detail [0,4]g - [1,4]A.

From Figure 4.16, the experimental results followed the linear regression with a R^2 of 0.992, which indicates a high linearity. The linear regression root-mean-square error to the experimental points was 0.247 g. The dynamic model also predicted a linear relation between conveyed mass and minimum driving current, but with a smaller slope. This means that the experimental results outperformed the predictions, resulting in a better performance than anticipated for heavier

loads. The model was accurate, staying on the 95% confidence interval, for masses up to 1 g. Inside this zone, the model correctly predicted the experimental points with negligible error. For masses up to 2 g the model had a root-mean-square-error of 0.217 g and mean-absolute error of 0.165 g. For heavier masses, the model deviates from the experimental values. This deviation could be caused by the friction model used by the dynamic model. The friction model parameters were identified using a 411 mg load on a 2×2 DAA. For heavier masses these parameters could change, affecting the results of the dynamic model.

4.3.6 Rotation

The other planar motion capability of the DAA is to rotate the conveyed object around a normal axis to the xy plane. To evaluate this, independent driving currents were injected into both wires (I_x and I_y) of each actuator of a 4×4 DAA. Multiple EDA movement superposition could produce an object rotation. The movement superposition represented in Figure 4.17 was used. The angle of object rotation to the y-axis was measured for one displacement step for multiple currents combinations (Figure 4.18). Then, the object was reset to the initial orientation before a new measurement. This process was repeated 20 times. The

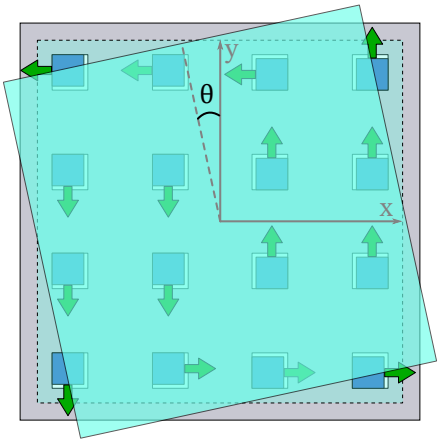

Figure 4.17: Object rotation on a 4×4 DAA. Multiple EDA movements could superpose to produce a rotation, only one solution represented.

pulse duration of the current pairs were larger than the kinematics of the MPMs as in Section 4.2. The results are presented in Figure 4.18a and Figure 4.18b.

The bubble chart (Figure 4.18a) presents the experimental angle as a function of both I_x and I_y. The area of the bubble is proportional to the angle value. This representation maps, geometrically, the influence of the current intensity on the generated angle.

The raincloud plot [All+19] (Figure 4.18b) presents the experimental data (dots) with its average (solid color line), the statistical box plot (percentiles) and

probability distribution of the rotation angle for each driving current combination.

At the present time, the dynamic model do not have the functionality to predict this rotation angle. This functionality would require a torque computation of each EDA to the object's center of mass at each time step. This will be discussed on the perspectives section of the dissertation.

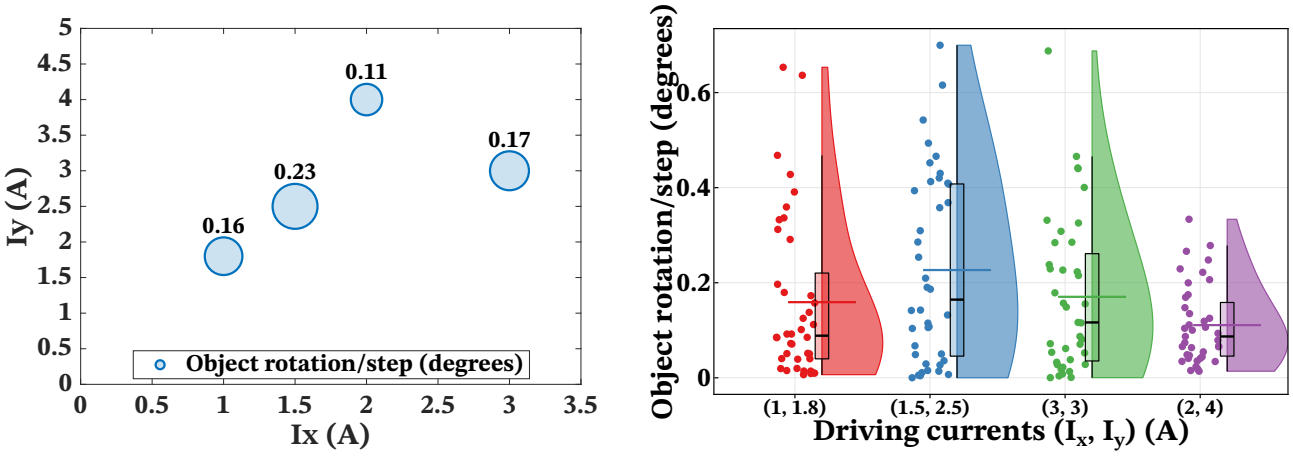

(a) (b)

Figure 4.18: Object rotation on a 4×4 DAA. (a) Bubble chart of I_x vs I_y with the bubble area proportional to the angle (degrees). (b) Raincloud plot.

From Figure 4.18a, the mean rotation angle ranged between 0.11° to 0.23° for the different current combinations. This is a small range. From Figure 4.18b, the experimental standard deviation of the points was important. The (2,4) driving current combination showed the smallest mean rotation and variability (0.11±0.08°). This point could be used for precise rotation of the conveyed object.

4.4 Summary & Discussion

The EDA and DAA performance varying all its input variables were characterized and compared with the developed dynamic model. Multiple configurations of the DAA (2×2, 3×3, 4×4 and 5×5) were tested. From the experimental measurements, the EDA obtained MPM rising times[1] from 0.8 ms and settling times[2] from 2.4 ms. The maximum conveyed object displacement per displacement step of the DAA was 204.5 µm, and the minimum was 7.9 µm. The minimum straightness error was measured at 5.2 µm and 3.88 µm (x-axis and y-axis respectively), and a position repeatability of 4.7 µm and 5.3 µm (x-axis and y-axis respectively). The planar motion capability of the array was demonstrated with bi-dimensional

[1]Time needed for the output to reach from 10% to 90% of its final value
[2]Time needed for the output to stay within 2% of the final value

object conveyance and object rotation tests. For the bi-dimensional conveyance, a spectrum of conveyed object angles from 1° to 88° was measured. From the rotation test, the minimum rotation angle per step was 0.11° and the maximum was 0.23°. The heaviest conveyed mass was 8.901 g with 9 A driving current.

Table 4.2 synthesizes all experimental conditions and model correlations presented in this chapter. Positive values of current represent driving currents and negative values holding currents.

From this table, the dynamic model correlated with the behavior of the system with low root-mean-square and mean-absolute errors for all the system's variables: DAA size and number of actuating EDAs; I_x and I_y current signals (intensity and time); and object mass. The EDA and conveyed object kinematics, uni- and bi-dimensional displacements of the conveyed object were predicted, allowing the understanding and explanation of the physical phenomena behind the system's behavior.

Table 4.2: System characterization & model validation tests.

System	N_a	DoF	Load (mg)	I_x (A)	I_y (A)	I_r (A)	t_x (ms)	t_y (ms)	t_r (ms)	RMSE (µm)	MAE (µm)	N. of tests
Kinematics												
EDA	1	x	0	[1.5 ; 9]	0	-	10	-	-	MPM: 5.72 ± 0.89	-	6
EDA	1	x	0	[1.5 ; 9]	-1	-	10	10	-		-	6
EDA	1	x	0	2	0	-	[2 ; 11]	-	-		-	6
2 × 2	4	x	202	2	0	-	[3 ; 5]	-	-		-	3
2 × 2	4	x	2050	[3.7 ; 5]	0	-	10	-	-		-	5
2 × 2	4	x, y, xy	217	[1.2 ; 8]	[-3 ; 7]	-	100	100	-	Obj: 7.38 ± 3.32	-	15
2 × 2	4	x, y, xy	2065	[2.2 ; 8.5]	[-3 ; 0]	-	100	100	-		-	8
2 × 2	4	x, y, xy	217	[1 ; 8]	[-2 ; 6.5]	[5 ; 6.5]	[10 ; 40]	[10 ; 40]	5		-	20
Driving current intensity												
2 × 2	4	x	411	[1.1 ; 9]	0	-	50	-	-	29.87	24	28 × 20
2 × 2	4	y	411	0	[1.25 ; 9]	-	-	50	-	19.05	16	28 × 20
2 × 2	4	x	411	[1.5 ; 6]	-1	-	50	50	-	31.07	30.25	10 × 20
2 × 2	4	y	411	-1	[1.5 ; 6]	-	50	50	-	26.92	23.06	10 × 20
3 × 3	9	x	267	[1 ; 6]	0	-	50	-	-	31.99	21.62	13 × 20
3 × 3	9	y	267	0	[1 ; 6]	-	-	50	-	22.86	17.49	13 × 20
3 × 3	9	x	267	[3 ; 6]	-1	-	50	50	-	10.84	9.57	6 × 20
3 × 3	9	y	267	-1	[3 ; 6]	-	50	50	-	15.66	13.8	6 × 20
4 × 4	16	x	468	[1.5 ; 5]	0	-	50	-	-	13.52	11.45	11 × 20
4 × 4	16	y	468	0	[1.5 ; 5]	-	-	50	-	11.23	10.17	11 × 20
4 × 4	16	x	468	[2 ; 5]	-1	-	50	50	-	11.02	8.44	11 × 20
4 × 4	16	y	468	-1	[2.5 ; 6]	-	50	50	-	26.12	22.82	10 × 20
5 × 5	25	x	468	[1.7 ; 4]	0	-	50	-	-	9.73	9.37	6 × 20
5 × 5	25	x	468	[2.5 ; 5]	-1	-	50	50	-	13.76	10.26	4 × 20
Driving current pulse duration												
2 × 2	4	x	411	2	0	-	[1 ; 50]	-	-	14.2	13	5 × 20
2 × 2	4	x	411	6	0	-	[1 ; 10]	-	-	6.86	5	4 × 20
Number of acting EDAs												
4 × 4	[11 ; 16]	x	468	3.5	0	-	50	-	-	7.63	6.65	6 × 20
4 × 4	[11 ; 16]	y	468	0	4	-	-	50	-	9	6.69	6 × 20
4 × 4	[11 ; 16]	x	468	4	-1	-	50	50	-	1.87	1.68	6 × 20
4 × 4	[11 ; 16]	y	468	-1	4	-	50	50	-	9.1	7	6 × 20
5 × 5	21	y	468	0	[1.8 ; 4]	-	-	50	-	23.22	20.28	6 × 20
5 × 5	21	y	468	-1	[2.5 ; 6]	-	50	50	-	29.6	21.42	4 × 20
Bi-dimensional displacement												
2 × 2	4	xy	411	[1.5 ; 9]	[1.75 ; 9]	-	50	50	-	12.3°	9.86°	20 × 20
Conveyable mass												
2 × 2	4	x	[411 ; 8901]	[1.6 ; 9]	-	-	200	-	-	217 mg	165 mg	13 × 20
Rotation												
4 × 4	16	xy	468	[1 ; 3]	[1.8 ; 4]	-	50	50	-	-	-	4 × 20
											Total tests:	316 (× 20)

Chapter 5

Model applications: Scaling laws, energy optimization and "Modular Modeling"

This chapter presents three model applications: the scaling laws study of the digital actuator, the energy optimization of the actuator operation and the extension of the model to any actuator geometry.

The first application, the scaling study of the actuator, is derived from the scaling laws, the interaction of the forces on the actuator and the developed dynamic model. From this study, the miniaturization potential of the square EDA is found.

The second application, the energy optimization of the actuator, deduces the current profile to minimize the energy consumption of the MPM movement from one discrete position to another using the dynamic model. This application also obtains a wished movement time, displacement, speed or acceleration profile of the MPM or conveyed object.

Finally, an implementation of the dynamic model in adaptable modules is presented. This "modular modeling" extends the dynamic model to any actuator and array geometry using the same principles as the square DAA. The modules and their information transfers are explained first. Then, the implementation of the modular modeling on a hexagonal digital actuator and array system is demonstrated.

5.1 Scaling physics of the elementary digital actuator

The aim of this study is to predict the miniaturization potential of the presented square elementary digital actuator (EDA). This potential is derived from the

scaling laws, the interaction of the forces on the actuator and the developed dynamic model. The scaling theory of the system is presented next to understand the relative magnitude of the forces interacting on the digital actuator.

5.1.1 Weight force scaling

An element with linear dimension S, e.g. cube with side S, has a volume V that varies as $V \propto S^3$. This implies that the mass m scale to $m \propto S^3$ (keeping density constant). As the weight force is $F_{weight} = mg$, with g the constant gravitational acceleration, then $F_{weight} \propto S^3$ [Wau01]. If the proportions of the system are scaled with this factor S, then the weight force scales as $F_{weight} \propto S^3$.

5.1.2 Friction force scaling

The basic model for friction interaction is the Coulomb friction model, which models the friction force as $F_{friction} = \mu F_{weight} = \mu mg$, where μ is the friction coefficient. Provided μ is constant, $F_{friction} \propto S^3$, as it depends on the mass. At the microscopic level the adhesive forces are larger and the surface roughness smoother. Striction (i.e. the combination of adhesion and friction) forces scale like the contact area, so $F_{striction} \propto S^2$ [Wau01]. Surface tension has a scaling of S^1 because it depends upon the length of the wet interface [Tri97]. Combining this factors, the scaling factor of the friction force is considered as $S^{1.5}$ in this discussion.

5.1.3 Magnetic force scaling

The potential magnetic interaction energy, $U_{\vec{B}}$ between two magnets, each with total magnetic moment m generating a magnetic flux density $\vec{B}$ in free space is given by [Jac99] as $U_{\vec{B}} = -m\vec{B}$. Supposing that the total volume of the magnet V has a magnetization $\vec{M}$ then $U_{\vec{B}} = -V\vec{M}\vec{B}$. As U is a function of volume, then $U_{\vec{B}} \propto S^3$. The magnetic interaction force is defined as [Zan13]:

$$F_{magnetic} = -\frac{\partial U_{\vec{B}}}{\partial \vec{r}} \tag{5.1}$$

As $F_{magnetic}$ is the derivative of the potential magnetic interaction energy by a dimensional unit, then $F_{magnetic} \propto S^2$

5.1.4 Electromagnetic force scaling

The electromagnetic force between a current-carrying wire and a magnetic flux density field source is given by the Lorentz's force [Gri05]

$$\mathrm{d}F_{em} = I\mathrm{d}l \times \vec{B} \tag{5.2}$$

With I the current intensity, l the wire length and $\vec{B}$ the magnetic flux density. The scaling of $\vec{B}$ is S^0, as it is an intensive variable and depends upon the saturation field of the material used [Tri89]. The wire length is scaled with the scale factor S. The electromagnetic force scaling depends then on the scaling of I. There are three possible cases for the scaling of I assuming different hypothesis: constant current density, constant heat flow through the wire's surface or constant temperature rise between the wire and surroundings [Tri89]. The three hypotheses are explained next.

5.1.4.1 Constant current density

Assuming the current density J as an intensive variable, i.e., J is kept constant under scaling ($J \propto S^0$), results in $I \propto S^2$. This is because $I = \int J\mathrm{d}A \Rightarrow I = JA$. This implies that $F_{em} \propto S^3$ as Equation (5.2) is integrated along a dimensional variable.

5.1.4.2 Constant heat flow

The heat flow Q per unit wire surface area A_s and resistivity ρ are assumed constants (Q/A_s) $\propto S^0$ and $\rho \propto 0$. The heat flow must be equal to the power dissipated in the wire, so:

$$Q = I^2R = I^2\left(\frac{\rho l}{A_e}\right) \tag{5.3}$$

With A_e the cross-sectional area of the wire. As $l \propto S$, and $A \propto S^2$ the previous expression gives:

$$\frac{Q}{A_s} \propto S^0 = \frac{I^2\rho l}{A_s A_e} \propto I^2 S^{-3} \tag{5.4}$$

Implying $I \propto S^{1.5}$, which implies that $F_{em} \propto S^{2.5}$.

5.1.4.3 Constant temperature rise

There is a maximum temperature that the wire and insulator can withstand. In this case, the maximum temperature between wire and ambient is assumed scale

constant. The equation of heat conduction is:

$$\frac{\mathrm{d}Q}{\mathrm{d}t} = -kA\frac{\mathrm{d}T}{\mathrm{d}r} \tag{5.5}$$

With k the thermal conductivity, A the surface area of the wire ($2\pi rl$) and r the dimension along the wire radius (supposing a cylindrical wire). This heat conduction is equal to the power dissipated inside the wire:

$$\frac{\mathrm{d}Q}{\mathrm{d}t} = I^2R = (JA_e)^2\frac{\rho l}{A_e} = J^2\rho l\pi r^2 \tag{5.6}$$

This means that Equation (5.5) for the wire is:

$$\frac{1}{2}\int_0^r J^2\rho r\mathrm{d}r = \int_{T_0}^{T_s} -k\mathrm{d}T \tag{5.7}$$

Integrating, and noting $T_s - T_0 = \Delta T$, results in:

$$J^2\rho\left(\frac{r^2}{4}\right) \propto S^2 = -k\Delta T \propto S^0 \tag{5.8}$$

As the assumption is $\Delta T \propto S^0$, then $J \propto S^{-1}$ and, as $I = JA$, then $I \propto S^1$. This implies that $F_{em} \propto S^2$.

5.1.5 Force scaling analysis

The developed dynamic model and the presented scaling laws are used to compute the force interactions on the EDA as a function of the scale factor S. Figure 5.1 presents the results. The vertical black line places the real EDA's side length (S = 9.6 mm).

From the general view of Figure 5.1a, if the system is up-scaled to macro dimensions ($\sim$ 1 m), the friction influence is reduced relative to all the other forces in the system. This is beneficial to the efficiency of the actuator but, on the other hand, the weight influence quickly becomes the main obstacle to surpass. Given the S^3 scaling factor of the weight, and the weaker scaling factor of the magnetic force (S^2), the digital aspect of the actuator would be lost at this scale as the magnetic force would not be able to move the MPM mass. If the system is down-scaled, the friction phenomena becomes the predominant force. The weight influence plunges with a S^3 factor. From the detailed view in Figure 5.1b, the point where the weight becomes less important than the friction (square 1 in Figure 5.1b) is S =5.4 mm). Down-scaling the system further, the electromagnetic force assuming constant current becomes unable to overcome

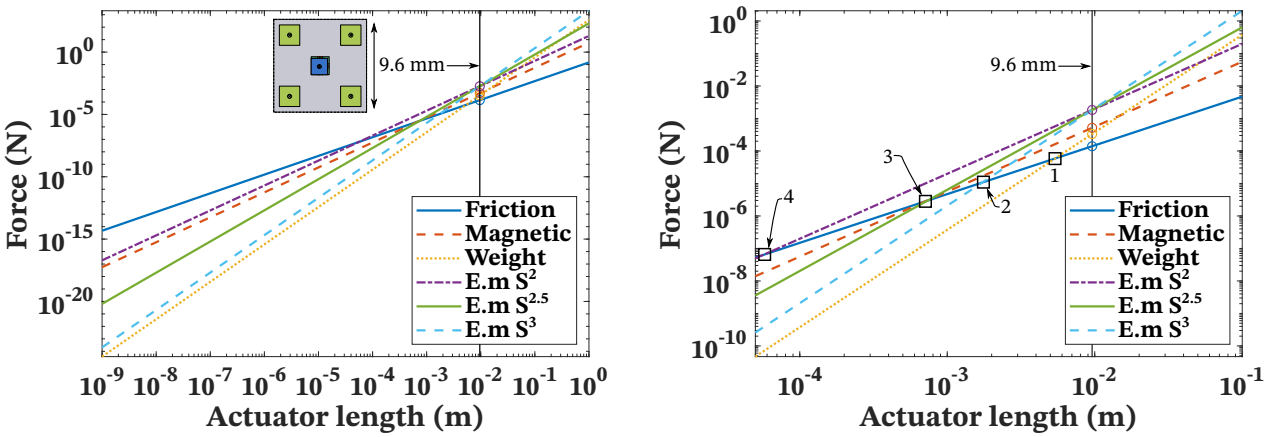

Figure 5.1: Force scaling of the EDA. The electromagnetic force assuming constant current, constant heat flow and constant temperature rise are abbreviated E.m S^3, E.m $S^{2.5}$) and E.m S^2. (a) Large interval. (b) 10 cm to 100 µm range and critical points of the EDA down scaling.

the friction at 2.3 mm (square 2). From this point onward the current density of the wires need to increase if the system is to work. Down-scaling further, the magnetic and electromagnetic (assuming constant heat flow) forces match the friction influence (square 3, L = 1.1 mm). On this critical point, the digital actuation of the EDA is lost and the electromagnetic force between the magnet and actuating wires (assuming constant heat flow) cannot overcome the friction. The minimal length of the *digital* actuator is then S =1.1 mm (square 3). This is the minimization potential of the EDA. The last resource to continue down-scaling is to use the electromagnetic force with constant temperature rise to actuate the system (that is no longer digital). The working limit of the actuator is then square 4 at 0.13 mm, where the friction overcomes this last resource.

If the EDA needs to attain smaller dimensions, the geometry of the actuator needs to produce larger magnetic and electromagnetic forces to overcome the friction phenomena at small scales. For example, an increase of 20% more magnetic force (reducing the distance between FPMs and MPM); and 50% more electromagnetic force (increasing the number of wires); reduces the minimal length to 0.75 mm but at the cost of energy efficiency.

5.2 Energy optimization and kinematic control

The aim of this application is to optimize the energy consumption of the EDA by finding optimal control currents profiles for the desired kinematics. Equation (3.1), in Section 3.2, stated Newton's Second Law for a single MPM (m_{MPM})

carrying its share of the conveyed object's mass (m_{object}), which is divided between the number of MPMs, N_{MPM}. Equation (5.9) is the same equation for the x-axis displacement.

$$\sum \vec{F}_x = \left(m_{MPM} + \frac{m_{object}}{N_{MPMs}}\right) a_{MPMx} = \vec{F}_{emx} + \vec{F}_{mx} + \vec{F}_{f1} + \vec{F}_{f2} + \vec{F}_{f3} \tag{5.9}$$

The dynamic model found expressions of the forces in Equation (5.9) that define the MPM's (and object's) kinematics. Those expressions can be represented as functions of the MPM's positions (x, y, z) and MPM's speed $(\dot{x}, \dot{y})$. The following expressions are then obtained:

$$\vec{F}_{emx} = I_x f(x, y, z) \tag{5.10}$$
$$\vec{F}_{emy} = I_y h(x, y, z) \tag{5.11}$$
$$\vec{F}_{emz} = I_x k(x, y, z) + I_y n(x, y, z) \tag{5.12}$$
$$\vec{F}_{mx} = p(x, y, z) \tag{5.13}$$
$$\vec{F}_{my} = q(x, y, z) \tag{5.14}$$
$$\vec{F}_{f1} = \mu_1(\dot{x}, \dot{y}) \left(m_{MPM} g - \vec{F}_{emz} + \frac{m_{object} g}{N_{MPM}}\right) \tag{5.15}$$
$$\vec{F}_{f2} = \mu_2(\dot{x}, \dot{y})(-\vec{F}_{my} - \vec{F}_{emy}) \tag{5.16}$$
$$\vec{F}_{f3} = \mu_1(\dot{x}, \dot{y}) \frac{m_{object} g}{N_{MPM}} \tag{5.17}$$

With f, h, k, n, p and q the mentioned functions of the MPM's position.

The system dynamics are then defined by the currents I_x and I_y for a given number of actuating EDAs and object mass. An interesting procedure is to substitute $a_{MPMx} = 0$ in Equation (5.9) and solve the system for I_x. This means, to find the current which brings the system to mechanical equilibrium (the one that cancels the magnetic and friction forces). This current is called *balance current* (I_{bx}). If a small current δI is injected in addition to I_{bx}, a displacement will be generated. Even more, the dynamics would follow the simple Equation (5.18), as the balance current cancels the "resistance" forces (magnetic and friction forces).

$$\sum \vec{F}_x = \vec{F}_{emx} = \left(m_{MPM} + \frac{m_{object}}{N_{MPMs}}\right) a_{MPMx} \tag{5.18}$$

This procedure can generate the wished kinematics of the system. The balance current was calculated for a 5×5 DAA carrying a 700 mg object without holding current. Static values of μ_1 and μ_2 were used (they are functions of $(\dot{x}, \dot{y})$). Figure 5.2 presents the balance current for the MPM position on its cavity.

Figure 5.2a, presents the solution along the x-axis fixing y at the lower discrete position ($-100\,\mu$m, touching the cavity wall). The balance current was 0.53 A at

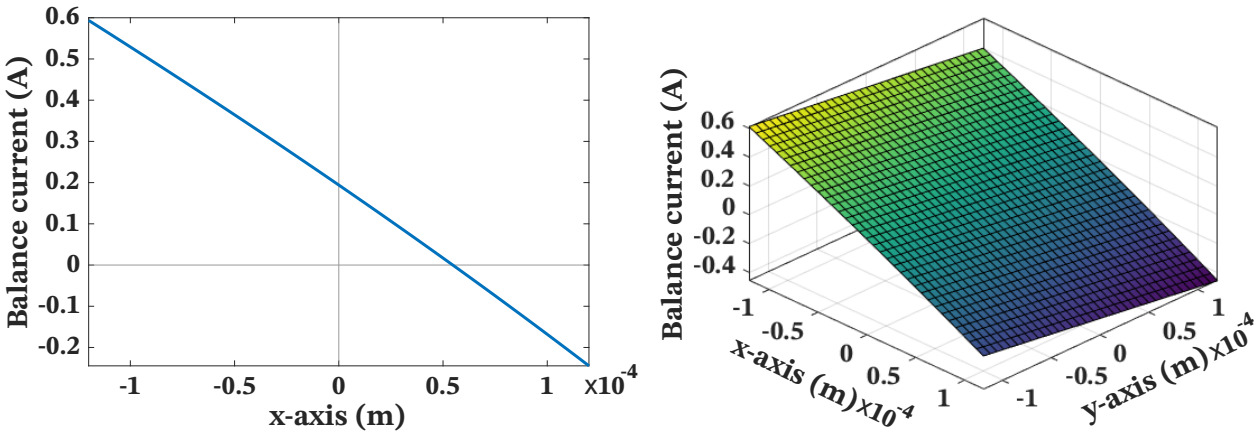

(a) (b)

Figure 5.2: Balance current I_b for an EDA of a 5×5 DAA carrying a 700 mg object without holding current. (a) Along the x-axis at $y = -100\,\mu$m. (b) As a function of xy position in the square cavity.

the discrete position ($x = -100\,\mu$m) and decreased as the MPM traveled towards the $+x$-axis. At $x = 0$ the balance current was 0.19 A. At this point, the only resistance forces are the friction forces, because the magnetic forces are naturally balanced). This means that the balance current compensates the static friction of the wall, glass floor and object. The balance current had a null value at $x = 54.67\,\mu$m. This is where the magnetic force attracts the MPM with enough force to overcome the static friction forces. From that point onward, the balance current had negative values, as it now needs to compensate the magnetic force attracting the MPM towards $x = 100\,\mu$m. Figure 5.2b presents the balance current as a function of (x, y) position on the square cavity. At $(x, y) = (0, 0)$ the balance current only needs to compensate for the static friction of the glass floor and conveyed object. The balance current was 0.11 A at this point. The balance current is not perfectly symmetrical for both axes as the z component of the electromagnetic force of both driving wires are directed in different directions on the four quadrants of the cavity.

The balance current computation and dynamic model (without rebounds) were implemented on a Simulink model. A constant MPM acceleration of $1\,\mathrm{m\,s^{-2}}$ was set as kinematic objective. A 2×2 DAA carrying a 411 mg object was used as simulation scenario. Using the balance current and Equation (5.18) to calculate the actuating current to obtain the wished acceleration (I_{ax}), the DAA was able to move the object at the imposed MPM acceleration, as presented in Figure 5.3. Figure 5.3a presents the total current injected to the system ($I_x = I_{bx} + I_{ax}$) and the portion of this current that is due to the balance current and actuating current.

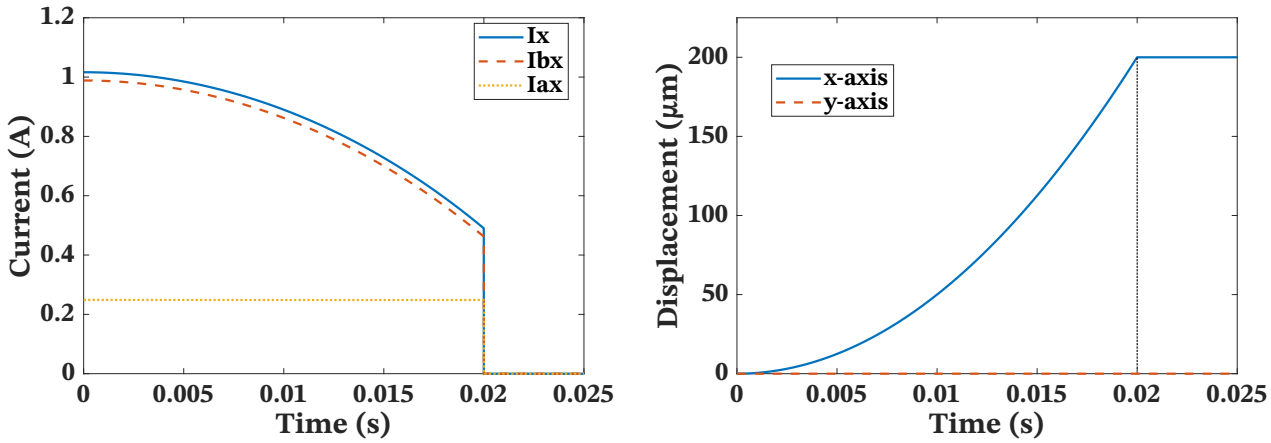

(a) (b)

Figure 5.3: Balance current and kinematic control results along the x-axis for a 2×2 DAA. (a) I_x current and its composition. (b) MPM kinematics.

From Figure 5.3b, the simulated kinematics of the EDA followed the constant acceleration objective. This is demonstrated by displacement curve shape and the time to reach the stroke value (200 µm). Assuming constant acceleration, the MPM should follow the kinematic equation $\Delta x = v_0 t + at^2/2$. The stroke corresponds to Δx, v_0 is zero for a static departure and the acceleration (a) is the commanded 1 m s^{-2}. Solving for the displacement time (t), the result is 0.02 s, as obtained in Figure 5.3b.

This application can therefore control the kinematic behavior of the DAA to obtain wished conveyance times or displacement, speed or acceleration profiles. For example, constant acceleration or speed displacements with an imposed conveyance time are possible. Even more, the wished displacement minimizes the consumed energy, as the balance current exactly balances the resistance forces. Therefore, only the needed current for the wished displacement is used to obtain mechanical motion.

5.3 Modular modeling

The aim of this application is to extend the developed dynamic model to any digital actuator and array geometry. For this, three adaptable model modules are developed. The first module recreates any actuator geometry and computes the discrete magnetic and electromagnetic forces on the actuator. The second module finds the continuous force functions of the actuator. The third module is the adapted dynamic model that predicts the dynamic behavior of the actuator and array.

Figure 5.4 is a flowchart of the modular modeling implementation.

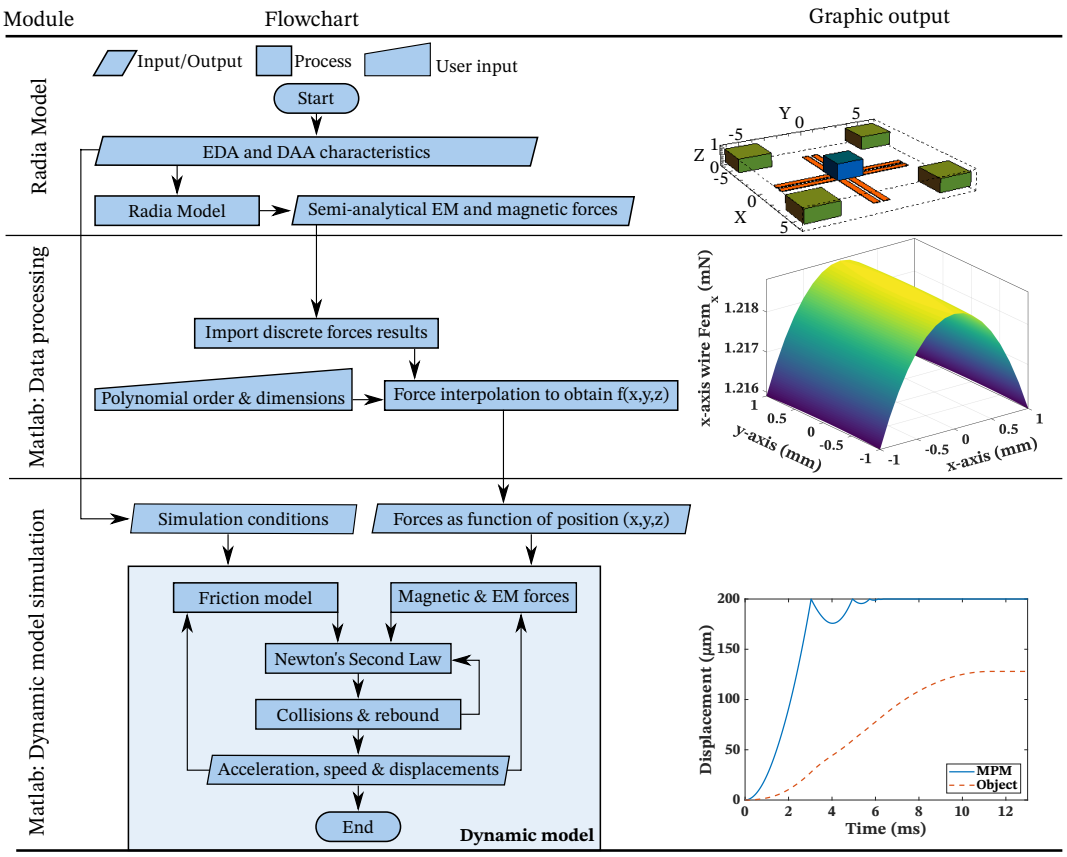

Figure 5.4: Modular model flowchart.

The implementation of this modular modeling to a hexagonal digital actuator is used to evaluate the application.

5.3.1 Modeling the given digital actuator

The DAA is based on a combination of individual actions of each digital actuator to obtain complex tasks. The principle of the dynamic model is to recreate the digital actuator and, assuming the array as homogeneous, sum the contribution of each actuator equally to obtain the resulting behavior of the array. This principle allows to dissociate the actuator and array geometry of the dynamic model. Under the previous assumption, the presented dynamic model can predict the system behavior with: the force analysis of the actuator; the stroke values; and the conveyance conditions (object mass, current inputs).

For the square DAA, the analytical solutions of the electromagnetic force and the magnets' B-field were used in the dynamic model. As explained in Chapter 3, the analytical solution of the magnets' B-field only exists for basic magnet geometries. Also, the magnetic force was discretized as its analytical expression can not always be evaluated. In the developed dynamic model the semi-analytical software Radia was used to compute this magnetic force. Radia

can also compute all electromagnetic and magnetic forces of a given digital actuator. The first module of the modular modeling is then a Radia model of the elementary digital actuator (EDA) of the system. This model needs the characteristics of the EDA as input (e.g. Table 3.1). An hexagonal EDA, built by Ajinkya Deshmukh in a parallel doctoral thesis of the ALVEO project [Des20], is used to demonstrate and evaluate the modular modeling application.

The hexagonal EDA is composed of seven gold-coated NdFeB permanent magnets placed in a silicon structure (Figure 5.5). The central hexagonal MPM has dimensions of ⬡ $5.0 \times 5.0 \times 2.2$ mm. The hexagonal cavity creates three stroke values: Stroke x_1, the long stroke in the x-axis (1000 µm); Stroke x_2, the short stroke in the x-axis (500 µm); and Stroke y, the stroke in the y-axis (866 µm). The other six fixed permanent magnets are fixed around the square cavity to create six exploitable discrete positions.

To actuate the digital actuator, three wires are placed under the cavity for each displacement axis. This maximizes the generated electromagnetic force for the heavier hexagonal MPM compared to the previously studied square MPM. The hexagonal digital actuator characteristics are presented in Table 5.1.

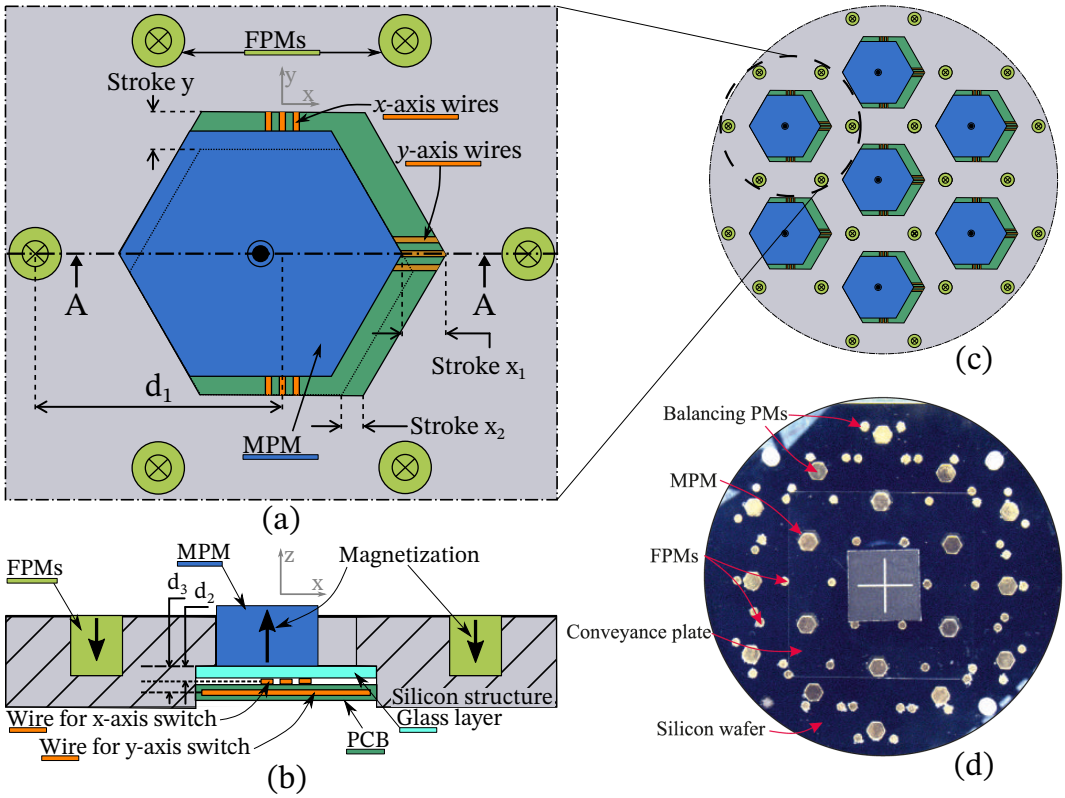

Figure 5.5: Hexagonal EDA (a) Top. (b) Front (A-A cut). (c) Hexagonal DAA. (d) Prototype.

The hexagonal DAA consists of a honeycomb arrangement of hexagonal digital actuators (Figure 5.5). As the square DAA, adjacent actuators share a pair

Table 5.1: Hexagonal EDA Characteristics

Element	Dimensions (mm)	Mass	Material	Mag. (T)
Hex. MPM	⬡ $5.0 \times 5.0 \times 2.2$	290 mg	NdFeB	1.37
FPM	⌀ 2.25×2	54 mg	NdFeB	1.43
Variable	**Distance between**			**Value (μm)**
d_1	Cavity and FPMs			1288
d_2	MPM and *x* wire			200
d_3	MPM and *y* wire (wire separation)			300
d_4	Mobile and FPMs thickness (*z*-axis)			200
Stroke x_1	Long stroke in the *x*-axis			1000
Stroke x_2	Short stroke in the *x*-axis			500
Stroke y	Stroke in the *y*-axis			866

of FPMs to decrease the array size. The array combines individual actions of each actuator to obtain complex tasks, as the square DAA. The same "stick-slip" strategy of the square DAA to convey an object is used. The hexagonal array is also a planar motion device. As the materials of this hexagonal system and the square systems are the same (gold-coated NdFeB MPM, silicon cavity and glass layers), the same friction model was used in the dynamic model.

Figure 5.6 presents the developed Radia models of the previously studied square EDA and the hexagonal EDA.

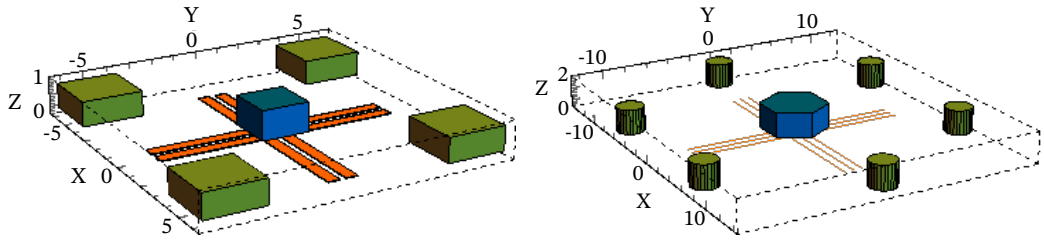

(a) (b)

Figure 5.6: Radia models (a) Square EDA. (b) Hexagonal EDA.

The Radia models are used to compute the magnetic and electromagnetic forces on the EDA's cavity. Figure 5.7 presents the results of the hexagonal actuator.

The Radia model computes the electromagnetic and magnetic forces of the actuator as functions of the MPM position in space. These are discrete positions, giving discrete values of force for each position. The dynamic model needs continuous functions of force to compute the acceleration of the MPM and object at any given time. For this, a second module processing the data from the Radia model and interpolating the discrete points to obtain a function of force vs

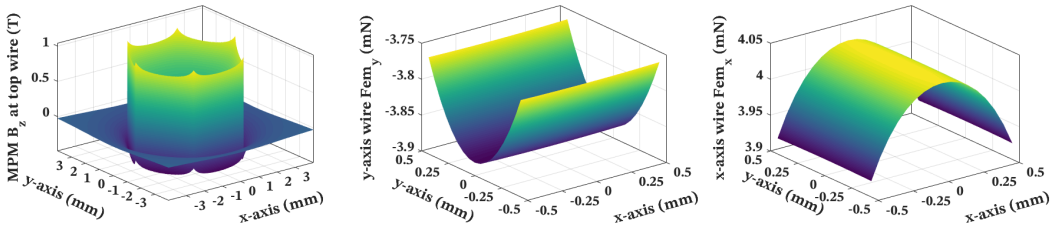

(a) (b) (c)

Figure 5.7: Hexagonal EDA Radia results. (a) MPM z component B-field. (b) x-axis component of electromagnetic force on x wire $\vec{F}_{emx_x}(x,y)$. (c) y-axis component of electromagnetic force on y wire $\vec{F}_{emy_y}(x,y)$.

position in space is needed. The user can define the interpolation method used by the module. The output of this module are continuous electromagnetic and magnetic force functions vs MPM position ($f(x,y,z)$).

Finally, these force functions are injected to the dynamic model. The EDA and DAA characteristics are needed to define the simulation conditions, like simulation time, simulation step time, number of EDAs in the array and number of actuating EDAs. The friction characteristics of the bodies in contact are crucial to construct the friction model based on Equation (3.19). The dynamic model is the principal block of this module, working as explained in Chapter 3. The output is the MPM and conveyed object displacement, speed, acceleration and mechanical forces though time. The experimental tests to validate the modular modeling of the hexagonal DAA are presented next.

5.3.2 Hexagonal geometry validation

To validate the modular modeling of the dynamic model, the Stroke x_1 (1000 µm) and Stroke y (866 µm) of the hexagonal DAA were used to convey a 957 mg object. The same driving current intensity test of Section 4.3.1 was executed on the hexagonal DAA.

The same materials and methods as the square DAA were used for this hexagonal test (Section 4.1). The Grasshopper camera, with a 2.45 µm/pixel resolution, was used to measure the object's displacement.

Figure 5.8 presents the driving current intensity influence on the object displacement of the 7 ⬡ DAA. A variable driving current intensity was injected in only one of the two pair of wires of each actuator at a time. This produced a linear motion of the MPM and the object along that axis only. A pulse duration of 200 ms was selected to ensure that the driving current was longer than the system kinematics. No holding current was used.

From Figure 5.8, the object displacement decreased as the driving current

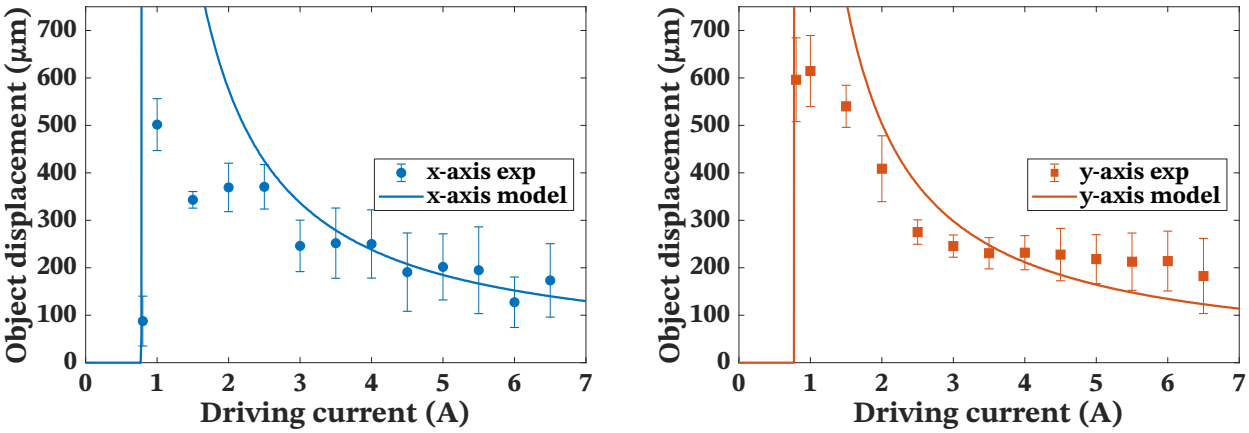

(a) (b)

Figure 5.8: Conveyed object displacement vs driving current intensity on the hexagonal DAA. (a) x-axis no holding current. (b) y-axis no holding current.

increased, as with the square DAA. The model predicted again this tendency correctly. Contrary to the square system, the error bars on the hexagonal DAA increased as the driving current increased. This is attributed to the angle of the hexagonal cavity that defines the discrete positions (60° compared to 90° of the square EDA). When the hexagonal MPM's impact speed increased, it had a tendency to rebound away from its discrete position due to this angle, increasing the uncertainty and straightness error of the conveyed object. On the square system, the impact occurs with a flat surface wall, fomenting rebounds on the same axis of the conveyed object, limiting the negative effects of the collision.

From Figure 5.8, the maximum experimental object displacement was (1 A, 501.7 µm) for the x-axis and (1 A, 614.6 µm) for the y-axis. The collaborative loss zones were under 1 A for both axes, and they were smaller than with the square system. Inside the collaborative loss zone, the experimental displacements of the object started from current values of 0.8 A for the x-axis and y-axis, in accordance with the model. This value is lower for the hexagonal system than the square system, given that the hexagonal EDA has 3 wires per axis, instead of 2 for the square EDA. The model, without considering the collaborative loss zone, predicted the x-axis measures with a root-mean-square error of 153.42 µm and a mean-absolute error of 128.35 µm. For the y-axis, the RMSE was 99.97 µm and MAE was 89.35 µm.

Table 5.2 summarizes the experimental test variables and results. The results show that the modular philosophy of the dynamic model allows it to be easily adapted to other EDA/DAA geometries and correctly predict their behavior.

Table 5.2: Modular modeling validation test on a hexagonal DAA.

System	N_a	DoF	Load (mg)	I_x (A)	I_y (A)	I_r (A)	t_x (ms)	t_y (ms)	t_r (ms)	RMSE (μm)	MAE (μm)	N. of tests
Driving current intensity												
7 ⬡	7	x	957	[0.8 ; 6.5]	0	-	200	-	-	153.42	128.35	13×20
7 ⬡	7	y	957	0	[0.8 ; 6.5]	-	-	200	-	99.97	89.35	13×20

Summary of Part II: Modeling, Identification & Validation

Chapter 3 explained the principles and characteristics of the elementary digital actuator (EDA) and the digital actuator array (DAA). The DAA conveyance strategy was explained, illustrated and its use in the microfactory context discussed. The fabrication and characteristics of a 5×5 DAA prototype were explained. Then, a dynamic model was developed starting from the force analysis of the EDA and its kinematic phenomena such as collisions and rebounds. The electromagnetic driving forces, magnetic holding forces, friction forces, collision and rebound events were studied, characterized and integrated in the dynamic model. Assuming that the array was homogeneous, and evaluating this assumption for the magnetic holding force, the dynamic model summed the contribution of the actuating EDAs equally to obtain the array behavior and the generated conveyed object displacements. The model uncertainties, assumptions and their implications were studied.

Chapter 4 presented the experimental array characterization and model validation. The materials and experimental setups were detailed. The input currents were characterized and their working limit determined. The experimental tests explored the influence of all inputs of the array (driving and holding current intensities and pulse duration, number of actuating EDAs on the array and object mass) on uni-dimensional and bi-dimensional motions of the EDA and conveyed object (single axis displacement, simultaneous displacement on two axes, object rotation). The displacement though time (kinematics) of the EDA and conveyed object were studied with a fast camera. These kinematics are the lower level physical events that occur on the DAA while conveying objects and are the basis of the DAA behavior. The capture and analysis of these events allowed to understand the interaction of the system parts and its global behavior.

From the experimental measurements, the EDA obtained rising times[1] from 0.8 ms and settling times[2] from 2.4 ms. The minimum and maximum conveyed object displacements per displacement step of the DAA were 7.9 µm and 204.5 µm, respectively. The minimum straightness error was measured at 5.2 µm and 3.88 µm (x-axis and y-axis respectively), and a position repeatability of 4.7 µm and 5.3 µm (x-axis and y-axis respectively). The planar motion capability of the array was demonstrated with bi-dimensional object conveyance and object rotation tests. For the bi-dimensional conveyance, a spectrum of conveyed object angles from 1° to 88° was measured. From the rotation test, the minimum rotation angle per step was 0.11° and the maximum was 0.23°. The heaviest conveyed mass was 8.901 g with 9 A driving current.

Table 4.2 synthesizes all experimental conditions and model correlations presented in this chapter. From this table, the dynamic model correlated with the behavior of the system with low root-mean-square and mean-absolute errors for all the system's control variables.

Finally, Chapter 5 presented three applications of the dynamic model. First, the scaling and miniaturization potential of the EDA were determined. Second, the current profile optimizing the energy consumption and kinematic behavior of the EDA was found. This principle can be used to find wished displacement, speed, acceleration profiles of the EDA and conveyed object on the DAA. Lastly, the dynamic model was extended to any EDA and DAA geometry with three flexible modules. The implementation of the modular modeling on a hexagonal actuator array was demonstrated. The modular model correctly predicted the hexagonal array behavior with low root-mean-square and mean-absolute errors.

[1] Time needed for the output to reach from 10% to 90% of its final value
[2] Time needed for the output to stay within 2% of the final value

Part III

Conveyance: Pathfinding & trajectory control

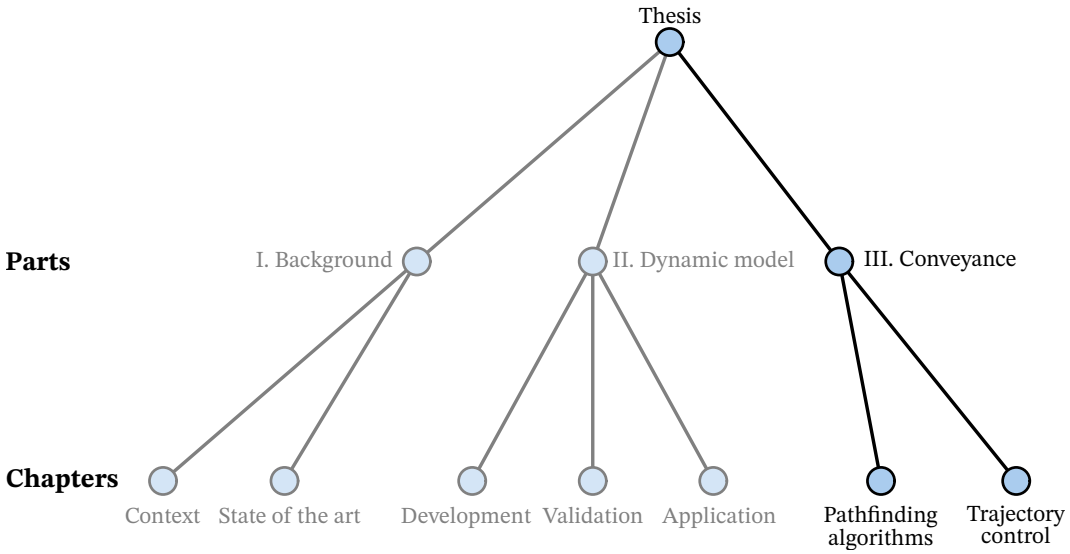

Chapter 6

Pathfinding algorithms & Trajectory control

In Section 2.3, pathfinding was defined as the geometric problem of determining a feasible path, from a start location to a goal location, through an environment with obstacles. Once the solution path is obtained for a given environment, how to execute this path on the system? This is the trajectory control problem, to translate the solution path into control variables to the system and execute the solution path.

This chapter explains the developed pathfinding and trajectory control of the studied square DAA. The pathfinding properties are described next, starting by the chosen real world representation: a discrete state-space (the grid). Then, the conveyance strategy to solve a basic trajectory control problem is explained. From this basic control strategy, the flowchart to solve the pathfinding and associated trajectory control is developed. Finally, the steps (blocks) to solve the problem, from inputs to a virtual prediction of the system behavior, are explained.

The DAA produces displacement steps, thus the displacement evolution in space is well represented by a discrete state-space, or a grid. Therefore, grid-based pathfinding algorithms are a good choice for the problem. A* and Theta* (Θ*) are chosen from the vast grid-based solutions.

A* is resolution complete, meaning it is guaranteed to return an optimal solution, if one exists (for the grid resolution given) [HNR68; Sha15]. A* is optimal in the number of expanded nodes. That is, any other equally informed search algorithm will have to expand all the nodes expanded by A* before identifying the optimal solution [HNR68; Sha15]. A* is also the base of other performance-enhancement algorithms like any-angle, real-time, any-time and even MAPF solutions. The A* adaptation to the DAA follows the idea of finding a fast solution for real-time, online implementations of the DAA as a conveyance device, where

execution time is important.

Θ* is an any-angle pathfinding algorithm based on A*. Θ* finds shorter real-life paths compared to A* as its solution is not limited to the grid nodes and edges, but it takes additional computation time to find the solution. The Θ* implementation to the DAA follows the idea of favoring performance and efficiency instead of execution time. Θ* also exploits the any-angle generation capabilities of the DAA.

In addition to the grid representation, the pathfinding problem on the DAA is informed and semi-static:

- Informed because the DAA has not a distributed sensor array, so it can not perform uninformed pathfinding problems (constant measurement of the environment). The DAA depends then on a global sensor like a camera or an user to input the target positions and space constraints to the pathfinding algorithm.[1]
- Semi-static because, once a solution path is calculated, the DAA executes this path in open-loop. The execution can be interrupted and a new path calculated if informed by the global sensor. Thus, it can adapt semi-statically on time.

6.1 Control strategy

The first step to control the trajectory of the conveyed object is to solve the simplest pathfinding and trajectory control problem: a straight line. This is because, as the DAA works digitally, i.e. in a step-by-step displacement output, the trajectories issued by any pathfinding algorithm will be approximated by digital linear steps (small straights).

Figure 6.1 presents this straight line case and the strategy to solve it. The idea is to cover the distance between the starting point and wished position executing the maximum displacement step available to the system (s_{max}). When the remaining distance between the object and the final position is smaller than s_{max}, a last tuning step ($s(I_d, I_h, N_a)$) is executed to attain the final position. This tuning step is a function of the control variables of the system: the driving and holding currents on the actuating wires (I_d, I_h); and the number of actuating EDAs (N_a). As the control variables of the system are determined for each displacement step (maximum and tuning), this strategy is called *control strategy*.

The dynamic model is used to compute the control variables that produce

[1] One can argue that if the camera is used as sensor, then the DAA could solve uninformed problems. This depends if the camera is taken as part of the system or not. This dissertation uses the camera to characterize the system, not to control it. Thus the DAA is an open loop system.

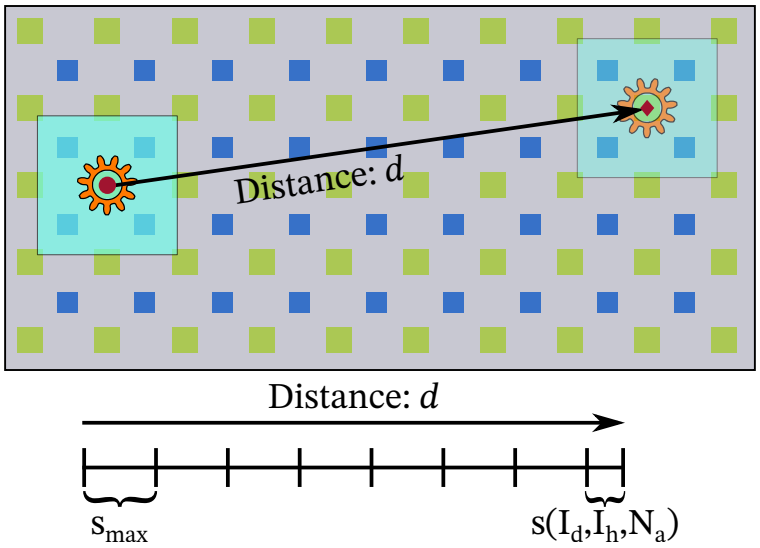

Figure 6.1: Straight trajectory control strategy.

the maximum and tuning steps. As explained in Chapter 4, the maximum displacement of the DAA was obtained with its maximum number of actuating EDAs (N_a), no holding current ($I_h = 0$) and its driving current (I_d) critical point. This is when the electromagnetic driving force is just greater than the magnetic and the friction forces. Due to the heterogeneity of the friction on the surfaces at the microscopic level, this critical point could slightly change between the EDAs. If this critical point is used for all the EDAs, the displacement could not occur as the collaborative action of the DAA is lost. To avoid this experimental problem, a margin from the collaborative loss zone, in terms of a minimum value of I_d, needs to be taken. For example, the 2×2 DAA minimum driving current could be 2 A (critical points at 1.5 A for the x-axis and 1.75 A for the y-axis).

With this control strategy, the complete pathfinding and trajectory control problem can be solved. Figure 6.2 presents the trajectory control flowchart. The use of the dynamic model, presented above, represents the "Dynamic model" block. The reminder blocks of the flowchart will be described next.

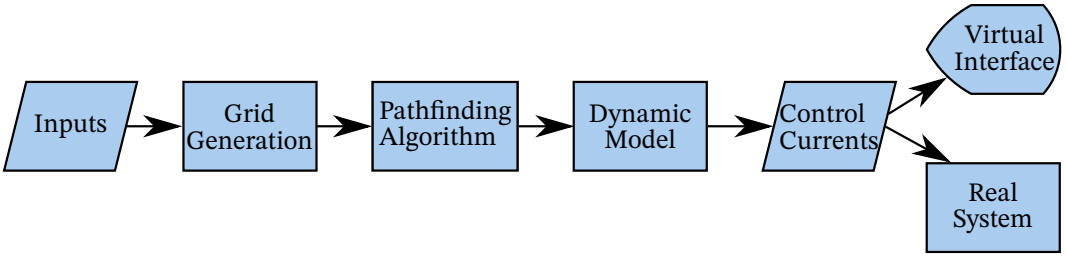

Figure 6.2: Trajectory control flowchart.

6.2 Inputs

The initial, intermediate and the final positions of the conveyed object (target positions) are the objectives of the pathfinding problem. Then, the obstacle positions and dimensions are asked to define the free space. The conveyed object size is also considered for the computations. Finally, an optional safety distance between the object and the obstacles can be added as constrain. These inputs are considered by the pathfinding algorithm to compute the solution path. This represents the “Inputs” block in Figure 6.2.

All the input information can be defined by the user or automatically injected into the algorithm via a text file. This is intended to automate the conveyance process in the microfactory, e.g., a camera with image processing software can generate the inputs, create the text file and pass it to the pathfinding algorithm (implemented in Matlab) to compute the solution path.

6.3 Grid generation

The grid generation is the most important step of the solution process, as both chosen algorithms are grid based. The grid defines the discrete free space of the object, thus defining the possible positions to explore and find a solution path. The solution path’s quality depends on the size of the grid (distance between nodes). A coarse grid produces faster solutions, but real-life sub-optimal paths (both algorithms find grid-resolution optimal paths). Coarse grids can also over-estimate obstacle sizes, reducing the path solution quality or even obtaining no results because close obstacles are taken as blocked regions. Finer grids improve the real-life solution path, but increase computation time. Figure 6.3 illustrates the grid size influence on the environment representation. The example shows how the real size of an obstacle represented on grids of different size. This shows how the grid size influences the solution path quality and number of nodes to explore to find a solution.

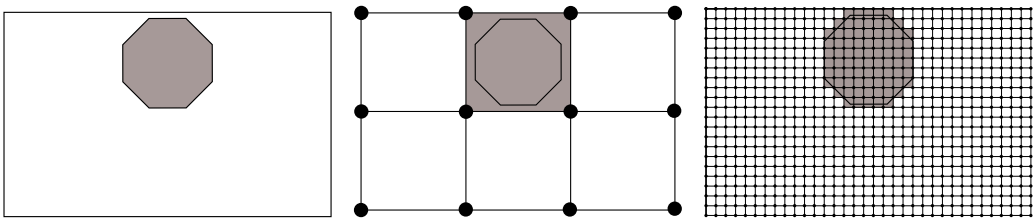

Figure 6.3: Grid representation of an environment . (a) Environment. (b) Coarse grid. (c) Fine grid.

An additional problem is to place the target positions on the grid. As the grid size is fixed, the target points can be outsize the node set. This last problem is treated in the next subsection. Thereafter, the grid construction for A* and Θ* is described.

6.3.1 Target points on the grid

Figure 6.4 presents the case where the target points are not in the node set (the points coordinates are not multiple of the grid size). The target points are approximated to a node. The differences between the approximation nodes coordinates and real target points coordinates are saved. For the object initial position, the closest node to the initial position is selected. The first option is to move the object to the initial node immediately and then execute the planned trajectory (continuous arrows in Figure 6.4). The second option is to save the distance between real initial position and initial node and add it to the tuning step at the end of the displacement (discontinuous arrows in Figure 6.4). For the target position, the node closer to the target position *and* object initial position is selected. This allows to control the object until this target node and then add the reminder distance to the target position to the tuning step. The first option follows the grid trajectory, whereas the second option has a constant static difference to the grid, but usually executes one step less than the first option. The option to be used is chosen by the user or automatically set in the algorithm input.

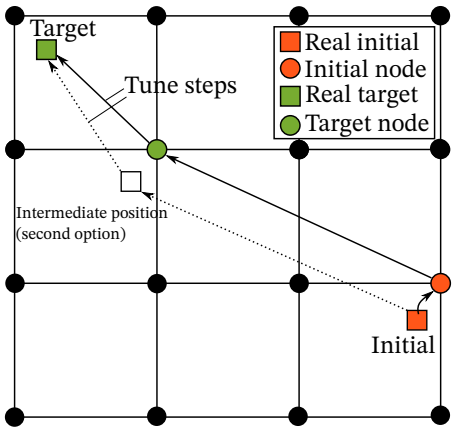

Figure 6.4: Target points approximation on the grid, option trajectories and tuning steps.

6.3.2 A* grid

The A* algorithm uses the nodes on the grid to explore the environment and find a path to the target points. The solution path passes *through* the nodes and edges of the grid. A* is intended to be a fast solution for real-time, online implementations of the DAA as a conveyance device, where execution time is optimized. To accomplish this, the grid should be the coarsest possible. The coarsest grid is build with the maximum displacement of the DAA on both axes. This gives a coarse grid for a fast solution, but retaining a good approximation of the environment. The maximum step in the x-axis (for the given DAA) is chosen as the distance between nodes along that axis, and likewise for the y-axis, as illustrated in Figure 6.5a. A 4-connected grid is chosen for A*. This reduces the edge set, accelerating the algorithm, but limits the displacement of the conveyed object to the x and y axes, i.e., no simultaneous xy (diagonal) displacements.

6.3.3 Θ* grid

The Θ* algorithm uses the nodes on the grid to explore the environment, but the solution path is not limited to the nodes and edges of the grid. An additional calculation allows Θ* to create any angle paths that do not belong to the grid set. Θ* prioritizes the shortest path instead of execution time. This is useful in offline and precise implementations of the DAA as a conveyance device. To accomplish this, the grid should be the finest possible regarding computation time. The finest grid is build with the minimum displacement of the DAA on both axes. This gives a fine grid for a short path solution, but keeping the computation time acceptable. The minimum step in the x-axis (for the given DAA) is chosen as the distance between nodes along that axis, and likewise for the y-axis, as illustrated in Figure 6.5b.

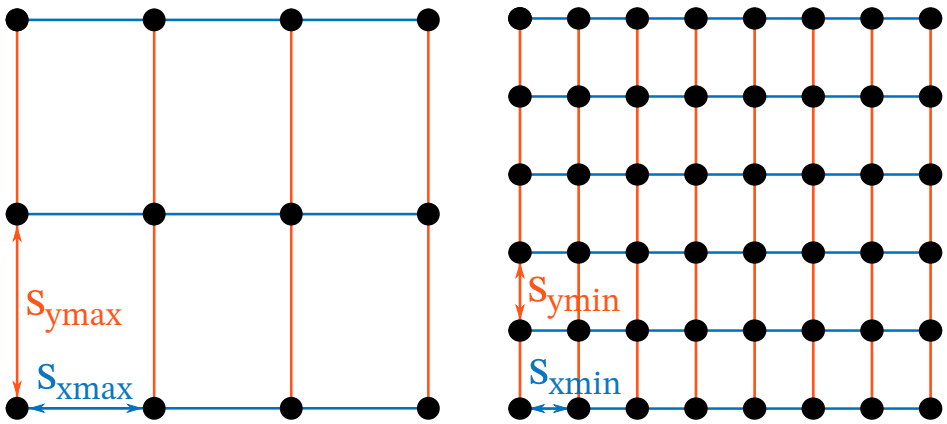

Figure 6.5: Grid definition for the pathfinding algorithms. (a) A*. (b) Θ*.

A 4-connected grid is chosen for Θ*. This reduces the edge set, accelerating the algorithm. Contrary to A*, this does not limit the displacement of the conveyed object to the x and y axes (xy plane displacements are effectuated), as Θ* optimizes the solution of A* with straights outside the edge set.

6.4 Pathfinding algorithms

The "Pathfinding algorithm" block in Figure 6.2 represents the injection of the grid, with all the environmental information, to the solving pathfinding algorithms (A* and Θ*).

6.4.1 A*

A* uses an heuristic function to guide the node exploration. Every node n is assigned a distance from the start node, $g(n)$, plus the heuristic function value: an assumption of the remaining distance to the goal $h(n)$, forming the total value function $f(n)$ (Equation (6.1)).

$$f(n) = g(n) + h(n) \tag{6.1}$$

The node with lower $f(n)$ is expanded, i.e., the connected nodes are evaluated. Once the goal node is chosen for expansion, A* halts and the found path to the goal is returned.

The available heuristic functions $h(n)$ on the DAA are: the Manhattan distance, the total difference between the coordinates of the node and goal; or the Euclidean distance, the straight-line distance between the node and goal. The heuristic function can be chosen by the user or passed automatically to the algorithm. As the adapted A* algorithm does not preprocess the obstacles of the environment, the heuristic function does not consider the obstacles to compute its value.

6.4.2 Θ*

Θ* is an any-angle path planning algorithm based on A*. Any-angle means that the algorithm uses the grid to link the start-goal nodes but, once the path is set, it is optimized. The optimization uses straights not contained in the grid edges to join grid nodes and form a shorter path than the grid edges path. This produces optimal or near-optimal paths in the free space rather than optimal paths on the grid. Θ* records the parent nodes that are in line of sight, linking them if: they belong to the grid solution path, skipping the nodes in between; and the

linking path is collision free. This produces a shorter path than A*. As A*, Θ* is complete.

Figure 6.6 presents the different solution path found by A* and Θ* for the same environment with different grids.

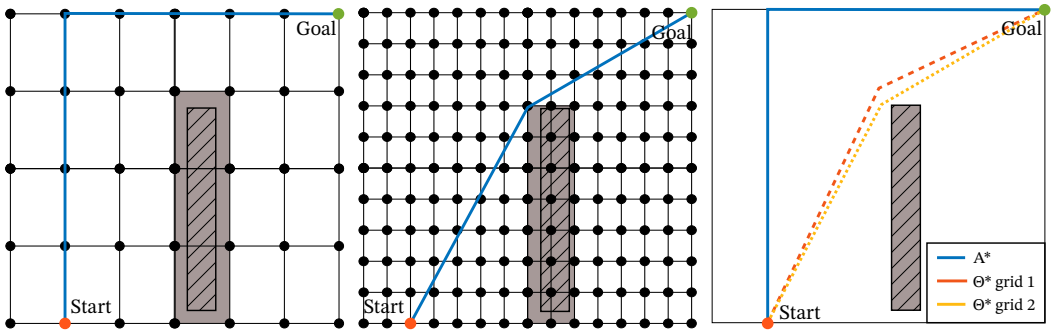

(a) (b) (c)

Figure 6.6: Grid definition for (a) A*. (b) Θ*. (c) Grid impact on solution.

Figure 6.6a shows how A* uses the grid edges as path solution. A horizontal or vertical displacement is equivalent for A*, so multiple solution paths are equivalent for solving the environment. The solution path chosen depends only on the node evaluation order of the expanding node. Figure 6.6b produces straight lines outside the grid edges. This shortens the solution path and exploits the planar motion capabilities of the DAA. A safety distance is usually added to Θ* because it tends to link the solution nodes at the edges of the obstacles, optimizing the solution path, but increasing the risk of collision. Figure 6.6c shows the impact of the grid on the solution path. Θ* produces shorter paths than A*, and with a finer grid, Θ* founds a shorter path than with a coarser grid.

Once the solution path is determined, it is divided in straight line sections. Then, the translation of solution path to control variables is done in the same way as for a straight line. The dynamic model determines the maximum displacement step. The maximum step is executed until the distance to the target point is smaller than the maximum step, when the dynamic model is used again to find the tuning step to reach the target point (“Dynamic model” block in Figure 6.2).

6.5 Virtual interface

A virtual interface (a virtual twin of the DAA) was developed to visualize and test the developed pathfinding algorithms and trajectory control. Once the control currents are determined by the dynamic model, they are injected to the virtual interface and the DAA prototype in parallel (last two blocks of Figure 6.2). The interface draws the predicted displacements of the conveyed object on the given

environment: target positions, obstacles, solution path and step by step displacement of the object. The interface works like an animation, presenting each state of the DAA through time. First, both the virtual interface and the real system are configured to produce the first conveyance step following the solution path: the EDAs are placed on the correct initial discrete position to execute the first conveyance step. Then the first conveyance step is executed and the object is displaced along the solution path. The return phase of the conveyance step is also illustrated in the virtual interface, where the EDAs are reset for the next conveyance step. This process repeats, while the conveyance path (done path) is marked in the virtual interface, until the object reaches its final position.

Figure 6.7 presents the interface for an environment with two obstacles, an initial, intermediate and final positions, solved with both pathfinding algorithms. Figure 6.7a presents the A* solution with an imposed safety distance of 1 mm to demonstrate this feature. The path done and trajectory are rectilinear (always along the x or y axes), as described above. The interface shows how the A* algorithm avoided the obstacles and reached the target positions with the imposed safety distance. Figure 6.7b presents the same environment solved by Θ* without safety distance. Θ* produces shorter paths to the target points by executing xy diagonals. The total solution path length found by Θ* was 102.6 mm, whereas the one found by A* was 123.68 mm. On the other hand, the computation time taken by Θ* to obtain the solution was 1.76 times the A* computation time for this example. This time can increase if Θ* executes more collision checks, i.e., there are more obstacles and more target points on the environment.

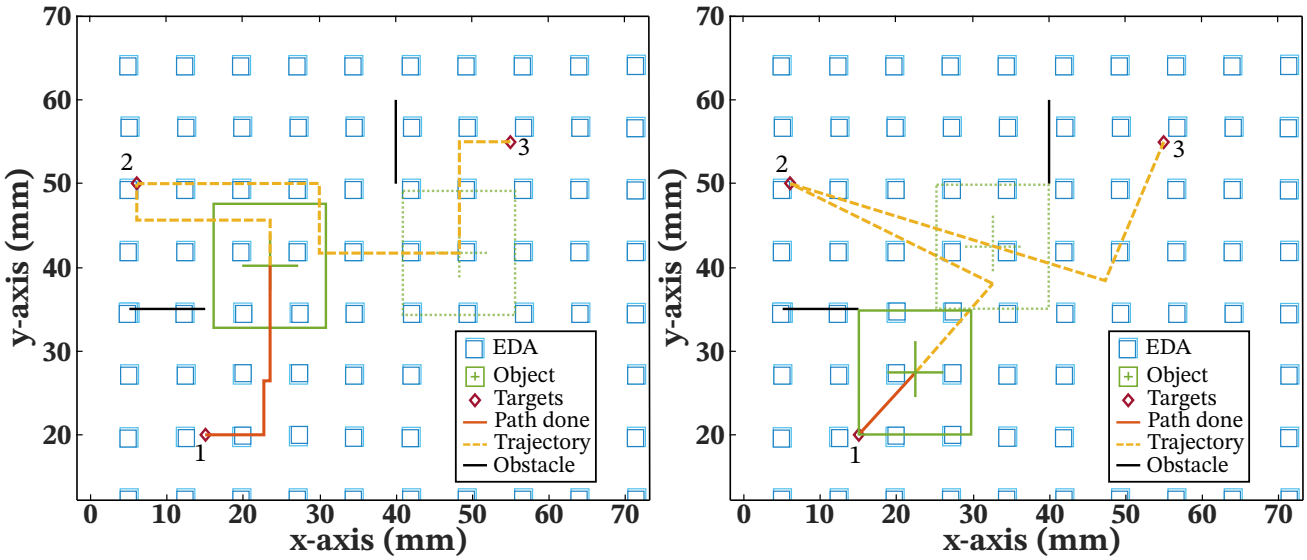

Figure 6.7: Interface sample for obstacles on the plane of the object (a) A* solution with 1 mm safety distance (b) Θ* solution with zero distance.

Chapter 7

Conveyance, pathfinding & trajectory control experiments

This chapter presents the experimental tests of the DAA as a conveyance device and the comparison with the developed dynamic model predictions. This means multiple conveyance steps, pathfinding and trajectory control experiments.

The first section presents the influence of the return current intensity on the return phase of the DAA conveyance strategy. Ideally, this return phase produces no displacement, but experimental observations discovered an unwanted displacement on this phase. The conditions to minimize this phenomenon are chosen for the rest of experiments.

The second section presents a characterization of multi-step conveyance performance under different conditions. The outputs of each condition are normalized to allow a comparison and study of the conditions on the DAA conveyance performance.

The third section presents an experiment demonstrating that the active area of the DAA is exploitable. This is obtained by conveying an object through different EDA columns of the DAA. The influence of this transition zone is analyzed.

Finally, bi-dimensional trajectories are executed with the DAA, following the trajectory control flowchart presented in Section 6.1. The execution of these trajectories and comparison with the dynamic model predictions are presented and analyzed.

The same materials and conditions used for the dynamic model validation (Section 4.1), are used for the experiments in this chapter. All experimental tests are summarized in the final section with Table 7.2.

7.1 Return current influence

The trajectory controller assumes that the return step (the MPM reset process once a displacement step has been done, Section 3.1.2, Figure 3.3) does not displace the object. In practice, a return displacement was observed, attributed to possible uneven distribution of the conveyed object weight on the MPMs and heterogeneity in friction conditions. The return current intensity influence on this return step was studied to find the best operating conditions for multi-step execution.

Different return current intensities along the x and y axes of a 2×2 DAA were injected following the return process (Figure 3.3). The DAA carried a 0.411 g object. The return current was injected for 50 ms to ensure that the pulse was longer than the response time of the system. Each return current intensity was executed 20 times to obtain a mean and standard deviation values. Figure 7.1 presents the return step displacement vs return current intensity. From Figure 7.1, different behaviors were observed for the x-axis and y-axis.

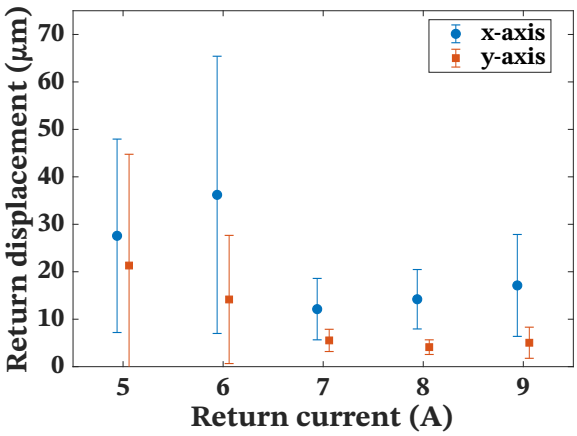

Figure 7.1: Return displacement vs return current intensity on a 2×2 DAA.

For the y-axis, the return displacement and standard deviation decreased as the current intensity increased, until 8 A. For the 9 A point, both return and standard deviation increased from the previous experimental point.

For the x-axis, the return displacement and its standard deviation increased when the return current intensity went from 5 to 6 A. Then, the return displacement and its standard deviation collapsed to a minimum at 7 A. Increasing the return current intensity further than 7 A resulted in a steady increase in return displacement and standard deviation. This behavior is attributed to the z component of the electromagnetic force. For such high intensity currents, this force component overcomes the MPM and conveyed object's section weight, making the magnet to "jump" inside one half of its cavity (the magnet is attracted to-

wards the wire on the other half of the cavity). This jump produces a highly variable movement on the object along the magnet's displacement axis. This phenomenon was correctly predicted by the dynamic model when the DAA executed the collaborative displacement step (see Appendix D.2.1, 3×3 DAA).

From these results, a return current intensity of 7 A was chosen for all multi-step conveyance operations of the 2×2 DAA. This value was a compromise for the two axes results: the y-axis achieved its second minimum value and standard deviation; and the x-axis its minimum value and standard deviation.

7.2 Conveyance performance

To evaluate the conveyance performance of the DAA under different operation points, multiple driving current intensities and pulse duration time pairs were injected into a 2×2 DAA. Each driving current intensity and pulse duration pair formed an operation point of the DAA. Three operation points near the critical point of the system were chosen (1.5 A for the x-axis). On this critical point, the maximum displacement per conveyance step was obtained (Section 4.3) and it used a low intensity current, theoretically improving energy efficiency. One operation point with a high current intensity was chosen to evaluate the performance tendencies of the system. Ten identical and consecutive steps along the x-axis were executed for each operation point. The previously explained return current of 7 A, with pulse width of 5 ms, was used. Once the 10 steps were finished and the measures taken, a new set of 10 steps were executed in the opposite direction under the same conditions. This procedure was repeated 5 times to get mean values and standard deviations of total displacement, cross-coupling error and conveyance speed (from initial position to final position of the object). The cross-coupling error, as a percentage of the total displacement, was calculated to compare between operation points. The energy consumed by the system to execute the 10 consecutive displacement steps was estimated for each operation point. This energy consumption was calculated using the formula $E = I^2Rt$, where I is the driving current intensity, t the pulse duration and R the measured electrical resistance of the DAA. The R measurement standard deviation generates a variability of consumed energy, which is reported for each energy value. Finally, a conveyance efficiency metric, on the form of distance per injected joule (μm J^{-1}), was computed for each operation point including standard deviations. Table 7.1 presents the results of all the explained quantities.

From Table 7.1, two phenomena impact the speed value of the DAA: the total displacement and the conveyance time for this displacement. The displacement

Table 7.1: Conveyance performance tests results. Best performance for each quantity (absolute value) in bold.

I_x (A)	t_x (ms)	Displacement (µm)	Cross error (µm)	Cross error/Displ. (%)	Speed (µm s^{-1})	Energy cons. (J)	Distance/Joule (µm J^{-1})
1.5	20	484.2 ± 146.9	**37.8 ± 9.2**	7.81 ± 1.90	444.7 ± 136.2	22.80 ± 1.84	21.24 ± 8.93
2	20	**1181.9 ± 143.6**	80 ± 29.6	6.77 ± 2.50	1085.3 ± 134.8	23.80 ± 1.92	49.66 ± 9.52
2	10	900.6 ± 142.9	46.7 ± 31.6	**5.19 ± 3.51**	1532 ± 272.6	11.90 ± 0.96	**75.68 ± 29.20**
6	5	682.7 ± 50.6	47.9 ± 19.1	7.00 ± 2.80	**1990.4 ± 167.5**	**10.70 ± 0.86**	63.80 ± 20.90

is maximized using a low driving current with a large pulse width (as explained in Section 4.3.1), but a high driving current needs a shorter pulse time to execute all the system kinematics (as explained in Section 4.2.1). The higher current intensity allows more steps in the same time than a low current intensity.

A maximum experimental speed of 1990.4 µm s^{-1} was obtained, using a current of 6 A for 5 ms. The maximum displacement of 1182 µm was observed with a 2 A, 20 ms current. These results follow the behavior previously explained. The average standard deviation on the displacement measure was 121 µm.

Using the critical point along the x-axis (1.5 A, 20 ms), which produced the maximum single step displacement in Section 4.3.1, resulted in a smaller-than-expected displacement and speed. This could be caused by the friction heterogeneity of the plate along the displacement changing the value of the critical point and losing the collaborative effect of the EDAs.

To compare the operation points and find the best for conveyance applications, the evaluation quantities (displacement, speed, etc.) need to be compared. To allow a relative comparison between the operation points, the evaluation quantities are grouped on vectors: a displacement vector, a cross-coupling error vector, and so on. Then, each vector is normalized by its euclidean norm. If v is a vector with components v_1, v_2, ... v_i, the euclidean norm is defined by $\|v\| = \sqrt{v_1^2 + v_2^2 + ... + v_i^2}$. This process yields a vector with component values between 0 and 1. Applying the same process to the standard deviations proportionally scales them to their corresponding quantity. Finally, the cross-coupling/distance percentage and the energy consumption vectors are inverted ($v_{new} = 1 - v_{old}$) to obtain a straightness and energy efficiency quantities. This inversion means that higher values for all quantities mean better performance. The results of this data processing are presented in Figure 7.2.

From Figure 7.2, the (1.5 A, 20 ms) point had the worst performance on every metric, except for energy efficiency, where it was second to last by a small difference (0.35 against 0.38). These results were caused by the smallest displacement along the conveyed axis, even when it used a low current intensity with a long pulse time. Again, this could be caused by the friction heterogeneity of the plate along the displacement, changing the value of the critical point and losing the

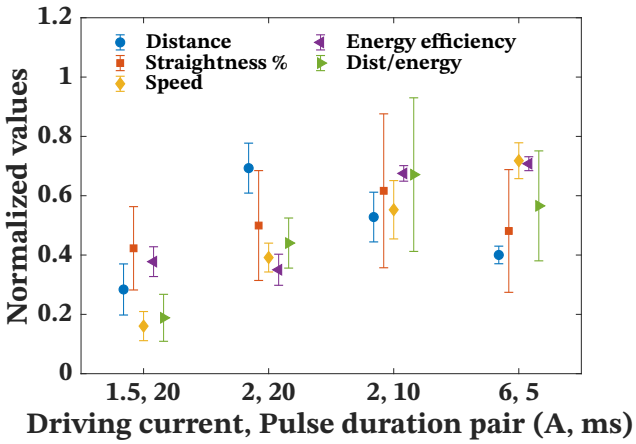

Figure 7.2: Normalized conveyance evaluation metrics for a 2×2 DAA. Higher values mean better performance.

collaborative effect of the EDAs.

The (2 A, 20 ms) achieved the maximum displacement and improved on all metrics with respect to the (1.5 A, 20 ms), except for the energy efficiency value (0.38 against 0.35). This drop in efficiency was due to the higher current intensity compared to the last studied point, but with the same pulse time, consuming more energy per step.

The (2 A, 10 ms) achieved the best distance per injected joule value and was a close second in energy efficiency (0.68 against 0.71). The speed value logically improved with the shorter pulse time, but the conveyance distance dropped from the last studied point. This point presented the best straightness percentage, although with the largest standard deviation for this metric.

The (6 A, 5 ms) evalued the DAA performance towards its operation limit. With this high intensity and short pulse time, the speed value was maximized. Interestingly, this point achieved the best energy efficiency and was second in distance per injected joule. On the other hand, the distance decreased from the last studied point.

Considering the previous results and analysis, the (2 A, 10 ms) point was found to be the best compromise as conveyance operation point. The best distance per joule injected and straightness and the second best energy efficiency, speed and distance mean a good performance.

The conveyance performance tests aimed at finding performance tendencies changing the control variables of the DAA. A general performance increase near the critical point, but with a higher current to avoid the friction heterogeneity and with a pulse value near the kinematic duration of the DAA was found. Nevertheless, more points should be evaluated to corroborate these tendencies and find other interesting operation points. For example: an optimum point

could exist between the (2 A, 10 ms) and (2 A, 20 ms) points, by changing the pulse time to further increase the conveyance distance.; a point with a very high current (9 A) could achieve a higher speed, if this metric needs to be maximized; a point in with a medium current (4 A) could achieve a lower standard deviation for all metrics.

7.3 Array column transition

This test's objective was to evaluate the long-range capability of the system, i.e. that the active area of the DAA was exploitable. For this, a 267 mg, 30 mm × 30 mm object (the area of a 3 × 3 DAA) was conveyed on a 5 × 5 DAA. A 3 A, 200 ms driving current was used to displace the object along the x-axis. After the driving current pulse, each column of the array was switched back with a 7 A, 50 ms return current pulse. Once all columns were switched back, the same procedure was executed in cycle. The object was actuated towards the next EDA column to evaluate the transition between columns and demonstrate that the active area of the array was exploitable for conveyance tasks. The conveyance speed was not an objective of the test, thus a slower execution was implemented to allow for visual inspection during the test.

Figure 7.3 shows a sequence of images where the array conveyed the object from left to right (+x-axis). During this movement, the conveyed glass plate reached a new MPM column (at its right). The glass plate, driven by the already engaged MPM columns, slid on top of the new MPM column which engaged in the conveyance and contributed to displace the object further.

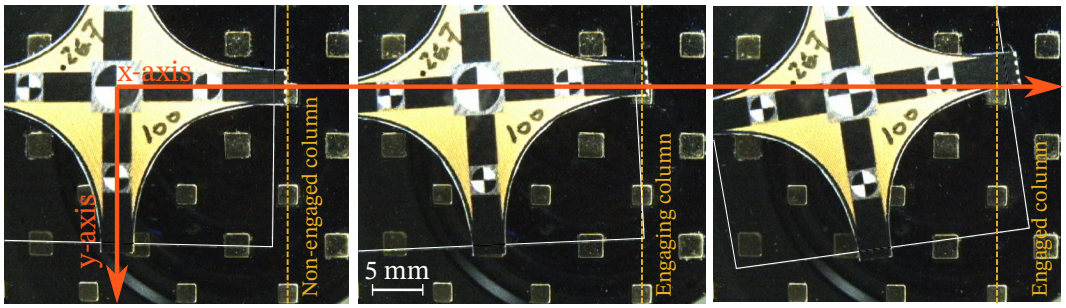

Figure 7.3: Conveyed object passing a transition zone along the x-axis.

From, Figure 7.3, the object was effectively conveyed between columns, demonstrating that transitions between columns are possible. The new EDA column engaged in the actuation of the object, continuing the displacement in the +x-axis. A 0.15 rad (8.6°) rotation of the object was observed on the transition. This could be produced by the asynchronous engagement of te MPM column: if a MPM of the column engages before the others, this MPM will generate a

rotation force to the object. The array can correct this rotation once the transition is finished or when the object arrives to its destination thanks to its planar motion capability.

Figure 7.4 plots the trajectory of the center of mass of the conveyed object.

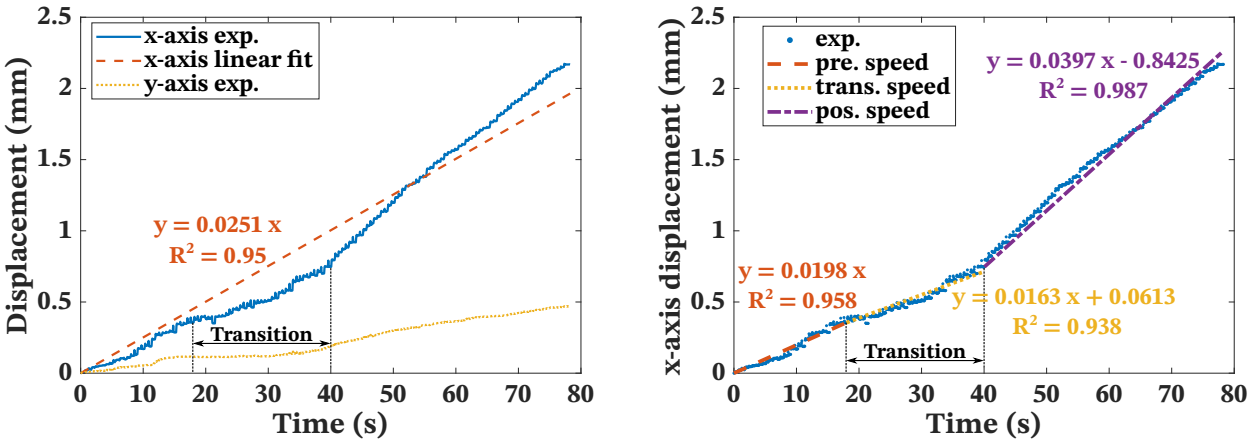

(a) (b)

Figure 7.4: Object transition between DAA columns on a 3×3 DAA. (a) x and y (cross error) axes displacements vs time and global speed (linear regression). (b) Speed (linear regression) before (pre) during and after (pos) transition.

From Figure 7.4a, the object was continuously conveyed along the $+x$-axis for 2.15 mm. A total deviation of 0.47 mm was measured along the y-axis. The transition zone effect on the object trajectory can be observed. From 18 to 40 s the object trajectory becomes less smooth, with a negative change in slope, i.e. conveyance speed. Then, once the transition zone passed (after 40 s), the object's conveyance speed increased significantly. The x-axis linear fit computes the speed that best fits a constant speed motion assumption (25.1 μm s^{-1} in Figure 7.4a). This fit had a root-mean-square error of 148 μm and a mean-absolute error of 126 μm.

Figure 7.4b fits a line to each of the three phases of the transition: before (pre), during and after (pos) the transition zone. The RMSE of the pre, during and pos fittings were 23.5 μm, 29.9 μm and 46.4 μm, respectively. The MAE of the pre, during and pos fittings were 19.4 μm, 26.4 μm and 40.6 μm, respectively. These errors indicate a very good fitting to the linear regression, indicating a constant speed actuation of the DAA.

From Figure 7.4b, the object approached the transition zone at a constant speed of 19.8 μm s^{-1} (from 0 to 18 s in Figure 7.4). Along the transition zone (from 18 to 40 s in Figure 7.4), the movement was slower and less stable, but the object was constantly actuated at 16.3 μm s^{-1}. After the transition zone, the speed increased to 39.7 μm s^{-1}, indicating the strong influence of the new EDA column

on the object's displacement. This speed difference is attributed to the mass distribution on the actuating MPMs. When the object approaches the transition zone, its weight is concentrated on the MPMs adjacent to the transition zone, limiting the force of the farther MPMs. Once the new MPM column engages, the object weight is better distributed among the MPMs, resulting in a better collaborative effort of the DAA.

7.4 Bi-dimensional trajectory control

To evaluate the bi-dimensional trajectory control of the DAA, presented in Chapter 6, a 411 mg object, with size 20 mm × 20 mm (the size of a 2 × 2 DAA), was conveyed on the 5 × 5 DAA. Five target points were given to the trajectory control algorithm using A* with a holding current of −1 A: (0,0); (0,−259);(296,−259); (296,0) and (0,0), all in μm. These points formed a rectangular objective trajectory. The trajectory control algorithm generated the control currents and injected them into the DAA to convey the object. The initial and final position measures of each conveyance step were taken using the Grasshopper camera. The initial position of each conveyance step was defined as the position before the displacement step and the final position as the position after the return phase of the DAA. Once the rectangular trajectory was performed, the system was reset and the same trajectory executed. This process was done 8 times to obtain a mean position for each conveyance step with its standard deviation in the x and t axes. Figure 7.5 presents the results for this bi-dimensional trajectory.

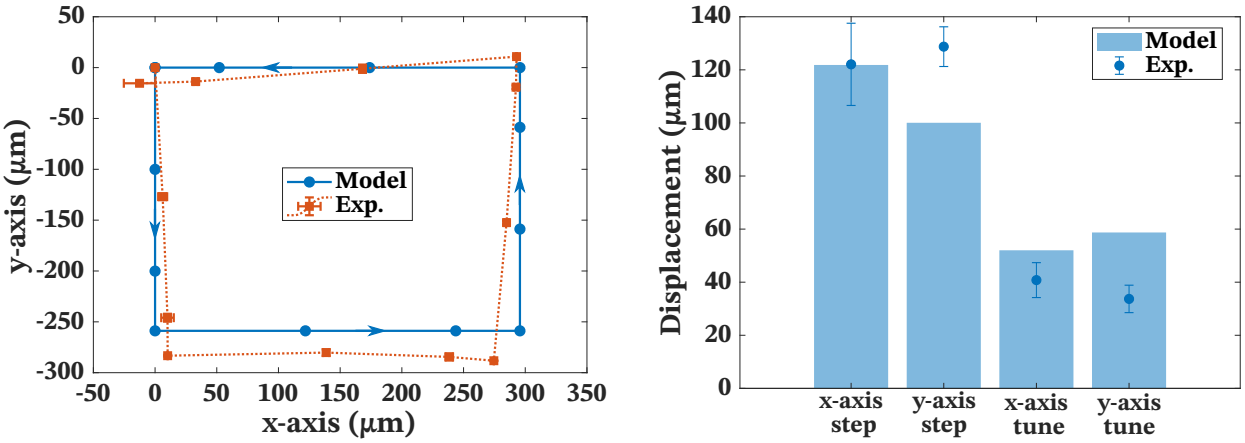

(a) (b)

Figure 7.5: Bi-dimensional trajectory control on a 2 × 2 DAA. (a) Trajectory in the xy plane. (b) Model and experimental comparison for the displacement and correction (tune) steps.

Figure 7.5a presents the objective rectangular trajectory with its target posi-

tions and predicted intermediate positions (noted "model") and the average of the experimental measurements. The standard deviation of the experimental results were small, indicating a repeatable outcome of the system. The system performed a rectangular-like shape. The DAA had a tendency to deviate towards the $+x$-axis while executing displacement steps on the y-axis. This could be the influence of the flatness conditions explained on Section 4.1. There was a deviation towards the $-y$-axis while executing displacement steps along the $-x$-axis, but when executing displacement steps along the $+x$-axis there was no deviation tendency (apart from the correction step to attain the (296,−259) point). This indicated that the flatness condition only affected one axis, which follows the conditions measurements in Section 4.1. Studying the displacement values, the system performed: larger-than-expected steps along the y-axis (both negative and positive); shorter-than expected steps along the $+x$-axis; and well-expected steps along the $-x$-axis. The final mean experimental position was (-12.56 µm, -15.52 µm) ± 12.75 µm for the x-axis and 2.2 µm for the y-axis. As the wished final position was (0,0), these values are also the final position error.

The rectangular trajectory is divided on its component displacement steps: eight normal displacement step and four tuning or adjusting steps. The tuning steps come from the trajectory control algorithm with A*: it executes the largest possible step in the wished direction, the maximum possible number of times and, once the object arrives near the wished position, the controller adjusts the last step to reach the position. On the rectangular trajectory there are four normal steps along each x and y axes and two tune steps along each x and y axes. Figure 7.5b compares the model-predicted displacement for each type of step with the appropriate experimental results. From Figure 7.5b, the x-axis displacement step was almost perfectly predicted (122.1 µm exp. against 121.1 µm model). It is worth noting the previously observed phenomena of shorter-than-expected steps along the $+x$-axis and well-expected steps along the $-x$-axis. These phenomena is accounted on the standard deviation value, which was the highest of the four step types. For the y-axis step, the experimental displacement was larger than expected (128.7 µm exp. against 100.1 µm model). The root-mean-square error for the four type of steps was 19.85 µm, and the mean-absolute error was 16.29 µm.

Finally, to evaluate longer and more complex trajectories, the trajectory controller was given a pre-defined trajectory forming the Université de Technologie de Compiègne acronym (UTC). The trajectory spanned a 1700 µm × 800 µm area. The trajectory algorithm with A* and −1 A holding current controlled the DAA. The results are presented in Figure 7.6.

From Figure 7.6, the trajectory was well executed, with a maximum position

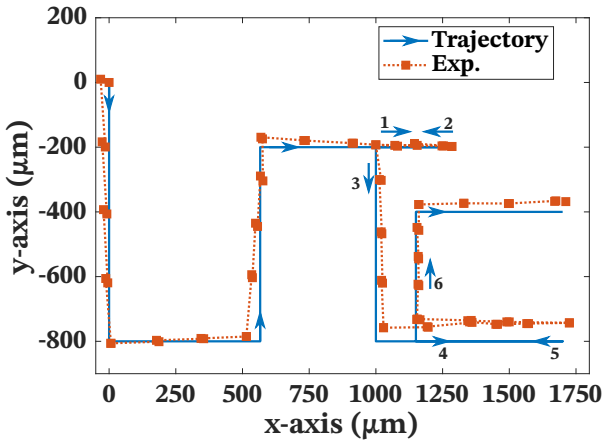

Figure 7.6: Bi-dimensional trajectory forming the Université de Technologie de Compiègne acronym on a 2×2 DAA.

error of 50.48 µm for the x-axis and 67.53 µm for the y-axis.

The tests in this section demonstrate the DAA can execute guided planar motions (trajectories) thanks to the adapted A* pathfinding algorithm and the developed feed-forward control strategy.

Table 7.2 synthesizes the experimental tests presented in this chapter.

Table 7.2: Multi-step and trajectory performance tests.

System	N_a	DoF	Load (mg)	I_x (A)	I_y (A)	I_r (A)	t_x (ms)	t_y (ms)	t_r (ms)	N. of tests
Return current intensity										
2×2	4	x, y	411	-	-	[4 ; 9]	-	-	50	6×20
Conveyance speed & energy consumption										
2×2	4	x	411	[1.5 ; 6]	-	6	[5 ; 20]	-	5	4×5
Array transition										
3×3	25	x	267	[1.5 ; 6]	-	7	[5 ; 20]	-	5	9
Bi-dimensional trajectory										
2×2	25	xy	411	[1.5 ; 9]	[1.75 ; 9]	7	[5 ; 100]	[5 ; 100]	5	21
									Total tests:	40 ($\times$ 5 $\vee$ 20)

Part IV

Conclusions & Perspectives

Chapter 8

Conclusions

The **research question** of this work was: How to exploit an *array* of *digital electromagnetic actuators* as a *conveyance system* to transport objects between different machining/quality stations of a *microfactory*, efficiently in terms of consumed energy, displacement time, final position and trajectory error, and avoiding collisions with obstacles or other transported objects?

To answer the research question, this thesis developed a dynamic model of the digital electromagnetic actuator array. The dynamic model was deduced from the physical principles behind the actuator's operation. The dynamic model was then used as a feed-forward control of the array to define the control variables needed to obtain a given displacement. To know which displacement is optimal for the given task, pathfinding algorithms were adapted to the array to convey the objects minimizing the consumed energy, displacement time, final position and trajectory error, and avoiding collisions with obstacles.

Chapter 1 introduced the concept of *digital actuator*, the discretization and holding functions it needs to operate and the advantages/drawbacks of digital actuation against analog actuation. A classification of digital actuators by the number and nature of its discrete positions was presented with examples for each type. Then, actuator arrays for planar motion were defined. The context and application of these arrays on this thesis, the microfactory, was explained in detail. This context went from the need of miniaturize the manufacturing systems to the place of microfactories in this challenge, along with microfactory examples from the research and industrial fields.

Chapter 2 presented the state of the art related to: micro planar motion systems (divided by physical principles of their actuators), contact mechanics modeling and pathfinding. The first section, micro planar motion systems, discussed the advantages and drawbacks of each physical principle. The contact mechanics section presented the modeling alternatives to study the collision and

friction phenomena on the array. The final section, pathfinding, presented the vast approaches developed in the literature to solve the conveyance problem.

Thanks to the literature review of Chapter 1 and Chapter 2 the solution road-map for this thesis research question was set.

In Chapter 3, a microfabricated prototype of a 5×5 array was the basis for the dynamic model development, experimental test and validation of the array as a microconveyor. The elementary digital actuator of this prototype had a square geometry, allowing the array to execute planar motion displacements of the conveyed object.

A dynamic model was developed starting from the force analysis of the digital actuator and its kinematic phenomena such as collisions and rebounds. The electromagnetic driving forces, magnetic holding forces, friction forces, collision and rebound events were studied, characterized and integrated in the dynamic model. The electromagnetic and magnetic forces of the square digital actuator were analytically solved. The friction forces were modeled with an adapted Bengisu & Akay model [BA94]. The impact and rebound phenomena were modeled using the Hertz impact theory and adapting the work of Weir and Tallon [WT05] for the coefficient of restitution equation. The magnetic homogeneity of the array was evaluated and assumed homogeneous. This allowed to generalize the dynamic model to the array. The implications of the model uncertainties and assumptions on the array's behavior were treated.

In Chapter 4, the prototype array was characterized with extensive experimental tests. The tests evaluated multiple input-output relations, i.e., the influence of the control variables on the object displacement were measured for different mass loads. The input variables were the driving and holding current intensities, the driving current pulse duration, the number of digital actuators on the array contributing to the object displacement. The output measures were: the actuator and object kinematics; uni- and bi-dimensional object displacement; and object rotation around its center of mass.

As seen in Chapter 1, digital actuators are mostly used on open-loop, as is the case for the studied array. This puts the onus on: manufacturing quality, as they cannot compensate for defaults with sensor-based control; and modeling or characterization precision, as it is the base for the open-loop control. The manufacturing influence was clearly seen on the studied array: the deviation from the predicted and/or optimal performance was tracked to manufacturing imperfections, assembly misalignment, as well as friction heterogeneity among the components. Modeling accuracy and precision were measured and presented in Table 4.2, which synthesized all experimental conditions and results. From this table, the dynamic model correlated with the behavior of the system with

low root-mean-square and mean-absolute errors for all the experiments.

In Chapter 5, the scaling and miniaturization potential of the actuator was studied. The minimal length of the digital actuator (as scale dimension) was found at 1.1 mm. Below this length, the digital actuation of the system is lost as the magnetic and the electromagnetic forces cannot overcome the friction (principally stiction).

The current profile balancing the forces on the digital actuator, for any position of its mobile part, was found. This current optimized the energy consumption on the actuator. This current profile could control the displacement, speed and acceleration profiles of the mobile part and conveyed object on the array.

The dynamic model was extended to any actuator and array geometry with three adaptable modules. The semi-analytical software Radia is used to find the magnetic and electromagnetic functions of any given actuator. The implementation of the modular modeling on a hexagonal actuator and array system was demonstrated to validate the idea. The modular model correctly predicted the experimental tests on the hexagonal array with low root-mean-square and mean-absolute errors.

In Chapter 6, two grid-based pathfinding algorithms, A* and Theta* (Θ*), were adapted to the array. A* found fast solution for real-time, online implementations of the array. Θ* found shorter real-life paths compared to A*, but took additional computation time to find the solution. Θ* exploited the any-angle generation capabilities of the array. The dynamic model was used to translate the solution path into control currents of the array. A virtual interface was developed to predict the behavior of the array with the given control inputs through time.

In Chapter 7, experimental tests to evaluate the array and developed trajectory control as a conveyor were performed.

A return current intensity of 7 A was chosen for all multi-step conveyance operations as it minimized the return phase displacement of the object on both actuating axes. The total active area of the array was demonstrated to be exploitable. The array continuously conveyed the object along the actuating axis, passing through an actuator column transition. The object trajectory on the transition zone was less stable, with a slower conveyance speed, and presented an unwished rotation but, once the transition zone passed, the object's conveyance speed was higher than the pre-transition value and the rotation could be corrected.

An experimental conveyance working point of 2 A, 10 ms driving current was found as best performance compromise. This point had the best distance per joule injected and displacement straightness of the evaluated operation points. It also had the second best energy efficiency, speed and total displacement distance.

Bi-dimensional trajectories of the conveyed object on the array were calcu-

lated and executed with the trajectory control. Both square and university's logo trajectories presented low position errors (repeatable conveyance steps) and low model-trajectory error.

An important product of the literature review (Chapter 2) was Table 2.2, were the performance of the literature conveyance devices was summarized and compared. This table represents a benchmark to which the work of this dissertation is compared. Table 8.1 presents this comparison between the presented work and literature-found solutions with common performance metrics between all systems.

Table 8.1: Microconveyors: Literature and presented digital actuator array comparison

Ref.	Contact	Array	DoF	A.P	Control	Surface (mm)	Object (mm)	Speed (mm s^{-1})	Resolution (µm)	Precision (µm)
Electrostatic conveyors										
[DPS11]	C	Yes	1	Digital	Open	6 width	0.5×0.25, 2 µg	1	21	-
[HYH15]	C	Yes	2	Analog	Open	264×264	132×132, 11 g	354	400	-
Electrothermal conveyors										
[Ell12]	C	Yes	3	Digital	Both	16×16	0.8×0.8, 78 µg	0.057	0.28	1
[Hus+18]	C	No	1	Digital	Open	0.12	-	0.029	10	0.1
Electrowetting conveyors										
[MK06]	C	No	1	Digital	Open	-	5×4, 180 mg	2.5	-	-
[Nie+18]	C	No	1	Digital	Open	25	6×8, 500 mg	1	500	-
[Geu18]	C	No	1	Digital	Open	-	-	4	333	-
Piezoelectric conveyors										
[Tia+18]	C	No	2	Digital	Open	-	-	1641	4.4	-
[RHL09]	C	No	2	Digital	Open	-	-	1.8	70×10^{-3}	5×10^{-3}
[Gab+19]	CF	Yes	2	Analog	Closed	10×10	ø300, 129 g	2	-	400
[LF13]	C	Yes	3	Analog	-	-	-	83	-	300
[FAO12]	C	No	3	Digital	Open	-	50×50,140 g	20	70	3%
[Sho+16]	C	No	3	Digital	Open	-	86×86,150 g	20	62	10×10^{-3}
Pneumatic conveyors										
[Lau+14]	CF	Yes	3	Analog	Closed	9×9	ø5, 19.4 mg	140	300	17.7
[Gue+17]	CF	Yes	3	Analog	Closed	75×75	ø150	300	-	93
[LCZ20]	CF	Yes	3	Analog	Closed	228×204	ø80, 17 g	80	200	-
Pneumatic soft actuator conveyors										
[DSX16]	C	Yes	3	Digital	Open	180×180	Smartphone	0.53	1000	-
[WT18]	C	Yes	2	Digital	Open	180×180	200 g	2.5	-	-
[Rob+19]	C	Yes	16	Analog	Closed	110×93	-	70	-	-
Electromagnetic conveyors										
[Pir+13]	C	Yes	2	Analog	Open	-	-	16.4	-	-
[Aro+19]	C	Yes	3	Analog	Closed	150×150	68×68, 3.6 g	12	-	7
[KKF90][a]	CF	Yes	2	Both	Open	50×50	1×4, 9 g	7.2	-	-
[ISF09][a]	CF	Yes	2	Both	Open	180×180	380 g	104	-	40
[KOS16][a]	CF	Yes	3	Analog	Open	Macro	ø60, 270 g	1.1	-	-
Presented digital actuator array										
Present	C	Yes	3	Digital	Open	100×100[b]	8.9 g	2	8	5

[a] System using the Meissner effect. Low temperatures needed to work (less than 130 K)

[b] The prototype array surface is reported, but the modular design could extend this surface

From Table 8.1, comparing the array with

- The electrostatic conveyors: the array compares on maximum conveyable mass and tops the resolution metric, being a far second on speed.
- The electrothermal conveyors: the array has a significantly larger conveyable mass, comparable speeds and better resolution.
- The piezoelectric conveyors: the hardest category. The array cannot match the conveyed mass and is on the lower speed trim, but has a positive resolution and precision results.
- The pneumatic conveyors: on average the fastest systems. The array cannot match their speed, but its conveyable mass is on the same order and achieves the best resolution and precision metrics.
- The pneumatic soft actuators conveyors: they excel on conveyable mass. The array cannot match this metric and is on the lower trim on speed, but has a competitive resolution and precision.
- The electromagnetic conveyors: the array obtains a medium result for all metrics, except for precision, where it tops.

The results show that the digital actuator array is a viable alternative to the microconveyors for the microfactory.

From the experimental measurements of Chapter 4, the digital actuator obtained rising times[1] from 0.8 ms and settling times[2] from 2.4 ms. The maximum conveyed object displacement per displacement step of the array was 204.5 µm, and the minimum was 7.9 µm. The minimum straightness error was measured at 5.2 µm and 3.88 µm (x-axis and y-axis respectively), and a position repeatability of 4.7 µm and 5.3 µm (x-axis and y-axis respectively). The planar motion capability of the array was demonstrated with bi-dimensional object conveyance and object rotation tests. For the bi-dimensional conveyance, a spectrum of conveyed object angles from 1° to 88° was measured. From the rotation test, the minimum rotation angle per step was 0.11° and the maximum was 0.23°. The heaviest conveyed mass was 8.901 g with 9 A driving current.

From the experimental measures of Chapter 7, the array obtained conveyance speeds of 1.99 mm s^{-1}. The best distance to energy efficiency was 75.68 µm J^{-1}. The mean cross coupling error (or straightness error), as a percentage of total displacement, was 6.7%. When executing a trajectory spanning a 300 µm × 250 µm area, the array had maximum trajectory errors of 21.2 µm for the x-axis and 29.35 µm for the y-axis. When executing a trajectory spanning a 1700 µm × 800 µm area, the array had maximum trajectory errors of 50.48 µm for the x-axis and 67.53 µm for the y-axis.

[1] Time needed for the output to reach from 10% to 90% of its final value
[2] Time needed for the output to stay within 2% of the final value

Chapter 9

Perspectives

9.1 Uncertainty & sensibility analysis

An uncertainty analysis assess a model's validity domain by analyzing the impact of uncertainty sources of the model into its outputs. The principal uncertainty sources of the dynamic model are its parameters and the semi-analytical solver used for the magnetic computations. The dynamic model parameters were identified with experimental tests and least square error optimization. The resulting parameters intrinsically carry uncertainties from the measuring systems and experimental conditions. Also, the (generalized) dynamic model used the semi-analytical program Radia to compute the magnetic field of the permanent magnets. The advantages and shortcoming of this software were discussed in Section 3.2.3.

Quantify these uncertainty sources, propagate them to the models output and analyze their impact relative to the experimental measurements would evaluate the dynamic model solidity and valid domain.

9.2 Analytic rotation model

In Section 4.3.6, independent driving currents were injected into both wires (I_x and I_y) of each actuator of the 4×4 DAA to obtain an object rotation around its center of mass. The generated mean rotation angle ranged between 0.11° to 0.23° for the different current combinations.

Using the dynamic model, an analytical prediction of the rotation of the object can be developed. The total torque τ on the object can be computed if the following variables are known: the position of the center of mass of the object on the xy; the distance to the center of mass of each mobile magnet r_i; and the force transmitted to the conveyed object of each mobile magnet F_i. The computation

would use the following equations:

$$\sum \tau = I\ddot{\theta} \tag{9.1}$$

$$\tau = \sum_{i=1}^{n} \vec{r_i} \times \vec{F_i} \tag{9.2}$$

$$\sum_{i=1}^{n} \vec{r_i} \times \vec{F_i} = I\ddot{\theta} \tag{9.3}$$

With I the object's moment of inertia and θ the rotation angle to the x-axis. Figure 9.1 schematizes this procedure with n the total number of mobile magnets.

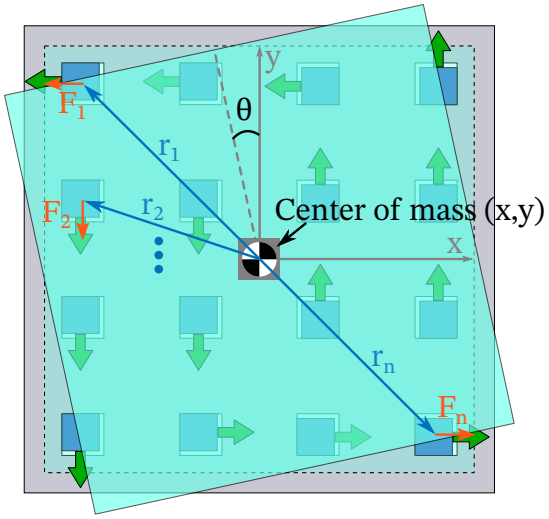

Figure 9.1: Analytical model for the rotation of an object on the DAA.

Also from Section 4.3.6, the mean rotation angle per actuation step of the array ranged between 0.11° to 0.23° for the different current combinations. This is a small range. The experimental standard deviation of the points was important. Multiple EDA movement superposition could produce an object rotation. The multiple options should be analyzed and compared to develop a rotation control strategy.

9.3 Friction model

Section 2.2.2 showed that static friction models needed less parameters and were faster in simulation but did not model all friction behaviors. Dynamic friction models were more accurate and reproduced complex friction phenomena but were heavier in simulation time, parameter identification and implementation.

From the static friction model comparison (Figure 2.58a), the Karnopp, Bengisu & Akay and Awrejcewicz models predicted very similar results, avoiding

simulation oscillations and predicting stick-slip phenomena. The Bengisu & Akay model, being the simpler of the three, predicted similar behaviors to the LuGre and Gonthier dynamic models (Figure 2.60a and Figure 2.60b) accurately predicting the oscillation lag and stick-slip when the spring reached its maximum length. This justified the choice of the Bengisu & Akay model for the dynamic model. Nevertheless, the Generalized Maxwell-slip (GMS) model demonstrated to be the most accurate and correctly predicted all friction phenomena. The identification process is not trivial, but a correct implementation of the GMS model into the dynamic model could improve the system's performance, e.g., the collaborative zone loss could be predicted.

9.4 Thermal model

The driving function of the digital actuators comes from the electrical currents in the wires beneath the mobile magnet. The current magnitudes used in the DAA attained 9 A and the wires dimensions are small to keep the DAA compact (see Figure 3.10 for the wires dimensions and shape). This combination of high currents and thin wires generated important heat in the system if multiple displacement steps were executed sequentially, like long trajectory control experiments. This heat could damage the system in two ways: melting the PCB circuit, risking an electrical short-circuit; or increasing the permanent magnets' temperature above their Curie temperature, demagnetizing them and losing the working principle of the system. The thermal working limit of the system is unknown. An interesting development would be a thermal model of the EDA and DAA to predict this thermal limit. The thermal model could also lead to thermal efficiency gains by integrating it in the design process of the EDA and DAA.

If the system is to be further miniaturized, the thermal dimension of the system becomes even more important, as explained in Section 5.1. The increased friction influence on smaller systems puts the onus on the electromagnetic force to overcome it, increasing the heat generation on the driving wires. For such smaller systems, a thermoelectric (Peltier) cooler beneath the PCB for temperature control could be necessary and the thermal model would be important to dimension and design this cooling device.

9.5 DAA lifespan

The DAA executes multiple switches of the mobile magnets for its conveyance strategy. Each switch represents an impact that demagnetizes and wears the mobile magnets. The silicon cavities of the EDA are also worn, as the repeated impacts increase the plastic damage to the material. What is the number of switches that the DAA can execute before its working principles are affected? An experimental campaign to measure the DAA lifespan would answer this question. The lifespan study could be the first step towards a lifecycle evaluation of the DAA as conveyor system: manufacture, implementation and maintenance cost are important for viable conveyance systems. Nevertheless, the DAA did not present any operation wear during the experimental test of this thesis.

9.6 Temporal EDA control

Section 6.1 explained the basis to control the trajectory of the conveyed object: to solve and execute a straight line trajectory. This was because the DAA works digitally, i.e. in a step-by-step displacement output. If all EDAs in the DAA are given the same current signal (intensity and pulse duration) the output step displacement would be a straight line. Therefore, the trajectories issued by any pathfinding algorithm will be approximated by linear steps.

The dynamic model predicts the kinematics of each EDA. Therefore, it could be used to control the kinematics of each EDA (activation time and driving current profile) and generate curved displacement of the conveyed object with one displacement step, instead of a straight one. This could improve the DAA execution of the solution paths or open new possibilities to the pathfinding algorithms.

9.7 Pathfinding algorithms

In Chapter 7, the experimental trajectories based on A* pathfinding algorithm were evaluated. On the other hand, Θ* based trajectories, able to execute *xy* plane displacements, were not evaluated due to time limitations. Testing and comparing these Θ* planar motion trajectories with the A* results would allow a comparison between both algorithms. Computation time, efficiency, speed, percentage of success and other metrics, under multiple environments, could be measured. This would be an important and readily set research topic.

Another perspective is to extend the developed A* algorithm to A*-based Multi-agent pathfinding algorithms. There are multiple reported alternatives

like EPEA*, ODA*, M* and the CA* family. This would allow the DAA to simultaneously solve the pathfinding problem for multiple objects.

9.8 Closing the loop

The DAA is controlled with a feed-forward open loop scheme. This aimed to keep the integration simple, aligned with the microfactory context. If the precision of the DAA is to be enhanced, closing the control loop would be necessary. To close the loop, a sensor to measure the objects position on the DAA is needed. Two options are viable: an integrated sensor in the EDA, like a pression sensor between the bottom glass layer of the EDAs and the electronic circuit could be used to determine the position of the carried object (like a smartphone screen); or a camera with an online image processing software to measure the object and obstacle positions. The latter option is readily adaptable to the system, given the trajectory control flowchart presented.

9.9 Miniaturization & integration of the DAA

Currently, the magnets are manually assembled, one by one, in the DAA structure, which is difficult if further miniaturization is wished. To allow further miniaturization of the DAA, MEMS permanent magnets could be a way forward. The DAA permanent magnets could be directly integrated in the microfabricated structure. Microfabricated permanent magnets require different design considerations compared to their macrofabricated pairs. For example, microfabrication can control the magnetization direction. Certain magnetic films and deposition processes lead to better in-plane performance, whereas others exhibit better out-of-plane performance. Isotropic materials are also possible, but these sacrifice performance [AW09]. In the case of the DAA, this characteristic is very important, as the in-plane attraction of the FPMs creates the discrete stable positions (and thus the digital principle), and the out-of-plane magnetization of the MPM is crucial to the electromagnetic interaction with the current wires (Lorentz force). The crucial DAA requirement is then high values of remanence (B_r). From [AW09], "Conventionally deposited micromagnets"[1] offer performance values aligned with the DAA requirements and miniaturization potential. This is backed by [RMP19], as illustrated in Figure 9.2

[Mal+19] microfabricated CoPtP pattern magnets by electrodeposition (Fig-

[1] Physical vapor deposition (sputtering, evaporation, and pulsed-laser deposition (PLD)) and electrochemical deposition (electroplating).

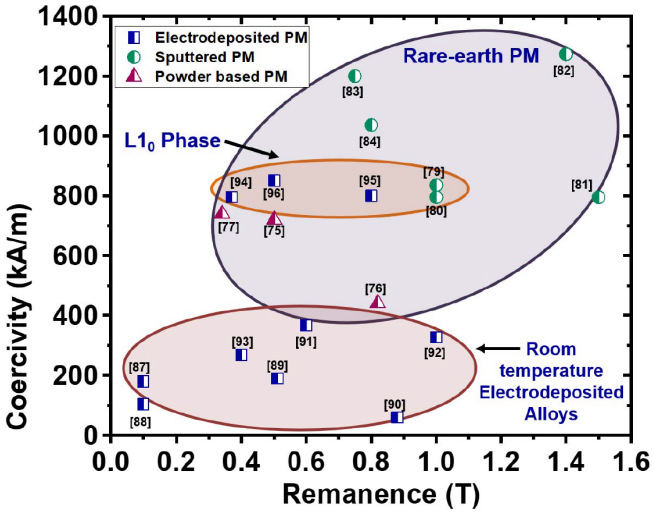

Figure 9.2: Comparison between the magnetic properties of different permanent magnets reported in the literature review by [RMP19].

ure 9.3). The magnet thickness and pattern inter-spacing effect on the magnetic properties were studied. They also studied the magnets' composition, crystalline structure, and grain size. They obtained remanence values of 0.4 T.

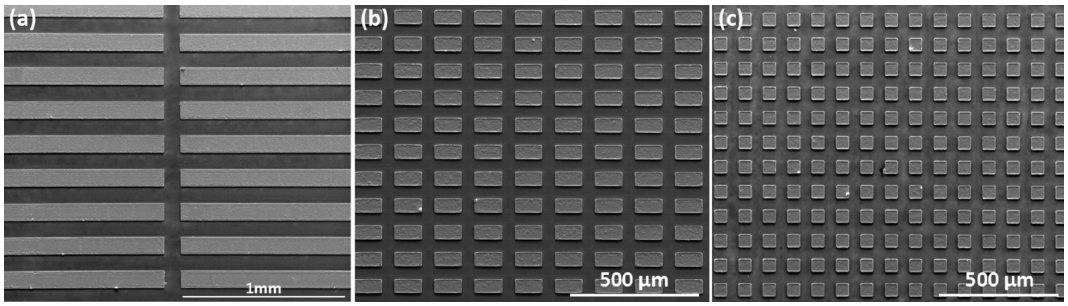

Figure 9.3: Micro-fabricated magnets. (a) 2500 µm × 50 µm stripes. (b) 100 µm × 50 µm rectangles. (c) 50 µm × 50 µm squares. Each pattern had a thickness of 10 µm ([Mal+19]).

[Nak+20] prepared a 250 µm-thick Pr-Fe-B film magnet by Pulsed Laser Deposition (PLD). The magnet was attached to a shaft, a difficult procedure in microfabrication (Figure 9.4). The influence of Pr content was studied. Augmenting Pr content increased coercivity and decreased remanence, respectively. A maximum remanence of 0.9 T was obtained.

9.10 Modular & scalable design

To enlarge the active area of the DAA, a modular and scalable design of the silicon structure of the DAA is proposed, in collaboration with the C2N laboratory, Parid-Sud University. This design is based on square interconnectable

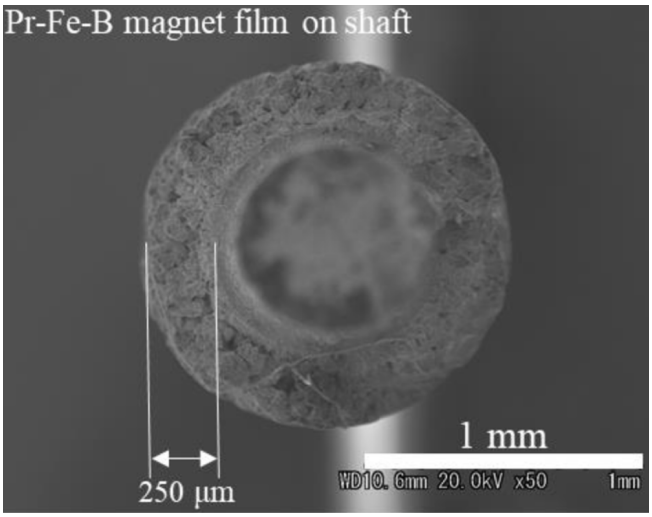

Figure 9.4: Pr-Fe-B film magnet deposited on a thin stainless shaft by [Nak+20].

modules. Each module is a square array of 7×7 EDAs, assembled to obtain a larger conveyance surface. Each silicon module has cavities for the MPMs, FPMs and a dedicated PCB to control its 49 EDAs. The interconnectable modules can be easily assembled thanks to trapezoid notches that ensures the correct positioning between them (Figure 9.5a). The geometry of the silicon modules enables to cover a large surface with a puzzle-shape assembly (Figure 9.5b and Figure 9.5c).

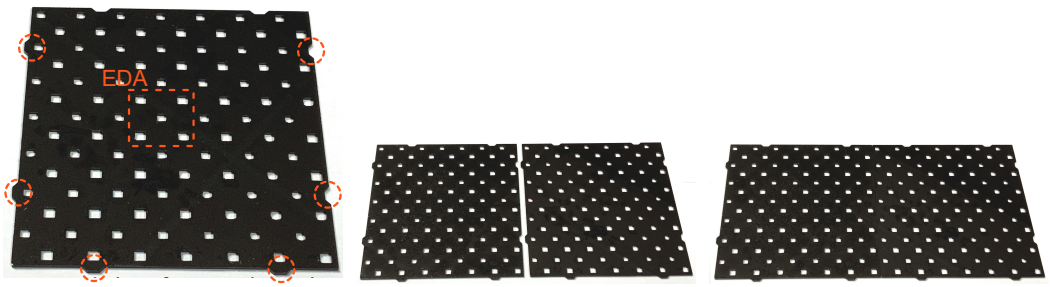

(a) (b) (c)

Figure 9.5: (a) Modular 7×7 DAA. (b) and (c) Interconnected DAAs.

The 7×7 DAA would work as the prototype presented in this thesis. The assembly and experimental validation of this 7×7 DAA would be the next development step of the ALVEO project.

Part V

Appendix

Appendix A

Definitions

A.1 Actuator performance metrics

To compare the wide variety of actuators, some evaluating criteria (metrics) are necessary. The mechanical requirements of an actuator application can be expressed in terms of force, stroke, stiffness, volume, mass, response time (or operating frequency), power, efficiency and resolution [HFA97]. The performance metrics are not completely exhaustive, as the lifespan, cost, sourcing, environment resistance, environmental impact and maintenance of the presented actuators are not always reported or evaluated. These criteria can be divided into three groups:

- The intrinsic properties of the actuator such as mass, volume and stiffness, determined by the construction, geometry and physical requirement of the actuator and application.
- The useful mechanical output obtained. Determined by the physical principles exploited by the actuator.
- The characteristics of the actuator output in relation with the injected input

The second and third groups are expanded hereafter.

A.1.1 Mechanical output metrics

This section explains and defines the characteristics of an actuator's mechanical output. The stroke notion is crucial for this dissertation, as it will define the digital/analog actuation principle (Section 1.2).

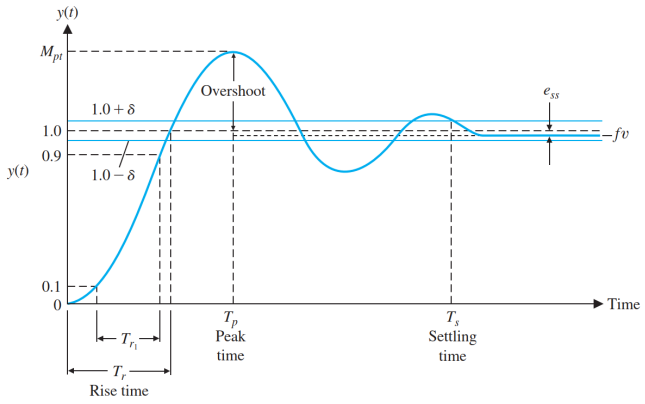

Figure A.1: Unitary step response of a second order system [DB17]

A.1.1.1 Stroke

The distance range in which an actuator can operate is called stroke. It is the maximum available displacement that the actuator can deliver [Pon05]. When the actuator is based in shape-changing phenomena such as piezoelectrics, or shape memory alloys, the stroke is also called maximum strain ϵ_{max} [HFA97].

A.1.1.2 Maximum output speed

The maximum speed that the actuator can deliver. It can be rotational speed (ω) or linear speed depending on the actuator's nature.

A.1.1.3 Response time

Normally the response time of an actuator is defined by its response to a step input considering the actuator as second order system (Figure A.1). From this response, multiple performances can be obtained (notably for the design and evaluation of a controller if the actuator is in closed loop). Two important time metrics are the rise time and settling time of the actuator to this step input:

A.1.1.3.1 Rise time The time taken by the actuator to go from 0% to the value of the input step (or 100%), noted as T_r in Figure A.1. This rise time is reduced to the time taken to go from 10% to 90% if the system is overdampened, noted T_{r_1} in Figure A.1 [DB17]. In this dissertation the 10%-90% rise time is used.

A.1.1.3.2 Settling time The settling time (T_s) is defined as the time required for the system to achieve and stay within a certain percentage δ of the reached final value [DB17]. In this dissertation $\delta = 2\%$.

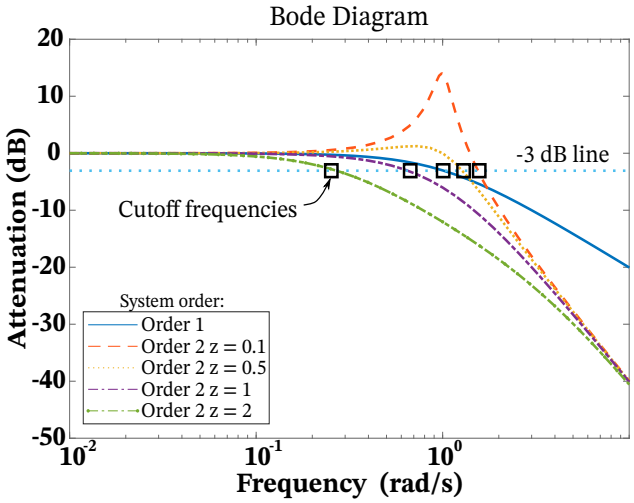

Figure A.2: Bandwidth for different order systems (same natural frequency $\omega_n = 1\,\mathrm{rad\,s^{-1}}$ for the second order systems). All actuators can be approximated by Order 1 or Order 2 underdampened, critically dampened or overdampened systems.

A.1.1.4 Operating frequency or bandwidth

When the actuator is coupled to its acting system, the mass and moment of inertia act as a load to the actuator, affecting its behavior. This load imposes a limit on the power delivered by the actuator. This translates to the typical low pass filter behavior of the actuator in the frequency domain [Pon05] (Figure A.2). This means that the actuation is only possible up to some cutoff frequency. The cutoff frequency is defined as the frequency at which a decay of 3 dB in the output of the actuator is observed. The range of frequencies in which the actuator can operate, or available bandwidth, is then defined by the cutoff frequency.

A.1.1.5 Maximum force

The maximum blocking effort or maximum force (F_{max}) is defined as the maximum force or torque that the actuator can deliver. This is the effort that will block the actuator so that no further displacement can be achieved against this load. In the case of rotational actuators, the blocking effort is usually referred to as "stall torque" [Pon05]. If divided by the contact area of the actuator, it can be given in terms of the maximum actuation stress (σ_{max}).

A.1.1.6 Power density or volumetric power

Power density (P_V) is the ratio of the maximum available mechanical output power (P_{out}) to the volume of the actuator (V) [Pon05]:

$$P_V = \frac{P_{out}}{V} \tag{A.1}$$

A.1.1.7 Work density per cycle

Work density per cycle, (W_V) , is defined as the total mechanical work output that an actuator can deliver during an actuation cycle to volume ratio [Pon05]:

$$W_V = \frac{W_{out}}{V} \tag{A.2}$$

A.1.1.8 Energy efficiency

The efficiency (η) is defined as the ratio of the output mechanical energy (W_m) to the input electrical energy (W_e):

$$\eta = \frac{W_m}{W_e} \tag{A.3}$$

The efficiency is a dynamic parameter, it is a function of the actuation conditions. The maximum efficiency is usually taken as the performance metric [Pon05].

A.1.2 Input-output characteristics

This section explains and defines the characteristics of an actuator's output relative to its input. The degree of freedom notion is important, as it will define the planar motion capability of the system (Section 1.3).

A.1.2.1 Degree of freedom (DoF)

The degree of freedom (DoF), also called the mobility, of a mechanical system is the number of independent input parameters that controls the system configuration or posture (position and inclination) in space [UPS18]. A rigid object floating in a fluid such as a ship in the sea, or a drone in the air, need 6 independent variables to define its position and inclination: 3 translational variables x, y and z (also called *sway*, *surge* and *heave*) and 3 rotation variables *pitch*, *roll* and *yaw* around the x-axis, y-axis and z-axis, respectively (Figure A.4).

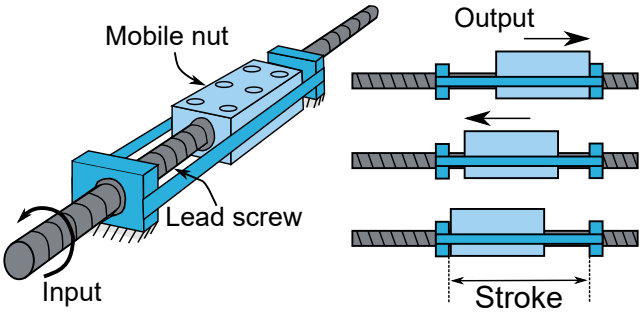

Figure A.3: A linear lead screw nut actuator: as the screw is turned, the nut on the screw is displaced in a single axis. The range in which the nut can travel is the stroke of the linear actuator. As there is no independent input other than the rotation of the screw to determine the position and inclination of the nut, the linear lead screw nut actuator has 1 DoF.

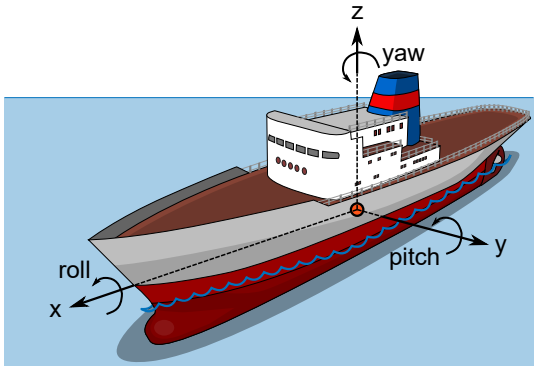

Figure A.4: A ship and the 6 DoF that define its position and rotation (configuration) in space.

A.1.2.2 Cross-coupling or straightness error

Cross-coupling or straightness error refers to the unwanted displacement or rotation that is produced along one degree of freedom of the actuator when it is actuated to move only in other(s) degree(s) of freedom [MFM17].

A.1.2.3 Linearity

Linear systems have the property or principle of superposition. Superposition is assured if the system presents two properties relating its input and output:

- Additivity: If the response of the system to input A is output $f(A)$, and the response to input B is output $f(B)$, then the response to input $C = A + B$ will be output $f(C) = f(A) + f(B)$.
- Homogenity of degree 1: If we scale the input by a factor $\alpha \in \Re$, then the output of the actuator is scaled by the same factor, i.e., $f(\alpha A) = \alpha f(A)$.

Linearity can be measured by any residual analysis from the actual output and the best-fit straight line to the output.

A.1.2.4 Repeatability (Reproducibility, Precision)

Repeatability, also called reproducibility or precision, is the actuator's ability to produce identical outputs for the same input under constant conditions. It can be measured as the dispersion or standard deviation of the actuator output to that same input. A precise or repeatable actuator has a small standard deviation as represented in Figure A.5a.

A.1.2.5 Accuracy

Accuracy is inversely proportional to the difference (error) between the actual output and the output measured by a reference measurement device. A very accurate actuator has a very small reference error. Linear actuator accuracy is influenced by the feedback sensor, drive mechanism, and ideal geometry (perfect straightness/parallelism) of its structure. In this work accuracy will be mostly used to evaluate the prediction of the model (model output) against the output of the system (mean value of multiple measurements under the same conditions as in Figure A.5b).

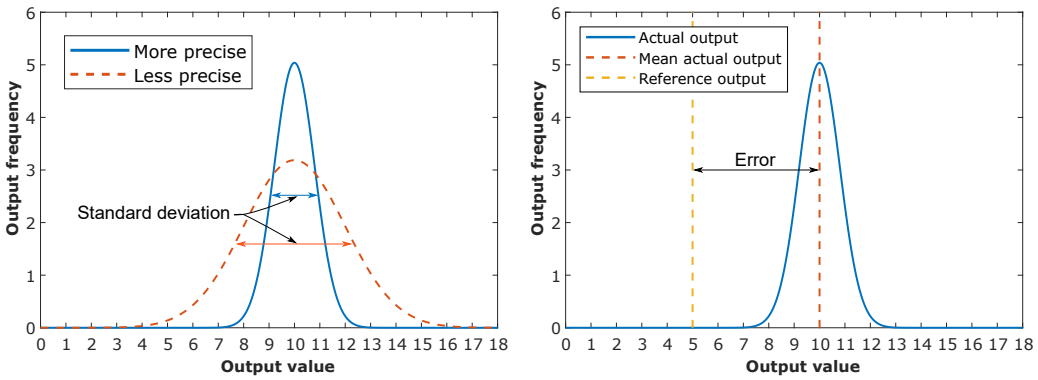

(a) (b)

Figure A.5: Actuator (a) Repeatability. (b) Accuracy.

A.1.2.6 Resolution

The smallest repeatable change in output achievable with a change in input. Also known as step size.

A.1.2.7 Non-linearities

When the principle of superposition can not be applied to a system, the system is non-linear. Several non-linearities commonly found in mechatronic systems include saturation, deadband and hysteresis [Bis06].

A.1.2.7.1 Saturation All real actuators have some maximum output capability, regardless of the input. This violates the linearity assumption, since at some point the input command can be increased without significantly changing the output; see Figure A.6a. This type of nonlinearity must be considered in mechatronic control system design, since maximum velocity and force or torque limitations affect system performance [Bis06].

A.1.2.7.2 Deadband If the output of an actuator stays at zero when a input is injected into the actuator and, once the input reaches a certain value, the output varies with the input, then the zone (band) where the actuator is unresponsive (dead) to the input variation is called deadband. The deadband is a nonlinear characteristic of the output of an actuator and is typically a region of input close to zero as represented in Figure A.6b.

A.1.2.7.3 Hysteresis The phenomenon in which the value of a physical property (output) lags behind changes in the effect causing it (input) [Oxf20] (Figure A.6c). This is a basic definition of a complex phenomena (refer to [May03] for a deeper treatment). Some models such as the Maxwell model, the Preisach model, the Bouc–Wen model and the generalized Prandtl–Ishlinskii model attempt to capture general features of hysteresis [May03].

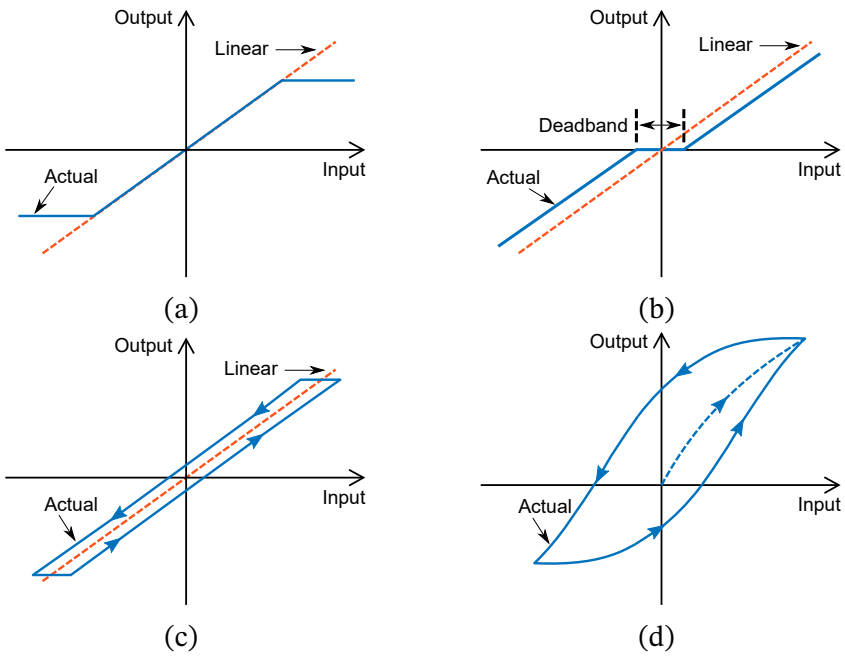

Figure A.6: Actuator non-linearities: (a) Saturation. (b) Deadband. (c) Hysteresis ("backlash"). (d) Typical hysteresis curve.

Appendix B

State of the art appendix

B.1 Friction

B.1.1 Friction variables

Contact time and direction Coulomb discovered that the static frictional force increases logarithmically with the amount of time an object is at rest [Pop17]. For metallic materials, the real contact area increases with time due to the creep processes. At higher temperatures, this increase is faster. When the contact area increases, the creep process slows, leading to a logarithmic dependence of contact area and, thus, a logarithmic dependence of the static frictional force. This increase begins at the instant of first contact on the atomic scale and does not stop even after very long time periods [Pop17]. For elastomers, this effect is tied to the increase in contact area due to the visco-elasticity of the material. Also, capillary forces attribute to frictional forces and lead to the approximate logarithmic time dependence of the static frictional force [Pop17]. The stop-restart motion increased the level of static friction force, while the stop-inversion motion reduced the static friction.

Normal force The linear dependence of the frictional force on the normal force is only met in a specific force domain. For metals, this domain goes from 1×10^{-4} to 1×10^{2} N. The linear dependence is no longer valid when the real contact area is comparable to the apparent contact area. This limit is easily reached for soft metals such as indium or lead, polymers and elastomers [Pop17].

Surface roughness Popov states that the frictional force is independent or only very slightly dependent on the roughness of the surfaces. Contrary to expectations, the coefficient of friction for especially smooth metal surfaces can be even larger than for rough surfaces. The influence of roughness on friction is

dependent on many factors, for instance, the presence of impurities or liquid films in the tribological contact, among others [Pop17]. Although, for many authors, the surface roughness is the principle for their friction models, as it will discussed below. [Çol+12] studied the surface roughness influence in the adhesion force of a 2 μm tip of a atomic force microscope with two silicon surfaces: one smooth surface with RMS roughness of 1 nm and an etched surface with RMS roughness of 15 nm. The **humidity** influence was measured in a range of 0 to 80%. They stated that the formation and breaking of the capillary water neck was stochastic. The roughness of the etched substrate reduced the adhesion by more than an order of magnitude, depending on the exact value of the relative humidity (64 times smaller for 0% humidity). The adhesion force increased with increasing humidity until 70%. This points to a higher dependency on **humidity**, and the capillary action between surfaces that depends on the topography of the surfaces, more than the roughness itself.

Temperature Popov states that friction is weakly dependent on the temperature for many metal pairings. Between 200 °C and 300 °C, a sharp increase in the friction force occurs (increasing up to threefold). At higher temperatures, it remains almost constant or increases at a slower rate [Pop17]. For low temperatures, the coefficient of friction is constant, relatively small, and only weakly dependent on material combination. Characteristic values are on the order of 0.16-0.22. In this domain oxide layers or other layers of impurities remain on the surface during the frictional process. The domain of higher coefficients of friction is for metal contacts [Pop17]. Microscale friction in silicon is also dependent on temperature, as shown by [Gko+18]. The authors found a maximum dynamic friction force at 80 °C for their apparatus (evaluating from 0 to 300 °C). They suspect that the dynamics of capillary condensation was responsible. Capillary menisci increase adhesion and friction. The formation of a capillary meniscus depends on both the amount of water molecules on the surface, as well as on their mobility. At room temperature, there are many water molecules present on the surface, but they are not very mobile. At a high temperature, the water molecules are very mobile, but only few are present. At the intermediate temperatures, sufficient water molecules are present, and they are mobile enough to form fully developed capillary menisci. Then again, **humidity** is an important factor (under the conditions imposed by the temperature and the topography of the surfaces in contact).

Number of cycles Continuous friction between the same moving object in the same zone affects the value of static friction force, as found by [KV19]. The

authors rubbed two MEMS silicon structures for 2 249 827 cycles in a controlled room at 25±5 °C and relative humidity below 5%. Measuring the applied force and generated displacement with 0.6 nN and 0.2 nm precision respectively. They used a slower speed for the first 200 cycles and then 50 μm s^{-1} for the reminder. They found that stiction was concentrated in very precise positions for the first 1700 cycles, with the highest static frictions of the experiment (Figure B.1). Then, stiction phenomena started to appear at other positions, increasing the overall static friction in the stroke, but with lower maximum static friction values. Finally, at 65 000 cycles, the friction force smoother evenly and a significant reduction in static friction values were observed (final value 75% less than initial value of static friction). This study demonstrated the influence of the number of cycles on the friction behavior.

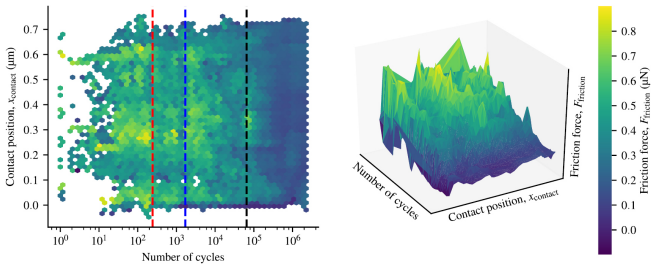

Figure B.1: Static friction dependence on cycle number and position ([KV19]).

B.1.1.1 Static friction models

Stribeck effect and Bo-Pavelescu model The Stribeck effect (named after Richard Stribeck's work in 1902) is the decrease from the static friction value to kinetic friction in a continuous process, contrary to Coulomb's model where it is abrupt. Multiple authors have proposed friction functions that account for this effect, with the most popular by Bo & Pavelescu [Mar+16]:

$$\vec{F_f} = \begin{cases} \left(F_k + (F_s - F_k)\, e^{-\left(\frac{||v||}{v_S}\right)^{\delta_\sigma}} \right) \mathbf{sgn}(v) & ||v|| \neq 0 \\ F_s \veebar -F_s & ||v|| = 0 \end{cases} \tag{B.1}$$

with $F_s = \mu_s F_N$ the static friction force, $F_k = \mu_k F_N$ the sliding friction force, v the relative velocity of the bodies in contact, v_S the "Stribeck velocity" (the velocity for minimum friction force) and δ_σ a geometric factor of the contacting surfaces (often $\delta_\sigma \approx 2$). This model still presents the discontinuity at null velocity.

Bengisu & Akay model In order to smooth the discontinuity at zero velocity, Bengisu and Akay proposed their model, also capable of capturing the Stribeck effect. This model is constituted by two equations (one for a finite velocity slope at zero and another to describe the Stribeck effect) [BA94]:

$$\vec{F_f} = \begin{cases} \left(-\frac{F_s}{v_0^2}\left(\|v\| - v_0\right)^2 + F_s\right)\mathbf{sgn}(v) & \|v\| < v_0 \\ \left(F_k + (F_s - F_k)e^{-\zeta(\|v\| - v_0)}\right)\mathbf{sgn}(v) & \|v\| \geq v_0 \end{cases} \tag{B.2}$$

With v_0 the transition speed between static friction and sliding friction and ζ the decay factor between static to sliding friction.

Seven parameter model This model includes the pre-sliding displacement, viscous friction, Stribeck effect and frictional lag. It consist in two equations, one for the adhesion and another one for the sliding regime [ADD94]:

$$\vec{F_f} = \begin{cases} \sigma_0 \vec{x} & \|v\| = 0 \\ \left(F_k + \dfrac{F_s(\gamma, t_d) - F_k}{1 + \left(\dfrac{\|v(t - \tau_l)}{v_S}\|\right)^2}\right)\mathbf{sgn}(v) + \sigma_v v & \|v\| \neq 0 \end{cases} \tag{B.3}$$

With

$$F_s(\gamma, t_d) = F_{s,a} + (F_{s,\infty} - F_{s,a})\frac{t_d}{t_d + \gamma} \tag{B.4}$$

Where σ_0 the tangential stiffness of contact, $\vec{x}$ the pre-slide displacement, σ_v the viscous friction coefficient, $F_{s,a}$ the previous static friction value, $F_{s,\infty}$ the static friction value after a long time at rest, τ_l the time constant of friction memory, γ the temporal parameter of rising static friction and t_d the dwell time or time at zero velocity.

This model describes most friction behaviors, but needs to identify seven parameters. Also, as it uses two separate-state equations, there is no criterion to switch between equations. Therefore, an eighth parameter to switch is needed, rendering the identification and implementation process hard and exhaustive [Mar+16].

Wojewoda model The motivation of the authors was to include the influence of some random factors (e.g. variations of normal pressure force or inhomogeneous asperity of contacting surfaces), include the stick-slip phenomena, but keep the numerical implementation simple. Their friction model is a hysteretic

static model with a stochastic component expressed as [Woj+08]:

$$\vec{F_f}(v,\dot{v}) = \begin{cases} F_{st}\mathbf{sgn}(v) & F_{st} \leq F_{d+} \wedge \mathbf{sgn}(v\cdot\dot{v}) \geq 0 \\ F_{d+}\mathbf{sgn}(v) & F_{st} > F_{d+} \wedge \mathbf{sgn}(v,\dot{v}) \geq 0 \\ F_{d-}\mathbf{sgn}(v) & \mathbf{sgn}(v,\dot{v}) < 0 \end{cases} \tag{B.5}$$

With

$$F_{st} = \frac{k_s\|v\|^2}{2F_N\|\dot{v}\|} - F_0 \tag{B.6}$$

$$F_{d+} = F_k + (F_s(v) - F_k)\,(g(v,\dot{v}) + f_R(x,v)) \tag{B.7}$$

$$F_{d-} = F_k - (F_s - F_k)\,(g(v,\dot{v}) + f_R(x,v)) \tag{B.8}$$

$$F_s(v) = F_s + \Delta F_s \frac{1}{1 + \frac{\|v\|}{v_A}} \tag{B.9}$$

Where F_{st} is the friction for the sticking phase, F_{d+} and F_{d-} represent the friction force in acceleration and deceleration, respectively, k_s is the contact stiffness, F_0 the initial value for sticking force, $g(v,\dot{v})$ is a function to model the Stribeck curve (e.g. the Bo-Pavalescu model), ΔF_s the range of breakaway force variation, v_A the average Stribeck velocity ($\approx 0.5{v_S}^{max}$) and $f_R(x,v)$ the stochastic function. $f_R(x,v)$ models the fluctuations of the friction force by a stationary Gaussian process with standard deviation σ. It can be generated with an autocorrelation coefficient $R(z)$, where z is the distance separating two asperities and the associated power spectral density function.

The model requires: five constant parameters ΔF_s, F_s, F_k, k_s and v_A; one varying parameter F_0; and the stochastic component f_R with standard deviation σ. The authors pointed out that the proposed model was valid for large macroscopic sliding. A precise description of microscopic sliding and stick–slip phenomena requires a further development [Woj+08].

B.1.1.2 Dynamic friction models

Dahl model Dahl developed a dynamic friction model considering the strain-stress curve of materials. He considered both materials acting as one, given the asperities bonds. When a force is applied, the material deforms elastically to resist the force. If the force increases, then the material deforms plasically and a maximum resistance force is reached (the static friction value). Finally, the applied force breaks the bondings and the objects slide. The bonding and breaking in this regime causes the kinetic friction force. Dahl stated that materials that present brittle rupture have almost indistinguishable static and kinetic friction

forces, as these materials do not deform plastically. For ductile materials, stick-slip was a marked behavior, as they deformed plastically [Dah68; Dah76]. Dahl showed that the friction force is dependent on relative velocity and displacement, expressing the strain-stress curve as:

$$\frac{d\vec{F_f}}{dx} = \sigma_0 \left\| 1 - \frac{\vec{F_f}}{F_k}\mathbf{sgn}(v) \right\|^{\alpha} \mathbf{sgn}\left(1 - \frac{\vec{F_f}}{F_k}\mathbf{sgn}(v)\right) \tag{B.10}$$

$$\frac{d\vec{F_f}}{dt} = \sigma_0 \left\| 1 - \frac{\vec{F_f}}{F_k}\mathbf{sgn}(v) \right\|^{\alpha} v \tag{B.11}$$

With σ_0 the stiffness coefficient and α a parameter defining the friction shape of the material curve. α is between 0 and 1 for brittle materials and higher than 1 for ductile materials. The Dahl model do not model the Stribeck effect and stiction, since it is based but it models the pre-sliding displacement through a new state variable, which eliminates the discontinuity at zero velocity [Mar+16].

LuGre model Canudas De Wit derivated this model from the Dahl model idea and included the Stribeck effect. The model considers friction as the interaction of elastic bristles. When a force is applied, the bristles start to deform with spring behavior during the sticking phase. Then if the force is sufficiently large, the bodies start to slip. The mean deflection of the bristles z is [Can+95; Ols+98]:

$$\frac{dz}{dt} = v - \frac{\sigma_0 z}{g(v)}\|v\| \tag{B.12}$$

$$\vec{F_f} = \sigma_0 z + \sigma_1 \frac{dz}{dt} + f(v) \tag{B.13}$$

$$g(v) = \alpha_0 + \alpha_1 e^{-v/v_0} \tag{B.14}$$

$$\tag{B.15}$$

With σ_0 the stiffness of the bristles, σ_1 the damping of the bristles, $g(v)$ a function to models the Stribeck effect and $f(v)$ a function to model the viscous friction (normally $f(v) = \sigma_2 v$).

Leuven model The LuGre model has less degrees of freedom available than the number of physically distinct phenomena to be modeled. Also, it inadequately models the hysteresis phenomena as it does not account for nonlocal memory. For this reason, the authors in [Swe+00] developed the Leuven model (with a

later modification to overcome a force discontinuity in [LSA02]):

$$\frac{dz}{dt} = v\left(1 - \mathbf{sgn}\left(\frac{F_h(z)}{g(v)}\right)\left|\frac{F_h(z)}{g(v)}\right|^n\right) \tag{B.16}$$

$$\vec{F_f} = F_h(z) + \sigma_1\frac{dz}{dt} + \sigma_2 v \tag{B.17}$$

$$F_h(z) = F_b + F_d(z) \tag{B.18}$$

Where: n is similar to the Dahl model α, a transition curve shape parameter depending on the material; $g(v)$ the Stribeck effect model; F_h the hysteresis force (i.e., the part of the friction force exhibiting hysteresis behavior with state variable z as input); F_b the force at the beginning of the transition curve for velocity reversal; and $F_d(z)$ the transition curve active at the simulation time.

Generalized Maxwell-slip model (GMS) The Leuven model was accurate and described all relevant friction phenomena but proved difficult to implement. For this reason, the same authors in [LSA02] proposed a modification of the Leuven model and then a generalization of this proposal in [ALS05]. The idea was to assemble N elasto-plastic (Maxwell or Jenkin) elements in parallel, which all have one common input displacement x (Figure 2.56b). Each element i has an output force F_i; the element is characterized by a stiffness k_i, a slip (or saturation) force limit W_i and a state variable z_i (representing the spring deflection). The elements are assumed to have no mass, so $F_i = k_i z_i$. The blocks stick each time there is a velocity reversal. The hysteresis force is equal to the sum of hysteresis forces (F_i) of each element:

$$\frac{dz_i}{dt} = v \qquad \text{if stick} \tag{B.19}$$

$$\frac{dz_i}{dt} = \mathbf{sgn}(v)C_i\left(1 - \frac{z_i}{g_i(v)}\right) \qquad \text{if slip} \tag{B.20}$$

$$\vec{F_f} = \sum_{i=1}^{N}\left(k_i z_i + \sigma_i\frac{dz_i}{dt}\right) + f(v) \tag{B.21}$$

With C_i an "attractor" parameter determining how fast z_i converges to $g_i(v)$ and σ_i the damping (visco-elastic) coefficient. The change from stick to slip is determined by $z_i = g_i(v)$. The change from slip to stick is done when $v = 0$. The number parameters in the model depends on the number of Maxwell elements. Each element needs k_i, σ_i, C_i and $g_i(v)$. This means three parameters for element plus $g_i(v)$ (that needs three if the Bo-Pavelescu model is used), totaling six per element. The authors proposed to use a scale parameter, α_i, to calculate C_i and $g_i(v)$ for each element as $C_i = \alpha_i C$ and $g_i(v) = \alpha_i g(v)$, with C and $g(v)$

global parameters. The condition $\sum_{i-1}^{N} \alpha_i = 1$ must be respected. This reduces the identification to three parameters per element and two global parameters. Nevertheless, the GMS model requires nontrivial identification efforts [YT14]. Another variable in the model is the number of elements to represent a system. On this matter, [KZ19] applied the GMS model to the translational actuator of a 3 DoF manipulator for handling and assembly of microparts. This actuator was a DC motor with a ball-screw transmission and ball bearings as support. The sensor was an encoder at the motor level, allowing nanometer precision movements. The authors applied the GMS with two to ten elements, identifying the parameters for the given number of elements. They found that the normalized mean square error was: more than 20% for three elements; decreased to less than 5% for four elements; was just about 1% for five elements; and attained 0.5% for six elements. More elements yielded gains of less than 0.1%, pointing to a optimum of six elements for the GMS model [KZ19].

Generalized asperity-based model The models presented so far are based on experimental observations and then theoretical replications, thus "empirical" models, in a way. The authors in [Al-+04; DAV10] present a theoretical, physical model of the contact as: a set of stochastic distributed asperity masses (represented by a mass connected to a normal and a tangential spring with nonlinear behavior in Figure 2.56c); and an elastic non-dissipative counter profile. The elastic–plastic behavior of each asperity is based on a two element GMS model. An adhesion law is imposed on the asperity mass when the asperity is in contact with the counter profile. All the model's parameters are material properties or stochastic distributions. The model simulates all the friction phenomena, static and dynamic, and makes it possible to study the influence and relevance of the numerous parameters involved in the model and to relate these parameters to macroscopically observable and measurable quantities.

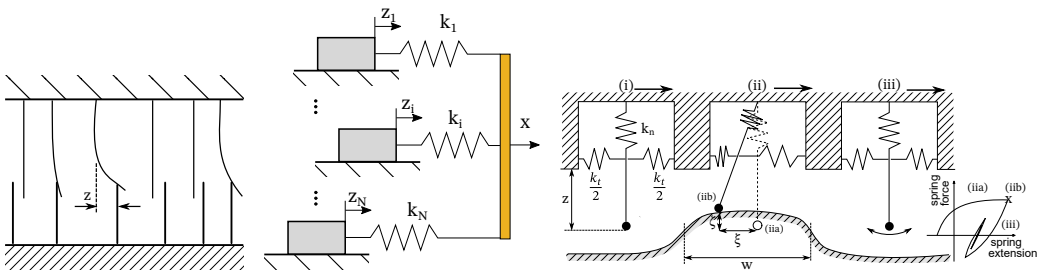

Figure B.2: Dynamic friction models (a) LuGre [Can+95; Ols+98]. (b) GMS [LSA02; ALS05]. (c) Generalized friction model [Al-+04; DAV10].

B.2 Pathfinding

B.2.1 Grid methods

B.2.1.1 Dijkstra

Dijkstra's algorithm (or Uniform Cost Search) [Dij59] finds the shortest path between nodes in a graph (grid). It associates a cost to the connections between the nodes (edges) to find the least expensive path (optimal path) between a given start node and all other nodes in the grid. It can also be used for finding the shortest paths from a single node to a goal node by stopping the algorithm once the shortest path to the goal has been determined. Dijkstra evaluates all the nodes in the grid until finding the solution, affecting its execution time in dense grids or high DoF problems.

B.2.1.2 A*

A*, developed by [HNR68], can be seen as an improved Dijkstra's algorithm (Figure B.3). A* uses an heuristic function to guide the node exploration. Every node n is assigned a distance from the start node $g(n)$ plus the heuristic function value, an assumption of the remaining distance to the goal $h(n)$, forming the total value function $f(n)$.

$$f(n) = g(n) + h(n) \tag{B.22}$$

The node with lower $f(n)$ is expanded, i.e., the connected nodes are evaluated. Once the goal is chosen for expansion, A* halts and the found path to the goal is returned. If $h(n)$ is *admissible*, i.e., it never overestimates the actual cost from n to the goal, then A* is guaranteed to return an optimal solution if one exists [HNR68; Sha15]. This also means that A* is resolution complete. A* is optimal in the number of expanded nodes. That is, any other equally informed search algorithm will have to expand all the nodes expanded by A* before identifying the optimal solution [HNR68; Sha15].

The most commonly used heuristic functions $h(n)$ are: the Manhattan distance, the total difference between the coordinates of the node and goal; the Euclidean distance, the straight-line distance between the node and goal; and the Move distance, the length of the path between the node and goal nodes following a 8-connected grid map. As A* does not pre-process the obstacles of the environment, these distances do not consider them for their value.

Incremental A* or Lifelong Planning A* (LPA*) LPA*, by [KL02a], is an incremental search algorithm. It can solve problems where the environment

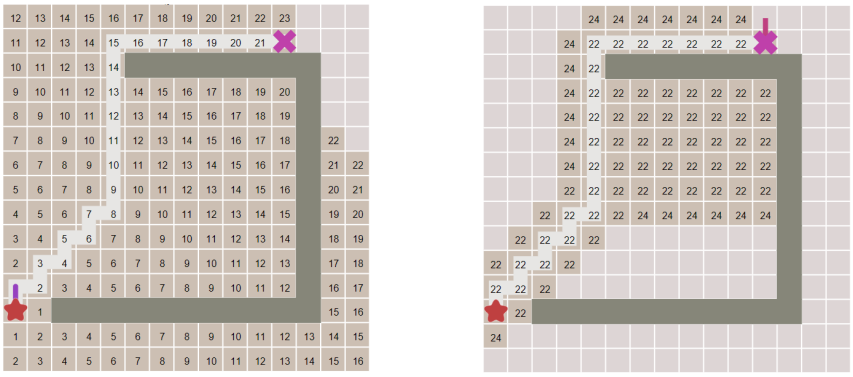

(a) (b)

Figure B.3: Same solution for the same problem, but different number of nodes evaluated for (a) Dijkstra (b) A*. The numbers in the cells represent the cost from start to the cell for (a) and the total path cost on (b). Unnumbered cells are non-evaluated nodes. The clear cells are the solution path [Pat16].

changes (edge cost changes) but some regions stay identical. LPA* saves the coast of each node and evaluates what nodes must be re-evaluated by the environment changes, thus saving those already created paths and execution time. The first search of LPA* is the same as A* but all subsequent searches are much faster. LPA* produces at least the search tree that A* would build.

B.2.1.3 Dynamic A* (D*)

D*, by [Ste94], can solve informed, semi-informed or uninformed problems by an incremental algorithm based in A* and a sensor. D* accepts any information of the environment, even the unknown region (approximate information, stochastic models for occupancy, or heuristic estimates). Once the available information is entered, D* finds an optimal path for this conditions and starts to execute it. The sensor is used to modify the cost of the near node edges (arcs). The fact that these arc cost changes while solving the problem is why it is called Dynamic A*. If the sensor detects obstacles, the nodes are modified and D* replans a new optimal path with the new information from its current location. It repeats the process until it reaches the goal coordinates or determines that the goal coordinates cannot be reached. The fact that it adds the information and does not re-calculate the entire problem from scratch makes D* more efficient than a reset A* solution [Ste94].

Focused-Dynamic A* (Focused-D*) The full generalization of A* for dynamic environments was proposed by the same author in [Ste95]. Focused-D* uses heuristics to focus the arc cost updates so to minimize node expansions. This reduce computational costs. The net effect is a reduction in run-time by a factor

of two to three against D*.

Focused-Dynamic A* Lite (Focused-D* Lite) Based on LPA* and with the aim to reproduce the behavior of Focused-D*, the authors in [KL02b; KL05] developed Focused-D* Lite. The authors argue that their solution is simpler to implement and achieves better or the same performance that Focused-D* (thus the add-on "Lite"). This change in base (from D* to LPA* base) provide mathematically proven properties of completeness and optimality to Foused-D* Lite by extension of LPA*.

B.2.1.4 Theta* (Θ*)

Theta* (Θ*), developed by [Nas+07; Nas+10], is an any-angle path planning algorithm based on A*. Any-angle means that the algorithm uses the grid to link the start-goal nodes, but once the path is set, it is optimized. The optimization uses straights not contained in the grid edges to join grid nodes and form a shorter path than the grid edges path. This produces optimal or near-optimal paths in the free space rather than optimal paths on the grid, which can be badly set for the problem. Θ* finds near-optimal paths in free space with execution times comparable to A*. Θ* records the parent nodes that are in line of sight, linking them if: they belong to the grid solution path, skipping the nodes in between; and the linking path is collision free (Figure B.4b). This produces a shorter path than A*. As A*, Θ* is complete.

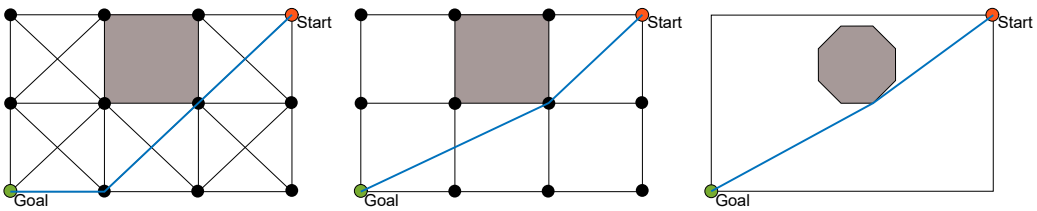

(a) (b) (c)

Figure B.4: Grid-based solutions of Figure 2.62. (a) A* solution with grid nodes and edges. (b) Θ* solution with grid nodes and free-space straights (any angle solution). (c) Real shortest path. Adapted from [Nas12].

Lazy Theta* (Lazy Θ*) Θ* performs a line-of-sight check for each unexpanded visible neighbor of each expanded vertex. This can get complex in dense grids like 3D scenarios (26-neighbor cubic grids vs 8-neighbor square grids). Therefore, the authors in [NKT10], introduced Lazy Θ*, which uses lazy evaluation to perform only one line-of-sight check per expanded vertex. Lazy Θ* finds paths faster than Θ* on cubic grids, with one order of magnitude fewer line-of-sight checks and

without an increase in path length. It does so by assuming nodes connections beforehand and drawing lines between its assumptions. Their experimental results demonstrated that all variants of Lazy Θ* were superior to Θ* and that Lazy Θ* had the best tradeoff between: the number of line-of-sight checks and runtime; and path length.

B.2.1.5 Jump point search (JPS) & JPS+

Jump point search, developed by [HG11; HG12], speeds up the search on rectangular grids by analyzing the grid structure of the environment. JPS combines A* with a simple node expansion operator that prunes potential successors if they can be reached by a path which is shorter than, or symmetric to, the current path (Figure B.5). JPS evaluates the horizontal and vertical lines of the current node. If it does not find the goal, it moves diagonally towards the goal (A*) and repeats. When it finds a node *y* that cannot be reached by a shorter path (generally near an obstacle) JPS adds it to the A* list as next node, and then repeats. This process makes A* to "jump" nodes without evaluating them, as the intermediate nodes could be reached in a equally cost path, thus accelerating A*. As evaluating nodes is slower than the line process, JPS is faster than A* and retains its characteristics.

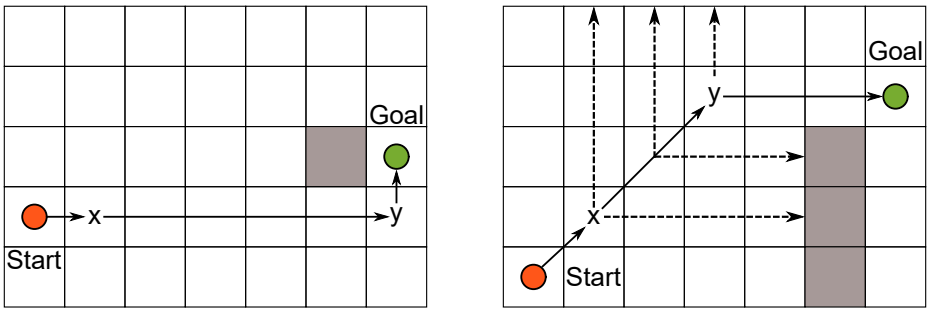

Figure B.5: Grid-based solutions of Figure 2.62. (a) A* solution with grid nodes and edges. (b) Θ* solution with grid nodes and free-space straights (any angle solution). (c) Real shortest path. Adapted from [Nas12].

Jumping from one point to another in the grid avoids many unnecessary A* open list operations. However, identifying these jump points becomes the new bottleneck of JPS. The same authors proposed JPS+ in [HG12]. JPS+ add jump points in the line expansion direction to avoid JPS to overrun or overshoot the goal when jumping, thus making it more efficient.

B.2.2 Sampling methods

Bidirectional RRT (B-RRT) B-RRT grows two trees: one "forward" from the start and one "backward" from the goal. The algorithm alternates between growing the forward tree and growing the backward tree, and it attempts to connect the two trees by choosing a sample from the other tree. The advantage is that a single goal state can be reached exactly, rather than just a goal region. Another advantage is that, in many environments, the two trees are likely to find each other more quickly than a single tree will find a goal region [LP17].

RRT*-Smart As RRT* is probabilistically complete, it never reaches that optimality in finite time. Also, the rate of convergence is slow. To address this, the authors in [Isl+12] developed the RRT*-Smart algorithm. RRT*-Smart initiates with a RRT*. Once the first path is found, the algorithm optimizes this path by interconnecting the directly visible nodes. This optimized path yields biasing points for a new RRT* sampling near the visible nodes, which gives a new best path. This process continues as the algorithm progresses and the path keeps on being optimized (Figure B.6). The algorithm is probabilistically complete, but converges far more quickly.

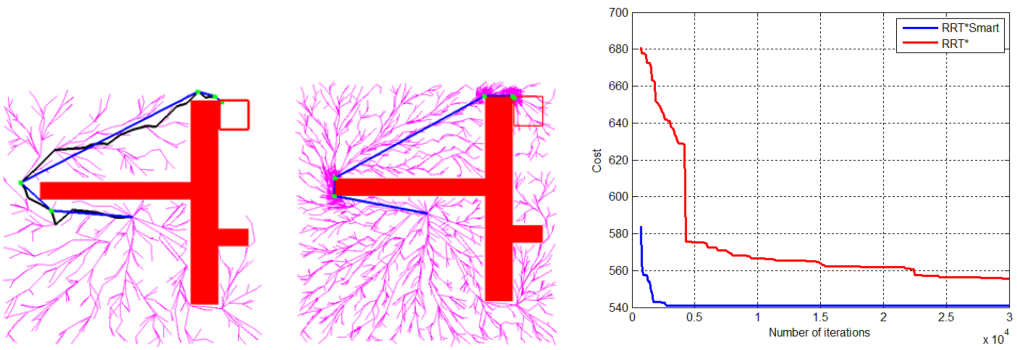

(a) (b) (c)

Figure B.6: RRT*-Smart algorithm by [Isl+12]. (a) First solution by a RRT* and initial path definition by visible nodes. (b) RRT* iterative optimization of the path until a given iteration. (c) Cost performance comparison between RRT* and RRT*-Smart.

RRT*-Quick RRT*-Quick, developed by [JLK15], uses the "Branch-and-bound technique" on a RRT* tree. This technique reduces the number of nodes in the tree. Once a feasible solution is found, the cost of the solution is used as an upper bound. Every node in the tree which has higher cost than the upper bound is removed from the tree along with its descendants. It makes RRT* focus on improving the solution. More nodes are pruned as the new solution lowers

the upper bound. The main idea of RRT*-Quick is based on the observation that nodes in local area tend to share a common parent because of the rewire operation of RRT*. The parents are good candidates for the Branch-and-bound technique. In addition to the nodes inside the RRT* radius, RRT*-Quick also takes account of the ancestors of them. This increased computation time is negligible compared to the load of a larger RRT* radius.

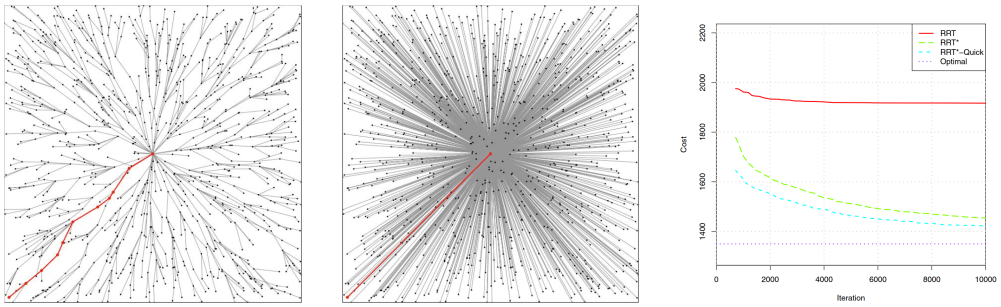

(a) (b) (c)

Figure B.7: RRT* and RRT*-Quick comparison by [JLK15]. (a) RRT*. (b) RRT*-Quick. (c) Performance comparison.

RRT-A* RRT-A*, developed by [Li+14], adds the A* cost function to the RRT algorithm to optimize the path performance (Figure B.8). As already seen, the cost in A* has an heuristic function and it can follow different metrics. The authors testes the Euclidean distance, Manhattan distance and Diagonal distance to evaluate their RRT-A* algorithm. The heuristic function is used to choose the connecting nodes of a new sample, given by the k-nearest neighbor and the heuristic cost of each node. The authors found that the Manhattan distance was the best for their testing scenarios.

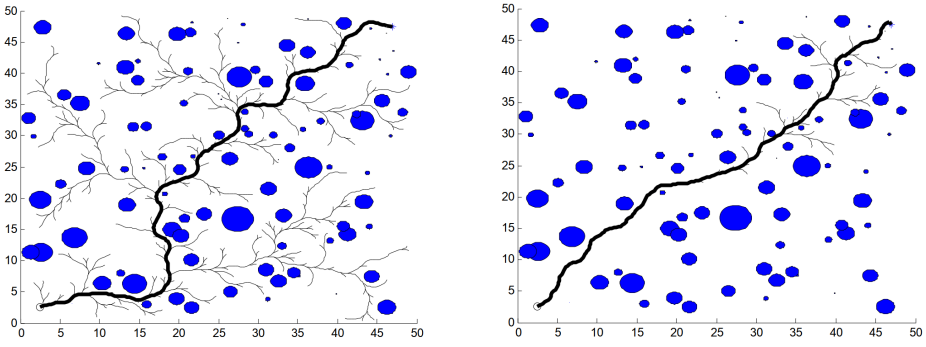

(a) (b)

Figure B.8: RRT and RRT-A* comparison by [Li+14]. (a) RRT. (b) RRT-A*.

A*-RRT & A*-RRT* These algorithms, developed by [BBS13], work in two phases. First, A* is used to find an initial path in a low-dimensional space (not

considering the complete state space), avoiding hazardous areas or obstacles and preferring low-risk routes. Then, this initial path focuses the RRT or RRT* search around it in the continuous high-dimensional space, optimizing the path. This strategy reduces the exploration of the free space, obtaining smaller trees, profit from the characteristics of A* at the grid resolution chosen and from the probabilistically completeness of RRT. The authors successfully applied this method to a tank-like mobile robot in rough terrain.

Theta*-RRT (Θ*-RRT) Following the same idea, [PKA16], presented the Θ*-RRT algorithm. This algorithm combines (discrete) any-angle search with (continuous) RRT. It improves the efficiency of RRT in high-dimensional spaces substantially by adding the properties of the any-angle pathfinding (Figure B.9). Θ*-RRT comes at the cost of having to find an any-angle path first, but the runtime of the discrete search is negligible compared to the overall planning time. Θ*-RRT normally produces shorter paths than A*-RRT or A*-RRT* as the inital path is already shorter.

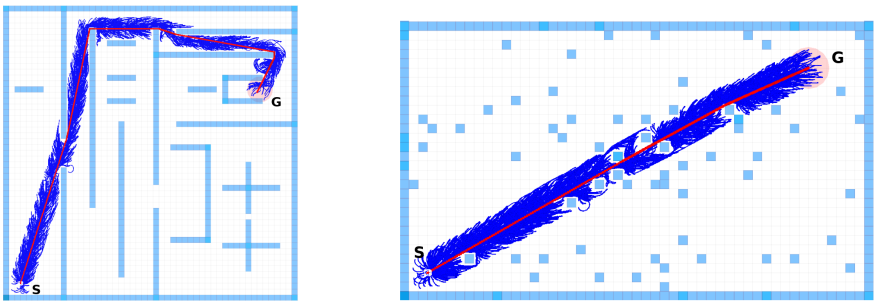

(a) (b)

Figure B.9: RRT and RRT-A* comparison by [PKA16]. (a) RRT. (b) RRT-A*.

RRT^X RRT^X, developed by [OF16], is an asymptotically optimal RRT for dynamic and static environments. RRT^X calculates an initial plan, then continually refines it toward the optimal solution during navigation, while also repairing the tree if an obstacle affects it. RRT^X uses the same graph/tree even when obstacles change it, remodeling and repairing the tree instead of pruning disconnected branches. RRT^X achieves a quick reaction time in dynamic environments by maintaining an "ϵ-consistent graph", a constant neighborhood size at each node, and then using rewiring methods to transfer information through the graph whenever obstacles affect the tree. RRT^X transfer information (and thus reaction time) is faster than RRT*.

RRT*-Sukharev vertices (RRT*-SV) The RRT*-SV, developed by [VMG19], uses two different sampling strategies for RRT*: the spatial distributions of samples based on Sukharev grids; and the application of samples defined by the convex vertices of the safety "hulls" of the obstacles (Figure B.10). The safety hull is a region that confines the whole body of an obstacle, with its vertices defined at a certain safety distance from the obstacle edges. Sukharev grid is part of a group of point dispersion approaches called low sampling, a way of generating a grid in space. The Sukharev grid achieves the most uniform distribution possible over the navigation environment. In the RRT*-SV sampling process, three attempts are made to generate a new sample. First, from the convex vertices of the safety hulls of the obstacles. If this is not possible, a new attempt is made through the Sukharev grid. Finally, randomly, as in the standard RRT. This order is logical, as the shortest path normally passes near the obstacles (first try), if it is not possible, then the optimal grid us used to cover the space efficiently (second try), and lastly, as a last resort, a random choice is made (third try). RRT*-SV was proven to plan shorter paths in less time than RRT*-Smart and RRT*.

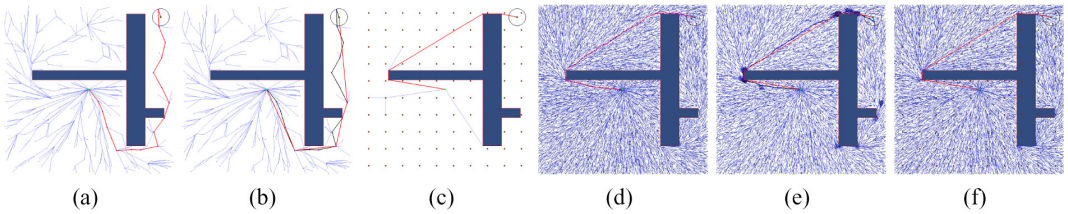

Figure B.10: Difference of RRT*-SV by [VMG19]. ((a) high level) First path planned by (a) RRT* in iteration 457. (b) RRT*-Smart in iteration 457. (c) RRT*-SV in iteration 10. Iteration 30 000 of each algorithm is shown in (d), (e), and (f). ((b) high level) RRT*, RRT*-Samrt and RRT*-SV comparison.

B.2.2.1 Probabilistic Road Map (PRM) & PRM*

PRM algorithm was developed by Kavraki in [Kav+96]. The PRM takes random samples from the free space and use a local planner to connect these samples to other nearby samples without collisions. The starting and goal locations are added to form a graph of the free space. A graph search algorithm is then applied to determine a path between the starting and goal locations (Figure B.11). PRM is probabilistically complete. The question turns into how to sample the free space, how to determine the nearby samples and what local planner use to connect the samples.

To connect samples, the standard solution is to use a straight line. To check if there is a collision on this line, two methods have been used: incremental and binary methods [GO04]. In the incremental method, small steps are taken along

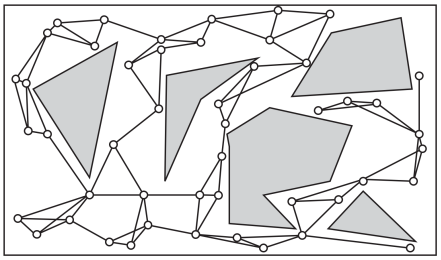

Figure B.11: PRM example with obstacles and with $k = 3$ nearest neighbors to connect the samples [LP17].

the path from start to goal. Each step is evaluated for collision. In the binary method the middle position along the path is checked first. If it is collision-free, the middle positions of the new path segments are checked, and so on until a step distance from the goal. The binary method have been found to work better as the middle point has higher probability to be in a collision [GO04].

How to detemine nearby samples is important for the PMR, as it defines the graph connection. On one hand, each nearest test is expensive, so it is better to minimize their number. On the other hand, if too few nearest test are performed, the graph will be loosely connected. The nearest-n (or k) technique has been shown to be efficient [GO04]. It tries to connect the new sample to the nearest n nodes in the graph. Another option is to use a fixed radius r around the new sample. The existing sample inside this radius are considered to be possible connections, and the algorithm starts with the closest one.

Finally, to sample the free space, multiple approaches are found in the literature: random, grid and Halton sequences. Additional techniques to refine the representation could be added, like gaussian sampling [GO04]. In the random approach, a sample is created by choosing random values from a probability distribution in all directions. The sample is added when it is inside the free space. In the grid approach the free space is represented as a grid and the samples are chosen from it. The Halton sequence, similarly to Monte Carlo simulations, uses this known sequence to generate points in space. The gaussian sampling add more samples near obstacles. This has been shown to increase performance in obstacle-dense environments [LP17]. It takes two random samples, where the distance between the samples is chosen according to a Gaussian distribution. The two samples are added only if one of the samples lies in free space and the other lies in an obstacle.

PRM* [KF11] presented an improved version of PRM called PRM*. This algorithm uses a variable radius $r(n)$ to connect the random samples, with n the total number of samples. Any node that falls within the radius value becomes

connected, making the graph a lot denser than the classical PRM. In the same work, the authors presented the nearest-k PRM*, analogously, setting $k(n)$, which produces a less dense graph but improving the PRM (Figure B.12). Both algorithms were proven to be probabilistically complete and asymptotically optimal.

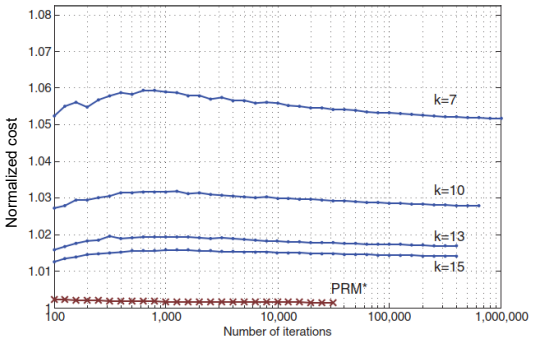

Figure B.12: Comparison between k-nearest PRM and PRM*. PRM* always finds a better route even when PRM uses a high number for k [KF11].

Appendix C

Dynamic model uncertainties and neglected phenomena

This section presents the neglected physical phenomena of the system. These assumptions have been made to optimize the execution and integration of the dynamic model into the trajectory algorithm.

C.1 Collision

Weir & Tallon partially based their study on Hertz's theory, which provides a good approximation for collisions between hard compact bodies where the contact region remains small in comparison to the size of either body [Str18]. In our case, the impact region of the MPM is a whole face of the $2\,\text{mm} \times 2\,\text{mm} \times 1.2\,\text{mm}$ MPM cube. This is not a small impact zone related to the size of the MPM. This means that the impact waves transiting the MPM could influence more than the described theory and equations, as well as increasing the plasticity of the impact.

Another possibility is a non-controlled rotation of the MPM during a switch, meaning that the impact would not be a plane-plane collision with the silicon structure. The leading cube edge would collide first, then the trailing edge, the last one accelerated by the driving force *and* the reaction force of the first impact.

C.2 Aerodynamic drag

The aerodynamic drag caused by the air inside the EDA's cavity on the MPM is estimated as follows: the aerodynamic drag force is modeled by the equation [Whi98]:

$$\vec{F}_{drag} = \frac{S_x \rho_{air} v^2 C_x}{2} \tag{C.1}$$

With S_x the surface exposed to the air flux, ρ_{air} the air density, v the speed of the MPM and C_x the aerodynamic drag coefficient for the MPM shape. For a cylindrical cube traveling in a fluid with Reynolds number $\geq 10^4$, $C_x = 2.1$ [Whi98]. ρ_{air} at 20 °C, 1 atm pressure (101.325 kPa) is 1.204 kg m^{-3} [Whi98].

To evaluate the maximum impact speed of the EDA the next elements are considered: the stroke value of the EDA (S) is 200 µm; the maximum driving force is 1.22 N A^{-1}; the mass of the MPM is 34 mg. Ignoring the magnetic and friction forces and supposing that all the driving force is transformed to mechanical momentum ($F = ma$), the maximum speed follows the formula $v_{max} = \sqrt{2aS}$. The maximum current from the V-to-I converters is 10 A (assuming a PCB resistance of 1 Ω). This yields an impact speed of 0.38 m s^{-1}.

The maximum impact speed produces an aerodynamic drag force of $\vec{F}_{drag} = 7.3 \times 10^{-7}$ N (this is 241 times smaller than the electromagnetic force for 1 A). In the light of this analysis, the aerodynamic drag is neglected.

C.3 Magnetization loss due to heat and impacts

The MPM impacts the wall cavity at the end of its movement at each displacement step. The DAA executes multiple displacements steps for its conveyance operation. At each impact, some kinetic energy of the impacting magnet is transferred to elastic deformation of the MPM and the silicon wall, which is then released as kinetic energy again, generating the rebound effect already explained. Some kinetic energy of the impact, in contrast, is transformed into plastic deformation of the magnet and silicon wall and this increases the internal energy of the MPM. The absorbed energy can disperse the magnetic domains of the MPM through heat and mechanic deformation and the MPM looses some of its magnetization value. The lifetime or working limit of the EDA is unknown, i.e., how the magnet looses its magnetization as a function of the number and speed of impacts is unknown. Joule effect heat of the actuating wires is transmitted to the MPM through the contacting PCB and glass layer. This heat can also increase the internal energy of the MPM and affect the magnetic domains.

C.4 Triboelectric effect of the EDA

Due to the relative movement between the MPM and the glass and silicon surfaces of the EDA, a possible triboelectric effect could develop. To assess this influence, multiple individual MPMs were rubbed against individual silicon and glass surfaces for 1 min. After the rubbing time, the same silicon and glass surfaces

were approached to the rubbed magnet. No attractive force was detected, between the bodies. Even after contact between the bodies, the magnet did not attach to any. This indicates that the triboelectric effect of the EDA is negligible.

C.5 Homogeneity hypothesis

The dynamic model assumes that all EDAs in the DAA are identical, homogeneous and distribute the mass of the conveyed object equally. Then, the displacement step is the sum of the efforts of each actuating EDA on the conveyed object. These assumptions mean that each step is identical under equal control conditions. In reality, fabrication and ambient variability produce heterogeneity among the EDAs. This can be in the form of surface and contact differences (friction and rebound), magnetization variability in the magnet construction (magnetic force), or misalignment of the PCB wires with the EDA cavities (electromagnetic force). All these are uncertainty sources for the dynamic model.

Appendix D

Additional results

D.1 Materials

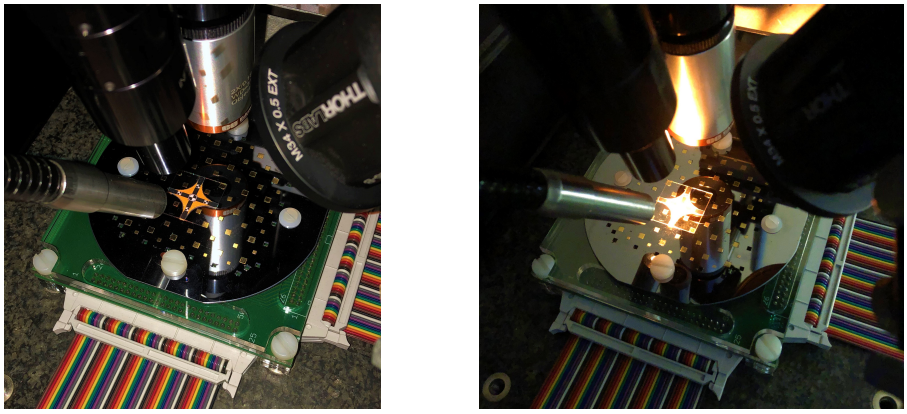

(a) (b)

Figure D.1: MPM and object kinematics on a 2×2 DAA experimental photos.

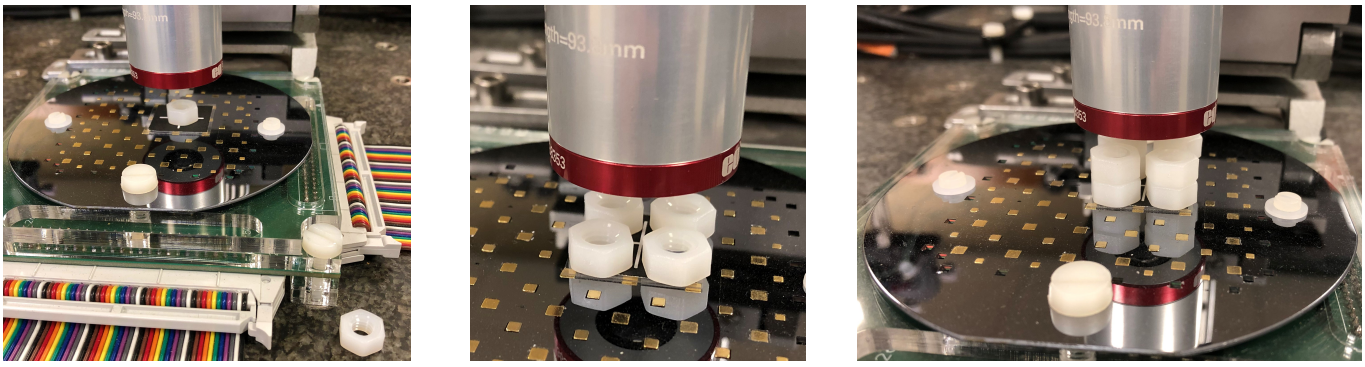

(a) (b) (c)

Figure D.2: Conveyed mass vs minimum driving current intensity on a 2×2 DAA experimental photos.

D.2 Conveyed object displacement results

D.2.1 Driving & holding current intensities influence

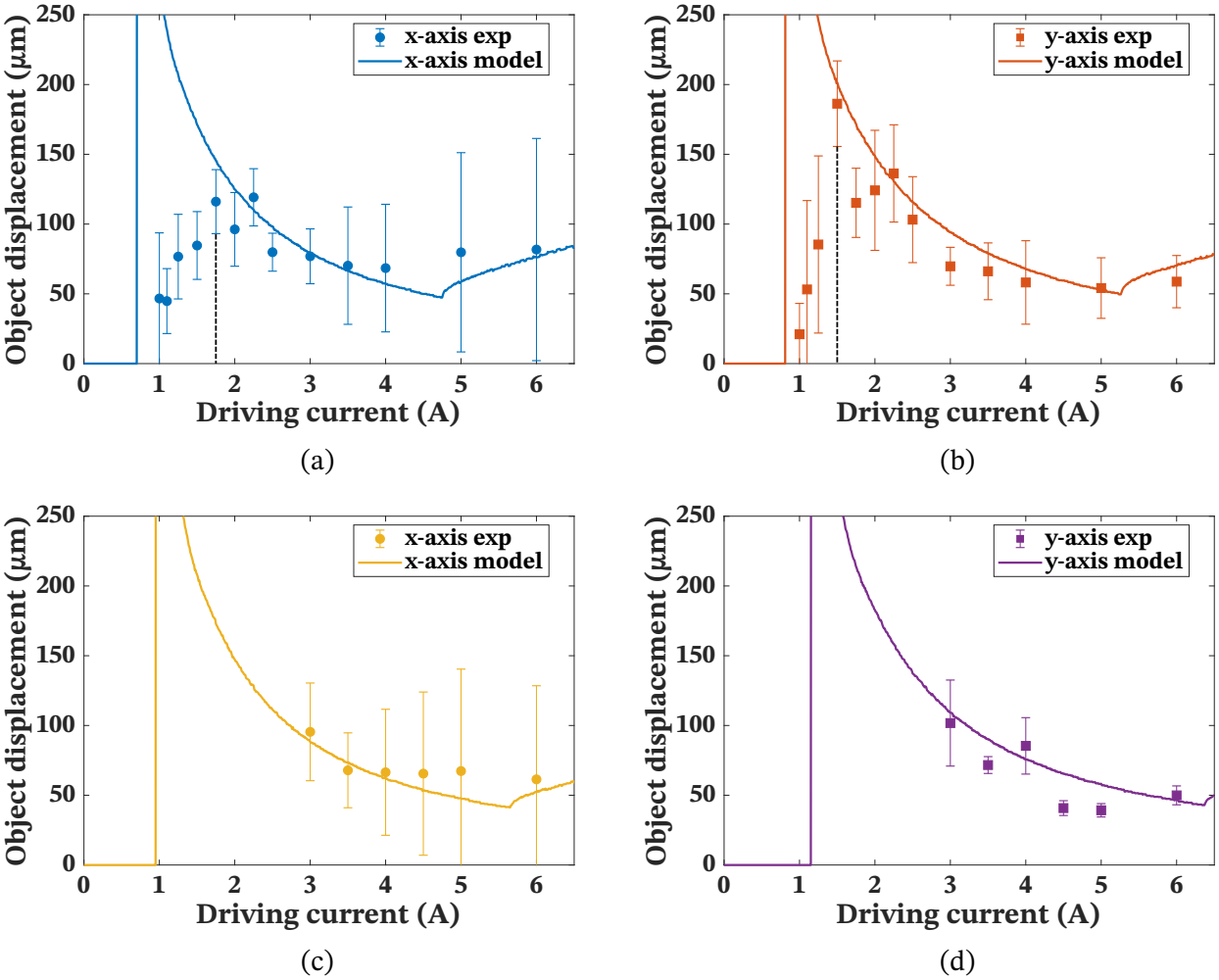

Figure D.3: Conveyed object displacement vs driving current intensity on the 3×3 DAA. (a) x-axis no holding current. (b) y-axis no holding current. (c) x-axis $I_h = -1$ A. (d) y-axis $I_h = -1$ A.

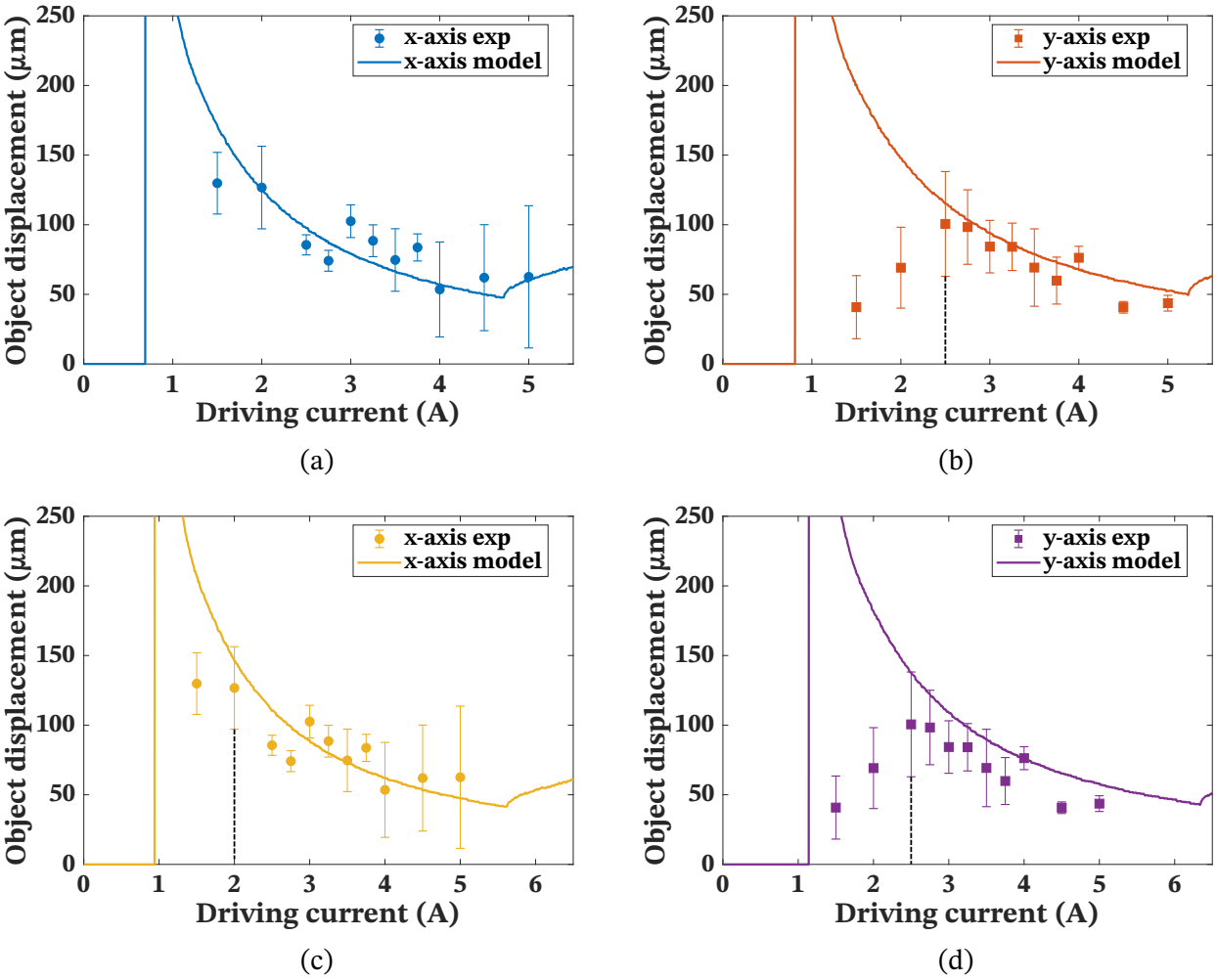

Figure D.4: Conveyed object displacement vs driving current intensity on the 4×4 DAA. (a) x-axis no holding current. (b) y-axis no holding current. (c) x-axis $I_h = -1$ A. (d) y-axis $I_h = -1$ A.

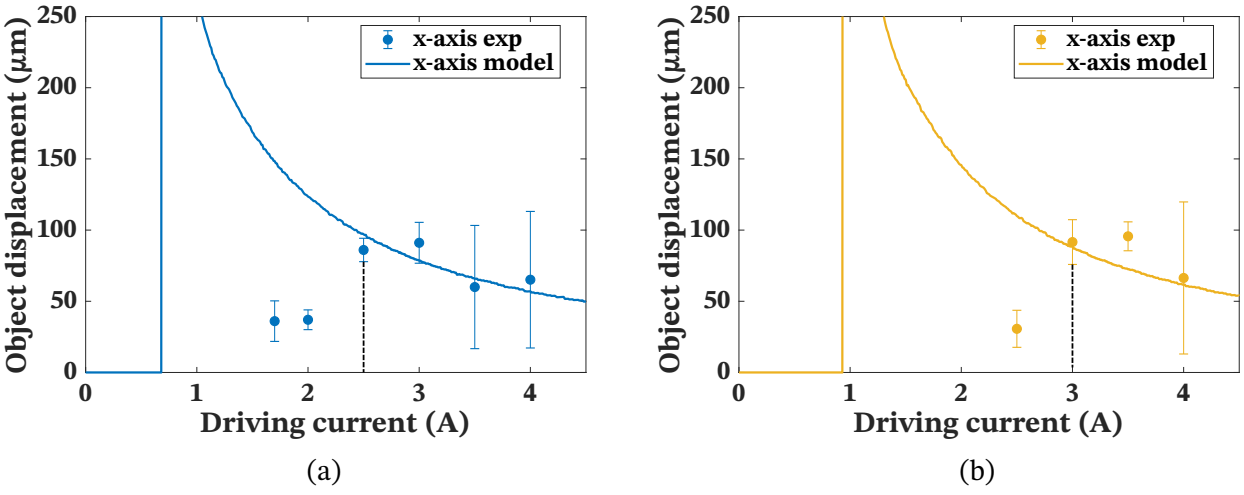

Figure D.5: Conveyed object displacement vs driving current intensity on the 5×5 DAA. (a) x-axis no holding current. (b) x-axis $I_h = -1$ A.

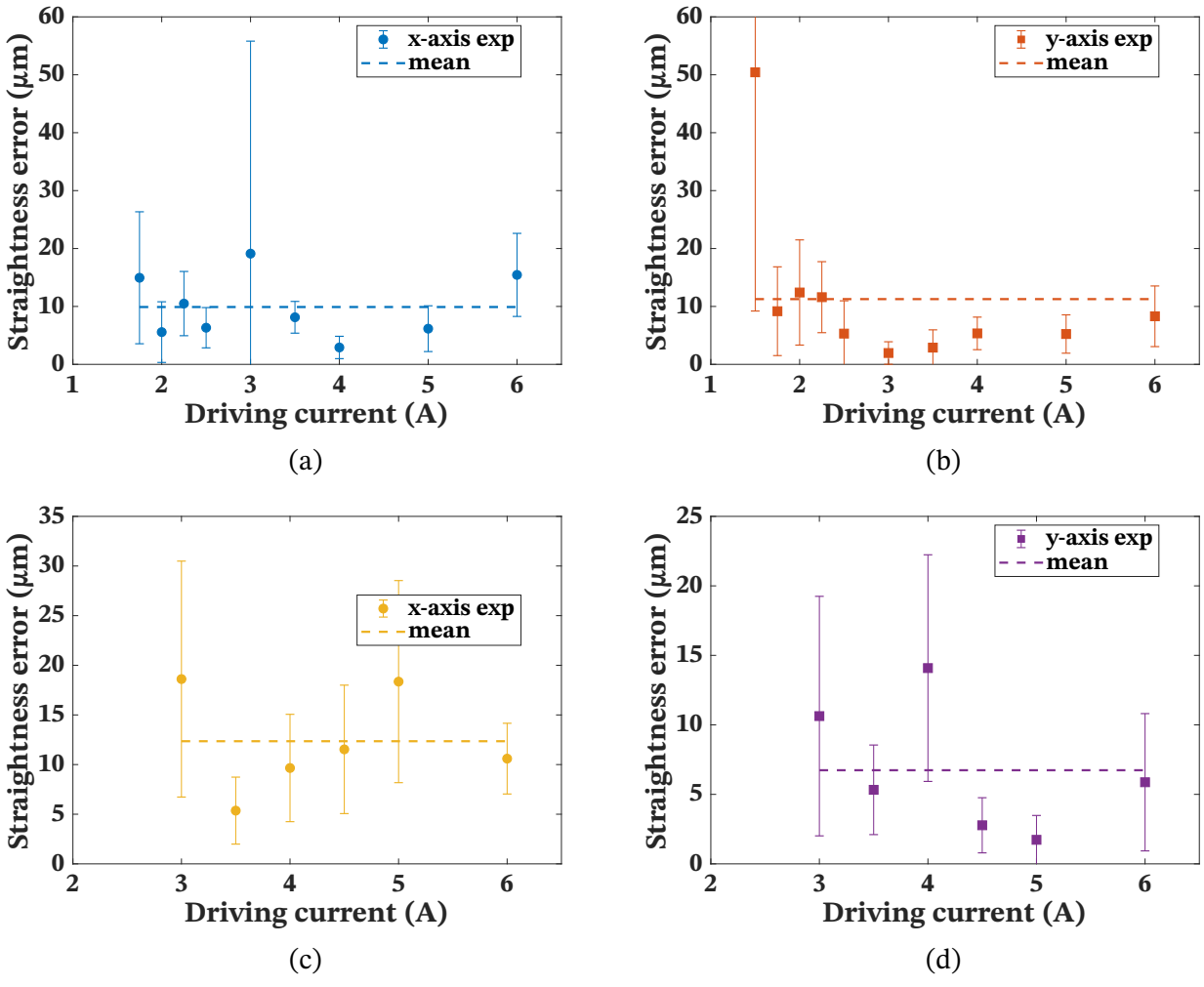

Figure D.6: Conveyed object displacement straightness error (involuntary y-axis displacement) vs driving current intensity on the 3×3 DAA. (a) x-axis no holding current. (b) y-axis no holding current. (c) x-axis $I_h = -1$ A. (d) y-axis $I_h = -1$ A.

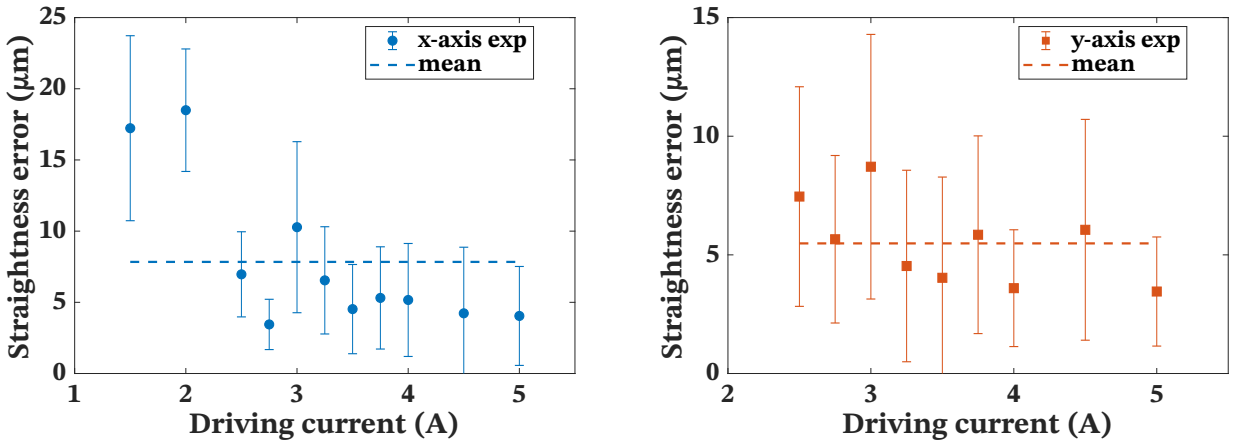

(a)

(b)

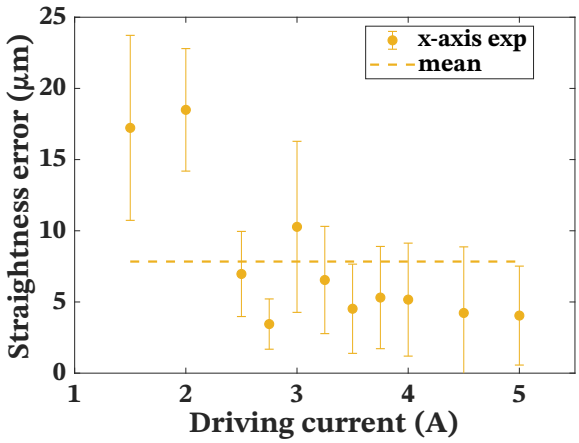

(c)

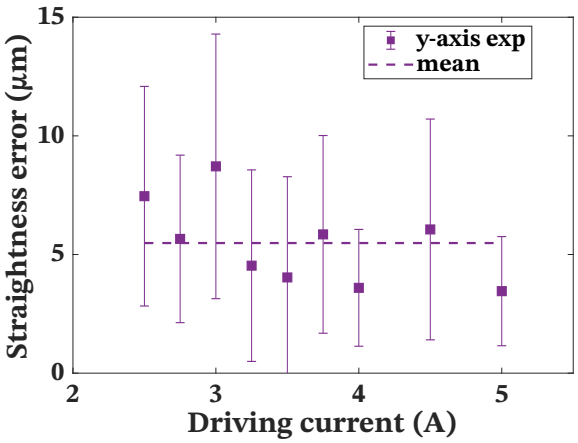

(d)

Figure D.7: Conveyed object displacement straightness error (involuntary y-axis displacement) vs driving current intensity on the 4×4 DAA. (a) x-axis no holding current. (b) y-axis no holding current. (c) x-axis $I_h = -1$ A. (d) y-axis $I_h = -1$ A.

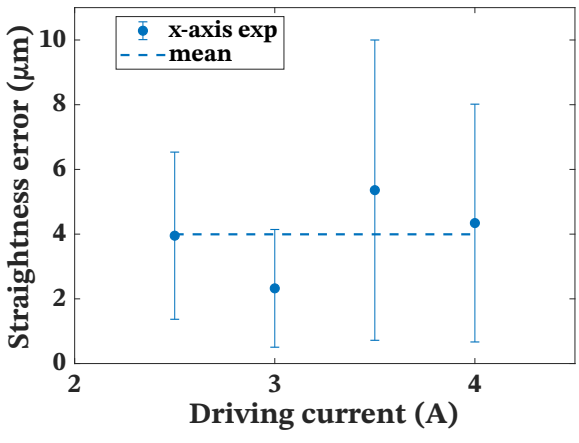

(a)

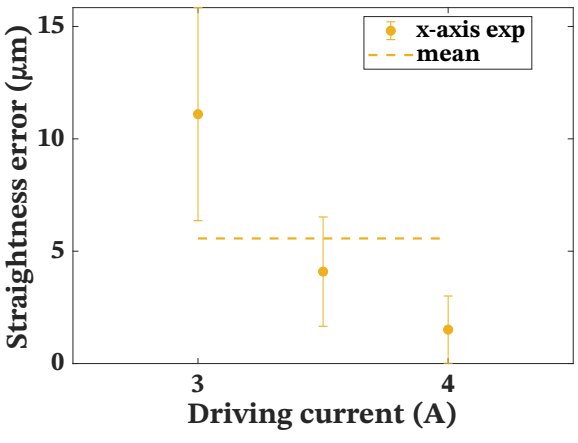

(b)

Figure D.8: Conveyed object displacement straightness error (involuntary y-axis displacement) vs driving current intensity on the 5×5 DAA. (a) x-axis no holding current. (b) x-axis $I_h = -1$ A.

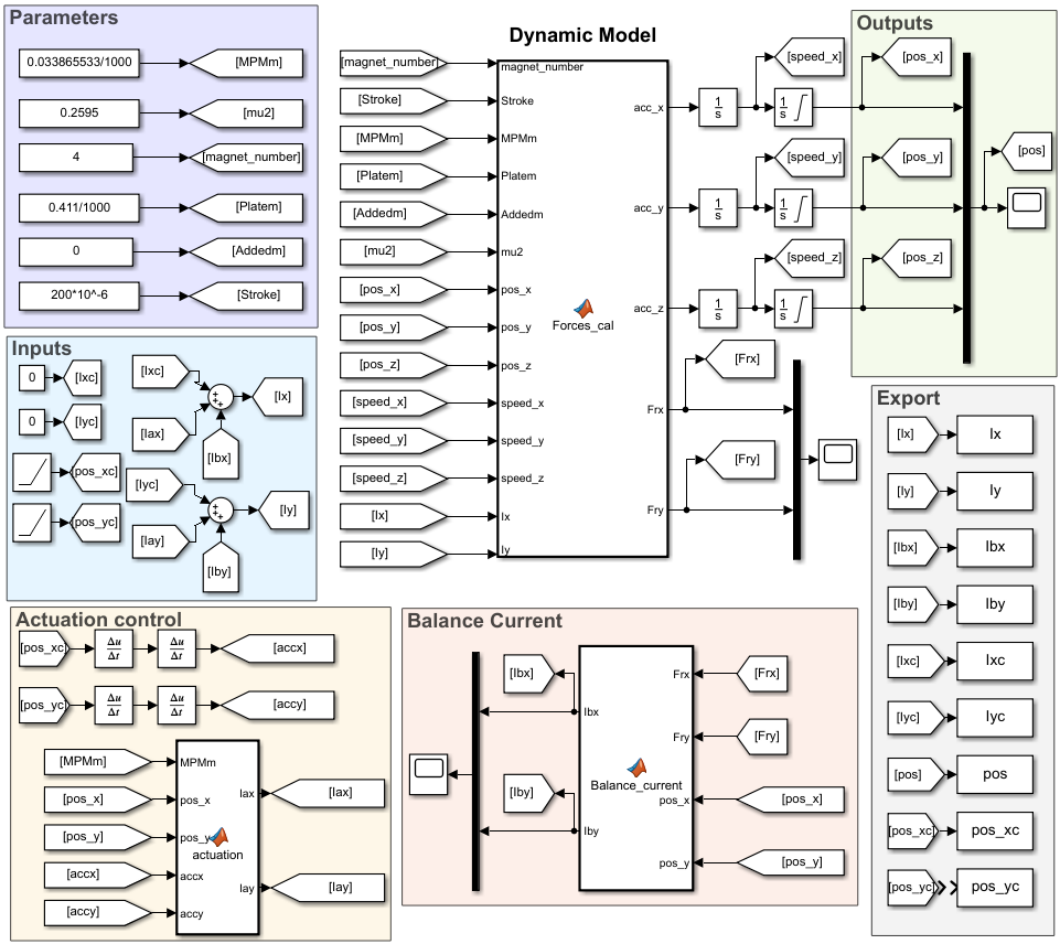

Figure D.9: Simulink implementation.

Appendix E

Bibliography

[ADD94] Brian Armstrong-Hélouvry, Pierre Dupont, and Carlos Canudas De Wit. "A survey of models, analysis tools and compensation methods for the control of machines with friction". In: *Automatica* 30.7 (1994), pp. 1083–1138. ISSN: 00051098. DOI: 10.1016/0005-1098(94)90209-7. arXiv: 94[0005-1098].

[Al-+04] Farid Al-Bender et al. "A novel generic model at asperity level for dry friction force dynamics". In: *Tribology Letters* 16.1-2 (2004), pp. 81–92. ISSN: 08880611. DOI: 10.1115/1.3167042.

[Al-10] Farid Al-Bender. "Fundamentals of Friction Modelling". In: *ASPE Spring Topical Meeting on Control of Precision Systems* (2010), pp. 117–122. ISSN: 0036-8733. DOI: 10.1361/asmhba000.

[All+19] Micah Allen et al. "Raincloud plots: A multi-platform tool for robust data visualization." In: *Wellcome Open Research* 4 (2019), pp. 1–41. ISSN: 2398502X. DOI: 10.12688/wellcomeopenres.15191.1.

[ALS05] Farid Al-Bender, Vincent Lampaert, and Jan Swevers. "The generalized Maxwell-slip model: A novel model for friction simulation and compensation". In: *IEEE Transactions on Automatic Control* 50.11 (2005), pp. 1883–1887. ISSN: 00189286. DOI: 10.1109/TAC.2005.858676.

[Aro+19] Neha Arora et al. "Design and Development of a Planar Electromagnetic Conveyor for the Microfactory". In: *IEEE/ASME Transactions on Mechatronics* 24.4 (2019), pp. 1723–1731.

[AW09] David P. Arnold and Naigang Wang. "Permanent magnets for MEMS". In: *Journal of Microelectromechanical Systems* 18.6 (2009), pp. 1255–1266. ISSN: 10577157. DOI: 10.1109/JMEMS.2009.2034389.

[BA94] M. T. Bengisu and A. Akay. "Stability of friction-induced vibrations in multi-degree-of-freedom systems". In: *Journal of Sound and Vibration* 171.4 (1994), pp. 557–570.

[Ban+19] Kaustubh Banerjee et al. "A 37-actuator polyimide deformable mirror with electrostatic actuation for adaptive optics microscopy". In: *Journal of Micromechanics and Microengineering* 29.8 (2019). ISSN: 13616439. DOI: 10.1088/1361-6439/ab2370.

[BBS13] Michael Brunner, Bernd Bruggemann, and Dirk Schulz. “Hierarchical rough terrain motion planning using an optimal sampling-based method”. In: *Proceedings - IEEE International Conference on Robotics and Automation* (2013), pp. 5539–5544. ISSN: 10504729. DOI: 10.1109/ICRA.2013.6631372.

[BC11] Douglas Brown and Wolfgang Christian. “Simulating What You See: Combining computer modeling with video analysis”. In: *MPTL 16 and HSCI 2011*. Ljubljana, Slovenia, 2011.

[Bis06] Robert H. Bishop. *Mechatronics: An introduction*. 2006, pp. 1–312. ISBN: 9781420037241. DOI: 10.1201/9781420037241.

[Boo07] Martin J. Booth. “Adaptive optics in microscopy”. In: *Philosophical Transactions of the Royal Society A: Mathematical, Physical and Engineering Sciences* 365.1861 (2007), pp. 2829–2843. ISSN: 1364-503X. DOI: 10.1098/rsta.2007.0013.

[Bor06] Alberto Borboni. “Microactuators”. In: *MEMS: Applications*. Ed. by Mohamed Gad-el-Hak. Boca Raton, FL: CRC Press Taylor & Francis Group, LLC, 2006. Chap. 5.

[Bor08] Alberto Borboni. *Meso- to micro- actuators: A theoretical and practical approach*. CRC Press Taylor & Francis Group, LLC, 2008, pp. 1–400. ISBN: 9781420008579.

[Boy+15] Eli Boyarski et al. “ICBS: Improved conflict-based search algorithm for multi-agent pathfinding”. In: *IJCAI International Joint Conference on Artificial Intelligence* 2015-Janua.Ijcai (2015), pp. 740–746. ISSN: 10450823.

[Bro20] Douglas Brown. *Tracker: Video analysis and modeling tool*. 2020.

[Can+95] C. Canudas de Wit et al. “A new model for control of systems with friction”. In: *IEEE Transactions on Automatic Control* 40.3 (1995), pp. 419–425. ISSN: 00189286. DOI: 10.1109/9.376053.

[CD14] T. Chai and R. R. Draxler. “Root mean square error (RMSE) or mean absolute error (MAE)? -Arguments against avoiding RMSE in the literature”. In: *Geoscientific Model Development* 7.3 (2014), pp. 1247–1250. ISSN: 19919603. DOI: 10.5194/gmd-7-1247-2014.

[CEC98] Oleg Chubar, Pascal Elleaume, and Joel Chavanne. “A three-dimensional magnetostatics computer code for insertion devices”. In: *Journal of Synchrotron Radiation* 5.3 (1998), pp. 481–484. ISSN: 09090495. DOI: 10.1107/S0909049597013502.

[Che+18] Xirui Chen et al. “Development of a contactless air conveyor system for transporting and positioning planar objects”. In: *Micromachines* 9.10 (2018). ISSN: 2072666X. DOI: 10.3390/mi9100487.

[CHL13] Vincent Chalvet, Yassine Haddab, and Philippe Lutz. “A microfabricated planar digital microrobot for precise positioning based on bistable modules”. In: *IEEE Transactions on Robotics* 29.3 (2013), pp. 641–649. ISSN: 15523098. DOI: 10.1109/TRO.2013.2240174.

[Cho+13] Dong Jin Cho et al. “Novel electromagnetic actuator using a permanent magnet and an inter-locking mechanism for a magnetic switch”. In: *IEEE Transactions on Magnetics* 49.5 (2013), pp. 2229–2232. ISSN: 00189464. DOI: 10.1109/TMAG.2013.2242432.

[Çol+12] Arzu Çolak et al. “Surface adhesion and its dependence on surface roughness and humidity measured with a flat tip”. In: *Applied Surface Science* 258.18 (2012), pp. 6938–6942. ISSN: 01694332. DOI: 10.1016/j.apsusc.2012.03.138.

[CP12] Patrick Chouinard and Jean Sébastien Plante. “Bistable antagonistic dielectric elastomer actuators for binary robotics and mechatronics”. In: *IEEE/ASME Transactions on Mechatronics* 17.5 (2012), pp. 857–865. ISSN: 10834435. DOI: 10.1109/TMECH.2011.2135862.

[Dah68] Philip R. Dahl. *A Solid Friction Model*. Tech. rep. 1968.

[Dah76] Philip R. Dahl. “Solid friction damping of mechanical vibrations”. In: *AIAA Journal* 14.12 (1976), pp. 1675–1682. ISSN: 00011452. DOI: 10.2514/3.61511.

[DAV10] Kris De Moerlooze, Farid Al-Bender, and Hendrik Van Brussel. “A generalised asperity-based friction model”. In: *Tribology Letters* 40.1 (2010), pp. 113–130. ISSN: 10238883. DOI: 10.1007/s11249-010-9645-x.

[DB17] Richard C Dorf and Robert H Bishop. *Modern control systems*. Pearson, 2017.

[Des20] Ajinkya Deshmukh. “Design and Realization of a 3D Digital Electromagnetic Micro-actuator Array for Conveyance Application”. PhD thesis. Université de Technologie de Compiegne, 2020, p. 148.

[Dij59] E.W Dijkstra. “A Note on Two Problems in Connexion with Graphs”. In: *Numerische Mathematik* 1 (1959), pp. 269–271. ISSN: 00426989. DOI: 10.1016/0042-6989(66)90039-3.

[DPS11] Dzung Viet Dao, Phuc Hong Pham, and Susumu Sugiyama. “Multimodule micro transportation system based on electrostatic comb-drive actuator and ratchet mechanism”. In: *Journal of Microelectromechanical Systems* 20.1 (2011), pp. 140–149. ISSN: 10577157. DOI: 10.1109/JMEMS.2010.2090503.

[DSX16] Zhicong Deng, Martin Stommel, and Weiliang Xu. “A novel soft machine table for manipulation of delicate objects inspired by caterpillar locomotion”. In: *IEEE/ASME Transactions on Mechatronics* 21.3 (2016), pp. 1702–1710. ISSN: 10834435. DOI: 10.1109/TMECH.2016.2519333.

[ECC98] P Elleaume, O. Chubar, and J Chavanne. “Computing 3D magnetic fields from insertion devices”. In: *Proceedings of the 1997 Particle Accelerator Conference (Cat. No.97CH36167)*. Vol. 3. IEEE, 1998, pp. 3509–3511. ISBN: 0-7803-4376-X. DOI: 10.1109/PAC.1997.753258.

[Ell12] Neil Ellerington. “3 DoF, long range planar lift and slice micro-conveyor with vision-based control system”. PhD Thesis. Dalhousie University, Halifax, Nova Scotia, 2012, p. 228. ISBN: 9788578110796. DOI: 10.1017/CBO9781107415324.004. arXiv: arXiv:1011.1669v3.

[Fan+15] S. Fanget et al. “Low Voltage MEMS Digital Loudspeaker Array Based on Thin-film PZT Actuators”. In: *Physics Procedia: 2015 International Congress on Ultrasonics*. Vol. 70. Metz, 2015, pp. 983–986. DOI: 10.1016/j.phpro.2015.08.205.

[FAO12] Ohmi Fuchiwaki, Kazushi Arafuka, and Suguru Omura. “Development of 3-DOF inchworm mechanism for flexible, compact, low-inertia, and omnidirectional precise positioning: Dynamical analysis and improvement of the maximum velocity within no slip of electromagnets”. In: *IEEE/ASME Transactions on Mechatronics* 17.4 (2012), pp. 697–708. ISSN: 10834435. DOI: 10.1109/TMECH.2011.2118764.

[Fir+18] Miguel Bande Firvida et al. “Decentralized omnidirectional route planning and reservation for highly flexible material flow systems with small-scaled conveyor modules”. In: *IEEE International Conference on Emerging Technologies and Factory Automation, ETFA* 2018-September (2018), pp. 685–692. ISSN: 19460759. DOI: 10.1109/ETFA.2018.8502655.

[FL12] J. Fleischer and U. Leberle. “Miniaturized piezoelectric vibratory conveyor for the flexible handling of very different small parts”. In: *Proceedings of the 12th International Conference of the European Society for Precision Engineering and Nanotechnology, EUSPEN 2012* 2.June (2012), pp. 59–62.

[FNU18] Katsushi Furutani, Yusuke Nakamura, and Akira Urita. “Conveyance Method of Thin Plate by Using Multiple-phase Air Flow”. In: *Electronics and Communications in Japan* 101.2 (2018), pp. 51–60. ISSN: 19429541. DOI: 10.1002/ecj.12044.

[For06] Sepehr Forouzanfar. “Micro-electro-thermo-magnetic Actuators for MEMS Applications”. Master Thesis. Univeristy of Waterloo, 2006.

[Fur01] Edward P. Furlani. *Permanent Magnet And Electromagnetical Devices*. Ed. by Isaak Mayergoyz. Elsevier, 2001.

[Gab+19] Ran Gabai et al. “A Contactless Stage Based on Near-Field Acoustic Levitation for Object Handling and Positioning-Concept, Design, Modeling, and Experiments”. In: *IEEE/ASME Transactions on Mechatronics* 24.5 (2019), pp. 1954–1963.

[Gao+19] Yang Gao et al. “A Planar Single-Actuator Bi-Stable Switch Based on Latch-Lock Mechanism”. In: *2019 20th International Conference on Solid-State Sensors, Actuators and Microsystems & Eurosensors XXXIII (TRANSDUCERS & EUROSENSORS XXXIII)*. June. IEEE, June 2019, pp. 705–708. ISBN: 978-1-5386-8104-6. DOI: 10.1109/TRANSDUCERS.2019.8808375.

[Gar07] Federico Garcia. “LATEX and the different bibliography styles”. In: *The PracTEX Journal* (2007), pp. 1–14.

[GC15] Amitabha Ghosh and Burkhard Corves. *Introduction to Micromechanisms and Microactuators*. Ed. by Marco Ceccarelli. Springer, 2015. ISBN: 9788132221432.

[Geu18] Laura Geukens. “Development of a miniaturized conveyor driven by electrowetting”. PhD thesis. Katholieke Universiteit Leuven, 2018.

[Gin18] Ginolis Ltd. *Xanthia Desktop automation platform*. 2018.

[Gin20] Ginolis Ltd. *Ginolis Ltd*. 2020.

[Gko+18] A. Gkouzou et al. “Friction and dynamically dissipated energy dependence on temperature in polycrystalline silicon MEMS devices”. In: *Microsystem Technologies* 24.4 (2018), pp. 1899–1907. ISSN: 09467076. DOI: 10.1007/s00542-017-3575-6.

[GO04] Roland Geraerts and Mark H. Overmars. “A comparative study of probabilistic roadmap planners”. In: *Springer Tracts in Advanced Robotics* 7 STAR (2004), pp. 43–57. ISSN: 16107438. DOI: 10.1007/978-3-540-45058-0_4.

[Gol+12] Meir Goldenberg et al. “A * Variants for Optimal Multi-Agent Pathfinding”. In: *Multiagent Pathfinding AAAI*. 2012, pp. 19–25. ISBN: 9781577355847.

[Gol+14] Meir Goldenberg et al. “Enhanced partial expansion A*”. In: *Journal of Artificial Intelligence Research* 50 (2014), pp. 141–187. ISSN: 10769757.

[Gol01] Werner Goldsmith. *Impact: The Theory and Physical Behaviour of Colliding Solids*. Dover Publications Inc., 2001, p. 461. ISBN: 978-0486420042.

[Gri05] David J. Griffiths. *Introduction to Electrodynamics*. Vol. 73. 6. 2005, pp. 574–574. ISBN: 9780321856562. DOI: 10.1119/1.4766311.

[Gue+17] Valerian Guelpa et al. “Modular Contact-Free Conveyors for Handling Planar Fragile Objects”. In: *IEEE Transactions on Robotics* 33.1 (2017), pp. 92–101. ISSN: 15523098. DOI: 10.1109/TRO.2016.2623340.

[HC75] K. H. Hunt and F. R.E. Crossley. “Coefficient of Restitution Interpreted As Damping in Vibroimpact.” In: *American Society of Mechanical Engineers (Paper)* 75 -APM-H (1975), pp. 440–445. ISSN: 04021215.

[Her+19] Etienne Herth et al. “Fast ultra-deep silicon cavities: Toward isotropically etched spherical silicon molds using an ICP-DRIE”. In: *Journal of Vacuum Science & Technology B* 37.2 (Mar. 2019), p. 021206. ISSN: 2166-2746. DOI: 10.1116/1.5081503.

[HFA97] J E Huber, N A Fleck, and M F Ashby. “The selection of mechanical actuators”. In: *Proceedings of the Royal Society of London. Series A: Mathematical, Physical and Engineering Sciences* 453.1965 (1997), pp. 2185–2205. DOI: 10.1098/rspa.1997.0117.

[HG11] Daniel Harabor and Alban Grastien. “Online Graph Pruning for Pathfinding On Grid Maps”. In: *25th AAAI Conference on Artificial Intelligence*. San Francisco, CA, 2011, pp. 1114–1119. ISBN: 9781577355090. DOI: http://dx.doi.org/10.1016/j.nmd.2014.06.416.

[HG12] Daniel Harabor and Alban Grastien. “The JPS Pathfinding System”. In: *Fifth Annual Symposium on Combinatorial Search*. Niagara Falls, Canada, 2012, pp. 207–208.

[Hir12] J. E. Hirsch. “The origin of the Meissner effect in new and old superconductors”. In: *Physica Scripta* 85.3 (2012). ISSN: 00318949. DOI: 10.1088/0031-8949/85/03/035704. arXiv: 1201.0139.

[HNR68] Peter E Hart, Nils J. Nilsson, and Bertram Raphael. “Formal Basis for the Heuristic Determination of Minimum Cost Paths”. In: *IEEE Transactions of Systems Science and Cybernetics* SSC-4.2 (1968), pp. 100–107.

[HS06] Philip Holmes and Eric Shea-Brown. “Stability”. In: *Scholarpedia* 1.10 (2006), p. 1838. ISSN: 1941-6016. DOI: 10.4249/scholarpedia.1838.

[Hsu02] Tai-ran Hsu. “Miniaturization. A paradigm shift in advanced manufacturing and education”. In: *2002 IEEE/ASME International conference on Advanced Manufacturing Technologies and Education in the 21st Century* (2002), pp. 1–19.

[Hus+18] Hussein Hussein et al. “Design and fabrication of novel discrete actuators for microrobotic tasks”. In: *Sensors and Actuators, A: Physical* 271 (2018), pp. 373–382. ISSN: 09244247. DOI: 10.1016/j.sna.2017.12.065.

[Hus15] Hussein Hussein. “Contribution to Digital Microrobotics: Modeling, Design and Fabrication of Curved Beams, U-shaped Actuators and Multistable Microrobots”. Doctoral Thesis. Université de Franche-Comté, 2015.

[Huy15] Pengfei Huyan. “Réseau d’actionneurs électromagnétiques numériques : caractérisation d’une application de type convoyage et conception optimisée”. Doctoral Thesis. Université de Technologie de Compiègne, 2015.

[HYH15] Takuya Hosobata, Akio Yamamoto, and Toshiro Higuchi. “Transparent Synchronous Electrostatic Actuator for Long-Stroke Planar Motion”. In: *IEEE/ASME Transactions on Mechatronics* 20.4 (2015), pp. 1765–1776. ISSN: 10834435. DOI: 10.1109/TMECH.2014.2353815.

[IF97] Tetsuhiko Iizuka and Hiroyuki Fujita. “Precise Positioning of a Micro Conveyor based on Superconducting Magnetic Levitation”. In: *International Symposium on Micromechanics and Human Science (Cat. No.97TH8311)*. Nagoya, Japan: IEEE, 1997, pp. 131–135. ISBN: 0780341716. DOI: 10.1109/MHS.1997.768870.

[Iiz+94] Tetsuhiko Iizuka et al. “Micro X-Y-Theta conveyor by superconducting magnetic levitation”. In: *IEEE Symposium on Emerging Technologies & Factory Automation* (1994), pp. 62–67. DOI: 10.1109/etfa.1994.402022.

[IM18] Shunsuke Izuhara and Tomoaki Mashimo. “Design and evaluation of a micro linear ultrasonic motor”. In: *Sensors and Actuators, A: Physical* 278 (2018), pp. 60–66. ISSN: 09244247. DOI: 10.1016/j.sna.2018.05.022.

[ISF09] Tetsuhiko Iizuka, Naomichi Sakai, and Hiroyuki Fujita. “Position feedback control using magneto impedance sensors on conveyor with superconducting magnetic levitation”. In: *Sensors and Actuators, A: Physical* 150.1 (2009), pp. 110–115. ISSN: 09244247. DOI: 10.1016/j.sna.2008.12.014.

[Isl+12] Fahad Islam et al. “RRT*-Smart: Rapid convergence implementation of RRT* towards optimal solution”. In: *2012 IEEE International Conference on Mechatronics and Automation, ICMA 2012*. Chengdu, China, 2012, pp. 1651–1656. ISBN: 9781467312776. DOI: 10.1109/ICMA.2012.6284384.

[Jac99] John David Jackson. *Classical electrodynamics*. 3rd ed. New York, NY: Wiley, 1999. ISBN: 9780471309321.

[Jan04] H. Janocha. *Actuators Basics and Applications*. First Edit. New York: Springer, 2004, p. 343. ISBN: 9783662055878.

[Jär+15] Eeva Järvenpää et al. “Micro-factories”. In: *Micromanufacturing Engineering and Technology: Second Edition*. Ed. by Yi Qin. Second Edi. William Andrew Publishing, 2015. Chap. Chapter 23, pp. 549–579. ISBN: 9780323312677. DOI: 10.1016/B978-0-323-31149-6.00023-2.

[JLK15] In-Bae Jeong, Seung-Jae Lee, and Jong-Hwan Kim. “RRT*-Quick: A Motion Planning Algorithm with Faster Convergence Rate”. In: *Robot Intelligence Technology and Applications 3. Advances in Intelligent Systems and Computing*. Ed. by Jong-Hwan Kim et al. Vol. 345. Advances in Intelligent Systems and Computing. Cham: Springer International Publishing, 2015, pp. 67–76. ISBN: 978-3-319-16840-1. DOI: 10.1007/978-3-319-16841-8_7.

[Joh85] K. L. Johnson. *Contact Mechanics*. Cambridge, Massachusetts - London, England: Cambridge University Press, 1985, p. 462. ISBN: 0 521 25576 7.

[Jot20] Jot Automation. *JOT V4 Assembly Cell*. 2020.

[KA19] Georgia Kritikou and Nikos Aspargathos. “Micro – Manipulation Methods And Assembly Of Hexagonal Microparts On A Programmable Platform With Electrostatic Forces”. In: *International Journal of Mechanics and Control* 20.1 (2019), pp. 71–80. ISSN: 15908844.

[Kav+96] Lydia E. Kavraki et al. “Probabilistic roadmaps for path planning in high-dimensional configuration spaces”. In: *IEEE Transactions on Robotics and Automation* 12.4 (1996), pp. 566–580. ISSN: 1042296X. DOI: 10.1109/70.508439.

[Ken10] B. J. Kenton. “Design, characterization, and control of a high bandwidth serial-kinematic nanopositioning stage for scanning probe microscopy applications”. Master’s Thesis. University of Nevada, 2010.

[KF11] Sertac Karaman and Emilio Frazzoli. “Sampling-based algorithms for optimal motion planning”. In: *International Journal of Robotics Research* 30.7 (2011), pp. 846–894. ISSN: 02783649. DOI: 10.1177/0278364911406761.

[Kit+19] P. Kitisri et al. “Simulation and measurement of electromagnetic undulator prototype for production of THz radiation”. In: *Journal of Physics: Conference Series* 1380.1 (2019). ISSN: 17426596. DOI: 10.1088/1742-6596/1380/1/012078.

[Kit04] Charles Kittel. *Introduction to Solid State Physics, 8th edition*. 8th Editio. New York: Wiley & Sons, 2004.

[KKF89] Yongkwon Kim, Makoto Katsurai, and Hiroyuki Fujita. “A proposal for a superconducting actuator using meissner effect”. In: *IEEE Micro Electro Mechanical Systems, , Proceedings, ’An Investigation of Micro Structures, Sensors, Actuators, Machines and Robots’*. Salt Lake City, UT, USA: IEEE, 1989.

[KKF90] Yong-Kweon Kim, Makoto Katsurai, and Hiroyuki Fujita. “Fabrication and Testing of a Micro Superconducting Actuator Using the Meissner Effect”. In: *Micro Electro Mechanical Systems, An Investigation of Micro Structures, Sensors, Actuators, Machines and Robots.* Napa Valley, CA, USA: IEEE, 1990.

[KL02a] S Koenig and M Likhachev. “Incremental A*”. In: *Advances in Neural Information Processing Systems 14 (NIPS 2001)*. Vancouver, Canada, 2002, pp. 1539–1546. DOI: 10.1093/bioinformatics/bts279.

[KL02b] Sven Koenig and Maxim Likhachev. “Star lite.D* Lite”. In: *Eighteenth national conference on Artificial intelligence*. Edmonton, Canada, 2002, pp. 476–483.

[KL05] Sven Koenig and Maxim Likhachev. “Fast replanning for navigation in unknown terrain”. In: *IEEE Transactions on Robotics* 21.3 (2005), pp. 354–363. ISSN: 15523098. DOI: 10.1109/TRO.2004.838026.

[KLA18] Georgia Kritikou, Nikos Lamprianidis, and Nikos Aspragathos. “A modified cooperative A* algorithm for the simultaneous motion of multiple microparts on a ”Smart Platform” with electrostatic fields”. In: *Micromachines* 9.11 (2018). ISSN: 2072666X. DOI: 10.3390/mi9110548.

[KOS16] S. B. Kim, S. Ozasa, and M. Sawae. “Dynamic Characteristics of a 3-D Superconducting Actuator with Arranged Permanent Magnets and Electromagnets”. In: *IEEE Transactions on Applied Superconductivity* 26.4 (2016), pp. 3–6. ISSN: 10518223. DOI: 10.1109/TASC.2016.2536440.

[KSO16] S. B. Kim, M. Sawae, and S. Ozasa. “Study of the Dynamic Properties of HTS Bulk Movers for Traveling Along Vertical Walls as a Three-Dimensional Actuator”. In: *IEEE Transactions on Applied Superconductivity* 26.4 (2016), pp. 5–8. ISSN: 10518223. DOI: 10.1109/TASC.2016.2535665.

[KV19] Jaap Kokorian and W. Merlijn Van Spengen. “Corrigendum: Improved analysis and visualization of friction loop data: Unraveling the energy dissipation of meso-scale stick-slip motion (Measurement Science and Technology (2017) 28 (115011) DOI: 10.1088/1361-6501/aa870a)”. In: *Measurement Science and Technology* 30.9 (2019). ISSN: 13616501. DOI: 10.1088/1361-6501/ab1d19.

[KZ19] Ervin Kamenar and Saša Zelenika. “Issues in validation of pre-sliding friction models for ultra-high precision positioning”. In: *Proceedings of the Institution of Mechanical Engineers, Part C: Journal of Mechanical Engineering Science* 233.3 (2019), pp. 997–1006. ISSN: 20412983. DOI: 10.1177/0954406218758797.

[LA12] Panos Lazarou and Nikos A. Aspragathos. *Mechatronics and manufacturing engineering: Research and development*. Ed. by J. Paulo Davim. Woodhead Publishing in Mechanical Engineering, 2012, p. 345. ISBN: 9780857091512.

[Lau+14] Guillaume J. Laurent et al. “Micropositioning and fast transport using a contactless micro-conveyor”. In: *Micromachines* 5.1 (2014), pp. 66–80. ISSN: 2072666X. DOI: 10.3390/mi5010066.

[LaV98] Steven M. LaValle. “Rapidly-Exploring Random Trees: A New Tool for Path Planning”. In: (1998).

[LC18] Lijie Li and Zheng J. Chew. “Microactuators: Design and Technology”. In: *Smart Sensors and MEMS: Intelligent Sensing Devices and Microsystems for Industrial Applications: Second Edition*. Elsevier Ltd, 2018. Chap. 12, pp. 313–354. ISBN: 9780081020562. DOI: 10.1016/B978-0-08-102055-5.00012-7.

[LCZ20] Yiheng Lin, Xirui Chen, and Wei Zhong. “Positioning of planar objects on an air film using a viscous traction principle”. In: *2019 IEEE 8th International Conference on Fluid Power and Mechatronics (FPM)*. IEEE, Apr. 2020, pp. 50–59. ISBN: 978-1-7281-0311-2. DOI: 10.1109/fpm45753.2019.9035757.

[Le +16] G. Le Bec et al. “High gradient quadrupoles for low emittance storage rings”. In: *Physical Review Accelerators and Beams* 19.5 (2016), pp. 1–13. ISSN: 24699888. DOI: 10.1103/PhysRevAccelBeams.19.052401.

[Leh+19] Philipp Lehman et al. *The BibLaTeX alphabetic style*. 2019. arXiv: 0307200v3 [arXiv:math].

[LF13] U. Leberle and J. Fleischer. "Automated modular part-flexible feeding system for micro parts". In: *Proceedings of the 13th International Conference of the European Society for Precision Engineering and Nanotechnology, EUSPEN 2013* 2.May (2013), pp. 27–29.

[LHM19] Jianping Li, Hu Huang, and Takeshi Morita. "Stepping piezoelectric actuators with large working stroke for nano-positioning systems: A review". In: *Sensors and Actuators, A: Physical* 292 (2019), pp. 39–51. ISSN: 09244247. DOI: 10.1016/j.sna.2019.04.006.

[Li+14] Jiadong Li et al. "RRT-A? Motion planning algorithm for non-holonomic mobile robot". In: *Proceedings of the SICE Annual Conference*. Hokkaido, Japan, 2014, pp. 1833–1838. ISBN: 9784907764463. DOI: 10.1109/SICE.2014.6935304.

[Li+17] Muhua Li et al. "Design and fabrication of a low insertion loss capacitive RF MEMS switch with novel micro-structures for actuation". In: *Solid-State Electronics* 127 (2017), pp. 32–37. ISSN: 00381101. DOI: 10.1016/j.sse.2016.10.004.

[Li+19] Jiaoyang Li et al. "Improved heuristics for multi-agent path finding with conflict-based search". In: *IJCAI International Joint Conference on Artificial Intelligence* 2019-Augus.2 (2019), pp. 442–449. ISSN: 10450823. DOI: 10.24963/ijcai.2019/63.

[LK01a] Steven M. LaValle and James J. Kuffner. "Randomized kinodynamic planning". In: *International Journal of Robotics Research* 20.5 (2001), pp. 378–400. ISSN: 02783649. DOI: 10.1177/02783640122067453.

[LK01b] Steven M. LaValle and James J. Kuffner. "Rapidly-Exploring Random Trees: Progress and Prospects". In: *Algorithmic and Computational Robotics: New Directions* 5 (2001), pp. 293–308.

[ŁK16] Grzegorz Łukaszewicz and Piotr Kalita. *Navier–Stokes Equations*. Advances in Mechanics and Mathematics. Cham: Springer International Publishing, 2016. ISBN: 978-3-319-27758-5. DOI: 10.1007/978-3-319-27760-8.

[LP17] Kevin Lynch and Frank Park. *Modern Robotics: Mechanics, PLanning and Control*. May. Cambridge University Press, 2017, p. 188. ISBN: 9781107156302.

[LSA02] Vincent Lampaert, Jan Swevers, and Farid Al-Bender. "Modification of the Leuven integrated friction model structure". In: *IEEE Transactions on Automatic Control* 47.4 (2002), pp. 683–687. ISSN: 00189286. DOI: 10.1109/9.995050.

[LSK19] Mousa Lahdo, Tom Ströhla, and Sergej Kovalev. "Design and Implementation of an New 6-DoF Magnetic Levitation Positioning System". In: *IEEE Transactions on Magnetics* 55.12 (2019), pp. 4–10. ISSN: 19410069. DOI: 10.1109/TMAG.2019.2936394.

[Mac+12] Margarida Machado et al. "Compliant contact force models in multibody dynamics: Evolution of the Hertz contact theory". In: *Mechanism and Machine Theory* 53 (2012), pp. 99–121. ISSN: 0094114X. DOI: 10.1016/j.mechmachtheory.2012.02.010.

[Mal+19] Dhiman Mallick et al. “Magnetic performances and switching behavior of Co-rich CoPtP micro-magnets for applications in magnetic MEMS”. In: *Journal of Applied Physics* 125.2 (2019). ISSN: 10897550. DOI: 10.1063/1.5063860.

[Mar+16] Filipe Marques et al. “A survey and comparison of several friction force models for dynamic analysis of multibody mechanical systems”. In: *Nonlinear Dynamics* 86.3 (2016), pp. 1407–1443. ISSN: 1573269X. DOI: 10.1007/s11071-016-2999-3.

[May03] Isaak Mayergoyz. *Mathematical models of hysteresis and their applications*. Elsevier, 2003, p. 498. ISBN: 978-0-12-480873-7.

[MC06] Keizo Miyahara and Gregory S. Chirikjian. “Optimal base placement for a discretely actuated robotic manipulator (D-ARM)”. In: *2006 IEEE International Conference on Mechatronics and Automation, ICMA 2006* 2006 (2006), pp. 159–164. DOI: 10.1109/ICMA.2006.257489.

[MFM17] Mohammad Maroufi, Anthony G. Fowler, and S. O.Reza Moheimani. “MEMS for Nanopositioning: Design and Applications”. In: *Journal of Microelectromechanical Systems* 26.3 (2017), pp. 469–500. ISSN: 10577157. DOI: 10.1109/JMEMS.2017.2687861.

[MGK18] Lior Medina, Rivka Gilat, and Slava Krylov. “Bistability criterion for electrostatically actuated initially curved micro plates”. In: *International Journal of Engineering Science* 130 (2018), pp. 75–92. ISSN: 00207225. DOI: 10.1016/j.ijengsci.2018.05.006.

[MH19] Frieder Mugele and Jason Heikenfeld. *Electrowetting: Fundamental Principles and Practical Applications*. Weinheim, Germany: Wiley, 2019, p. 299. ISBN: 978-3-527-41229-7.

[Mis+02] Nozomu Mishima et al. “Design of a Microfactory”. In: *ASME 2002 Design Engineering Technical Conferences and Computer and Information Engineering Conference*. Montreal, Canada, 2002. ISBN: 8129861720.

[Miy11] Keizo Miyahara. “Distributed-controlled multiagent mobile platform with digital actuation concept for space applications”. In: *Journal of Aerospace Engineering* 24.3 (2011), pp. 389–396. ISSN: 08931321. DOI: 10.1061/(ASCE)AS.1943-5525.0000066.

[MK06] Ilju Moon and Joonwon Kim. “Using EWOD (electrowetting-on-dielectric) actuation in a micro conveyor system”. In: *Sensors and Actuators, A: Physical* 130-131.SPEC. ISS. (2006), pp. 537–544. ISSN: 09244247. DOI: 10.1016/j.sna.2005.12.016.

[MKD17] Frantisek Mach, Martin Kurfirt, and Ivo Dolezel. “Bistable Fully Electromagnetic Valve for High-Speed and Fail-Safe Operations”. In: *IEEE Transactions on Industrial Electronics* 66.1 (2017), pp. 349–357. ISSN: 0278-0046. DOI: 10.1109/TIE.2017.2767522.

[MT09] Tomoaki Mashimo and Shigeki Toyama. “Rotary-linear piezoelectric actuator using a single stator”. In: *IEEE Transactions on Ultrasonics, Ferroelectrics, and Frequency Control* 56.1 (2009), pp. 114–120. ISSN: 08853010. DOI: 10.1109/TUFFC.2009.1010.

[Nak+20] M. Nakano et al. “PLD-fabricated Pr-Fe-B thick film magnets applied to small motors”. In: *AIP Advances* 10.1 (2020). ISSN: 21583226. DOI: 10.1063/1.5130004.

[Nas+07] A Nash et al. “Theta*: Any-Angle Path Planning on Grids”. In: *AAAI Conference on Artificial Intelligence*. Vancouver, Canada, 2007. DOI: 10.1613/jair.2994. arXiv: arXiv:1401.3843.

[Nas+10] A Nash et al. “Theta*: Any-Angle Path Planning on Grids”. In: *Journal of Artificial Intelligence Research* 39 (2010), pp. 533–579. ISSN: 1076-9757. DOI: 10.1613/jair.2994. arXiv: arXiv:1401.3843.

[Nas12] Alex Nash. “Any-Angle Path Planning”. Doctoral Thesis. University of Southern California, 2012, p. 258.

[Neu+10] Reimund Neugebauer et al. “Reconfigurable microfactory for the automated assembly of a novel piezo-metal- module”. In: *The 7th International Workshop on Microfactories*. October 2010. Daejeon, Korea, 2010.

[Nie+18] Jinhui Nie et al. “Self-Powered Microfluidic Transport System Based on Triboelectric Nanogenerator and Electrowetting Technique”. In: *ACS Nano* 12.2 (2018), pp. 1491–1499. ISSN: 1936086X. DOI: 10.1021/acsnano.7b08014.

[NK13] Vu Huy Nguyen and Won-jong Kim. “Design and Control of a Compact Light-Weight Planar Positioner Moving Over a Concentrated-Field Magnet Matrix”. In: *IEEE/ASME Transactions on Mechatronics* 18.3 (2013), p. 1090. DOI: 10.1115/DSCC2011-5962.

[NKD19] Milad Nazarahari, Esmaeel Khanmirza, and Samira Doostie. “Multi-objective multi-robot path planning in continuous environment using an enhanced genetic algorithm”. In: *Expert Systems with Applications* 115 (2019), pp. 106–120. ISSN: 09574174. DOI: 10.1016/j.eswa.2018.08.008.

[NKT10] A. Nash, S. Koenig, and C. Tovey. “Lazy Theta *: Any-Angle Path Planning and Path Length Analysis in 3D”. In: *Third Annual Symposium on Combinatorial Search (SOCS-10)*. Atlanta, GA, 2010, pp. 153–154. ISBN: 9781577354642.

[OF16] Michael Otte and Emilio Frazzoli. “RRTX: Asymptotically optimal single-query sampling-based motion planning with quick replanning”. In: *International Journal of Robotics Research* 35.7 (2016), pp. 797–822. ISSN: 17413176. DOI: 10.1177/0278364915594679.

[Ols+98] H. Olsson et al. “Friction Models and Friction Compensation”. In: *European Journal of Control* 4.October (1998), pp. 1–37. ISSN: 09473580.

[OMA04] Yuichi Okazaki, Nozomu Mishima, and Kiwamu Ashida. “Microfactory—Concept, History, and Developments”. In: *Journal of Manufacturing Science and Engineering* 126.4 (2004), p. 837. ISSN: 10871357. DOI: 10.1115/1.1823491.

[OMS19] Ulises Orozco-Rosas, Oscar Montiel, and Roberto Sepúlveda. “Mobile robot path planning using membrane evolutionary artificial potential field”. In: *Applied Soft Computing Journal* 77 (2019), pp. 236–251. ISSN: 15684946. DOI: 10.1016/j.asoc.2019.01.036.

[Oxf20] Oxford. *Hysteresis*. In: *Oxford Dictionary*. Oxford University Press, 2020.

[Pal10] William J. Palm III. *System dynamics*. Second. McGraw-Hill, 2010, p. 900. ISBN: ISBN 978–0–07–352927–1.

[Pat16] Amit Patel. *Introduction to the A* Algorithm*. 2016. URL: https://www.redblobgames.com/pathfinding/a-star/introduction.html (visited on 05/24/2020).

[PDD07] Jean-Sébastien Plante, Lauren M. Devita, and Steven Dubowsky. "A road to practical dielectric elastomer actuators based robotics and mechatronics: discrete actuation". In: *Electroactive Polymer Actuators and Devices (EAPAD) 2007* 6524 (2007), p. 652406. ISSN: 0277786X. DOI: 10.1117/12.715236.

[Pen+15] Yuxin Peng et al. "A review of long range piezoelectric motors using frequency leveraged method". In: *Sensors and Actuators, A: Physical* 235 (2015), pp. 240–255. ISSN: 09244247. DOI: 10.1016/j.sna.2015.10.015.

[Pen+16] Ettore Pennestrì et al. "Review and comparison of dry friction force models". In: *Nonlinear Dynamics* 83.4 (2016), pp. 1785–1801. ISSN: 1573269X. DOI: 10.1007/s11071-015-2485-3.

[Pet+15] Laurent Petit et al. "Design and Characterization of a High-Precision Digital Electromagnetic Actuator with Four Discrete Positions". In: *Actuators* 4.4 (2015), pp. 217–236. ISSN: 2076-0825. DOI: 10.3390/act4040217.

[Pet09] Laurent Petit. "Contribution aux techniques d'actionnement numérique Cas d'un système électromagnétique 2D". Doctoral Thesis. Université de Technologie de Compiègne, 2009, p. 196.

[Pet18] Laurent Petit. *Micro-actionneurs et microsystèmes : Méthodes et applications*. Master course. 2018.

[Pir+13] Benoît Piranda et al. "A new concept of planar self-reconfigurable modular robot for conveying microparts". In: *Mechatronics* 23.7 (2013), pp. 906–915. ISSN: 09574158. DOI: 10.1016/j.mechatronics.2013.08.009.

[PKA16] Luigi Palmieri, Sven Koenig, and Kai O. Arras. "RRT-based nonholonomic motion planning using any-angle path biasing". In: *Proceedings - IEEE International Conference on Robotics and Automation* 2016-June (2016), pp. 2775–2781. ISSN: 10504729. DOI: 10.1109/ICRA.2016.7487439.

[Pon05] José L. Pons. *Emerging Actuator Technologies, A Micromechatronic Approach*. 2005, pp. 1–275. ISBN: 0470091975. DOI: 10.1021/jm500475k.

[Pop17] Valentin L Popov. *Contact Mechanics and Friction*. Berlin, Heidelberg: Springer Berlin Heidelberg, 2017, pp. 55–70. ISBN: 978-3-662-53080-1. DOI: 10.1007/978-3-662-53081-8. arXiv: arXiv:1011.1669v3.

[PW19] Alissa Potekhina and Changhai Wang. "Review of electrothermal actuators and applications". In: *Actuators* 8.4 (2019). ISSN: 20760825. DOI: 10.3390/ACT8040069.

[Ras+17] Yadollah Rasekhipour et al. "A Potential Field-Based Model Predictive Path-Planning Controller for Autonomous Road Vehicles". In: *IEEE Transactions on Intelligent Transportation Systems* 18.5 (2017), pp. 1255–1267. ISSN: 15249050. DOI: 10.1109/TITS.2016.2604240.

[RHL09] Micky Rakotondrabe, Yassine Haddab, and Philippe Lutz. "Development , Modeling , and Control of a Stick – Slip Device". In: *IEEE/ASME Transactions on Mechatronics* 14.6 (2009), pp. 733–745. DOI: 10.1109/TMECH.2009.2011134.

[Rib+19] F. Ribet et al. “Zero-insertion-loss optical shutter based on electrowetting-on-dielectric actuation of opaque ionic liquid microdroplets”. In: *Applied Physics Letters* 115.7 (2019). ISSN: 00036951. DOI: 10.1063/1.5108936.

[RMP19] Saibal Roy, Dhiman Mallick, and Kankana Paul. “MEMS-Based Vibrational Energy Harvesting and Conversion Employing Micro-/Nano-Magnetics”. In: *IEEE Transactions on Magnetics* 55.7 (2019). ISSN: 19410069. DOI: 10.1109/TMAG.2019.2896105.

[Rob+19] Matthew A. Robertson et al. “A Compact modular soft surface with reconfigurable shape and stiffness”. In: *IEEE/ASME Transactions on Mechatronics* 24.1 (2019), pp. 16–24. ISSN: 10834435. DOI: 10.1109/TMECH.2018.2878621.

[Roh94] James William Rohlf. *Modern Physics from αlpha to Z0*. New York: John Wiley & Sons, 1994, p. 671.

[RSM06] Jonathan Rossiter, Boyko Stoimenov, and Toshiharu Mukai. “A self-switching bistable artificial muscle actuator”. In: *2006 SICE-ICASE International Joint Conference*. 2006, pp. 5847–5852. ISBN: 8995003855. DOI: 10.1109/SICE.2006.315374.

[Sha+13] Guni Sharon et al. “The increasing cost tree search for optimal multi-agent pathfinding”. In: *Artificial Intelligence* 195 (2013), pp. 470–495. ISSN: 00043702. DOI: 10.1016/j.artint.2012.11.006.

[Sha+15] Guni Sharon et al. “Conflict-based search for optimal multi-agent pathfinding”. In: *Artificial Intelligence* 219 (2015), pp. 40–66. ISSN: 00043702. DOI: 10.1016/j.artint.2014.11.006.

[Sha15] Guni Sharon. “Novel Search Techniques for Path Finding in Complex Environment”. PhD thesis. Ben-Gurion University, Negev, Beersheba, Israel, 2015.

[Shi17] Zhichao Shi. “Micro-actionneurs numériques en silicium pour la réalisation d’un micro-convoyeur”. PhD thesis. Université Paris-Saclay, 2017.

[Sho+16] Fumiya Shono et al. “Simulation of 3-axis state feedback controller with bang-bang control for positioning mechanism driven by 6 piezoelectric actuators”. In: *IEEE/ASME International Conference on Advanced Intelligent Mechatronics, AIM* 2016-Septe (2016), pp. 1533–1538. DOI: 10.1109/AIM.2016.7576988.

[Sil+11] Niko Siltala et al. “Modular microfactory system for gas sensor assembly”. In: *Proceedings - 2011 IEEE International Symposium on Assembly and Manufacturing, ISAM 2011* (2011). DOI: 10.1109/ISAM.2011.5942333.

[Sil05] D Silver. “Cooperative Pathfinding”. In: *AIIDE’05 Proceedings of the First AAAI Conference on Artificial Intelligence and Interactive Digital Entertainment*. Marina del Rey, California, 2005. ISBN: 1584504579.

[SK58] Henry Semat and Robert Katz. “Momentum and Impulse”. In: *Physics*. Robert Katz Publications, University of Nebraska-Lincoln, 1958. Chap. 10, p. 142.

[SS11] M. Staab and H. F. Schlaak. “Novel electrothermally actuated magnetostatic bistable microrelay for telecommunication applications”. In: *Proceedings of the IEEE International Conference on Micro Electro Mechanical Systems (MEMS)* (2011), pp. 1261–1264. ISSN: 10846999. DOI: 10.1109/MEMSYS.2011.5734662.

[SSB18] Luka Skrinjar, Janko Slavič, and Miha Boltežar. “A review of continuous contact-force models in multibody dynamics”. In: *International Journal of Mechanical Sciences* 145.July (2018), pp. 171–187. ISSN: 00207403. DOI: 10.1016/j.ijmecsci.2018.07.010.

[Ste94] Anthony Stentz. “Optimal and efficient path planning for partially known environments”. In: *Robotics and Automation, 1994. Proceedings., 1994 IEEE International Conference on* 3.1 (1994), pp. 3310–3317. ISSN: 10504729. DOI: 10.1109/ROBOT.1994.351061.

[Ste95] Anthony Stentz. “The focussed D* algorithm for real-time replanning”. In: *14th International Joint Conference on Artificial intelligence*. August. Montreal, Canada, 1995, pp. 1652–1659. ISBN: 1-55860-363-8. DOI: 10.1080/0305792950250302.

[Str18] W. J. Stronge. *Impact Mechanics*. Second Edi. Cambridge University Press, 2018, p. 384. ISBN: 9781139050227. DOI: 10.1017/9781139050227.

[Suz+16] Masato Suzuki et al. “A Bistable Comb-Drive Electrostatic Actuator Biased by the Built-In Potential of Potassium Ion Electret”. In: *Journal of Microelectromechanical Systems* 25.4 (2016), pp. 652–661. ISSN: 10577157. DOI: 10.1109/JMEMS.2016.2582215.

[Swe+00] Jan Swevers et al. “An integrated friction model structure with improved presliding behavior for accurate friction compensation”. In: *IEEE Transactions on Automatic Control* 45.4 (2000), pp. 675–686. ISSN: 00189286. DOI: 10.1109/9.847103.

[Swi20] Swisslog. *AutoStore*. 2020.

[SYS18] S. Mark Spearing, Leong Yee Mei, and G.K. Sujan. *Characteristics and Selection of Materials Used in Microelectromechanical Systems (MEMS)*. October 2017. Elsevier Ltd., 2018, pp. 1–10. ISBN: 9780128035818. DOI: 10.1016/b978-0-12-803581-8.01843-9.

[SZF18] Ethan W. Schaler, Tarek I. Zohdi, and Ronald S. Fearing. “Thin-film repulsive-force electrostatic actuators”. In: *Sensors and Actuators, A: Physical* 270 (2018), pp. 252–261. ISSN: 09244247. DOI: 10.1016/j.sna.2017.12.054.

[Tay05] John Robert Taylor. *Classical mechanics*. University Science Books, 2005.

[Ten+20] Peicheng Teng et al. “Recent progress of electrowetting for droplet manipulation: From wetting to superwetting systems”. In: *Materials Chemistry Frontiers* 4.1 (2020), pp. 140–154. ISSN: 20521537. DOI: 10.1039/c9qm00458k.

[The18] The Editors of Encyclopaedia Britannica. *Meissner effect*. 2018.

[Tho97] C Thornton. “Coefficient of Restitution for Collinear Collisions of Elastic-Perfectly Plastic Spheres”. In: *Journal of Applied Mechanics* 64.2 (1997), pp. 383–386. ISSN: 0021-8936. DOI: 10.1115/1.2787319.

[Tia+18] Xinqi Tian et al. “An Inchworm Type Piezoelectric Actuator Working in Resonant State”. In: *IEEE Access* 6 (2018), pp. 18975–18983. ISSN: 21693536. DOI: 10.1109/ACCESS.2018.2814010.

[Tia+20] Xinqi Tian et al. “A review on piezoelectric ultrasonic motors for the past decade: Classification, operating principle, performance, and future work perspectives”. In: *Sensors and Actuators, A: Physical* 306.92 (2020), p. 111971. ISSN: 09244247. DOI: 10.1016/j.sna.2020.111971.

[Tin96] Michael Tinkham. *Introduction to Superconductivity*. Second. New York: McGraw-Hill, 1996, p. 456. ISBN: 978-0-486-43503-9.

[Tri89] William Trimmer. "Microrobots and micromechanical systems". In: *Sensors and Actuators* 19.3 (1989), pp. 267–287.

[Tri97] William Trimmer. *The scaling of Micromechanical devices*. 1997.

[UPS18] John Joseph Uicker, G. R. Pennock, and Joseph Edward Shigley. *Theory of machines and mechanisms*. Oxford University Press, 2018.

[Uri+16] Claudio Uriarte et al. "Flexible automation of logistics processes by means of modular robotic and material flow systems". In: *Logistics Journal* (2016). ISSN: 18607977. DOI: 10.2195/lj_Proc_uriarte_de_201605_01.

[Uri+19] Claudio Uriarte et al. "Control strategies for small-scaled conveyor modules enabling highly flexible material flow systems". In: *Procedia CIRP* 79 (2019), pp. 433–438. ISSN: 22128271. DOI: 10.1016/j.procir.2019.02.117.

[Vak+18] A. I. Vakis et al. "Modeling and simulation in tribology across scales: An overview". In: *Tribology International* 125.November 2017 (2018), pp. 169–199. ISSN: 0301679X. DOI: 10.1016/j.triboint.2018.02.005.

[VMG19] Luiz G.D.O. Véras, Felipe L.L. Medeiros, and Lamartine N.F. Guimarães. "Rapidly exploring Random Tree* with a sampling method based on Sukharev grids and convex vertices of safety hulls of obstacles". In: *International Journal of Advanced Robotic Systems* 16.1 (2019), pp. 1–19. ISSN: 17298814. DOI: 10.1177/1729881419825941.

[VV15] Anders Strand-Holm Vinther and Magnus Strand-Holm Vinther. "Pathfinding in Two-dimensional Worlds". Master's Thesis. 2015.

[Wan+07] Kerwin Wang et al. "An electrostatic zigzag transmissive microoptical switch for MEMS displays". In: *Journal of Microelectromechanical Systems* 16.1 (2007), pp. 140–154. ISSN: 10577157. DOI: 10.1109/JMEMS.2006.888913.

[Wan+18a] Fujun Wang et al. "A Novel Actuator-Internal Micro/Nano Positioning Stage with an Arch-Shape Bridge Type Amplifier". In: *IEEE Transactions on Industrial Electronics* 66.12 (2018), pp. 9161–9172. ISSN: 02780046. DOI: 10.1109/TIE.2018.2885716.

[Wan+18b] Shupeng Wang et al. "A novel inchworm type piezoelectric rotary actuator with large output torque: Design, analysis and experimental performance". In: *Precision Engineering* 51.October 2017 (2018), pp. 545–551. ISSN: 01416359. DOI: 10.1016/j.precisioneng.2017.10.010.

[Wau01] Michel Wautelet. "Scaling laws in the macro-, micro-, and nanoworlds". In: *European Journal of Physics* 22 (2001), pp. 601–611.

[WC11] Glenn Wagner and Howie Choset. "M*: A complete multirobot path planning algorithm with optimality bounds". In: *IEEE/RSJ International Conference on Intelligent Robots and Systems*. Vol. 57 LNEE. San Francisco, CA: IEEE, 2011, pp. 167–181. ISBN: 9783642339707. DOI: 10.1007/978-3-642-33971-4_10. arXiv: /www.renhyd.org/index.php/renhyd/article/view/5/6 [http:].

[WCP14] Dung An Wang, Jyun Hua Chen, and Huy Tuan Pham. “A tristable compliant micromechanism with two serially connected bistable mechanisms”. In: *Mechanism and Machine Theory* 71 (2014), pp. 27–39. ISSN: 0094114X. DOI: 10.1016/j.mechmachtheory.2013.08.018.

[WDM17] James Wissman, Michael D. Dickey, and Carmel Majidi. “Field-Controlled Electrical Switch with Liquid Metal”. In: *Advanced Science* 4.12 (2017). ISSN: 21983844. DOI: 10.1002/advs.201700169.

[Whi98] Frank M. White. *Fluid Mechanics*. Fourth. McGraw-Hill, 1998.

[Woj+08] Jerzy Wojewoda et al. “Hysteretic effects of dry friction: modelling and experimental studies”. In: *Philosophical Transactions of the Royal Society A: Mathematical, Physical and Engineering Sciences* 366.1866 (2008), pp. 747–765. ISSN: 1364503X. DOI: 10.1098/rsta.2007.2125.

[WT05] Graham Weir and Stephen Tallon. “The coefficient of restitution for normal incident, low velocity particle impacts”. In: *Chemical Engineering Science* 60.13 (2005), pp. 3637–3647. ISSN: 00092509. DOI: 10.1016/j.ces.2005.01.040.

[WT18] Masahiro Watanabe and Hideyuki Tsukagoshi. “Flexible sheet actuator that generates bidirectional traveling waves”. In: *IEEE/ASME International Conference on Advanced Intelligent Mechatronics, AIM* 2018-July (2018), pp. 328–333. DOI: 10.1109/AIM.2018.8452700.

[Xu+19a] Fengqiu Xu et al. “Development and validation of numerical magnetic force and torque model for magnetically levitated actuator”. In: *IEEE Transactions on Magnetics* 55.1 (2019), pp. 1–9. ISSN: 00189464. DOI: 10.1109/TMAG.2018.2879872.

[Xu+19b] Fengqiu Xu et al. “Motion Control of a Magnetic Levitation Actuator Based on a Wrench Model Considering Yaw Angle”. In: *IEEE Transactions on Industrial Electronics* 0046.c (2019), pp. 1–1. ISSN: 0278-0046. DOI: 10.1109/tie.2019.2949519.

[Xu+20] Jiale Xu et al. “Fabrication and characterization of SMA film actuator array with bias spring for high-power MEMS tactile display”. In: *Microelectronic Engineering* 227.March (2020), p. 111307. ISSN: 01679317. DOI: 10.1016/j.mee.2020.111307.

[Yah+12] Réda Yahiaoui et al. “A MEMS-based pneumatic micro-conveyor for planar micromanipulation”. In: *Mechatronics* 22.5 (2012), pp. 515–521. ISSN: 09574158. DOI: 10.1016/j.mechatronics.2011.04.005.

[YL16] Jingjin Yu and Steven M. LaValle. “Optimal Multirobot Path Planning on Graphs: Complete Algorithms and Effective Heuristics”. In: *IEEE Transactions on Robotics* 32.5 (2016), pp. 1163–1177. ISSN: 15523098. DOI: 10.1109/TRO.2016.2593448.

[Yon+12] Y. K. Yong et al. “Invited review article: High-speed flexure-guided nanopositioning: Mechanical design and control issues”. In: *Review of Scientific Instruments* 83.12 (2012). ISSN: 00346748. DOI: 10.1063/1.4765048.

[YT14] Jun Young Yoon and David L. Trumper. “Friction modeling, identification, and compensation based on friction hysteresis and Dahl resonance”. In: *Mechatronics* 24.6 (2014), pp. 734–741. ISSN: 09574158. DOI: 10.1016/j.mechatronics.2014.02.006.

[Zan13] Andrew Zangwill. *Modern Electrodynamics*. Cambridge, Massachusetts: Cambridge University Press, 2013, p. 977. ISBN: 978-0-521-89697-9.

[ZEN16] Li Zhu, Didier El-Baz, and Huangsheng Ning. "Survey on air levitation conveyors with possible scalability properties". In: *Proceedings - 2015 IEEE 12th International Conference on Ubiquitous Intelligence and Computing, 2015 IEEE 12th International Conference on Advanced and Trusted Computing, 2015 IEEE 15th International Conference on Scalable Computing and Communications, 20* (2016), pp. 802–807. DOI: 10.1109/UIC-ATC-ScalCom-CBDCom-IoP.2015.158.

[Zha+17] Zhenishbek Zhakypov et al. "Modular and reconfigurable desktop microfactory for high precision manufacturing". In: *International Journal of Advanced Manufacturing Technology* (2017). ISSN: 14333015. DOI: 10.1007/s00170-016-9689-7.

[Zha+19] Ruoshi Zhang et al. "Design and characterization of solid articulated four axes microrobot for microfactory applications". In: *Journal of Micro-Bio Robotics* 15.2 (2019), pp. 119–131. ISSN: 21946426. DOI: 10.1007/s12213-019-00118-y.

[Zie19] Tomasz G. Zielinski. *Fundamentals of piezoelectricity*. 2019.

[ZK18] Christian Zammit and Erik Jan van Kampen. "Comparison between A* and RRT algorithms for UAV path planning". In: *AIAA Guidance, Navigation, and Control Conference, 2018* 210039 (2018), pp. 1–23. DOI: 10.2514/6.2018-1846.

[ZTP19] Haiyue Zhu, Tat Joo Teo, and Chee Khiang Pang. "Magnetically Levitated Parallel Actuated Dual-Stage (Maglev-PAD) System for Six-Axis Precision Positioning". In: *IEEE/ASME Transactions on Mechatronics* 24.4 (2019), pp. 1829–1838.

Colophon

Document created using LaTeX 2$_\varepsilon$ written on TeXStudio. Typesetting used LuaLaTeX and fonts by Ross Mills and John Hudson of Tiro Typeworks. Bibliography managed and created using Mendeley and BibLaTeX. Illustrations and schema drawn with Inkscape: Open Source Scalable Vector Graphics Editor. Graphs and plots generated with Matlab.